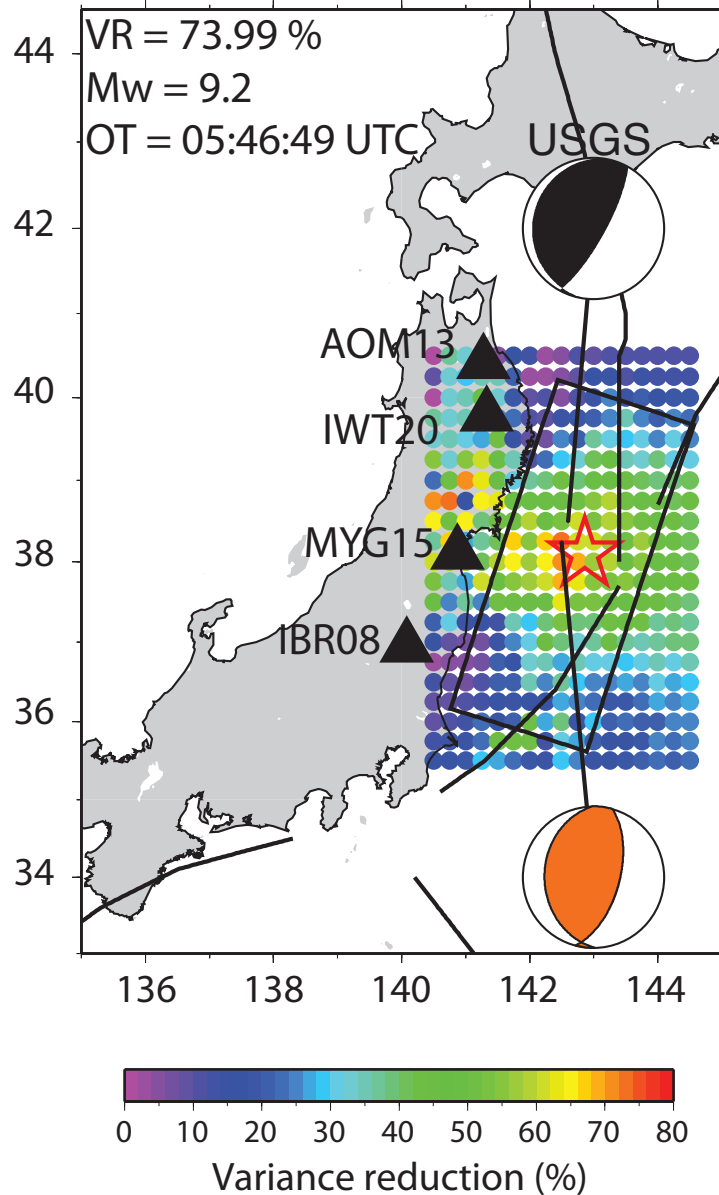


Berkeley Seismological Laboratory



Annual Report
July 2010 - June 2011

Berkeley Seismological Laboratory
Annual Report
July 2010 - June 2011

Cover Picture

From Research Section 6: Rapid characterization of great subduction zone earthquakes, such as the 2011 M9.0 Tohoku-oki, Japan, event, is vital for quickly assessing the likelihood of tsunami generation. We have developed an approach, called GridMT, that continuously scans a grid of possible sources along the subduction zone surface.

When energy arrives at the seismic stations it is used to estimate the location, size and mechanism of the earthquake. We applied it to the 2011 Tohoku-oki earthquake. This figure shows a map of virtual sources distributed along the slab. They are color-coded by the best variance reductions (VR) that are obtained from the continuous moment tensor analysis of long-period (100-200 sec) strong-motion data recorded at four K-NET stations (triangles).

The best GridMT solution (Mw9.2 and VR=73.99)

Contents

1	Director's Report	1
1	Introduction	1
2	History and Facilities	2
3	BSL Staff News	3
4	Acknowledgements	4
2	Research Studies	5
1	ElarmS Earthquake Early Warning	6
2	ShakeAlert: A Unified EEW System for California	8
3	Validation of Coda-derived Source Parameters using Strong and Weak Ground Motion Records of the 2008 Wells, Nevada Sequence	10
4	Quantitative Analysis of Coda Window Length: How Much Length of Coda is Enough for Stable Amplitudes?	12
5	Source Characterization of Mendocino Offshore Earthquakes for Improvements in Monitoring Active Deformation and Estimates of Earthquake Potential in the Mendocino Triple Junction Region	14
6	Detecting the 2011 M9.0 Tohoku Earthquake with Moment Tensors	16
7	Time-Lapse Monitoring for Detection of Transient Stress Changes in Geysers Geothermal Field	18
8	Measuring Fault-Zone Rheology at Depth from Characteristically Repeating Earthquakes	20
9	Free-Surface Vanishing Traction Effects on Shallow Sources	22
10	Moment Tensors for Aftershocks of the M 7.9 Wenchuan Earthquake	24
11	Focal Depth of the 2008 Panzhihua Earthquake from Depth Phase sPL and Joint Inversion of Local and Teleseismic Waveforms	26
12	Deviatoric Moment Tensor Analysis at The Geysers Geothermal Field	28
13	Slip Transients, Deficit and Release from Repeating Earthquakes	30
14	Immediate Triggering of Small Repeating Earthquakes at Parkfield	32
15	Joint Inversion of Seismic and Geodetic Data for the Source of the 4th March 2010 M_w 6.3 Jia-Shian, SW Taiwan, Earthquake	34
16	Tidal Triggering of LFEs near Parkfield, CA	36
17	TremorScope: Imaging the Deep Workings of the San Andreas Fault	38
18	Search for Transient Deformation Following an Earthquake Sequence near San Juan Bautista	40
19	Probing the Deep Rheology of Tibet: Constraints from 2008 M_w 7.9 Wenchuan, China Earthquake	42
20	Joint Seismic and Geodetic Analysis of the 2009 Padang, Sumatra Intraslab Earthquake	44
21	Rapid Detection of Large Earthquakes Using Quasi-Finite-Source Green's Functions in Moment Tensor Analysis	46
22	Identifying Undetected Early Aftershocks Associated with the 12 August 1998 M_w 5.1 San Juan Bautista Earthquake	48
23	Persistent Scatterer InSAR Analysis of Berkeley Hills Landslides	50
24	Toward Global Waveform Tomography with the SEM: Improving Upper-Mantle Images at Shallow Depths	52
25	On the Interpretation of SKS Splitting Measurements in the Presence of Several Layers of Anisotropy	54
26	Anisotropic Stratification in the Continental Upper Mantle	56
27	Refining the Cratonic Upper Mantle Using RegSEM	58
28	Investigating Upper Mantle Discontinuities Beneath Subduction Zones	60
29	Small-scale Variation of SS Precursors Observed by US Transportable Array	62
30	Investigation of Cascadia Segmentation with Ambient Noise Tomography	64

31	Characterization of the Pacific Superplume Boundary	66
32	An Automated Despiking Algorithm for Seismic Normal Mode Data	68
33	Seismic Imaging of the San Andreas Fault in Northern California using Receiver Functions	70
3	BSL Operations	73
1	Berkeley Digital Seismic Network	75
2	California Integrated Seismic Network	85
3	Northern Hayward Fault Network	90
4	Parkfield Borehole Network (HRSN)	99
5	Bay Area Regional Deformation Network	110
6	Northern California Earthquake Data Center	115
7	Data Acquisition and Quality Control	125
8	Northern California Earthquake Monitoring	135
9	Outreach and Educational Activities	141
	Glossary	143
	Appendix I Publications, Presentations, Awards, and Panels 2010-2011	145
	Appendix II Seminar Speakers 2010-2011	157
	Appendix III Organization Chart 2010-2011	159

Chapter 1

Director's Report

1 Introduction

As in previous years, I am pleased to introduce the 2010-11 Berkeley Seismological Laboratory Annual Report, the last one under my tenure as BSL director. This report covers two coupled activities at BSL: basic research and real-time earthquake monitoring operations. Chapter 2 describes the research accomplishments; Chapter 3 details progress in our development of infrastructure and facilities.

The basic research spans many topics in seismology and tectonics. They range from studies of the earth's deep structure and dynamics to various aspects of earthquake physics; from microearthquakes and tremor studies to studies of earthquake mechanisms and rupture spanning different time scales; and from slow tectonic deformation to real-time seismology and earthquake early warning. These are described in 32 "two-pager" contributions in Chapter 2 of this report.

A highlight of this year has been the participation of BSL scientists in a symposium: "Earthquakes, Tsunamis, and Nuclear Fallout: Is California at Risk Like Japan?" hosted by the Berkeley Institute for the Environment, the Department of Earth and Planetary Science, the Berkeley Seismological Laboratory, and the Pacific Earthquake Engineering Research Center following the March 11, 2011 disastrous M9 Great Tohoku earthquake. The BSL also hosted a successful Earthquake Early Warning Summit on April 4-5, 2011, in response to the increased interest in real-time earthquake information and early warning specifically following the Japan earthquake.

Another highlight of this year is the funding by the Gordon and Betty Moore Foundation of "Tremorscope," a program which aims at understanding deep tremor activity on the San Andreas Fault near Parkfield, right below the nucleation zone of the great 1857 Fort Tejon ("Los Angeles") earthquake. The program includes the deployment of eight stations, of which four will be in boreholes, centered on the tremor source.

On the operational side of the BSL, owing to significant funding received through the USGS in the framework of the American Recovery and Reinvestment Act (ARRA),

the focus has been on upgrading the recording systems at many of our broadband and borehole stations. These upgrades were much needed, as many of the recording systems were more than 15 years old, well beyond the expected lifetime of computer hardware. At the time of the writing of this report, we have completed the upgrade of our broadband stations with state of the art Quanterra Q330 data loggers, while the upgrade of our borehole stations with Kinometrics BASALT data loggers is well under way. We also received funding to upgrade receivers at our 29 BARD stations and to add GPS receivers at 7 of our BDSN stations. The new receivers allow us to stream high rate (1 Hz sampling) GPS data and to start implementing the use of GPS data in our real-time earthquake analysis procedures. At the time of this report, 12 stations have been upgraded with TopCon receivers. When these receivers were originally delivered, they did not have all the needed functionalities for smooth remote real-time continuous operation. It took many months of tests and iterations with the manufacturer to get them to work to our satisfaction. Given these difficulties, the USGS approved a six month extension on this ARRA grant. The work will be completed by the end of December, 2011. Notwithstanding this situation with upgrades, all BARD stations have been streaming 1 Hz continuous data since December 2010. These data are available through the recently redesigned BARD webpage at the Northern California Earthquake Data Center (NCEDC).

The joint BSL/USGS earthquake notification system had been redesigned in previous years. The new integrated Northern California Earthquake Management Center (NCEMC) has now been in operation for two years. We had an opportunity to thoroughly test the robustness of the new AQMS software on two occasions: (1) when the USGS component of our joint system was shut down for a test of the USGS power system and (2) when upgrades to Warren Hall at UC Berkeley impacted the operations of the Berkeley component. In both cases, all operations were transferred seamlessly to the single operational component for the duration of the disturbance.

The redesign of the STS-1 very broad band seismometer under Metrozet's leadership has been completed, with

funding from the NSF EAR-Instruments and Facilities Program. The M9 03/11/2011 Tohoku (Japan) earthquake was well recorded on the entire BDSN network as well as at test sites for the new STS-1's at Harvard (HRV) and the Albuquerque Seismological Laboratory, providing an opportunity to confirm the superior performance of the new instruments at very low frequencies.

The following sections give a brief historical overview of the BSL, and finally some BSL staff news.

2 History and Facilities

The Berkeley Seismological Laboratory (BSL), formerly the Berkeley Seismographic Stations (BSS), is the oldest Organized Research Unit (ORU) on the UC Berkeley campus. Its mission is unique in that, in addition to research and education in seismology and earthquake-related science, it is responsible for providing timely information on earthquakes (particularly those that occur in Northern and Central California) to the UC Berkeley constituency; to the general public; and to various local and state governments, and private organizations. The BSL is therefore both a research center and a facility/data resource, which sets it apart from most other ORUs. A major component of our activities is focused on developing and maintaining several regional observational networks, and participating, along with other agencies, in various aspects of the collection, analysis, archival, and distribution of data pertaining to earthquakes, while maintaining a vigorous research program on earthquake processes and Earth structure. In addition, the BSL staff spends considerable time on public relations activities, including tours, talks to public groups, response to public inquiries about earthquakes, and World-Wide-Web presence (<http://seismo.berkeley.edu/>).

UC Berkeley installed the first seismograph in the Western Hemisphere at Mount Hamilton (MHC) in 1887. Since then, it has played a leading role in the operation of state-of-the-art seismic instruments and in the development of advanced methods for seismic data analysis and interpretation. Notably, the installation, starting in 1927, of Wood-Anderson seismographs at four locations in Northern California (BKS, ARC, MIN, and MHC) allowed the accurate determination of local earthquake magnitude (M_L) from which a unique historical catalog of regional earthquakes has been maintained to this day, providing crucial input to earthquake probabilities studies.

Over the years, the BSS continued to keep apace of technological improvements. The first centrally telemetered network using phone lines in an active seismic region was installed by BSS in 1960. The BSS was the first institution in California to operate a 3-component "broadband" system (1963). It played a major role in

the early characterization of earthquake sources using "moment tensors" and source-time functions. The BSS also made important contributions to the early definitions of detection/discrimination of underground nuclear tests and, jointly with UCB Engineering, to earthquake hazards work. Starting in 1986, the BSS acquired four state-of-the-art broadband instruments (STS-1), while simultaneously developing PC-based digital telemetry, albeit with limited resources. As telecommunication and computer technologies made rapid progress, in parallel with broadband instrument development, paper record reading was completely abandoned in favor of largely automated analysis of digital data.

The current facilities of BSL have been built progressively over the last two decades, with efforts initiated by significant "upgrade" funding from UC Berkeley in 1991-1995. The BSL currently operates and acquires data, continuously and in real time, from over 60 regional observatories. These house a combination of broadband and strong motion seismic instrumentation installed in vaults, borehole seismic instrumentation, the permanent GPS stations of the Bay Area Regional Deformation (BARD) network, and electromagnetic sensors. The seismic data are fed into the BSL real-time processing and analysis system. Since 1996, they are used in conjunction with data from the USGS Northern California Seismic Network (NCSN) in the joint earthquake notification program for Northern California. This program capitalizes on the complementary capabilities of the networks operated by each institution to provide rapid and reliable information on the location, size and other relevant source parameters of regional earthquakes. In recent years, a major emphasis in BSL instrumentation has been in densifying the state-of-the-art seismic and geodetic networks. At the same time, research efforts have been directed toward the development of robust methods for quasi-real time, automatic determination of earthquake source parameters and predicted strong ground motion, using a sparse network combining broadband and strong motion seismic sensors, as well as permanent geodetic GPS receivers. Recently, research emphasis has been directed toward the development of "earthquake early warning" capabilities.

The Berkeley Digital Seismic Network (BDSN), a regional network of 32 digital broadband and strong motion seismic stations with continuous telemetry to UC Berkeley, is the backbone of the BSL operations. This network contributes basic regional data for real-time estimation of location, size and rupture parameters for earthquakes in Central and Northern California. It is the Berkeley contribution to the California Integrated Seismic Network (CISN). In June 2009, our operational software, the Rapid Earthquake Data Integration (REDI) program, was replaced by the CISN, now AQMS, software (see Chapter 3, Operational Section 8). The data

from the BDSN also provide a fundamental database for the investigation of three-dimensional crustal structure and its effects on regional seismic wave propagation. This is ultimately crucial for estimating ground shaking for future earthquakes. Most stations also record auxiliary temperature/pressure channels, valuable in particular for background noise quality control. Complementing this network is a ~ 25 station “high-resolution” network of borehole seismic sensors located along the Hayward Fault (HFN) and under the Bay Area bridges, operated jointly with the USGS/Menlo Park and linked to the Bridge Safety Project of the California Department of Transportation (Caltrans). The latter has facilitated the installation of sensor packages at 15 bedrock boreholes along 5 East Bay bridges in collaboration with Lawrence Livermore National Laboratory (LLNL). A major science goal of this network is to collect high signal-to-noise data for micro-earthquakes along the Hayward Fault to gain insight into the physics that govern fault rupture and its nucleation. The BSL also operates and maintains the 13 element Parkfield borehole seismic array (HRSN). This array provides high quality data on micro-earthquakes, clusters and, most recently, tremors, and is an important reference for the San Andreas Fault Observatory at Depth (SAFOD). Since April 2002, the BSL collaborates with MBARI on the operation of a permanent broadband ocean bottom station, MOBB.

In addition to the seismic networks, the BSL operates, maintains and processes data from the 26 permanent geodetic stations of the BARD Network. It archives and distributes this data as well. Where possible, BARD sites are collocated with BDSN sites to minimize telemetry costs. In particular, all sites have now been upgraded to 1 Hz sampling. This supports one focus of BSL research, the development of analysis methods which combine seismic and geodetic data to rapidly estimate source parameters of significant earthquakes.

Finally, two of the BDSN stations (PKD, SAO) also share data acquisition and telemetry with 5-component electromagnetic sensors installed with the goal of investigating the possibility of detection of tectonic signals. In 2002-2003, automated quality control software was implemented to monitor the electromagnetic data.

Archival and distribution of data from these and other regional networks is performed at the Northern California Earthquake Data Center (NCEDC), operated at the BSL in collaboration with USGS/Menlo Park. The data reside on a mass-storage device (current holdings ~ 58 terabytes), and are accessible online over the Internet (<http://www.ncedc.org>). Among others, data from the USGS Northern California Seismic Network (NCSN), are archived and distributed through the NCEDC. The NCEDC also maintains, archives and distributes the ANSS earthquake catalog.

Core University funding to our ORU has until now

provided salary support for one staff scientist and several technical and administrative staff members, representing about 30% of the total infrastructure support. The remaining support comes from extramural grants and contracts, primarily from the USGS, the NSF, and the State of California, through its Emergency Management Agency (CalEMA, formerly OES). We acknowledge valuable recent contributions from other sources such as Caltrans and PEER, as well as our Earthquake Research Affiliates. The effects of drastic budget cuts in FY09-10 are temporarily being offset by ARRA funding from the USGS.

3 BSL Staff News

Changes in BSL staff in 2010-11 are as follows.

In the past year, none of the graduate students associated with BSL completed their PhD's.

One new graduate student, Andrea Chiang, joined the BSL as a graduate student in the fall of 2010. We also have one new post-doc, Seung-Hoon Yoo.

BSL hosted a number of visiting scientists and students in 2010-11. Ruiqing Zhang joined us from the Chinese Earthquake Administration in Beijing, China. Visiting graduate students included Xiangdong Lin, from the Beijing Earthquake Administration and graduate student at the Institute of Geophysics of the China Earthquake Administration; and Jiajun Chong, from the University of Science and Technology in China. In January, Ling Lei returned to School of Electronic and Information Engineering (EIE) at Beihang University to complete her Ph.D. Matt Wilks, an undergraduate at Imperial College London, spent the academic year at the BSL. Matthias Obrebski left his post-doc position at the BSL to join IFREMER Brest in France, while another post-doc, Paul Cupillard, is now at now a post-doctoral researcher in the Institute de Physique du Globe de Paris seismology group.

There have been major changes in the administration of the BSL: Kate Lewis left in January 2011 to work for SPO. Following a year under Research Enterprise Services (RES), BSL administration has now been regrouped in a joint EPS/BSL administrative unit headed by Earth and Planetary Science Department (EPS) Manager Judith Coyote. The administrative functions are now coordinated between the two units, with Dawn Geddes taking on the responsibility of the BSL operational budget and its associated grants and contracts and Raluca Iordache and Clarissa Foreman taking on the research grant administration for BSL PIs. Micaelee Ellswythe now assists PI Romanowicz with administrative tasks related to the CIDER program. Two new members of the EPS/BSL administrative team have joined Dawn in the BSL administrative office: Marion Banks, who started in May 2011 and is in charge of reception and travel, and Matt

Carli, who started in June 2011 and deals with purchasing. Owing to Judith's efforts, the reorganization is now complete and we are finally able to resume smooth administrative operations.

There have also been significant changes in the field engineering staff at the BSL. Rick Lellinger and Jarrett Gardner left mid-year, accepting job offers at LBNL and from a private company, respectively. Since then, assistant engineers Josh Miller and Aaron Enright have joined the team. Finally, John Friday retired in June 2011. We miss him and hope he will come back part time this fall!

In the IT team, Oleg Khainovsky left in January 2011, and Ivan Henson joined the team in April 2011, to work on software development for the Earthquake Early Warning project and the CISN.

Tom Weldon joined the research staff in January 2011.

The greater BSL family has continued to grow in the past year, when baby Roger Brown was born to Holly Brown and her husband Tom in December 2010.

4 Acknowledgements

I wish to thank our technical and administrative staff, scientists and students for their efforts throughout the year and their contributions to this annual report. Individual contributions to activities and report preparation are mentioned in the corresponding sections, except for the appendix sections, which were prepared by Jennifer Taggart.

I also wish to specially thank the individuals who have regularly contributed to the smooth operation of the BSL facilities: Mario Aranha, Doug Dreger, Aaron Enright, John Friday, Jarrett Gardner, Peggy Hellweg, Ivan Henson, Ingrid Johanson, Bill Karavas, Oleg Khainovski, Rick Lellinger, Josh Miller, Pete Lombard, Rick McKenzie, Bob Nadeau, Doug Neuhauser, Charley Paffenbarger, Jennifer Taggart, Taka'aki Taira, Stephen Thompson, Bob Uhrhammer, Tom Weldon, and Stephane Zuzlewski, and, in the administrative office, Marion Banks, Matt Carli, Judith Coyote, Dawn Geddes, Kate Lewis, and Gretchen vonDuering. I also wish to thank our undergraduate assistants, Chris Rawles, David Tang, Landon Turner, Ryan Turner, and Tam Visher, for their contributions to our research and operations activities.

I am particularly grateful to Jennifer Taggart and Peggy Hellweg for their help in putting together this annual report and bringing it to completion.

The Annual Report of the Berkeley Seismological Laboratory is available on the Web at http://seismo.berkeley.edu/annual_report.

Chapter 2

Research Studies

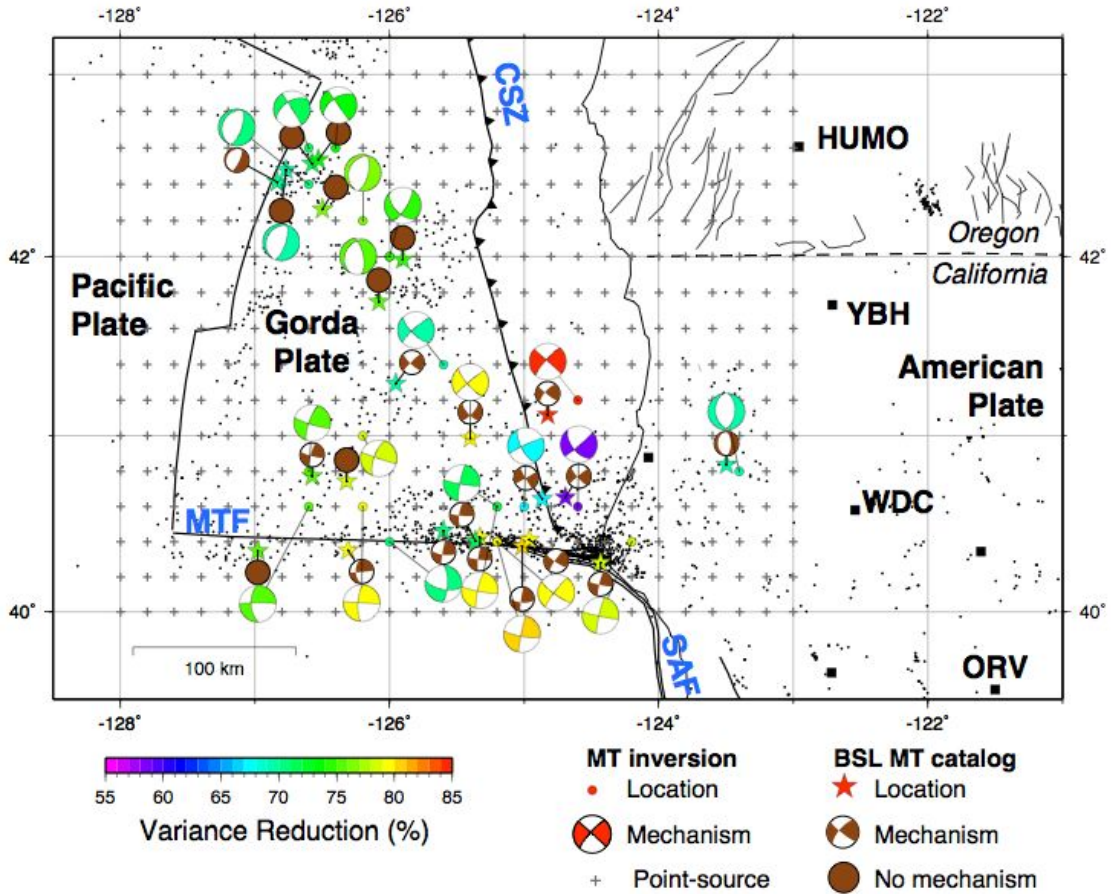


Figure 2.1: For large earthquakes that may produce tsunamis, it is important to determine the size and type of faulting of the event rapidly. We have developed a method to continuously scan an offshore region for earthquakes, and quickly determine their size and mechanism (see Research Section 21). The method is currently being applied to the region of the Mendocino Triple Junction, using data from four BDSN stations (HUMO, ORV, WDC and YBH). The pluses are the grid locations used in the search, while black dots show the region's seismicity since 1990. Mechanisms for the events studied are given from this analysis (large, light gray) and compared with solutions from the Berkeley moment tensor catalog (small, dark gray). For a color version of this figure see Research Section 21.

1 ElarmS Earthquake Early Warning

Holly Brown, Richard Allen, Douglas Neuhauser, Ivan Henson, Margaret Hellweg, Lim InSeub (KIGAM), Alon Ziv (BenGurion University)

1.1 Introduction

ElarmS is a network-based earthquake early warning (EEW) algorithm developed at UC Berkeley for rapid earthquake detection, location and hazard assessment. ElarmS operates as part of the greater ShakeAlert EEW system, an ongoing project by the California Integrated Seismic Network (CISN). ShakeAlert combines three different EEW algorithms, one of which is ElarmS, into a unified system for providing warnings for events throughout the state. Output from the three algorithms is compared and consolidated by the ShakeAlert Decision Module into a single alert messaging system. In fiscal year 2011-2012, these alert messages will be sent to industrial test users of the ShakeAlert system.

ElarmS consists of two primary parts: (1) a waveform processing algorithm, which runs in parallel at UC Berkeley, Caltech, and USGS Menlo Park to continuously filter real time seismic data, and (2) a single state-wide event detection algorithm which operates at UC Berkeley. The event detection module analyzes the incoming data from the three waveform processing streams and identifies earthquakes in progress.

1.2 Current Progress

In March 2011, ElarmS began sending event messages to the ShakeAlert Decision Module for events in the greater San Francisco Bay Area and Central Coast. Between March 17th and July 26th, 2011, there were 49 events of magnitude 3.0 or greater in the ElarmS alert region. ElarmS sent alert messages for 45 of them, and missed 4 (Figure 2.2). ElarmS also sent two false alerts. In both false alert cases, there was a single real event which ElarmS processed as two separate events - associating some triggers with one event and some triggers with the other. The alert message sent for the second “event” is thus a false alarm, although based on real seismic activity.

In 2010 and 2011, we developed second generation ElarmS waveform processing and event detection algorithms, based in C++ for speed and adaptability. The new event detection module (E2) utilizes the established location and magnitude relations, but has an updated method of associating triggers together to form events. One goal of the new associator is to prevent split events such as those that caused the false alerts mentioned above. E2 has been processing statewide real-time data in test mode since December 2010 and will become the authoritative ElarmS version in fall 2011.

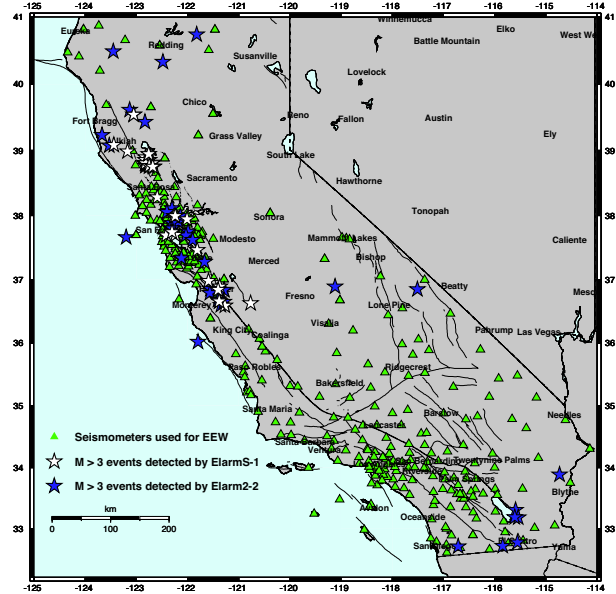


Figure 2.2: ElarmS events, March 17 - July 26, 2011

In addition to the second generation ElarmS algorithms, we developed a KML-based method of visually inspecting and assessing system performance. The assessment software automatically evaluates station latencies, promptness of alerts, accuracy of magnitude/location/ground-shaking estimates, and number of successful event detections, false alarms, and missed events. This information is displayed in Google Earth for quick, intuitive understanding of system health.

1.3 Investigation of GPS

In 2011 we also began investigating the use of GPS for earthquake early warning, focusing on the M_w 7.2 El Mayor-Cucapah earthquake, which had both real-time GPS and seismic data available. We developed a simple algorithm to extract the permanent displacement at GPS sites starting one oscillation after triggering on the dynamic long period signal. The estimate is continually improved with time. These permanent displacements can then be inverted for source characteristics given an approximate estimate of the fault plane. Initial results suggest that GPS would provide a valuable contribution to EEW. The new approach provides an independent estimate of magnitude, which is particularly important for the largest events.

1.4 Acknowledgements

This project is funded by USGS/NEHRP award 06HQAG0147.

1.5 References

Brown, H., R.M. Allen, M. Hellweg, O. Khainovski, D. Neuhauser, and A. Souf, Development of the ElarmS methodology for earthquake early warning: Realtime application in California and offline testing in Japan, *Soil Dynamics and Earthquake Engineering*, 31, 188-200, 2011.

Allen, R.M., Seconds before the big one, *Scientific American*, 2011.

Allen, R.M. and A. Ziv, On the potential implementation of real-time GPS in earthquake early warning systems: The Mw 7.2 El Mayor-Cucapah Earthquake test case, *Geophys. Res. Lett.*, in review.

2 ShakeAlert: A Unified EEW System for California

Margaret Hellweg, Richard Allen, Maren Böse (Caltech), Holly Brown, Georgia Cua (ETH), Egill Hauksson (Caltech), Thomas Heaton (Caltech), Margaret Hellweg, Ivan Henson, Doug Neuhauser, Kalpesh Solanki (Caltech), Michael Fischer (ETH)

2.1 Introduction

Earthquake Early Warning (EEW) is a method of rapidly identifying an earthquake in progress and transmitting alerts to nearby population centers before damaging ground shaking arrives. The first few seconds of the initial P-wave arrivals at one or more stations are used to detect the event, and predict magnitude and peak shaking. Detections from several stations are combined to locate the event. A warning of imminent shaking can be used to activate automatic safety measures, such as slowing down trains, isolating sensitive factory equipment, or opening elevator doors. Warnings can also be sent directly to the public via cell phone, computer, television, or radio.

With support from the United States Geological Survey (USGS), the California Integrated Seismic Network (CISN) hosted a three-year proof of concept project for EEW algorithms in 2006-2009. Following that successful project, the Berkeley Seismological Laboratory (BSL) together with its CISN EEW partners, the California Institute of Technology (Caltech), and the Swiss Institute of Technology Zürich (ETH), are collaborating to build a single, integrated, end-to-end system for testing real-time EEW in California. The new system, called CISN ShakeAlert, will be capable of continuous long-term operation and rapidly provide alerts to test users across the state.

2.2 Project Status

The new ShakeAlert system combines the best aspects of the three methods from the proof-of-concept project. Caltech's OnSite algorithm uses P-wave data from the single station nearest the epicenter to provide extremely rapid estimates of likely ground shaking. The BSL's ElarmS algorithm and ETH's Virtual Seismologist algorithm use data from several stations around an event epicenter to produce a slightly slower but more reliable estimate of magnitude and location. Combining these methods produces an algorithm which has the speed of a single-station method but is then promptly confirmed and adjusted by additional station data to form a more accurate description of the event. When an identified event exceeds a defined combination of magnitude threshold, ground shaking intensity and statistical likelihood, information is broadcast to system users. Currently, during the development phase, only project participants receive event information. By the fall of 2011, event information will be sent to a small group of test users outside

the seismological community.

These tasks of the end-to-end system are accomplished in four primary software components (Figure 2.3). First, the Waveform Processing (WP) Module receives seismic waveforms from all early-warning capable seismic equipment in California. It identifies P-wave arrivals, and calculates the relevant P-wave parameters necessary for EEW magnitude estimation. Next, the Event Monitoring (EM) Module comprising the OnSite, Virtual Seismologist, and ElarmS algorithms recognizes events in progress and calculates event magnitude and location. It passes this information to the third component, the Decision Module (DM). The DM can receive event notifications from several systems, including the three algorithms of the EM module. It reviews events and determines whether to send warnings to users. The final component is the User Display (UD), which will be installed at an EEW user's site. When the UD receives a warning from the DM, it sounds an alarm and generates an alert message, a map of expected ground shaking intensities, or other output, depending on the user's settings.

The end-to-end system is now in operation. Caltech programmers developed the UD, while Berkeley programmers built the DM. The three CISN EEW partners (Caltech, BSL, ETH) are working together to jointly build a new, quicker and robust Waveform Processing Module.

2.3 Perspectives

During the coming year, the CISN EEW project members will continue to operate and improve the elements of the end-to-end system, including efforts to improve the speed and accuracy of alerts. We will recruit a group of test users outside of the seismology community and interact with them to develop improvements to the system, as well as to learn about the advantages of EEW to users and to society. Finally, results from the prototype system will flow into the CISN Testing Center (CTC) software, so that the results and output can undergo objective evaluation.

2.4 Acknowledgements

This project is supported at UC Berkeley by USGS Cooperative Agreement G09AC00259, at Caltech by Agreement G09AC00258, at USC/SCEC by Agreement G09AC00255 and at ETH Zürich by Agreement G09AC00256.

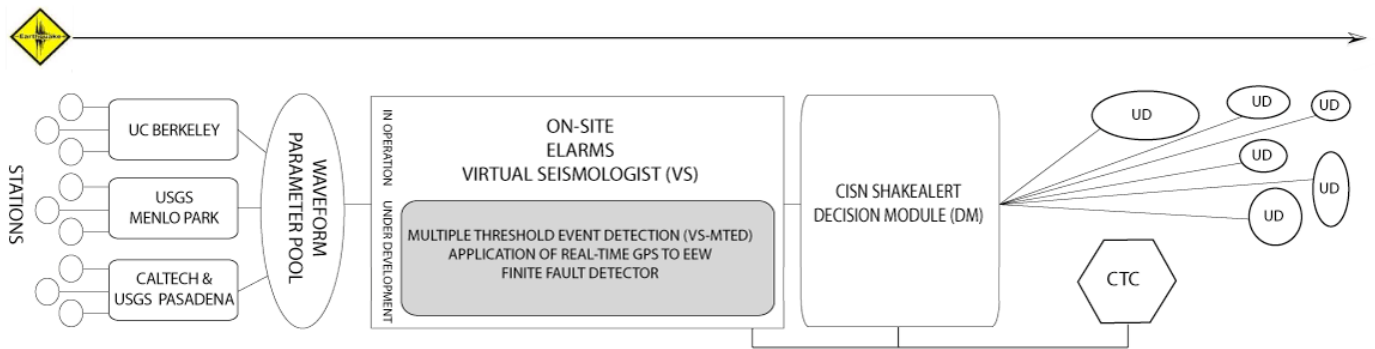


Figure 2.3: Components of the new ShakeAlert EEW System. From left to right the elements of the system are waveform processing, event detection, decision module (DM), CISN ShakeAlert user displays (UD), and the CISN testing center (CTC) software. *Waveform Processing:* Each data center processes telemetered digital waveform data collected from seismic stations throughout California. Critical waveform parameters are calculated from this data, then dumped into a statewide parameter pool. *Event Detection:* From the parameters, CISN’s EEW algorithms rapidly detect and characterize an event within seconds of its initiation. Several EEW detection algorithms run in parallel to provide the Decision Module with the best available source parameters. *Decision Module:* The DM combines earthquake information from each algorithm and delivers a “ShakeAlert” xml message about an earthquake in progress to subscribed users. *CISN ShakeAlert User Displays:* The ShakeAlert UD receives xml messages from the DM and displays their content in a simple and easily understandable way. *CISN Testing Center Software:* The CTC Software provides automated and interactive performance evaluations of ShakeAlert forecasts.

3 Validation of Coda-derived Source Parameters using Strong and Weak Ground Motion Records of the 2008 Wells, Nevada Sequence

Seung-Hoon Yoo, Douglas S. Dreger, and Kevin Mayeda

3.1 Introduction

Well-determined source parameters, such as corner frequency and stress drop, and their scaling relation, can play an important role in assessing the seismic hazard in a specific region, especially in regions where we do not have enough strong ground motion records. In general, ground motions at higher frequencies (1-10 Hz), which may cause damage to surface structures, can be considerably varied depending upon the stress drop of the earthquake, even for events with similar moment magnitude.

Petersen et al. (2011) found that while observed ground motions from the 2008 Wells mainshock are similar to values predicted by the Next Generation Attenuation (NGA) equation by *Campbell and Bozorgnia* (2008), the ground motion from the M 4.7 (M_w 4.4 from the Saint Louis University Earthquake Center moment tensor catalog, courtesy of *R. B. Herrmann* and this study) aftershock, which occurred the day after the mainshock, are much lower than values from the NGA equation. However, they estimated this aftershock’s stress drop as 220 bars, which is much higher than typical stress drops observed in the Basin and Range.

In this study, we revisited the 2008 Wells, Nevada sequence to examine a marked discrepancy in the observed strong and weak ground motion with the NGA predictions. We estimated the source parameters of the seismic sequence using the coda spectral ratio method (*Mayeda et al.*, 2007). And, we examined the observed strong and weak ground motion with the derived parameters and self-similar scaling relation.

3.2 Data and Method

We calculated source spectral ratios between the mainshock and the six aftershocks using the coda spectral ratio method (*Mayeda et al.*, 2007). We used a grid-search scheme to estimate the source parameters from the source spectral ratios. The program finds a corner frequency of the mainshock, and the corner frequency and adjusted seismic moment of the aftershocks from a given ratio dataset, simultaneously. To get the optimum source parameters and their errors, we performed bootstrap tests, which sample four event pairs of the six total ratio curves (~67 % sampling of a population), then calculated the averages and standard deviations for the results of the 15 possible combinations (Figure 2.4). Next, we calculated theoretical source ratios for periods of 0.2, 0.5, and 1 second using the derived source parameters. And we also calculated the theoretical values based on

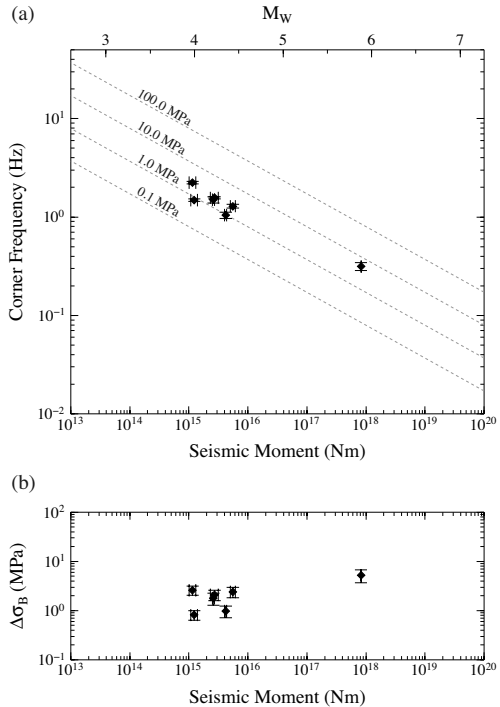


Figure 2.4: Estimates of the (a) corner frequency and (b) stress drop for the 2008 Wells, Nevada seismic sequence. The dotted lines in (a) represent the corner frequencies from the self-similar scaling for a given stress drop, $\Delta\sigma_B$.

the self-similar scaling with respect to the mainshock.

The Fourier amplitude spectrum of ground acceleration, $A(M_0, R, f)$, can be expressed as

$$A(M_0, R, f) = CM_0 (2\pi f)^2 S(f) D(R, f) P(f) I(f),$$

where C is a constant of proportionality, M_0 is the seismic moment, $S(f)$ is the source spectrum, $D(R, f)$ is an attenuation term as a function of distance R due to the geometrical spreading and anelastic attenuation, $P(f)$ is a high-cut filter, $I(f)$ is a filter used to shape the spectrum to correspond to the particular ground motion (e.g., *Boore*, 1983). If we calculate a ratio of the ground motions between the two collocated events, the ratio can be simply approximated by a source spectral ratio between the two events.

We computed the 5% damped pseudo spectral acceleration (SA) for the periods 0.2, 0.5, and 1 seconds as a geometric mean of two horizontal components (Figure 2.5a). Then, we calculated the ratios between the mainshock and the aftershocks for a given period and averaged

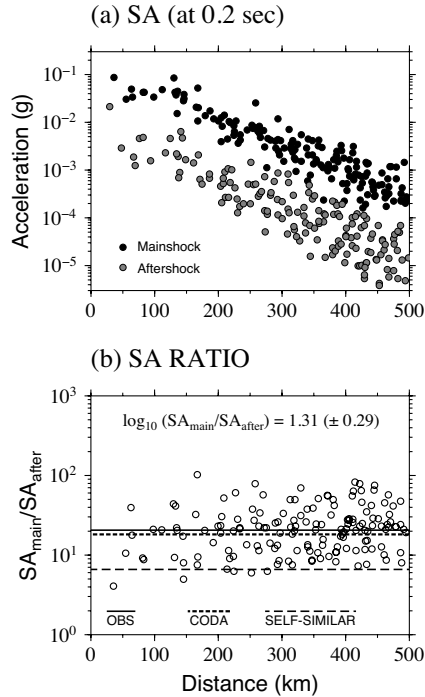


Figure 2.5: (a) The 5 % damped pseudo spectral acceleration (SA) of the mainshock (MS; black solid circles) and the aftershock (A3; gray solid circles), (b) comparison of the observed SA ratio (open circle and solid line) with the two theoretical values from the coda-derived source parameters (fine dotted line) and self-similar scaling relation (coarse dotted line).

using all the stations (Figure 2.5b).

3.3 Results and Discussions

The stress drop of the mainshock, $5.20 (\pm 1.52)$ MPa, is consistent with 7.2 MPa from an empirical Green's function finite fault inversion by *Mendoza and Hartzell* (2009), more or less. However, the stress drop of the aftershock A3, $1.00 (\pm 0.27)$ MPa, is much smaller than 22 MPa from Fourier spectra analysis by *Petersen et al.* (2011), and it is also about five times smaller than that of the mainshock in our estimation.

We compared the averaged SA ratio, $\log(SA_{main}/SA_{after})$, with theoretical values from the coda-derived source parameters and the self-similar scaling relation with respect to the mainshock. For the MS/A3 event pair, the observed SA ratio values at 0.2, 0.5, and 1 second periods are 1.31, 1.38, and 1.52, respectively, which are much more consistent with the theoretical values, 1.26, 1.34, and 1.53, from the coda estimates, than 0.82, 1.02, and 1.36 from the self-similar source scaling relation (Figure 2.5). For all the other event pairs, the theoretical values from coda estimates are more consistent with the observations than those from the self-similar scaling (Figure 2.6).

In conclusion, the stress drops of the aftershocks are 2-5 times smaller than that of the mainshock in this seis-

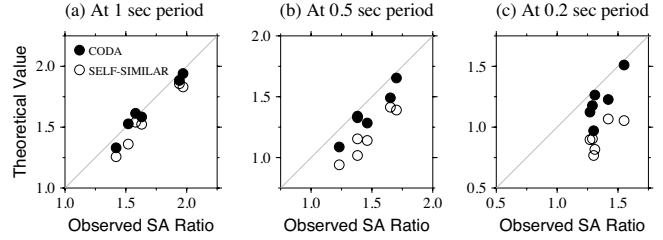


Figure 2.6: Comparisons of the theoretical source ratios for the coda-derived source parameters (solid circles) and self-similar scaling (open circles) with the observed SA ratios between the mainshock and six aftershocks at the 1, 0.5, and 0.2 second periods.

mic sequence. This indicates that weak ground motion of the aftershocks can be overestimated to be higher than the real observation using strong ground motion of the mainshock based on a self-similar scaling relation. Assuming that the scale-dependent stress drop is real, at least in some specific regions, predicting ground motion using weak ground motion records without considering the scaling relation could lead to an underestimate of strong ground motions for future large earthquakes. For the region, considering the differences in the stress drop between the small and large earthquake might help to enhance the prediction capability of the strong ground motion.

3.4 Acknowledgements

S.-H Yoo was partially supported by the National Research Foundation of Korea under Grant NRF-2010-357-C00135. S.-H. Yoo would like to thank Taka'aki Taira for beneficial comments and discussions.

3.5 References

- Boore, D. M., Stochastic simulation of high-frequency ground motions based on seismological models of the radiated spectra, *Bull. Seismol. Am.*, *73*, 1865-1894, 1983.
- Campbell, K. W., and Bozorgnia, Y., NGA ground motion model for the geometric mean horizontal component of PGA, PGV, PGD, and 5 % damped linear elastic response spectra for period ranging from 0.01 to 10 s, *Earthquake Spectra*, *24*, 139-172, 2008.
- Mayeda, K., Malagnini, L., and Walter W. R., A new spectral ratio method using narrow band coda envelopes: Evidence for non-self-similarity in the Hector Mine sequence, *Geophys. Res. Lett.*, *34*, L11303, doi:10.1029/2007/GL030041, 2007.
- Mendoza, C., and Hartzell, S., Source analysis using regional empirical Greens functions: The 2008 Wells, Nevada, earthquake, *Geophys. Res. Lett.*, *36*, L11302, doi:10.1029/2009GL038073, 2009.
- Petersen, M., Pankow, K., Biasi, G., Meremonte, M., Harmsen, S., Mueller, C., and Zeng, Y., Ground motions from the 2008 Wells, Nevada earthquake sequence and implications for seismic hazard, *Nevada Bureau of Mines and Geology Special Publication*, *36*, 163-172, 2011.

4 Quantitative Analysis of Coda Window Length: How Much Length of Coda is Enough for Stable Amplitudes?

Seung-Hoon Yoo, Kevin Mayeda, and William R. Walter (LLNL)

4.1 Introduction

In earthquake source estimation, coda-derived source methods provide more stable source parameters than methods using direct waves due to the inherent averaging nature of coda waves (Mayeda and Walter, 1996; Mayeda *et al.*, 2007). Unlike conventional direct-phase regional measurements (e.g., *Pg* or *Lg*), which take peak amplitude at the specific arrival time, the coda amplitude measurement through a relatively long time window can dramatically reduce the inter-station scattering by smoothing out 3-D path variability, source radiation pattern, and directivity effects (Mayeda and Malagnini, 2010).

Although a number of studies have shown this stability of the coda measurement, it is still unclear how much length of coda is enough for accurate measurements of coda amplitudes. Inappropriate short window measurement can not only lead to higher inter-station scatter of coda amplitudes, but can also give a distorted amplitude by using only earlier parts of a coda envelope, which shows a radical change in energy density with increasing lapse time. But long-lasting coda, which guarantee a stable measurement, are not always easy to obtain, because of small magnitude, low signal to noise ratio, and interfering aftershocks.

In this study, to address this unsettled question and quantify the optimum window length for accurate coda measurements, we analyze inter-station standard deviation of the coda ratios as a function of the time window length using an earthquake sequence data set that was well-recorded by a dense broadband seismic array. This allows us an in-depth look at the effects of coda on averaging over source radiation pattern and directivity and can help serve as a guide to future coda-based studies regarding how much window length is needed to get good measurements.

4.2 Data and Method

We use the broadband records of the 2008 Wells, Nevada seismic sequence to quantify the window length effect for coda amplitudes and source ratios in terms of reducing variance due to radiation pattern and directivity. Fortunately, because the EarthScope USArray temporary seismic network was operating in this region at the time of the earthquakes, this sequence can offer a great opportunity with a number of high-quality records and perfect distances and azimuthal coverage.

The seismic sequence consists of an M 6 mainshock

and its six aftershocks with magnitudes ranging between M 4.0 and 4.5. We select 162 broadband stations within about 500 km epicentral distance of the Wells mainshock. For each event at each station, we measure the coda amplitude for 24 narrowband frequencies ranging from 0.05 to 15 Hz. All amplitudes are measured from a one second window length to the end of the possible record for coda measurement based on signal to noise or existence of an interfering aftershock.

4.3 Preliminary Results and Discussions

Figure 2.7 shows the amplitude ratio between the mainshock and an M 4.4 aftershock for the direct *Lg* and coda waves. In general, the direct *Lg* amplitude ratios vary considerably with azimuth due to the source radiation pattern or directivity effects of the two events. The coda amplitude ratios with a relatively short window length (2nd row entries in Figure 2.7) behave similarly to the direct *Lg* ratio. With increasing window length (T_L), however, the azimuthal variations of the coda amplitude ratio decrease significantly.

To quantify a reduction of the standard deviation, we normalize the standard deviation values with the standard deviation values at the 1 second window length and divide the window length (T) by a central period (T_0). We found that normalized standard deviations linearly decrease with \log_{10} scales of T/T_0 , and the reduction rates depend on the central frequency (Figure 2.8). The higher frequency bands show a larger slope of reduction than lower frequency bands.

To find a best fitting curve, we used an empirical equation,

$$\sigma(\tau = T/T_0) = \begin{cases} 1 & (\tau < \tau_0) \\ 1 - p \log_{10}(\tau/\tau_0) & (\tau > \tau_0) \end{cases},$$

where p represents a reduction rate, while τ_0 represents a starting point of decay with reduction rate p .

Though these preliminary results show very interesting properties of coda stability for the Wells, Nevada sequence, they leaves us with other questions and ideas that we wish to pursue in the near future, namely: 1) To what extent does the reduction rate, p , behave the similarly for other parts of the world? 2) Can a single functional form that is frequency-dependent be used to characterize coda amplitude error as a function of measurement window length? 3) We would like to study other sequences with good signal-to-noise ratio in a variety of different tectonic settings. 4) We plan to test the methodology

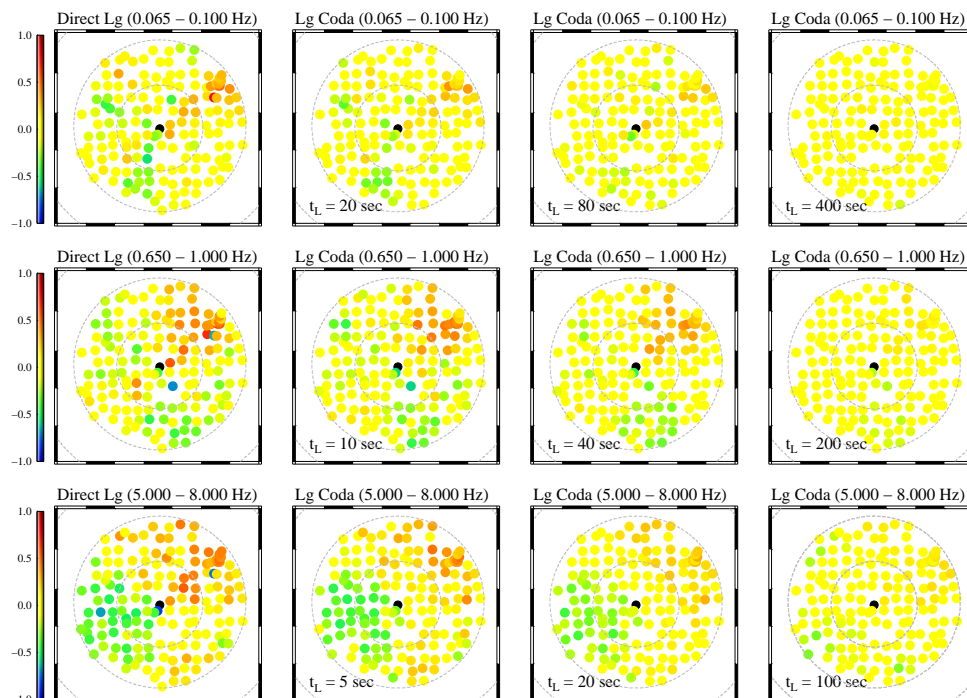


Figure 2.7: Coda amplitude ratios between the 2008 Wells mainshock and M 4.4 aftershock. Rightmost plots show the direct Lg amplitude ratios for given narrowband frequencies. The left side plots of the direct Lg ratio plots show the coda amplitude ratios with different window length (T_L) for the same frequency bands. The black circles in the subplot represent the location of the mainshock, and each colored circle represents a station. The small and large dotted circles represent 250 and 500 km iso-epicentral distance, respectively.

using a much smaller subset of stations, since the large amounts of data are not usually common.

4.4 Acknowledgements

S.-H Yoo was supported by the National Research Foundation of Korea under Grant NRF-2010-357-C00135. K. Mayeda was partially funded through LLNL’s GNEM program.

4.5 References

Mayeda, K., and Malagnini L., Source radiation invariant property of local and near-regional shear-wave coda: Application to source scaling for the Mw 5.9 Wells, Nevada sequence, *Geophys. Res. Lett.*, *37*, L07306, doi:10.1029/2009GL042148.

Mayeda, K., Malagnini, L., and Walter W. R., A new spectral ratio method using narrow band coda envelopes: Evidence for non-self-similarity in the Hector Mine sequence, *Geophys. Res. Lett.*, *34*, L11303, doi:10.1029/2007/GL030041, 2007.

Mayeda, K. and Walter, W. R., Moment, energy, stress drop, and source spectra of western United States earthquakes from regional coda envelopes, *J. Geophys. Res.*, *101*(B5), 11195-11208, 1996.

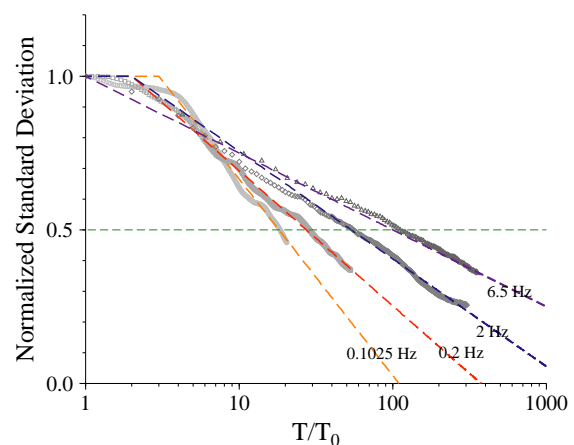


Figure 2.8: Normalized standard deviation versus normalized window length, T/T_0 , for the mainshock and M 4.4 aftershock pair. The dotted lines represent a best fit model for each data set (gray symbols). The reduction rates of normalized standard deviation vary with frequency and linearly decrease in a \log_{10} scale with T/T_0 . To reach 50 % reduction, higher frequencies need much larger T/T_0 values than lower frequencies.

5 Source Characterization of Mendocino Offshore Earthquakes for Improvements in Monitoring Active Deformation and Estimates of Earthquake Potential in the Mendocino Triple Junction Region

Taka'aki Taira and Robert M. Nadeau

5.1 Introduction

The Mendocino Triple Junction (MTJ), a fault-fault-trench junction, is one of the most seismogenic regions of California. The MTJ region has experienced a number of different fault slips (Figure 2.9), such as aseismic slip events (Szeliga *et al.*, 2004), non-volcanic tremors (Boyarko and Brudzinski, 2010), slow/low-stress-drop earthquakes (Guilhem *et al.*, 2007), deep low-frequency earthquakes (Boyarko and Brudzinski, 2010), and characteristically repeating microearthquakes (Waldhauser and Schaff, 2008). Apparently, the small-magnitude ambient seismicity (regular and characteristically repeating microearthquakes) is spatially anticorrelated with the distribution of non-volcanic tremor sources and low-frequency events (Boyarko and Brudzinski, 2010). However, the locations of those fault slips are not well constrained because of greater distances between the offshore fault slips and the available land seismic stations. Subsequently, the nature of interactions between seismic and aseismic deformation processes remains unclear.

We seek to integrate secondary phase arrivals with a local three-dimensional structure (Hole *et al.*, 2000) for improving the locations of fault slips, especially characteristically repeating earthquakes whose locations would delineate regions of locked fault zones. Additionally, repeating earthquake systematics (frequency and magnitude) can be used to estimate deep fault creep rates. Here we show an example of results from our frequency-wavenumber analysis and the preliminary result for the identification of characteristically repeating earthquakes.

5.2 Frequency-Wavenumber Analysis

We make use of seismic data from the Canadian Yellowknife Array (YKA), a small-aperture array consisting of 19 short-period stations, in order to identify secondary phase arrivals, particularly depth phases (pP and sP phases) and their phase conversions for $M > 4$ MTJ earthquakes (Figure 2.10). It appears that the YKA recorded depth phases from MTJ earthquakes well - particularly sP phases - because of larger S-wave energy from the source due to the combination of geometry between YKA and MTJ earthquakes and the majority of right lateral strike-slip faulting in the MTJ fault zone (Figure 2.10b). With the depth phase identified from the YKA seismic array data, we were able to constrain the focal depth of the 2007 M_w 5.0 MTJ event to be 24 km (Fig-

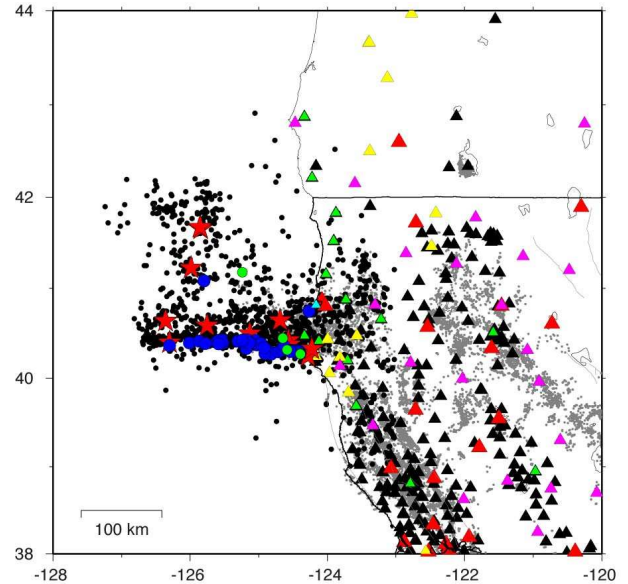


Figure 2.9: Location of the MTJ earthquakes (gray circles) during 1984-current from the NCEDC catalog. Back dots are $M > 3$ earthquakes analyzed in our preliminary analysis to identify characteristically repeating earthquakes. Blue circles are identified repeating earthquakes. Also shown are slow/low-stress-drop earthquakes (green circles) (Guilhem *et al.*, 2007) and $M > 6$ earthquakes (red stars). Triangles are seismic stations. Red triangles are the broadband stations of BDSN. Black and green ones are USGS's short-period and broadband seismic stations, respectively. Yellow triangles are the PBO borehole seismometers and the light blue one is the CGS borehole seismic array. Also shown are broadband seismometers of EarthScope Transportable Array (purple triangles).

ure 2.10c).

5.3 Characteristically Repeating Microearthquake

Our preliminary search for repeating microearthquakes in the MTJ region has revealed numerous and distributed sites of repeating microearthquake activity in the MTJ region (Figures 2.9 and 2.11). In the preliminary work, we have focused on $M > 3$ earthquakes in the MTJ region. We are currently extending our analysis to smaller earthquakes and are particularly interested in detecting temporal changes in fault creep rates inferred from re-

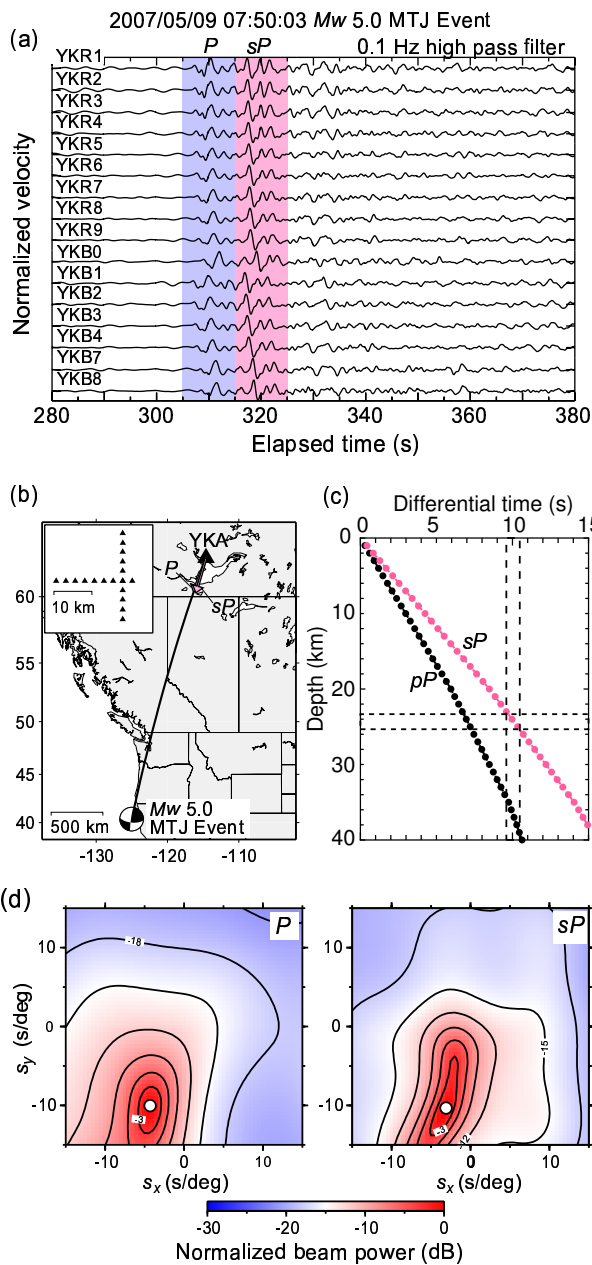


Figure 2.10: (a) An example of observed YKA data for the 9 May 2007 M_w 5.0 MTJ earthquake. The direct P and sP phases are seen at 310 s and 320 s, respectively. (b) Map view of the MTJ event and the YKA. Also shown are estimated back azimuths for P and sP phases. (c) Predicted time difference between P and sP (and pP) phases as a function of source depth using the ak135 velocity model (Kennett *et al.*, 1995). The time difference between sP and P phases of 10 s indicates the focal depth to be 24 km. (d) Frequency-wavenumber diagrams for P and sP phases. The slowness and back azimuth of the maximum power is marked by the white circle.

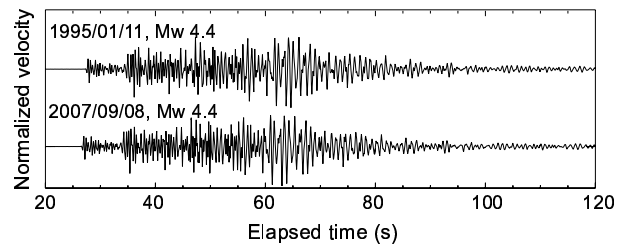


Figure 2.11: Characteristically repeating earthquakes identified from our preliminary analysis. An example of vertical seismograms recorded at station WDC for an earthquake doublet in the MTJ region. This earthquake doublet has the largest magnitude (M_w 4.4) among the identified repeating earthquake sequences. A 1-4 Hz bandpass filter was applied.

peating microearthquakes accompanying tectonic events (for example, the 9 January 2010 M 6.5 Gorda Plate earthquake).

5.4 Acknowledgements

We thank J. Hole for sharing the three-dimensional seismic velocity model with us. This work is supported by the U.S. Geological Survey NEHRP program under grant number G11AP20168.

5.5 References

- Boyarko, D.C. and M.R. Brudzinski, Spatial and temporal patterns of nonvolcanic tremor along the southern Cascadia subduction zone, *J. Geophys. Res.*, *115*, B00A22, doi:10.1029/2008JB006064, 2010.
- Guilhem, A., D.S. Dreger, and R.M. Nadeau, Scanning of unusual seismic activity in the Mendocino Triple Junction region, *EOS Trans. AGU*, *88*(52), Fall Meet. Suppl., Abstract S43-1047, 2007.
- Hole, J.A., B.C. Beaudoin, and S.L. Klemperer, Vertical extent of the newborn San Andreas fault at the Mendocino triple junction, *Geology*, *28*, 1111-1114, 2000.
- Kennett, B.L.N., E.R. Engdahl, and R. Buland, Constraints on seismic velocities in the Earth from traveltimes, *Geophys. J. Int.*, *122*, 108-124, 1995.
- Szeliga, W., T.I. Melbourne, M.M. Miller, and V.M. Santillan, Southern Cascadia episodic slow earthquakes, *Geophys. Res. Lett.*, *31*, L16602, doi:10.1029/2004GL020824, 2004.
- Waldhauser, F. and D.P. Schaff, Large-scale relocation of two decades of Northern California seismicity using cross-correlation and double-difference methods, *J. Geophys. Res.*, *113*, B08311, doi:10.1029/2007JB005479, 2008.

6 Detecting the 2011 M9.0 Tohoku Earthquake with Moment Tensors

Aurelie Guilhem and Douglas S. Dreger

6.1 Introduction

The M9 Tohoku earthquake offshore Japan that occurred on May 11, 2011 triggered strong local and regional shaking as well as a large-scale tsunami that caused major damage in both the near- and far-field. The Japanese earthquake and tsunami warning systems were able to detect and locate the earthquake; however information regarding the focal mechanism of the event was unknown until the moment tensor from the W-phase was published about 20 minutes after the event. Because of the dense Japanese seismic network of strong-motion stations (K-NET), this event gives us the opportunity to test the approach proposed by *Guilhem and Dreger, 2011* to rapidly detect, locate, and obtain the moment magnitude and mechanism of megathrust earthquakes.

6.2 Method

We use the method proposed by *Guilhem and Dreger (2011)* to automatically compute moment tensors on a grid of virtual sources distributed every 0.25 in latitude and longitude and at the slab depth, following a streaming data procedure. Here, the grid is defined by 357 nodes and overlaps the rupture of the M9 Tohoku earthquake (Figure 2.12). Moment tensors are computed every second, and the detection of the earthquake and its source information (location, seismic moment, mechanism, origin time) is obtained once the variance reduction (VR), which measures the fit between the data and the synthetics, reaches a maximum value and is above a threshold value (65%, for example). Velocity Green's functions (GFs) for each virtual source, and corresponding slab depths are pre-calculated using a 1D velocity model used by *Tsuruoka et al. (2009)* for the GridMT technique used in Japan. Because we target a large-scale earthquake, we include a source time duration in the GFs of 150 seconds.

6.3 Data

We download the strong-motion records of the M9 earthquake from the K-NET database, corresponding to a dataset of three-component acceleration seismograms for 273 stations. We select a set of 12 stations distributed along the earthquake rupture that recorded 300 seconds of data at 100 samples per second. We first correct the data for the instrumental gain and decimate them to 1 sample per second. Because the proposed method of *Guilhem and Dreger (2011)* for the rapid detection of $M > 7$ earthquakes uses very long-period (100-200 second) data and inverts 8 minutes of records, we extend the

strong-motion records by adding zeros to generate seismograms of 30 minutes in length; then we integrate them to velocity and use a causal bandpass filter with corner frequencies of 0.005 and 0.01 sec.

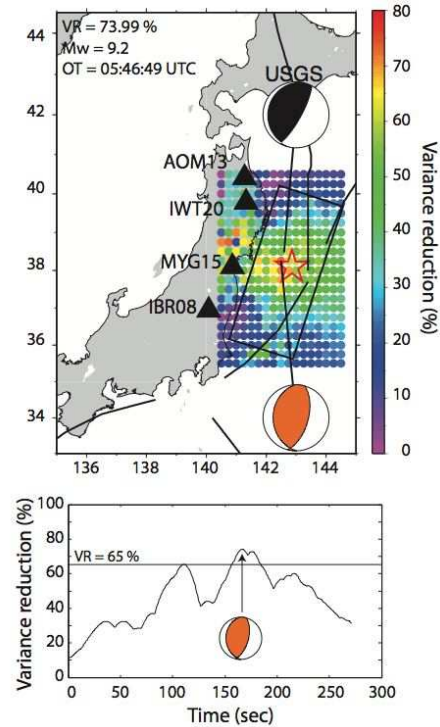


Figure 2.12: Map of the best moment tensor solutions using a set of strong motion stations distributed along the rupture. The star shows the JMA location, the black beach ball diagram shows the Global CMT USGS solution and the colored mechanism corresponds to the best solution using the grid. (See color version of this figure on the front cover.)

We use sets of four strong-motion stations per calculation, and we test the sensitivity of the moment tensor analysis for different limited station coverages (Figure 2.12).

6.4 Results

Figure 2.12 shows that the long period single point-source GFs used in the moment tensor approach allow the detection and characterization of the megathrust event with a high level of confidence (i.e. $>70\%$) even if the station coverage is limited. The best solutions are cen-

tered within the rupture segment, and our best solutions (i.e. with the largest VRs) are in close proximity to the USGS CMT solution (black mechanism in Figure 2.12) and to the JMA epicenter (red star). The origin time, the moment magnitude, and the mechanism that we find are in agreement with other datasets (USGS CMT, USGS W-phase, Global CMT). This shows that this analysis that uses a 100-200 sec passband does not suffer from saturation, which is a common problem observed for such large earthquakes, and was observed again for the M9 Tohoku earthquake. Also, the higher variance reduction estimates do appear to define the limits of the main slip area.

Finally, we find similar results when using restricted data coverage; i.e. when we use stations that are only located in the northern part of the rupture and inversely with stations located to the south of it (Figure 2.13). However, as Figure 2.13 shows, having stations located along the entire rupture enables us to better define the area of slip with the best VRs for the earthquake.

6.5 Conclusion

These results are very promising for the rapid detection and characterization of the major M9 Tohoku earthquake and other large magnitude subduction zone earthquakes. The 100-200 sec period strong-motion data do not saturate, and, as a consequence, the seismic moment and mechanism can be obtained within 8 minutes of the origin time. Because the M9 Tohoku earthquake had a compact slip region over a relatively small rupture length for similar sized earthquakes, the single point-source GFs work well. However, for more elongated slip models with multiple large slip areas, the use of quasi-finite-source GFs might provide better constraints on the events, as demonstrated by *Guilhem and Dreger* (2011).

6.6 Acknowledgements

Strong motion data for the 2011 M9.1 Japan earthquake are from the K-NET, National Research Institute for Earth Science and Disaster Prevention (NIED).

6.7 References

Guilhem, A., and D. S. Dreger, Rapid detection and characterization of large earthquakes using quasi-finite-source Green's functions in continuous moment tensor inversion, *Geophys. Res. Lett.*, 38, L13318, doi:10.1029/2011GL047550, 2011.

Tsuruoka, H., H. Kawakatsu, and T. Urabe, GRiD MT (grid-based real-time determination of moment tensors) monitoring the long-period seismic wavefield, *Physics of the Earth and Planetary Interiors*, 175, 8-16, doi:10.1016/j.pepi.2008.02.014, 2009.

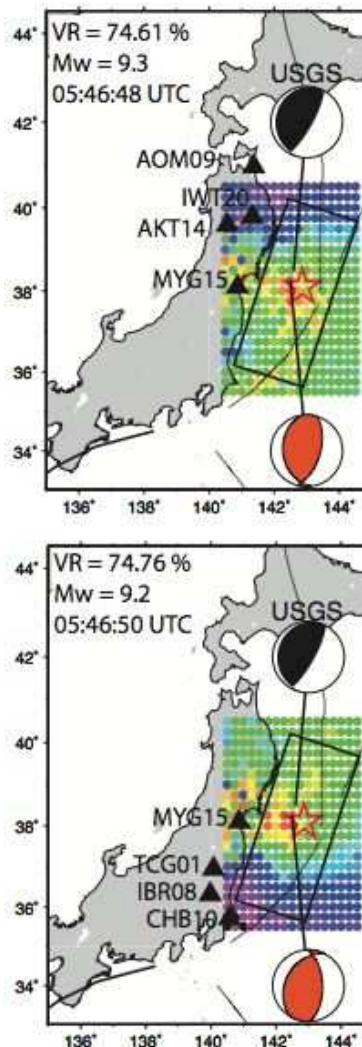


Figure 2.13: Map of the best moment tensor solutions using a set of strong motion stations distributed along the rupture.

7 Time-Lapse Monitoring for Detection of Transient Stress Changes in Geysers Geothermal Field

Taka'aki Taira

7.1 Introduction

Temporal changes in the properties of seismic structures are indicators of stress changes at depth, providing a means of continually monitoring the state of stress at seismogenic depth. At the Geysers geothermal field, we investigate stress-induced structural changes by making use of continuous seismic data at high sampling rates from dense seismic networks operated by LBNL and the USGS. Of particular importance to our work is the LBNL seismic network that contains 28 seismic stations distributed over the geothermal field (Figure 2.14). Each station consists of 3-component sensors with a natural frequency of 4.5 Hz sampled at 500 Hz.

7.2 Seismic Velocity Change

Our principal focus is on the imaging of time-varying properties of the seismic noise wavefield. Following *Bensen et al.* (2007), we analyzed data from August to December 2006, spanning the time of the 20 October 2006 M_w 4.6 Geysers earthquake. A reference Green's function was computed for each station pair by stacking the daily cross-correlations for the entire 5-month period (Figures 2.15a and b). The changes in seismic structure were determined by measuring time delays between the reference Green's function and 30-day stacks of cross-correlation functions in the frequency range from 0.1 to 0.9 Hz. Our preliminary result shows a change in cross-correlation function immediately after the 2006 M_w 4.6 Geysers earthquake, indicating that the delay time was increased by 0.08 s (Figure 2.15c). We infer the increased delay time to be a change in seismic velocity structure due to fluid redistribution around the fault resulting from a combination of both post-seismic stress relaxation and fault-zone damage induced by the M_w 4.6 earthquake.

7.3 Seismic Anisotropy Change

We additionally explore changes in seismic anisotropy properties through rotation of quasi-Rayleigh and quasi-Love wave polarization angles. In our preliminary analysis, we calculated the average noise cross-correlation functions between all components of the seismic noise wavefield between LBNL stations FUM and STY (Figure 2.16). Our result shows that a strong Rayleigh pulse at 0.4 s for both the vertical and radial point-force sources and a Love pulse at 0.3 s for the transverse point-force source are retrieved, which will allow us to investigate temporal changes in seismic anisotropy in this area.

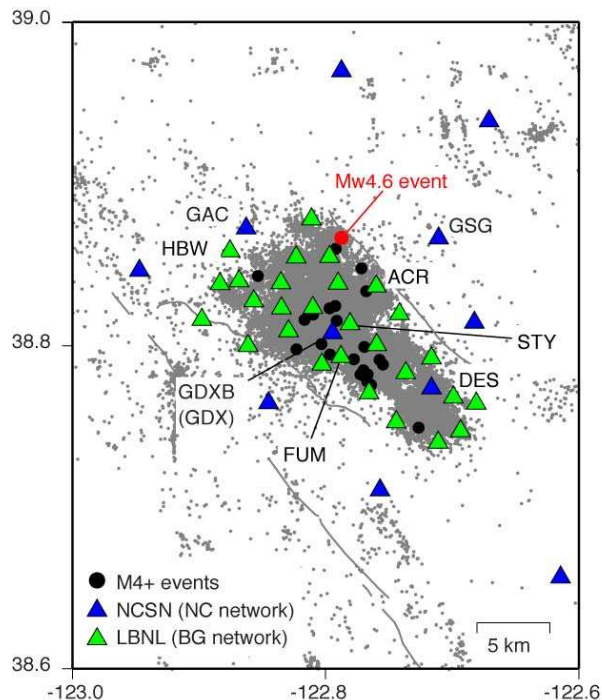


Figure 2.14: Map view of the Geysers area showing the 28 LBNL (green triangles) and USGS (blue triangles) seismic stations. Gray dots are locations of relocated earthquakes in this area during 1984 - 2008 (*Waldhauser and Schaff, 2008*). Also shown are M_4+ earthquakes (solid circles) since 1984. Red circle is the epicenter of the 2006 M_w 4.6 Geysers earthquake.

7.4 Acknowledgements

We thank P. Cupillard for discussion, and the NCEDC and LBNL for data collection and distribution. This work is supported by the National Science Foundation grant EAR-1053211.

7.5 References

- Bensen, G.D., M.H. Ritzwoller, M.P. Barmin, A.L. Levshin, F. Lin, M.P. Moschetti, N.M. Shapiro, and Y. Yang, Processing seismic ambient noise data to obtain reliable broadband surface wave dispersion measurements, *Geophys. J. Int.*, 169, 1239-1260, doi:10.1111/j.1365-246X.2007.03374.x, 2007.
- Waldhauser, F. and D. P. Schaff, Large-scale relocation of two decades of Northern California seismicity using cross-correlation and double-difference methods, *J. Geophys. Res.*, 113, B08311, doi:10.1029/2007JB005479, 2008.

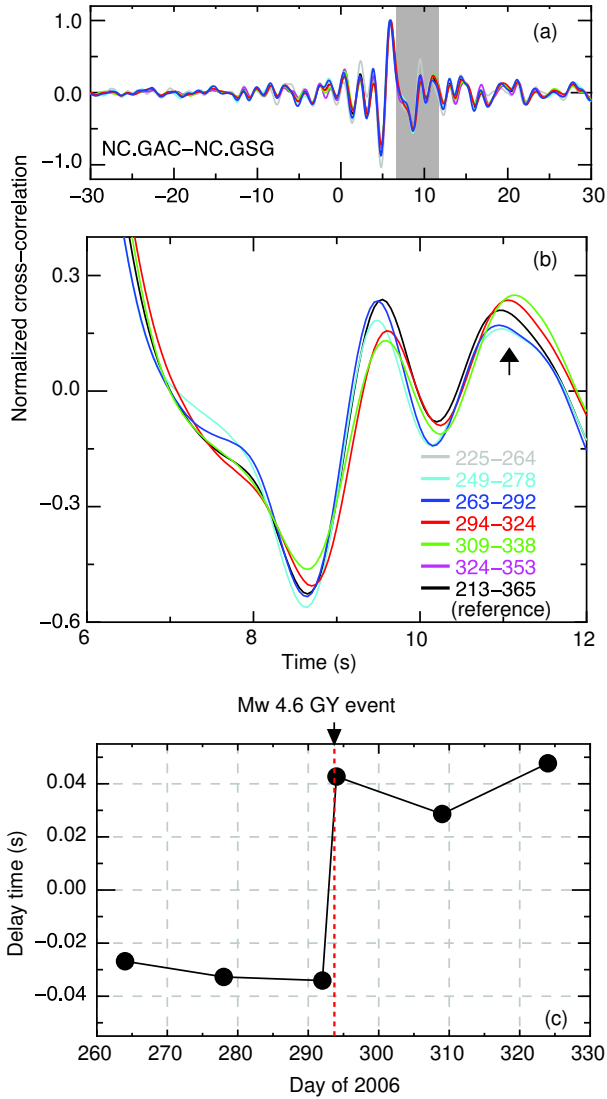


Figure 2.15: Stacked cross-correlation function between stations GAC and GSG. (a) Black waveform is the reference Green's function determined by noise cross-correlation functions during a 5-month period from August to December 2006. Other colored waveforms are stacked 30-day cross-correlation functions. (b) Enlarged view of five noise cross-correlation functions (the reference Green's function and four cross-correlation functions from day of year, 249 through 338), shown in the gray area in Figure 2.15a. Note that a change in cross-correlation function occurred after the 20 October 2006 M_w 4.6 Geysers earthquake (day of year 293), which strongly suggests a change in seismic structure associated with this earthquake. (c) Delay time measurement from noise cross-correlation analysis. An abrupt temporal change in delay time is seen around the occurrence of the M_w 4.6 Geysers earthquake.

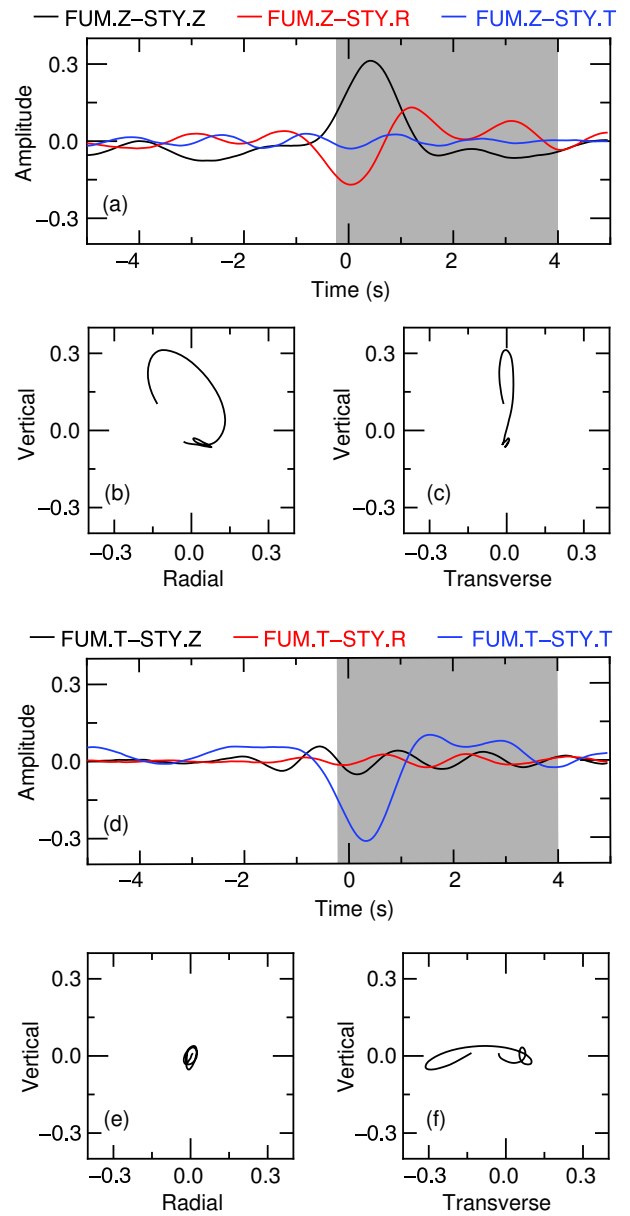


Figure 2.16: Recovered Rayleigh and Love pulses. (a) Measured Green tensor from vertical-component records at station FUM and vertical (black), radial (red), and transverse (blue) component records at station STY. Particle motion plots for (b) vertical-radial and (c) vertical-transverse planes in the gray area in Figure 2.16a. (d) Measured Green tensor from transverse-component records at station FUM and vertical (black), radial (red), and transverse (blue) component records at station STY. Particle motion plots for (e) vertical-radial and (f) vertical-transverse planes in the gray area in Figure 2.16d.

8 Measuring Fault-Zone Rheology at Depth from Characteristically Repeating Earthquakes

Taka'aki Taira, Robert M. Nadeau, Douglas S. Dreger

8.1 Introduction

Measuring fault-zone rheological properties at *in-situ* conditions is a crucial key to understanding the mechanics of postseismic deformation, aftershocks and the occurrence of triggered earthquakes following larger seismic events. However, it is fundamentally difficult to infer rheological properties at greater depth from surface measurements of strain. Here we introduce a methodology for directly measuring *in-situ* fault-zone rheological parameters at seismogenic depth that makes use of time evolutions of fault creep inferred from time-dependent recurrence intervals and seismic moments of characteristically repeating microearthquakes as deep creepmeters.

8.2 Transient Deep Fault Creep Induced by the 2004 Parkfield Mainshock

We observe the deep creep response to the abrupt change of stresses triggered by the 2004 M_w 6.0 Parkfield earthquake from time-varying source properties of repeating earthquake sequences. Frequencies of repeating earthquakes in sequences were greatly accelerated by the 2004 Parkfield earthquake. Subsequently they decayed through the stress relaxation process (Figure 2.17a).

Temporal changes in fault creep rate inferred from repeating earthquakes have been thought to be the result of localized transient stress changes near sequences (Nadeau and McEvilly, 2004). In this interpretation, temporal evolutions of inferred stress-driven creep events will be controlled by a single rheological model in the subsequent postseismic period, compared with geodetic measurements of surface displacement that are likely the result of combinations of multiple postseismic relaxation processes such as pore fluid diffusion, frictional slip and viscoelastic stress relaxation. This sensitivity to near-field deformation, in principle, provides a means of directly measuring *in-situ* fault-zone rheological properties.

8.3 Modeling Deep Fault Creep

We inverted calculated cumulative seismic slips of the postseismic time series over four years to resolve the rheology model controlling the temporal behavior of the individual fault creep events, using the postseismic relaxation law introduced by Montési (2004). In this constitutive relation in Montési (2004), frictional slip and the viscoelastic relaxation process are the two end-members of the stress-driven creep rheology model that are determined through the estimation of the stress exponent

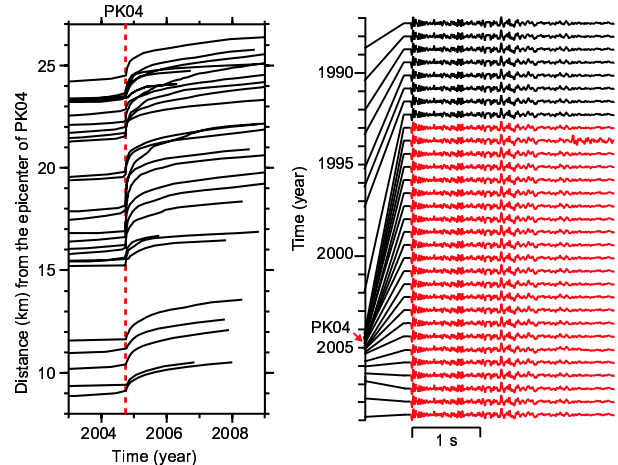


Figure 2.17: (a) Transient deep fault creeps inferred from characteristically repeating earthquake sequences. (b) Waveforms recorded at one of the HRSN borehole stations for one repeating earthquake sequence.

n . For viscoelastic creep, n ranges from 1 to 4, and for frictional sliding, $n \gg 1$.

We utilized six subsets of repeating earthquake sequences that are spatially clustered (Figure 2.18), determining the best-fitting n and other constants using a simultaneous inversion approach with the assumption that all sequences in individual subsets have the same value of n , but with different other constants. Of the six subsets, five subsets yield n larger than 10, indicating that the time evolutions of the inferred fault creep events from those five subsets can be governed by frictional sliding (Figure 2.19). On the other hand, the evolution of the deep fault creep events inferred from the remaining deepest subset shows that it is most consistent with ductile creep ($2 < n < 4$) rather than frictional sliding (Figure 2.20).

8.4 Rate-Strengthening Frictional Sliding

We estimated the friction parameter, $A = a\sigma_n$, where a is a constitutive parameter and σ_n is the effective normal stress, surrounding the fault patches in which the characteristically repeating earthquakes occur, with the co-seismic Coulomb stress change (ΔCFF) (Figure 2.18a) based on the source model of the 2004 Parkfield mainshock (Kim and Dreger, 2008). In the rate-

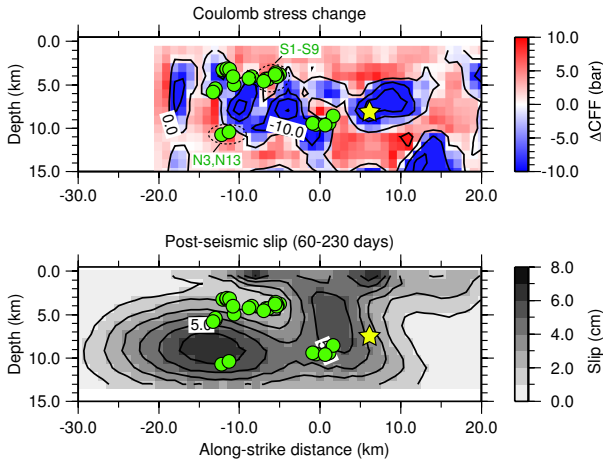


Figure 2.18: Cross-section views of (a) the Coulomb stress change computed from the coseismic model (*Kim and Dreger, 2008*) and (b) the postseismic slip model (*Murray and Langbein, 2006*) between days 60 and 230 of the postseismic period. Green circles are the locations of the repeating earthquake sequences. Yellow star is the hypocenter of the 2004 Parkfield mainshock.

strengthening sliding model in *Perfettini and Avouac (2004)*, the friction parameter A can be written as $A = \Delta CFF / \ln(V_+ / V_{pl})$ where V_+ and V_{pl} are the sliding velocity immediately after the mainshock and the interseismic slip rate. We estimated V_+ and V_{pl} from time evolutions of seismic slip with a least-squares method for individual subsets. Resulting A are estimated to be 0.05 to 0.15 MPa.

8.5 Viscoelastic Relaxation

Our result shows that the evolution of seismic slips from the deepest subset sequence exhibits viscoelastic creep response (Figure 2.20), suggesting that they may be governed by viscous flow in the ductile lower crust. The resulting 6-cm deep postseismic deformation between days 60 and 230 of the postseismic period near this deepest subset sequence (Figure 2.18b) could be a response to ductile deformation.

8.6 Acknowledgements

We thank A. Kim for providing us with the coseismic slip model and J. Murray for the postseismic slip model. This work is supported by the National Science Foundation grant EAR-0910322 and by the USGS NEHRP program under grant number 07HQAG0014.

8.7 References

Kim, A. and D.S. Dreger, Rupture process of the 2004 Parkfield earthquake from near-fault seismic wave-

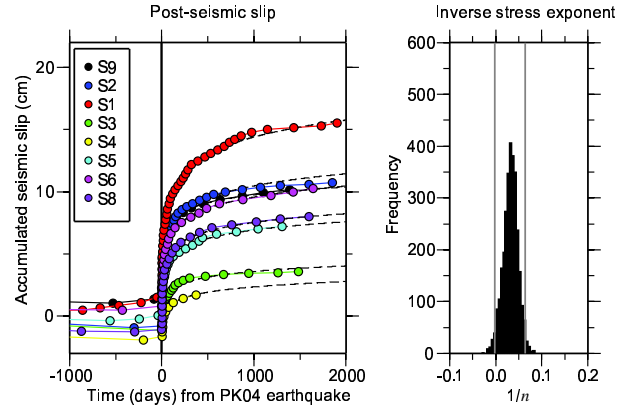


Figure 2.19: (a) Inferred deep fault creeps (circles) from eight clustered repeating earthquake sequences. Dashed lines are predicted fault creeps with the best-fitting n . (b) Bootstrap distributions for n , with 3,000 subsample data sets. Gray lines are 95% confidence intervals.

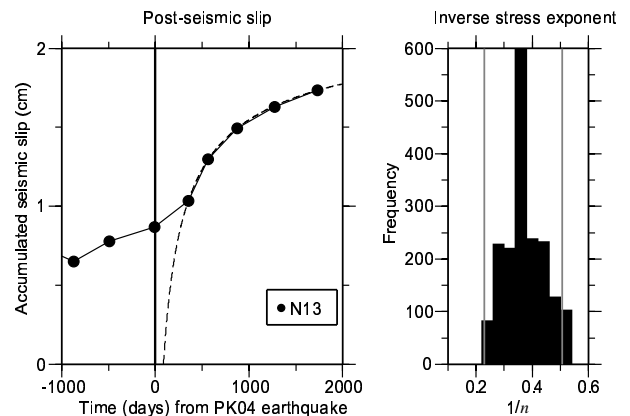


Figure 2.20: Same as Figure 2.19 except for the deep repeating earthquake sequence N13 (focal depth is 10 km).

form and geodetic records, *J. Geophys. Res.*, *113*, B07308, doi:10.1029/2007JB005115, 2008.

Montési, L.G., Controls of shear zone rheology and tectonic loading on postseismic creep, *J. Geophys. Res.*, *109*, doi:10.1029/2003JB002925, 2004.

Murray, J. and Langbein, J., Slip on the San Andreas Fault at Parkfield, California, over two earthquake cycles, and the implications for seismic hazard, *Bull. Seismol. Soc. Am.*, *96*, S283-S303, 2006.

Nadeau, R. M. and T.V. McEvilly, Periodic pulsing of characteristic microearthquakes on the San Andreas Fault, *Science*, *303*, 220-222, 2004.

Perfettini, H. and J.-P. Avouac, Postseismic relaxation driven by brittle creep: A possible mechanism to reconcile geodetic measurements and the decay rate of aftershocks, application to the Chi-Chi earthquake, Taiwan, *J. Geophys. Res.*, *109*, B02304, doi:10.1029/2003JB002488, 2004.

9 Free-Surface Vanishing Traction Effects on Shallow Sources

Andrea Chiang and Douglas S. Dreger

9.1 Introduction

Waveform inversion to determine the seismic moment tensor is a standard approach in determining the source mechanism of natural and man-made seismicity. The moment tensor is a general representation that includes the double-couple (DC) and non-double-couple sources such as explosions, opening and closing cracks, and volume compensated linear vector dipoles (CLVD). Previous studies (*Ford et al., 2009; Ford et al., 2009; Ford et al., 2010*) have shown that regional full waveform moment tensor inversion can discriminate isotropic events due to nuclear explosions from other seismic sources such as earthquakes and mine collapses. The method is robust and capable for source-type discrimination applications at regional distances. There can be complications, however, and as part of our continuing efforts to investigate and improve the capabilities of regional full waveform moment tensor inversion for source-type identification purposes, we address the issue of the effect of free-surface vanishing traction on recovering the seismic moment tensor, scalar seismic moment, and explosive yield.

9.2 Problem of Vanishing Traction for Shallow Sources

For shallow seismic sources that are effectively at the free surface, the vanishing traction at the free surface will cause the associated Green's function coefficients to have vanishing amplitude (*Julian et al., 1998*). This results in the indeterminacy of the M_{xz} and M_{yz} components of the moment tensor, and bias in the isotropic and total scalar seismic moments.

9.3 Source Depth Sensitivity Analysis

Using the Song velocity model (*Song et al., 1996*), we generate Green's functions at regional distance (100 km) with source depths ranging from 1200 m to 200 m and compute the ten fundamental Green's function time series at each depth. The Green's functions were bandpass-filtered between 10 and 50 seconds period. As shown in Figure 2.21, there is strong source depth sensitivity on the vertical dip-slip (DS) Green's functions associated with the M_{xz} and M_{yz} elements for all three components (ZDS, RDS and TDS) in which there is a systematic reduction in displacement amplitude with shallowing source depth. This effect was noted in a study on fundamental Love and Rayleigh waves for nuclear explosions and associated tectonic release (*Given and Mellan, 1986*). In contrast, the vertical strike-slip Green's functions for all three components (ZSS, RSS and TSS) and the explosion Green's functions for the vertical and radial components (ZEP, REP) show little to no variation in amplitude

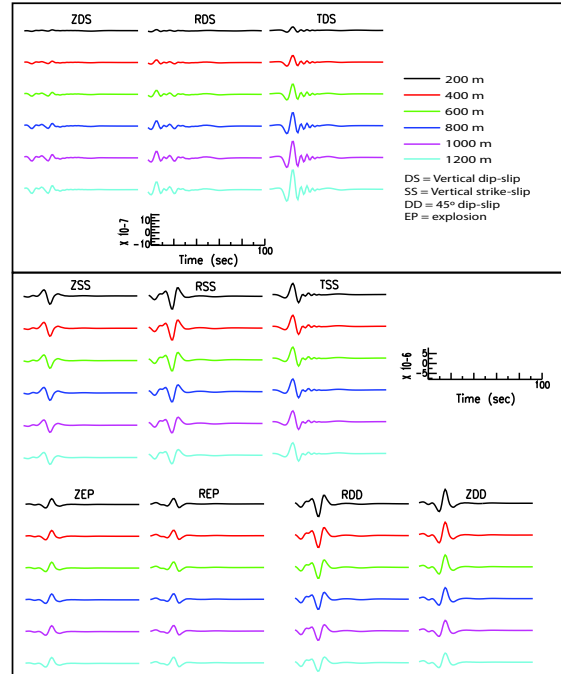


Figure 2.21: Fundamental displacement Green's functions calculated using the *Song et al. (1996)* velocity model and bandpass-filtered between 10-50 seconds. Z, R and T are the vertical, radial and tangential components, respectively.

and waveform. The 45°dip-slip Green's functions (ZDD and RDD) show minor variations in waveforms due to the constructive and destructive interference of waves interacting with the free surface. While this interference appears minor in the 10 to 50 second period passband (Figure 2.21) it is more pronounced in the unfiltered synthetics.

The weak DS component Green's functions can lead to bias in seismic moment tensor results, particularly when noise in the data is considered. However, we note that while there are strong effects on amplitude, the waveforms remain similar and there is little effect on the phase of the waveforms on these components. This suggests that it should be possible to develop correction terms for seismic moment tensor results when source depth is not known. Additionally, it suggests that pure-explosion models should not suffer from the free-surface bias. We will investigate both possibilities by introducing a correctional term to scale the Green's functions for shallow sources prior to the moment tensor inversion, or to incorporate a damping factor in the inversion to minimize the free-surface vanishing traction effect on shallow sources.

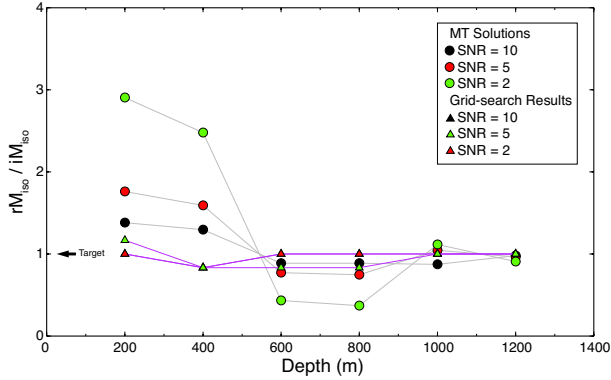


Figure 2.22: Depth sensitivity analysis where the ratios (circle and triangles) between recovered isotropic moment (rMiso) and the input value (iMiso) are shown over the depth range for different SNR scenarios. Results for SNR of 10 and 5 using the grid-search method overlaps.

9.4 Scalar Seismic Moment Sensitivity

A second set of synthetic tests is performed using complete moment tensor inversion (*Minson and Dreger, 2008*) and a grid-search method. This is an attempt to explore the free-surface effects on isotropic moment estimation and hence the yield. Since the vanishing traction at the free-surface shows little effect on the explosion Green’s functions, we expect the inversion to be stable. However, noise and tectonic release associated with the explosion will bias the full moment tensor estimates. Using the same set of Green’s functions calculated in the waveform analysis, we generate synthetic data for a pure explosion case with different signal-to-noise ratios (SNR) by adding random Gaussian white noise. The synthetic data is then inverted using the Green’s functions at the correct source depths, ranging from 1200 m to 200 m.

For a four-station, semi-ideal coverage (source-station distance distributed at regular intervals and in semi-regular azimuths) we see a strong effect on the isotropic moment at depths shallower than 400 m (Figure 2.22) for $\text{SNR} \leq 5$. At 200 m and 400 m depths, the inversion over-estimates the isotropic moment by a factor of ~ 3 , depending on the SNR. However, the effect diminishes rapidly at depths ≥ 600 m, and with relatively good SNR of 5 and 10 the inversion method can recover the isotropic moment, while with an SNR of 2 it is not possible to recover the isotropic moment at depths < 1000 m. Based on the moment tensor analysis, it is possible to recover the isotropic moment for long period waves (10-50 second) with SNR down to 5 at depths ≥ 600 m, and possibly shallower sources with a SNR of 10 or at depths ≥ 1000 m with a SNR of 2. We also invert the synthetic data using a grid-search method for a pure explosion model at each depth. Using this method, we can recover the isotropic moment at each depth for all three different SNR scenarios (Figure 2.22). In this case, a

simpler explosion model can better recover the isotropic moment.

9.5 Conclusions

Preliminary results indicate that the DS Green’s functions associated with the M_{xz} and M_{yz} components are affected by the vanishing traction effect at the free-surface, and this leads to biases in the recovered full moment tensor solutions. The amplitude of the Green’s functions decrease systematically, and the waveforms look similar over the targeted depth range with little phase distortion. Initial synthetic testing shows a dependence on source depth and SNR regarding the waveform moment tensor inversion’s ability to recover the isotropic moment of a pure explosion source. The inversion can recover the isotropic moment at all depths with a SNR of 10 and at depths ≥ 600 m for a SNR of 5. However, noise and the free-surface have minor effects on the isotropic moment recovery for a simple explosion model using a grid-search method. The next step is to continue testing different velocity models and compare their waveforms, and to introduce a correctional term either applied directly to the Green’s function calculations or in the moment tensor inversion to minimize the vanishing traction effect and improve the stability of the inversion for shallow sources.

9.6 Acknowledgements

This work is supported by the Air Force Research Laboratory (Award No. FA9453-10-C-0263).

9.7 References

- Ford, S.R., D.S. Dreger, and W.R. Walter, Source analysis of the Memorial Day explosion, Kimchaek, North Korea, *Geophys. Res. Lett.*, *36*, L21304, 2009. doi:10.1029/2009gl040003.
- Ford, S.R., D.S. Dreger, and W.R. Walter, Identifying isotropic events using a regional moment tensor inversion, *J. Geophys. Res.*, *114*, B01306, 2009. doi:10.1029/2008jb005743.
- Ford, S.R., D.S. Dreger, and W.R. Walter, Network Sensitivity Solutions for Regional Moment-Tensor Inversions, *Bull. Seismol. Soc. Amer.*, *100*, 1962-1970, 2010.
- Given, J.W., and G.R. Mellman, Estimating explosion and tectonic release source parameters of underground nuclear explosions from Rayleigh and Love wave observations, *Air Force Geophysics Laboratory Technical Report No. AFGL-TR-86-0171(I)*, 1986.
- Julian, B.R., A.D. Miller, and G.R. Foulger, Non-double-couple earthquakes 1. Theory, *Rev. Geophys.*, *36*, 525-549, 1998. doi:10.1029/98rg00716.
- Minson, S.E. and D.S. Dreger, Stable inversions for complete moment tensors, *Geophys. J. Int.*, *174*, 585-592, 2008. doi:10.1111/j.1365-246X.2008.03797.
- Song, X.J., D.V. Helmberger, and L. Zhao, Broad-Band Modelling of Regional Seismograms: the Basin and Range Crustal Structure, *Geophys. J. Int.*, *125*, 15-29, 1996. doi:10.1111/j.1365-246X.1996.tb06531.

10 Moment Tensors for Aftershocks of the M 7.9 Wenchuan Earthquake

Xiangdong Lin and Douglas Dreger

10.1 Introduction

On 12 May 2008, a magnitude 7.9 earthquake occurred beneath the steep eastern margin of the Tibetan plateau in Sichuan. This earthquake and its aftershocks caused huge losses in human life and property. To mitigate disasters caused by great earthquakes in the future, it is necessary to study the source properties and triggering mechanisms of the Wenchuan earthquake and its aftershocks. In this study, we use the wave field expression produced by the dislocation of a point source in the lateral layer and the frequency-wavenumber integration (F-K) method (Wang, *et al.*, 1980) to calculate the theoretical surface displacement caused by the earthquake. We obtain the seismic moment tensor solution, using the linear least squares method to minimize the fitting residual between theoretical and observational displacement of the fixed source depth earthquake (Dreger, 1993.)

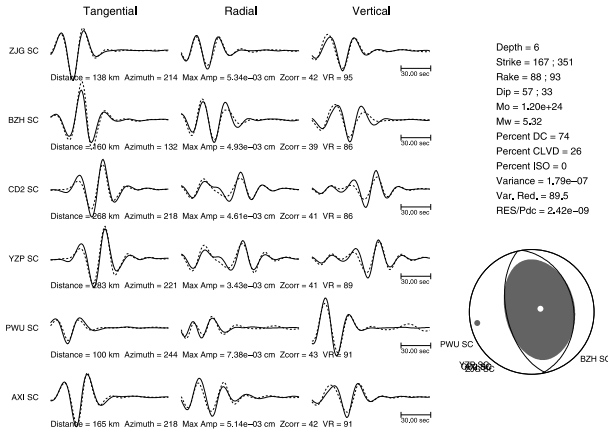


Figure 2.23: The moment tensor solution for the ninth Wenchuan aftershock in our study.

10.2 Data

In this study, we collect about 200 high signal-to-noise ratio waveforms (Zheng *et al.*, 2010) ($M_s \geq 4.0$) of Wenchuan series' aftershocks from the local seismic network. The stations involved are the broadband stations within 500 km of the epicenter. We remove the instrument response and trend; integrate the waveforms to displacement; and rotate the three component waveforms into the vertical, radial and tangential direction for the inversion.

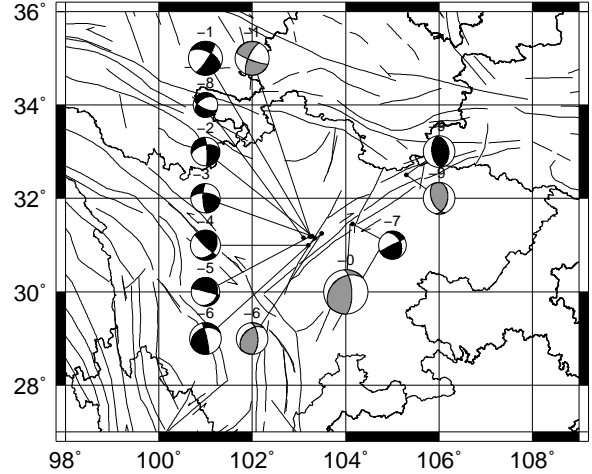


Figure 2.24: Moment tensor solutions for the mainshock and for the nine aftershocks in our study (red beach balls represent moment tensors calculated in this study, while green ones are cited from GCMT solutions.)

10.3 Preliminary results

In the vicinity of the 12 May 2008 earthquake, hereafter referred to as the Wenchuan earthquake, the eastern margin of the Tibetan plateau rises steeply westward from 500 m to > 4000 m elevation. Mountain peaks within the Longmen Shan reach elevations higher than 6000 m (Burchfiel *et al.*, 2008). The eastern plateau margin formed by the Longmen Shan coincides with steep gradients in crustal thickness (from 60~65 km in the west to ~ 40 km in the east; Xu *et al.*, 2007) and seismic wave speed changes from slow in the west to fast in the east, showing that the tectonic structure is very complex in this region. Following previous velocity structure study results, we established four 1-D models for the basin area and for the southwest, northeast and northwest mountain areas, respectively. Using these models, we obtained nine aftershock moment tensor solutions (see Figures 2.23 and 2.24.) The moment tensor solutions for aftershocks No. 1, No. 6, and No. 9 in our study are very close to results from the USGS (Figure 2.24.) The rupture plane and the aftershock sequence extend northeast of the Longmen Shan range, and the faulting geometry along the rupture appears to be complex. Reverse and right-slip components are of comparable magnitude along the southwestern portion of the rupture, but right-slip dominates the northeastern portion of the rupture (Zhao *et al.*, 2010). The nine aftershocks solutions also coincide with results

Table 2.1: The catalog of studied earthquakes

No.	Occurrence time	Latitude	Longitude	Magnitude	Depth
1	20080512191100.1	31.18	103.25	M_S 6.0	9
2	20080512230529.3	31.15	103.34	M_S 5.1	13
3	20080512230542.6	31.19	103.28	M_S 5.2	15
4	20080512232852.3	31.00	103.20	M_L 5.3	11
5	20080513012904.4	31.18	103.23	M_L 5.1	9
6	20080513040848.5	31.25	103.49	M_S 5.6	10
7	20080513044530.8	31.45	104.15	M_S 5.0	7
8	20080513050812.1	31.16	103.10	M_S 4.4	6
9	20080724035443.7	32.50	105.30	M_S 5.6	17

from Zhao *et al.*, 2010; earthquakes No. 1~8 have a large strike-slip component, while No. 9 is reverse.

10.4 Future work

In the future, we intend to calculate moment tensor solutions for our full set of ~ 200 Wenchuan aftershock waveforms for use in our investigation of the dynamic crustal characteristics of this area.

10.5 Acknowledgements

Waveform data for this study are provided by the Data Management Centre of the China National Seismic Network at the Institute of Geophysics, China Earthquake Administration.

10.6 References

- Burchfiel, B.C., L.H. Royden, R.D. vander Hilst, and B.H. Hager, A geological and geophysical context for the Wenchuan earthquake of 12 May 2008, Sichuan, People's Republic of China, *GSA Today*, 18(7), doi: 10.1130/GSATG18A.1, 2008.
- Dreger, D. Determination of Source Parameters at Regional Distances With Three-Component Sparse Network Data, *J. Geophys. Res.*, 98(B5), 8107-8125, doi:10.1029/93JB00023, 1993.
- Xu, L., S. Rondenay, and R.D. Van der Hilst, Structure of the crust beneath the southeastern Tibetan Plateau from teleseismic receiver functions, *Phys. Earth Planet. In.*, 165, 176193, 2007.
- Wang, C.Y., L. Zhu, H. Lou, et al., Crustal thicknesses and Poisson's ratios in the eastern Tibetan Plateau and their tectonic implications, *J. Geophys. Res.*, 115, B11301, doi:10.1029/2010JB007527, 2010.
- Wang C.Y., R.B. Herrmann, A numerical study of P, SV, SH-wave generation in a plane layered medium. *Bull. Seismol. Soc. Am.*, 70, 1015-1036, 1980.
- Zhao CP, ZL Chen, et al., Rupture process of the Wenchuan M8.0 earthquake of Sichuan, China: the segmentation feature, *Chinese Science Bulletin* 55(3), 284-292, doi: 10.1007/s11434-009-0425-7, 2010.
- Zheng X.F., Z.X. Yao, J.H. Liang and J. Zheng, The role played and opportunities provided by IGP DMC of China National Seismic Network in Wenchuan earthquake disaster relief and researches. *Bull. Seismol. Soc. Am.*, 100(5B), 2866-2872, doi: 10.1785/0120090257, 2010.

11 Focal Depth of the 2008 Panzhihua Earthquake from Depth Phase sPL and Joint Inversion of Local and Teleseismic Waveforms

Jiajun Chong, Zhenjie Wang (USTC), Sidao Ni (KLDG), Barbara Romanowicz

11.1 Introduction

On August 30th, 2008, an M_s 6.1 earthquake occurred near Panzhihua city and Huili county, Sichuan Province (hereafter referred to as the Panzhihua earthquake). Proposed to be on the Yuanmou-Lvzhijiang fault, this earthquake sequence provides us an opportunity to study properties of the Yuanmou-Lvzhijiang fault and thus helps us to understand the seismogenic processes of this region. However, there is a controversy over the focal depth of the main shock. The focal mechanisms given by USGS and GCMT are similar, but the focal depths are quite different: 17.0 km and 24.1 km for the USGS and GCMT solutions, respectively. Moreover, some waveform based studies suggest a much shallower depth (Long *et al.*, 2010). Thus, it is important to study focal depths of the Panzhihua earthquake sequence, which may be crucial parameters for constraining the brittle - ductile transition depth in this region and also important for strong ground motion studies. In this study, two approaches are employed to obtain a reliable focal depth of the Panzhihua earthquake. First, whole waveform inversion of local and teleseismic waveforms with CAP (Cut and Paste) method (Zhu and Helmberger, 1996) is used to invert for the focal mechanism and focal depth of the mainshock. Then, a waveform comparison method (WCM) with a recently proposed depth phase sPL (Chong *et al.*, 2010) is verified with the focal depth from waveform inversion. After that, we estimate depths of six M_L4+ aftershocks using the sPL phase observed at a station located about 37 km from the mainshock.

11.2 Focal depth and mechanism from waveform inversion

We use a modified version of the CAP method to invert for focal mechanism and focal depth by fitting local and teleseismic waveforms simultaneously (Wang *et al.*, 2011). Local and teleseismic data from the mainshock are collected from 6 local broadband stations and 17 IRIS/GSN teleseismic stations. The velocity model for calculating local and teleseismic Greens functions is constructed by taking the average of a 2D profile from deep seismic sounding in west Panzhihua. It is adjusted so as to try and get the same focal depth from both waveform inversion and depth phase sPL (Wang *et al.*, 2011).

The joint inversion shows that the Panzhihua earthquake is a predominantly strike-slip earthquake, and the best focal depth is 11km (Figure 2.25); at this depth both local and teleseismic datasets are matched by synthetic seismograms very well (Figure 2.26). Our best fault plane solutions (strike/dip/rake) for the mainshock

are, I: $194^\circ/78^\circ/12^\circ$ and II: $102^\circ/78^\circ/168^\circ$; they are similar to that of USGS (I: $195^\circ/89^\circ/19^\circ$, II: $104^\circ/71^\circ/179^\circ$) and GCMT (I: $190^\circ/90^\circ/4^\circ$, II: $100^\circ/86^\circ/180^\circ$), but different in dip angle (fault plane I should be the ruptured fault plane according to the fault geometry and the distribution of aftershocks). However, our focal mechanism is closer to the fault geometry according to field studies (Liu, 2008). This suggests that teleseismic waveforms can constrain the dip angle of near vertical faults very well because of their small take off angles. The moment magnitude is 5.9, which is consistent with M_w 6.0 from GCMT, and the minor difference in moment magnitude may be due to inaccurate t^* used in computing the teleseismic body waves (for our study, t^*p is chosen to be 1.0 second, and t^*s is 4.0 seconds, which is usually adopted in teleseismic waveform modeling, Kikuchi and Kanamori, 1982).

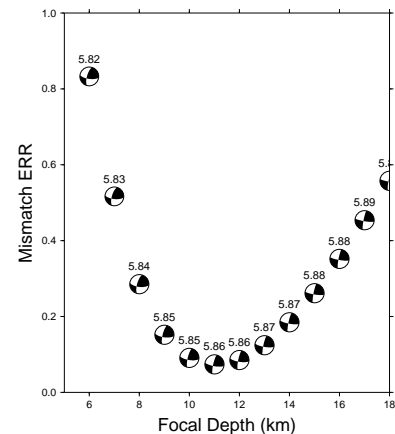


Figure 2.25: Variation of scaled misfit with focal depth in inversion the focal mechanism of the Panzhihua earthquake. Moment magnitude and focal mechanism are shown for each depth as well.

11.3 Focal depths from depth phase sPL

sPL is a local seismic phase that is usually well observed in the distance range of less than 50km, depending on the focal depth and velocity structure. The differential time between sPL and direct P is insensitive to epicentral distance but increases almost linearly with focal depth, and it has been successfully used to determine focal depth with only one station at near distance (Chong *et al.*, 2010). With the obvious observations of sPL at station PZH, which is 37km away from the mainshock, we determined focal depths of the mainshock and

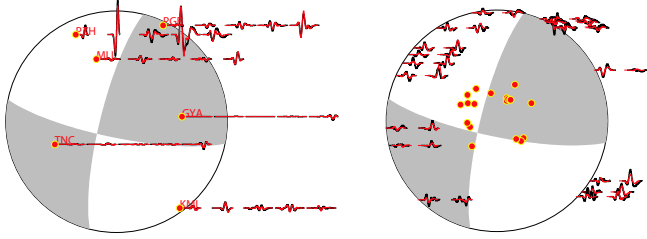


Figure 2.26: Waveform fitting between synthetics (red) and observations (black) for the Panzhihua earthquake with focal depth at 11km for synthetics. (a) Five segments of local waveforms: vertical Pnl, radial Pnl, vertical, radial and tangential surface wave, filtered in the frequency range 0.03~0.1 Hz with a 4th order Butterworth filter. (b) Teleseismic waveforms: vertical P and SH, filtered in the frequency range 0.02~0.1 Hz with 4th order Butterworth filter.

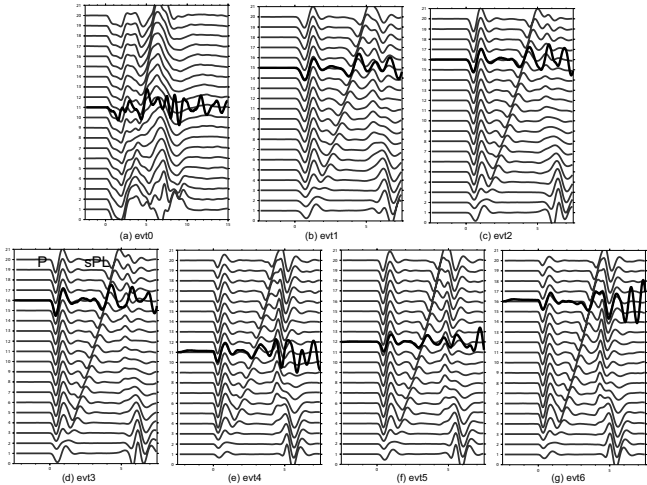


Figure 2.27: Focal depth determination for mainshock and six aftershocks. Radial component waveforms (velocity) are used for waveform comparison by fitting the differential time between sPL and direct P. Gray for synthetics and black for data, filtered in the frequency range 0.01~1 Hz.

Table 1 Focal depths from sPL and from catalog by China Earthquake Network Center (CENC)

Event ID	Origin time (UTC)	Longitude (degree)	Latitude (degree)	Depth from sPL (km)	Depth from CENC (km)	Source duration time (Sec)
Evt_0	2008 08 30 08:30:52	102.06	26.30	11	19	3.5
Evt_1	2008 08 31 08:31:10	102.06	26.27	15	13	1.0
Evt_2	2008 08 31 09:34:49	102.06	26.25	16	12	0.6
Evt_3	2008 08 31 11:00:30	101.99	26.16	16	14	0.4
Evt_4	2008 09 05 08:24:15	101.98	26.23	11	16	0.2
Evt_5	2008 09 30 01:16:38	101.94	26.24	12	13	0.4
Evt_6	2008 10 25 02:13:59	102.01	26.21	16	15	0.2

its six aftershocks following the approach of *Chong et al.* (2010). As shown in Figure 2.27, differential times between sPL and the direct P phase are well fitted for all events. And as a comparison, in Table 1, we see that focal depths of some events such as evt0 (mainshock), evt2, and evt4, from our study are quite different from those of the CENC catalog. Since the differential time between sPL and P is insensitive to epicentral distance but increases almost linearly with focal depth, we can arrange aftershocks in the order of focal depth by comparing the differential times between sPL and P. So, we conclude that evt2, evt3 and evt6 are at almost the same depth and deeper than other events, while evt0 and evt4 are at almost the same depth but shallower than the other earthquakes.

11.4 Conclusions

Our study indicates that the focal depth of the mainshock of the 2008 M6 Panzhihua earthquake sequence can be well constrained with two approaches: (1) using the depth phase sPL and (2) using whole waveform inversion of local and teleseismic data. We also show that precise focal depths of aftershocks can be determined using the depth phase sPL with only one broadband seismic station. Our study indicates that the mainshock is located at a depth of 11km, which is much shallower than those from other studies, confirming that the earthquake occurred in the upper crust. Aftershocks are located in the depth range 11-16 km, which is consistent with a ruptured near-vertical fault whose width is about 10 km, as expected for an M6 earthquake.

11.5 Acknowledgements

Supported by China Earthquake Administration fund 200808078, and NSFC funds 40821160549 and 41074032

11.6 References

- Chong, J.J., Ni, S.D., Zeng, X.F., sPL, an effective seismic phase for determining focal depth at near distance, *Chinese J. Geophys.*, (in Chinese), 53, 2620-2630, 2010
- Liu, M.F., A Study on Genesis of Hongge Hot Spring in Yanbian, Sichuan Province, *Coal Geology Of China*, (in Chinese), 20, 45-48, 2008
- Long, F., Zhang, Y.J., Wen, X.Z., Ni, S.D., Focal mechanism solutions of $M_L \geq 4.0$ events in the $M_s 6.1$ Panzhihua-Huili earthquake sequence of Aug 30, 2008, *Chinese J. Geophys.*, (in Chinese), 53, 2852-2860, 2010
- Kikuchi, M., and Kanamori, H., Inversion of complex body waves, *Bull. Seismol. Soc. Am.*, 72, 491-506, 1982
- Wang, Z.J., Chong, J.J., Ni, S.D., Romanowicz, B., Determination of focal depth by two waveform based methods, a case study for the 2008 Panzhihua earthquake, *Earthquake Science*, (accepted)
- Zhu, L.P., Helmberger, D.V., Advancement in source estimation techniques using broadband regional seismograms, *Bull. Seis. Soc. Am.*, 86, 1631-1641, 1996

12 Deviatoric Moment Tensor Analysis at The Geysers Geothermal Field

Sierra Boyd, Douglas Dreger, Sean Ford (LLNL), Peggy Hellweg, Peter Lombard, Jennifer Taggart, and Tom Weldon

12.1 Introduction

Geothermal energy has been produced at The Geysers Geothermal Field in Northern California for more than forty years. It has been demonstrated that increased steam production and fluid injection correlates positively with changes in earthquake activity, resulting in thousands of tiny earthquakes each year with events ranging in magnitude up to 4.5. We determine source parameters for the largest of these earthquakes using a regional distance moment tensor method. We invert three-component, complete waveform data from broadband stations of the Berkeley Digital Seismic Network for the complete, six-element moment tensor. Some solutions depart substantially from a pure double-couple (DC), with some events having large volumetric components.

Care is needed in the assessment of the significance of the non-double-couple terms. We have worked to develop a systematic procedure for the evaluation of aleatoric and epistemic solution uncertainty (e.g. *Ford et al., 2009; Ford et al., 2010*). We will present the solutions for The Geysers events together with estimates of random errors and systematic errors due to imperfect station coverage and knowledge of the velocity structure, which are needed to compute Green's functions for the inversion. Preliminary results indicate that some events have large isotropic components that appear to be stable and suggestive of fluid or gas involvement during the rupture processes.

We are presently working to incorporate full moment tensor capability in the Berkeley Seismological Laboratory's automatic processing system and analyst interface. This upgrade will enable improved monitoring at The Geysers and volcanically active regions of California.

12.2 Methodology

In this investigation, two source models, namely a deviatoric moment tensor (DC + compensated linear vector dipole [CLVD]) and a full moment tensor (DC+CLVD+isotropic component [ISO]), are evaluated as possible source mechanisms for three M4+ events. The objective is to determine the best fitting source model, and then evaluate the significance and resolution of possible non-double-couple source types that might arise from fluid-related processes in the geothermal system.

We start by determining the deviatoric moment tensors for a range of possible source depths, from 2 to 11 km, using six seismic stations as shown in Figure 2.28. These stations provide good coverage of the focal sphere,

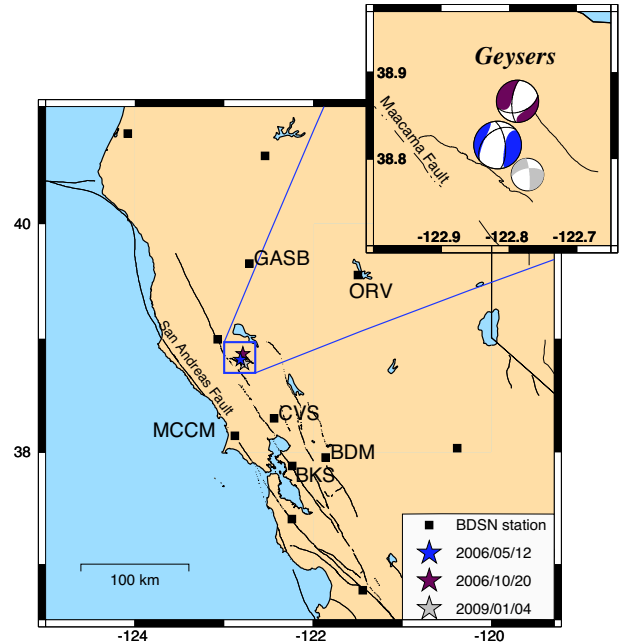


Figure 2.28: Map showing BDSN stations (squares) and analyzed Geysers events (colored stars).

and were chosen based on their signal to noise levels and availability for all the studied events to better enable event-to-event comparison.

We found that depth sensitivity using data filtered between 0.02 to 0.05 Hz is limited, so we therefore restrain our analysis to event depths determined from the Northern California Seismic System and Lawrence Berkeley National Laboratory catalogs. Following the determination of best-fit solutions for each category, we then evaluate the solutions using a battery of statistical, error estimation, and solution sensitivity tools. These tools include the statistical F-Test to evaluate the significance of improved fit with higher degrees of freedom in more complex source models, a bootstrap procedure to estimate aleatoric uncertainty, a station Jackknife test to assess solution stability and to possibly identify problematic source-receiver paths where additional velocity model calibration may be warranted, and tests using Green's functions for different velocity models. These tests provide good assessments of random (aleatoric) uncertainty as well as systematic or model (epistemic) uncertainties. This report explores the relevance of various source models, focusing on the Jackknife test and F-Test portion of this analysis.

12.3 Data Processing

Three M4+ earthquakes have been studied thus far with this battery of tests. The events occur on May 12, 2006, October 20, 2006 and January 4, 2009. We restrain the depths of the analysis to 3.5 km for the 2006 events and 4.5 km for the 2009 event.

Broadband seismic data are recorded from a sparse network operated by UC Berkeley. Five minutes of velocity data are downloaded from the Northern California Earthquake Data Center (NCEDC) for six stations ranging in distance from 55 to 140 km from the events of interest. The stations include BDM, BKS, CVS, MCCM, ORV, and GASB. Preprocessing of the seismic data includes removing the instrument response, integrating to ground displacement and filtering the data between 0.02 and 0.05 Hz. Synthetic waveforms are generated using FKRPROG, written by Chandan Saikia, and the GIL7 1D velocity model (e.g., *Pasyanos et al.*, 1996) and filtered between 0.02 and 0.05 Hz with an acausal Butterworth filter.

12.4 Deviatoric moment tensor analysis

The deviatoric moment tensor solution is composed of double-couple (DC) and compensated linear vector dipole (CLVD) components. The deviatoric moment tensor solutions derived from six stations show differences in the percentage of the non-double-couple component, with the highest percentage for the May 12, 2006 event. This event also has the lowest variance reduction. The deviatoric solutions for the 2006 events are shown in Figure 2.28.

The stability of the deviatoric moment tensor solutions is investigated with a Jackknife test using all possible groups of 5-, 4- and 3-stations. There are six groups of 5 stations, fifteen groups of 4 stations and twenty groups of 3 stations. The 5-station Jackknife analysis shows minor differences in the weighted variance reduction and percent double couple compared to the 4- and 3-station Jackknife plots. The fluctuations seen in the 4- and 3-station Jackknife plots may arise from imperfect station coverage and a velocity model that may not be ideal for all event-station paths. The variations are more evident when particular stations are grouped together.

Deviatoric	6-sta	5-sta	4-sta	3-sta
05-12 2006				
VRw%	77.6	78.1±1.6	78.7±2.3	79.7±3.3
%DC	30	31±5	31±9	34±14
10-20 2006				
VRw%	82.6	83.1±1.3	83.8±1.8	84.9±2.2
%DC	65	66±7	67±12	67±14
0-04-2009				
VRw%	81.8	82.8±1.8	84.0±2.6	85.7±3.5
%DC	67	68±6	68±10	69±14

The Jackknife analysis suggests overall stability in the deviatoric moment tensor solutions with fluctuations above and below mean trends, with consistently lower values of VRw and percent double-couple for the May 12, 2006 event.

12.5 Full moment tensor analysis

The 6-element full moment tensor solution includes the isotropic component and is representative for source processes with a volumetric response. The fits are higher when more degrees of freedom are used compared to the deviatoric solutions. The full moment tensor solutions for the 2006 events show higher percentages of non-double-couple components compared to the 2009 event. However, the F-Test reveals that the full moment tensor solution is somewhat significant for only the October 20, 2006 event, with a 91 percent confidence level of significance. A Jackknife test of this event shows the isotropic component to be stable at slightly above 40 percent for all groups of 5-, 4- and 3-stations, as shown below. In summary, the October 20, 2006 event exhibits a stable and somewhat significant (91% confidence level of significance) isotropic component of approximately 42 percent.

Full solution	6-sta	5-sta	4-sta	3-sta
10-20-2006				
VRw%	85.3	85.8±1.4	86.5±1.9	87.6±2.3
%DC	47	43±10	46±10	43±10
%CLVD	10	15±10	12±10	15±10
%ISO	43	42±2	43±2	42±3

Other models considered were the pure DC and DC+ISO. F-test results show the DC model to be most appropriate for the 2009 event. This initial analysis defines the framework with which we will determine and review moment tensor solutions for M>3 seismicity occurring in the region.

12.6 Acknowledgements

This work was supported by the Assistant Secretary for Energy Efficiency and Renewable Energy, Office of Geothermal Technologies, of the U.S. Department of Energy under Contract No. DE-EE0002756.

12.7 References

- Ford, S.R., D. S. Dreger, and W. R. Walter, Identifying isotropic events using a regional moment tensor inversion, *J. Geophys. Res.*, 114, B01306, 2009.
- Ford, S.R., D. S. Dreger, and W. R. Walter, Network Sensitivity Solutions for Regional Moment-Tensor Inversions, *Bull. Seism. Soc. Am.*, 100, 1962-1970, 2010.
- Pasyanos, M. E., D. S. Dreger, and B. Romanowicz, Toward real-time estimation of regional moment tensors, *Bull. Seism. Soc. Am.*, 86, 1255-1269, 1996.

13 Slip Transients, Deficit and Release from Repeating Earthquakes

Robert M. Nadeau and Ryan C. Turner

13.1 Introduction

To better understand interactions between seismic and aseismic deformation, deep aseismic fault slip rates (Vd) from characteristically repeating microearthquake sequences (CS) (Nadeau and McEvilly, 1999) along the central San Andreas Fault (SAF) were compiled and analyzed. Previous CS based Vd studies have shown that spatial and temporal variations in Vd can be resolved over large contiguous regions, in diverse tectonic settings, and back in time to well before the advent of satellite-based geodesy (e.g., GPS, InSAR) (Nadeau and McEvilly, 1999 and 2004; Bürgmann et al., 2000; Igarashi et al., 2003; Chen et al., 2008). Such studies have also revealed systematics in Vd indicative of slip transients associated with post-seismic deformation, slow-slip events, quasi-periodic slip pulsing, and regions of slip-deficit accumulation.

13.2 Activities

We searched for CSs along a 200 km stretch of the SAF in Central California and identified and compiled a catalog of 343 CSs comprised of 2854 microearthquakes ranging in magnitude from 1.5 to 3.5 and occurring over a 27.333 year period between 1984 and April of 2011 (inclusive). The CSs were located between the approximate southern terminus of the 1989 M6.9 Loma Prieta (LP) and the northern terminus of the 1857 M7.8 Ft. Tejon (FT) earthquakes, and the catalog includes CS activity associated with the 2004 M6.0 Parkfield earthquake (PF) rupture, its aftershock zone, and the aftershock zone south of the LP earthquake rupture.

We used the method of Nadeau and McEvilly (2004) to convert the the locations, times and magnitudes of the CS micro-events to map the time histories of Vd within the study region.

13.3 Findings

Figure 2.29 shows profiles of the CS derived short- and long-term Vd behavior in the study zone in the context of the spatio-temporal distributions of the 1989, M6.9 LP and 2004, M6.0 PF earthquake rupture zones. The locked (inferred rupture) zone associated with the 1857, M7.8 FT earthquake occurs immediately to the southeast.

Moving northwestward from 20 km along the long-term profile (left), a sharp reduction in long-term Vd is observed at ~ 95 km. This corresponds to the bifurcation of the SAF system into the SAF and the sub-parallel Calaveras fault (not shown) strands. The sum of long-

term rates on these strands is comparable to the tectonic plate rate (~ 3.0 to 3.5 cm/yr), consistent with the sharing of tectonic load release by the strands.

Between 20 and 95 km, no significant difference between long-term Vd before PF (pre-PF) and Vd for the entire study period are observed. However, southeast of 20 km, long-term pre-PF rates are lower and are below the plate rate, indicating slip deficit accumulation. The reduced pre-PF rates are also apparent in the short-term contoured profile. Following PF, short-term Vd increases dramatically in the PF rupture and after-slip zones. By April 2011, long-term Vd southeast to -15 km has caught up to the plate rate. A similar pattern is seen in the LP after-slip zone northwest of ~ 125 km, suggesting a general pattern where slip deficit accumulates and releases both seismically (on rupture zones) and aseismically (on adjacent regions). This has important implications for estimating the dimensions of future earthquake rupture and magnitude from inter-seismic patterns of slip deficit accumulation or paleoseismic observations of fault slip from past earthquakes.

Southeast of -15 km, long-term Vd lags behind the plate rate. Our search also revealed no CSs in the -35 to -50 km segment that was included in the 1857 FT rupture zone. This suggests considerable seismic and aseismic slip release in a future large event which, if it happened today, would average ~ 4.5 meters of seismic slip.

13.4 Acknowledgements

Research supported by NSF grant EAR-0951430. Data provided by the Northern California Earthquake data center (NCEDC).

13.5 References

- Nadeau, R.M., and T.V. McEvilly, Fault slip rates at depth from recurrence intervals of repeating microearthquakes, *Science*, 285, 718-721, 1999.
- Nadeau, R. M. and T. V. McEvilly, Periodic Pulsing of Characteristic Microearthquakes on the San Andreas Fault, *Science*, 303, 220-222, 2004.
- Bürgmann, R., D. Schmidt, R.M. Nadeau, M. d'Alessio, E. Fielding, D. Manaker, T.V. McEvilly, and M.H. Murray, Earthquake Potential along the Northern Hayward Fault, California, *Science*, 289, 1178-1182, 2000.
- Igarashi, T., T. Matsuzawa and A. Hasegawa, Repeating earthquakes and interplate aseismic slip in the northeastern Japan subduction zone, *J. Geophys. Res.*, 108, 2249, doi:10.1029/2002JP001920, 2003.
- Chen, K. H., R.M. Nadeau and R.-J. Rau, Characteristic repeating earthquakes in an arc-continent collision boundary zone: The Chihshang fault of eastern Taiwan, *Earth Planet. Sci. Lett.*, 276, 262-272, doi:10.1016/j.epsl.2008.09.021, 2008.

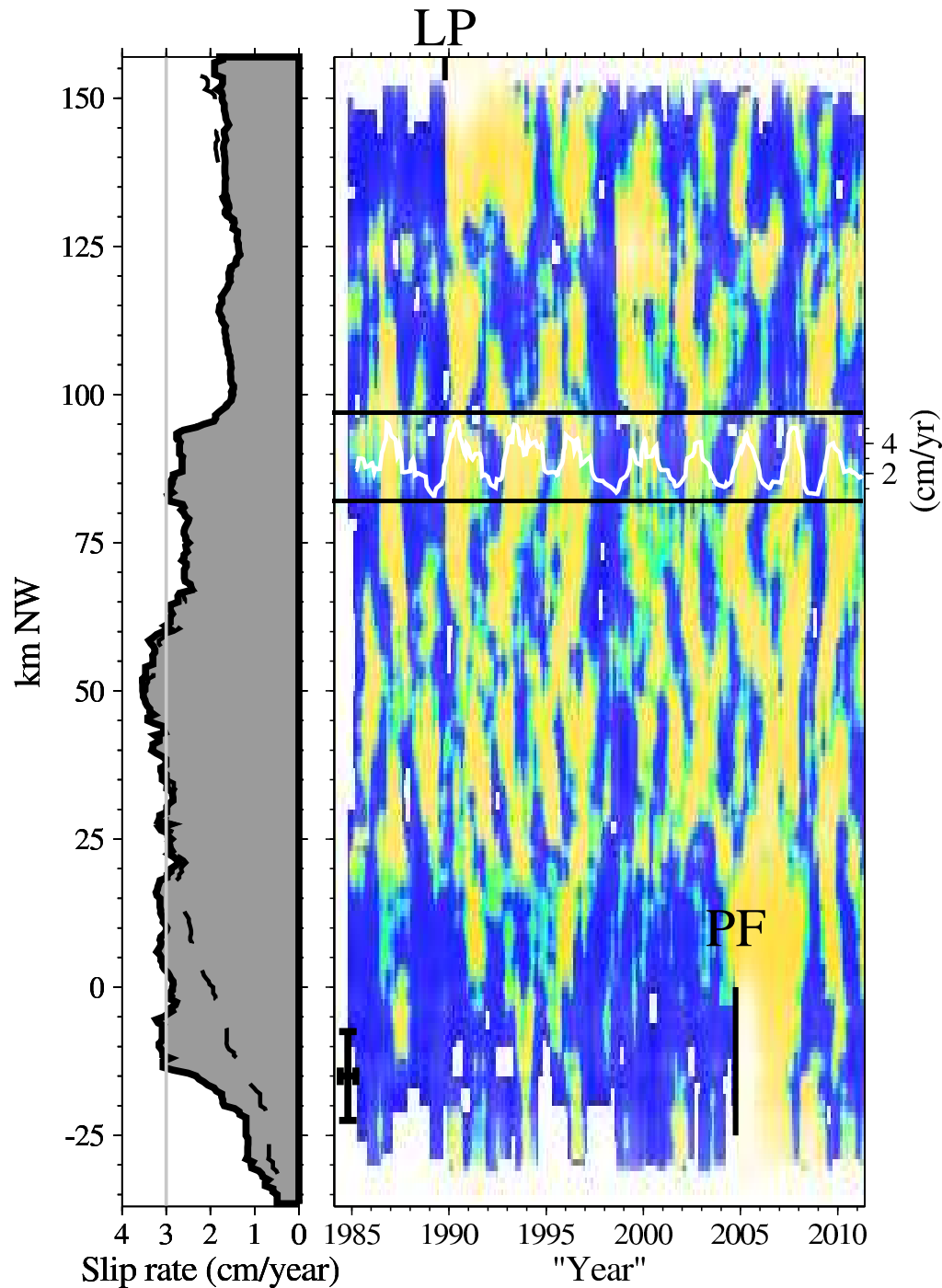


Figure 2.29: Profiles of the short- and long-term V_d behavior in the study zone in the context of the spatio-temporal distributions of the M6.9 LP and M6.0 PF earthquake rupture zones. The locked (inferred rupture) zone associated with the M7.8 FT earthquake occurs immediately to the southeast. Left panel: profiles of long-term V_d (15 km smoothing) along the SAF for the entire observation period (solid black curve with grey fill) and for the period preceding the 2004 PF event (dashed black curve). Thin gray line represents a tectonic plate-rate of 3.0 cm/yr. Right panel: colored/contoured profile of % variations in short-term V_d (0.8 year averaging window) relative to the long-term average (entire observation period). Light gray (yellow) regions show periods when short-term V_d exceeds the long-term average by 20% or more. Dark gray (blue) regions show periods when long-term rate is below average, and intermediate gray (blue-green) regions are those with V_d within $\pm 20\%$ of average. Rupture zones of PF and LP events within the study area are black vertical lines, and the slip rate history (in cm/yr.) of a 15 km segment (centered at ~ 90 km) with nine cycles of particularly periodic aseismic slip-transient pulsing is shown with a white curve.

14 Immediate Triggering of Small Repeating Earthquakes at Parkfield

Kate Huihsuan Chen (National Taiwan Normal Univ.), Roland Bürgmann, Robert M. Nadeau

14.1 Introduction

We analyze 112 M -0.4 \sim 3.0 repeating earthquake sequences (RESs) to examine the triggering effect from nearby microseismicity. For each RES event, the time difference (DT) with all other earthquakes within a distance of 5 km is considered, together with the stress change induced by preceding neighboring events (preshocks) and vice versa for events following the RES events (postshocks). We use the moment of RES and background events in the stress calculation (Equation 2.1) for the postshocks (DT < 0) and preshocks (DT > 0), respectively. Here we introduce a simple expression for the static shear stress change ($\Delta\sigma$) (Aki and Richards, 1980):

$$\Delta\sigma = 1/6\pi M_o/r^3, \quad (2.1)$$

where r is the distance from a RES to the hypocenter of each neighboring event (with seismic moment M_o). Empirical tests using the shear stress change calculated from an elastic-dislocation model (Okada, 1992) produce values of in-plane stress changes consistent with Equation 2.1. In this calculation, we assume that all earthquakes lie on a single plane and thus increase stress on their neighbors, which is clearly not always the case.

14.2 Short-term triggering by nearby events

The number and occurrence rate of events appears to be increased for DT \leq 5 days, suggesting an apparent preponderance of triggering events over small time spans for both pre-RES events and postshocks. In 2.30a, we plot short-DT > 1kPa preshocks and postshocks showing clear evidence of immediate triggering by and of very close-by events. The close-by background events have a large magnitude range, as shown in Figure 2.30b. A cluster of M2 events occurs very close to the RESs in space and time, as illustrated by the circles near (0,0), whereas the M3 and M4-5 events do not show such an obvious tendency. This suggests that in the DT \leq 1 window, very high stress changes are likely a result of small earthquakes triggering others over very short distances.

A remarkable difference between the number of preshocks and postshocks appears if only events with higher stress change are considered, as illustrated by the measures for the events with > 1 kPa stress in Figure 2.30c. The > 1 kPa preshocks are much more frequent within 5 days preceding the RES (solid line with filled square), whereas the rate of postshocks does not show much change with time following the RES (solid line with open circle). Given that the events used to determine

stress change in the preshock and postshock domains are background seismicity and repeating events (smaller magnitude in general), the larger number of higher stress changes for preshocks may be expected. After the 5-day time window, both \geq 1-kPa preshocks and postshocks exhibit a similar occurrence rate, as shown by the similar slope of the solid lines in Figure 2.30c. Additionally, the event rates reveal a systematic decrease out to 30-300 day windows.

Do the trigger stresses need to be of a certain magnitude to lead to immediate triggering? To answer this, the data number in the varying DT window (<5000s, 5000s-1 day, 1-10 days, 10-20 days, 20-30 days, and 30-300 days) is divided by the total number of >1 kPa events. The percentage of high stress change preshocks is the greatest for the DT<5000 s window, with declining percentages for longer DT intervals. The largest difference in data percentage between DT< 5000s and \geq 1 day, 30%, appears at log stress = 1.5 (\sim 30 kPa), whereas the difference among the DT \geq 1 day windows is less than 7%. This may suggest that a stress increment of \sim 30kPa or more is needed to produce effectively immediate triggering (DT \leq 1 day) of RES events.

14.3 Conclusion

We examined interactions between RESs and nearby earthquakes at a fine scale in an attempt to identify systematic interaction and to infer the possible physics behind it. The joint occurrence of RESs and nearby background earthquakes indicates that short-term triggering (<10% of its own average recurrence interval) between neighboring events may be taking place and influencing the timing of repeating events. Immediate triggering within a few seconds to minutes can happen when the separation distance is less than a few km. When earthquakes are separated by longer distances, their communication (triggering) becomes less efficient. An apparent preponderance of triggering of RES events over time spans as small as one day is more evident when the stress change imposed on the RES site is higher than \sim 30 kPa.

14.4 References

- Aki, K., and P. G. Richards (1980), *Quantitative Seismology*, Freeman, New York.
- Chen, K. H., Bürgmann, R., and Nadeau, R. M. (2010), Triggering effect of M 4-5 earthquakes on the earthquake cycle of repeating events at Parkfield, *Bull. Seismol. Soc. Am.*, 100, 2, doi:10.1785/0120080369.
- Okada, Y. (1992), Internal deformation due to shear and tensile faults in a half space, *Bull. seismol. Soc. Am.*, 82, 1018-1040.

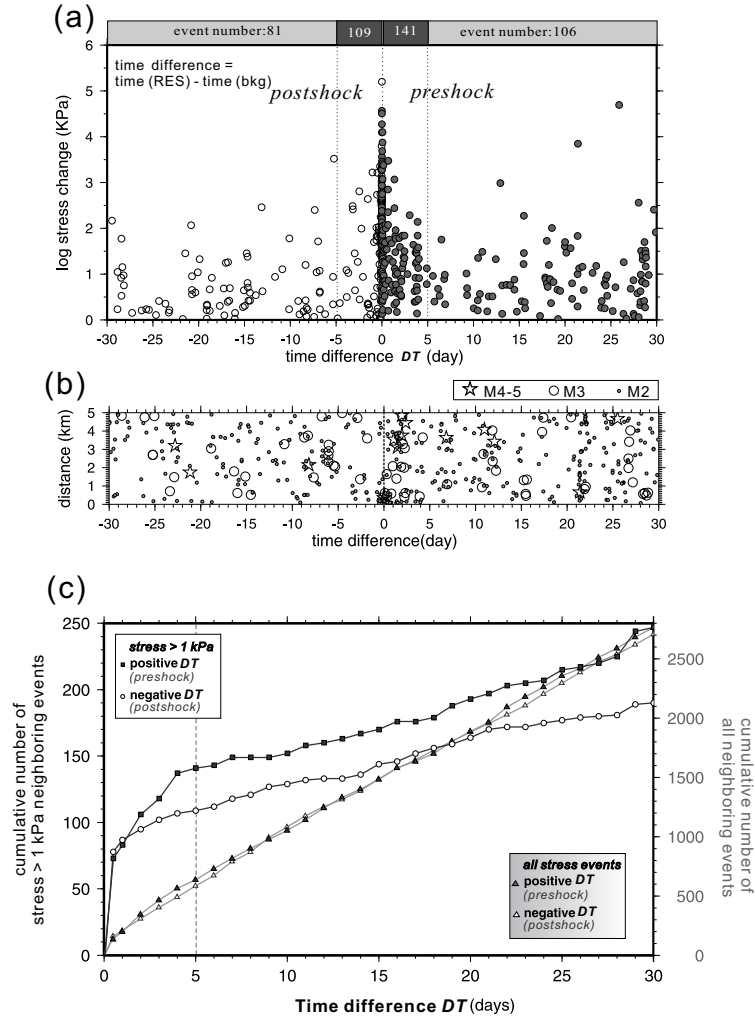


Figure 2.30: (a) Static stress change as a function of time difference between repeating events and nearby non-repeating background earthquakes (bkg) within 5 km distance. Stress changes computed in the postshock case are those imposed by the RES on the subsequent events, whereas in the preshock case the stress changes are those imposed on the RES event. The labels in the upper panel indicate the number of nearby events with stress changes > 1 kPa within 5 days and 5-30 days following/preceding the RES shown by circles. The total number of preshocks and postshocks within 30 days and 5 km from all RES events (without considering their stress change) are 2763 and 2708, respectively. (b) Separation distance versus time difference between RESs and nearby $M4 \sim 5$ (star), $3 \leq M \leq 4$ (circle), and $2 \leq M < 3$ (square) non-repeating events. (c) Cumulative number of background events with increasing time difference DT from RES events for preshocks and postshocks, as denoted by solid triangles and open triangles with dashed line, respectively. The measures for the events with higher stress changes (> 1 kPa) are shown by a solid line, where the solid square and open circles denote the preshocks and postshocks, respectively. There is a large number of stress > 1 kPa preshocks within 5 days of impending RES (solid squares) events, as shown by vertical dashed line. There are somewhat more high-stress preshocks than postshocks associated with the RES events during that period, which may partly be due to the smaller average magnitude of the RES events.

15 Joint Inversion of Seismic and Geodetic Data for the Source of the 4th March 2010 M_w 6.3 Jia-Shian, SW Taiwan, Earthquake

Mong-Han Huang, Douglas Dreger, Seung Hoon Yoo, and Roland Bürgmann

15.1 Introduction

The 4th of March 2010 Jia-Shian (M_w 6.3) earthquake occurred in southwestern Taiwan and caused moderate damage. Compared with other M_w 6+ events in the world (e.g. 2004 M_w 6.1 Parkfield earthquake), this event has a smaller coseismic slip and no fault related surface rupture, reflecting an unusually deep source in west Taiwan. The reported focal depth is 23 km, below the fold and thrust belt of Taiwan. In this study, we inverted geodetic (GPS and InSAR) and seismic waveform (strong motion and broadband) data for finite-source models. We compare inversions from each individual data set to better understand their respective contributions and to determine the appropriate weights and smoothing parameters for a joint inversion. A joint inversion of the geodetic and seismic data reveals a preferred model that shows a primary slip patch that is approximately 20 km in diameter with a peak slip of 28 cm and total scalar seismic moment of 3.65×10^{25} dyne cm (M_w 6.34).

15.2 Inversion and Preliminary Result

We use a linear least squares inversion code based on the method of *Hartzell and Heaton* (1983) in which the finite source is discretized with a finite distribution of point sources in both space and time. A damped, linear least squares inversion with a positivity constraint (allowing only for thrust dip-slip component) is used to determine the spatiotemporally distributed slip. A single time window is used with a fixed dislocation rise time (0.5 s) propagating away from the hypocenter with a constant rupture velocity (2.6 km/s). A spatial smoothing with linear equations minimizing differences in slip between subfaults is applied to stabilize the seismic and geodetic inversion. Different weighting and smoothing parameters are applied to the simultaneous inversion using the method proposed by *Kaverina and Dreger* (2002). The Green's functions for southern Taiwan are taken from *Chi and Dreger* (2004). For the geodetic inversion, the geodetic Green's functions are computed by assuming the same layered elastic structure as for the seismic inversion. A 50×50 km NW dipping fault geometry with 625 subfaults was considered for the inversions. The coseismic slip distribution is estimated from the inversion of each data set separately and jointly.

Eight strong motion and three broadband seismic stations are used for the seismic inversion, and 108 GPS stations and three ALOS PALSAR interferograms are used for the geodetic inversion. Both geodetic and seismic in-

versions reveal a consistent pattern for the main rupture asperity near the hypocenter (Figure 2.31b). The joint inversion shows a coseismic slip covering a 15×20 km area northwest of the hypocenter with an average slip of 15 cm and a peak slip of 28 cm.

15.3 Discussion and Future Work

Both seismic and geodetic inversions obtain good fits to the data, but the predicted moment magnitudes from the two inversions are slightly different (M_w 6.3 for seismic; M_w 6.34 for geodetic). The difference of the two predicted moments is equivalent to a M_w 5.7 earthquake. We note that the geodetic inversion shows more slip near the largest (M_w 5.0) aftershock (Figure 2.31b), which suggests that the difference may in part be due to deformation from the early aftershocks spanned by the geodetic data. Consideration of both seismic and geodetic inversions can provide information about the main shock and the early aftershocks.

Further work will focus on additional improvements of the seismic inversion and the aftershocks analysis. For example, the seismic inversion does not fit the directivity in station CHY089 well (Figure 2.31a), which might be due to an over-simplified fault geometry or improper Green's functions. With these improvements, we will aim to better understand the kinematic process of this event and its tectonic framework in west Taiwan.

15.4 Acknowledgements

We thank the Institute of Earthscience, Academia Sinica, Taiwan for providing seismic and geodetic data. We thank H.-H. Huang of National Taiwan University for providing the aftershock catalog.

15.5 References

- Chi, W.-C. and Dreger, D., Finite fault inversion of the September 25, 1999 ($M_w = 6.4$) Taiwan earthquake: Implications for GPS displacements of Chi-Chi, Taiwan earthquake sequence, *Geophys. Res. Lett.*, 29, doi:10.1029/2002GL015237, 2002.
- Hartzell, S. H., and T. H. Heaton, Inversion of strong ground motion and teleseismic waveform data for the fault rupture history of the 1979 Imperial Valley, California, earthquake, *Bull. Seismol. Soc. Am.*, 73, 1553-1583, 1983.
- Kaverina, A., Dreger, D., and Price, E., The combined inversion of seismic and geodetic data for the source process of the 16 October 1999 M_w 7.1 Hector Mine, California earthquake, *Bull. Seismol. Soc. Am.*, 92, 1266-1280, 2002.

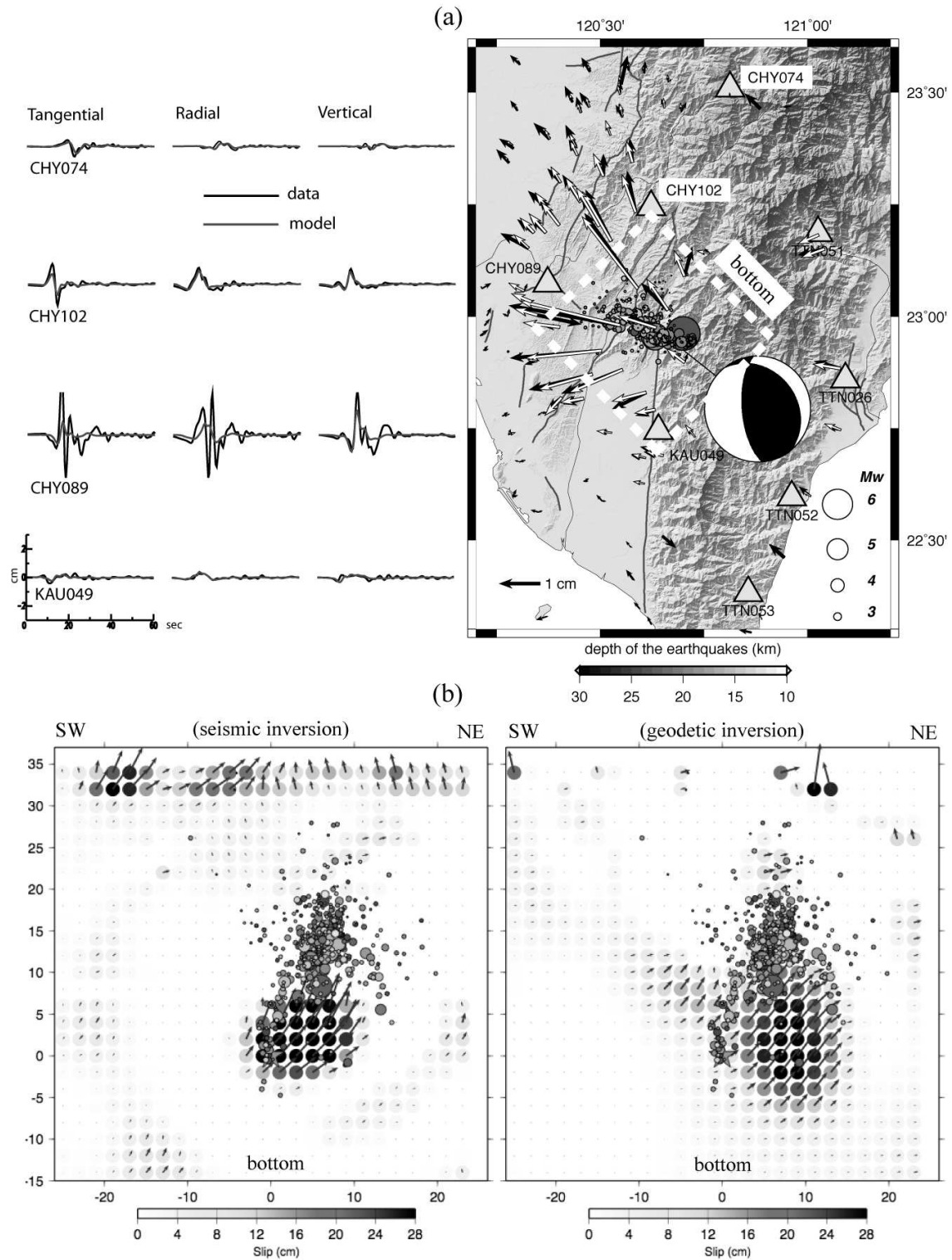


Figure 2.31: (a) Right: The study area and the comparison of the GPS data (black arrows) and model prediction (white arrows) using the finite source inversion. The circles are the aftershocks for the first 24 hours. The triangles show the locations of the seismic station. The white dashed rectangle shows the fault geometry. Left: The comparison of the strong motion seismic data (black) and the predicted models (gray) using the finite source inversion. Note that the larger amplitude of station CHY089 is due to the directivity of this event. (b) The comparison of the coseismic fault slip based on seismic (left) and geodetic (right) inversions. The arrows indicate the slip orientation of each subfault. The circles show the distribution of the aftershocks.

16 Tidal Triggering of LFEs near Parkfield, CA

Amanda M. Thomas, Roland Bürgmann, David Shelly, Nick Beeler, and Maxwell Rudolph

16.1 Introduction

We study the influence of the ocean and solid earth tides on low frequency earthquakes in Parkfield, CA. Several spatially localized families at ~ 25 km depth seem to fail preferentially when the tides are inducing negative fault-normal stress, or clamping, inconsistent with conventional models of fault strength. The hypocenters of these earthquake families are spatially coincident with a right-stepping bend in the San Andreas Fault near Gold Hill. This observation argues that deformation can remain localized well below the brittle-ductile transition. High pore-fluid pressures provide a potential mechanism for maintaining localized, brittle deformation deep in the crust.

16.2 Data

The 2001- January 2010 low-frequency earthquake catalog of (*Shelly and Hardebeck, 2010*) is composed of $\sim 550,000$ Low Frequency Earthquakes (LFEs) grouped into 88 different families based on waveform similarity. Locations of LFE families in Parkfield are tightly constrained by numerous P- and S-wave arrival times at densely distributed stations. The location procedure involves visually identifying individual LFE template event candidates and then cross-correlating and stacking those waveforms with continuous seismic data to detect other LFEs in the same family. The most similar events are stacked at all regional stations, and P- and S-wave arrivals are identified on these stacked waveforms. LFEs are located by minimizing travel time residuals in a 3D velocity model of the Parkfield area (for further details see *Shelly and Hardebeck, 2010*). Hypocenters of LFE families, shown in Figure 2.32, are distributed along ~ 150 km of the San Andreas Fault, from Bitterwater to south of Cholame. Estimated source depths extend from just below the base of the seismogenic zone to the Moho (16-30 km depth) on the deep extension of the San Andreas Fault, a zone previously thought incapable of radiating seismic waves.

16.3 Methods

We compute tidally-induced strains at the centroid of the tremor source region (-120.525, 35.935, 25 km depth) using the tidal loading package Some Programs for Ocean Tide Loading (*Agnew, 1996*), which includes both solid earth and ocean tidal loading. Displacements from the solid earth tide are very long wavelength compared to the source region depth; thus we assume that the strains

modeled at the surface are not significantly different from those at 25km depth. At the surface in Parkfield, the ocean loading component is small compared to the solid earth tides; however, the magnitude of the ocean loading component should increase with depth, potentially impacting the validity of the strains computed at the surface. To resolve this potential issue, we calculate depth dependent, spherical Green's functions which are used to compute the strains from only the ocean loading component at depth. The dimension of the LFE source region is small with respect to the degree two pattern of the tides, but to validate the assumption that tidal stress changes are small over the ~ 140 km section of the San Andreas Fault under consideration, we computed and compared strain timeseries at the center and end of the LFE source region and found that the difference was insignificant.

Assuming 2D plane strain (no depth dependence) in a homogenous medium, we convert strain to stress using a linear elastic constitutive equation. Stresses are then resolved onto the San Andreas Fault assuming a strike of $N42^\circ W$, parallel to the San Andreas Fault. The vast majority of the stress amplitudes are due to only the body tides, as the ocean loading contribution diminishes with distance inland. Also, the body tides induce largely volumetric stresses in the earth's lithosphere: thus the resulting shear stress on the SAF fault due to the tides is approximately an order of magnitude smaller than the normal stress.

16.4 Results

One spatially localized group of LFE families that exhibit statistically significant correlation with compression, or negative fault-normal stress (FNS), warrants further discussion. A simplified Coulomb friction model cannot explain preferential triggering during times of compression, as Coulomb failure stress depends positively on fault normal stress, meaning that earthquakes should preferentially trigger during times of extension and not clamping. However, appealing to a more complicated model seems unnecessary, as the remaining families have either insignificant, or positive significant correlations with the FNS and right-lateral shear stress (RLSS).

The mapped surface trace of the San Andreas Fault has a small releasing bend, in the Gold Hill region between Parkfield and Cholame where the fault orientation oscillates between $N43^\circ W$ and $N30^\circ W$ degrees west of north in a distance of ~ 10 km. While the 88 hypocentral locations are too sparse to map fault geometry to depth over the 160 km section of the SAF, the majority

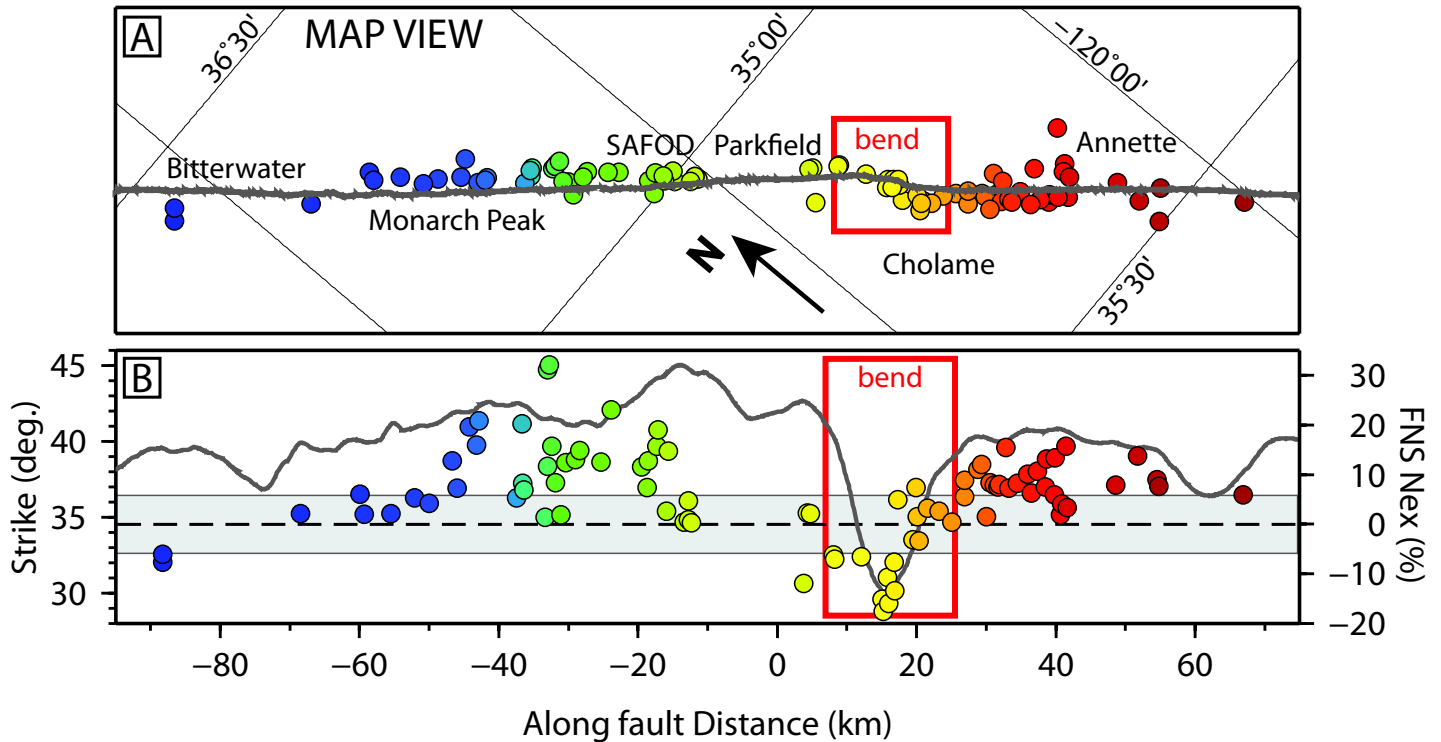


Figure 2.32: (a) A rotated map view of LFE locations color coded by family ID number as in figure 2. The stepover region is outlined in red to highlight the common morphology of the surface fault strike and the LFE hypocentral locations at depth. (b) The mapped fault strike, dark grey solid line, in degrees west of north (left axis) derived from the strike in Panel A as a function of distance along the fault. Colored circles correspond to families in Panel A. Their vertical position, measured relative to the right axis, is their FNS Nex value. Dark grey dashed line marks the zero FNS Nex value with 99% confidence intervals indicated in light grey. The stepover region is marked in red and correlates well with the negative FNS Nex values.

of locations seem to lie on one coherent fault strand with very few events deviating substantially from the mapped trace. This observation suggests that while some small amount of the total slip budget is accounted for off-fault, tremor-producing deformation largely remains localized at depths up to 25 km, and if hypocenters are closely spaced, their geometry may reflect the geometry of the San Andreas Fault at depth. If the majority of LFE hypocenters are on fault, the similar morphology of both the LFE hypocentral locations and the mapped fault trace within the fault-bend region suggests that roughness on length scales of ten kilometers is preserved at depth.

Panel B in Figure 2.32 compares the local fault orientation derived from the mapped surface trace of the San Andreas Fault to the observed FNS Nex values. The most striking feature of this comparison is that nearly all families within the fault bend have either insignificant or negative values of FNS Nex values, suggesting that fault geometry may be responsible for the mechanically implausible correlation with clamping. While changing the fault azimuth to account for local geometry in a 2D

plane strain model does not produce positive, or insignificant Nex values, variable fault strike is still a reasonable explanation for the anomalous Nex values, as the model may not be sufficiently complicated to adequately characterize the magnitude of stresses resulting from such a geometry.

16.5 Acknowledgements

This work is funded by the United States Geological Survey and a National Science Foundation Graduate Research Fellowship.

16.6 References

- Agnew, D.C., SPOTL: Some programs for ocean-tide loading, *SIO Ref. Ser.*, 96-8, 35 pp., Scripps Institution of Oceanography, La Jolla, CA, 1996.
- Shelly, D.R. and J.L. Hardebeck, Precise tremor source locations and amplitude variations along the lower-crustal central San Andreas Fault, *Geophys. Res. Lett.*, 37, L14301, 2010.
- Thomas, A.M., R.M. Nadeau, and R. Bürgmann, Tremor-tide correlations and near-lithostatic pore pressure on the deep San Andreas fault, *Nature*, 462, 1048-1051, 2009.

17 TremorScope: Imaging the Deep Workings of the San Andreas Fault

Roland Bürgmann, Richard Allen, Pascal Audet, Douglas Dreger, Robert Nadeau, Barbara Romanowicz, Taka'aki Taira, Margaret Hellweg

17.1 Introduction

Until recently, active fault zones were thought to deform via seismic earthquake slip in the upper, brittle section of the crust, and by steady, aseismic shear below. However, in the last few years, this view has been shaken by seismological observations of seismic tremor deep in the roots of active fault zones. First recognized on subduction zones in Japan and the Pacific Northwest, tremor has also been found to be very active on a short section of the San Andreas to the southeast of one of the most densely monitored fault segments in the world, near Parkfield (*Nadeau and Dolenc, 2005*). This deep (20-30 km) zone of activity is located right below the nucleation zone of the great 1857 Fort Tejon earthquake. Thus, understanding the temporally and spatially complex faulting process in this zone may help us better understand the conditions that lead to such large ruptures.

17.2 The Project Plan

Although the tremor source region is away from existing seismic networks in and around Parkfield, early studies of the deep tremor have led to dramatic revisions in our views about how faults behave at depth (e.g., *Nadeau and Guilhem, 2009; Thomas, Nadeau and Bürgmann, 2009; Shelly, 2010; Shelly and Hardebeck, 2010*). These studies reveal behavior of faulting in the deep crust that is complex and dramatically different from the “normal” earthquakes that occur in the shallow crust. By adding seismic stations around the tremor source zone, we will complement the existing monitoring around Parkfield. The result, the TremorScope network, will sharpen our ability to explore this fascinating natural laboratory of active lower crustal faulting.

The proposed network consists of eight new stations to be centered on the tremor source (Figure 2.33). Four sites will have borehole installations and an accelerometer at the surface. The target is to install the equipment in boreholes that are 300 m deep. Each hole will have a three-component set of gimballed, 2 Hz geophones cemented at the bottom that will be digitized at the surface. In three boreholes, a Guralp downhole sensor package, consisting of a three-component broadband seismometer, a three-component accelerometer and a digitizer, will also be deployed. The other four stations will be surface installations consisting of a broadband seismometer, an accelerometer and a digitizer. At all locations, data will be logged onsite and forwarded to Berkeley for real-time processing. The data will be used in real-time earthquake monitoring (see Operations Sec-

tion 8), as well as for tremor studies. The borehole sites (CASS, SCN, NC.PBP and NC.PPG) will be at some distance from the tremor source centroid, to offer low-noise, high quality recordings that offer good constraints on the tremor locations and depth. The four surface stations, closer to the tremor centroid, will have broadband seismometers, accelerometers and digitizers, as well as data loggers.

The project began in January 2011. We have ordered equipment and found sites for the stations (Figure 2.33). During the summer, we will be performing telemetry tests. We expect to install the stations in the fall of 2011.

17.3 Perspectives

Data from the TremorScope project will improve earthquake monitoring in the region south of Parkfield. Insights from the project will also contribute to understanding tremor and slip in other regions of the world where such phenomena have been observed, but are not nearly as accessible. Should a great San Andreas earthquake occur during this experiment, the network would also provide unprecedented and exciting insights into the seismic rupture process.

17.4 Acknowledgements

This work is funded by grant 2754 from the Gordon and Betty Moore Foundation.

17.5 References

- Nadeau, R., and D. Dolenc (2005), Nonvolcanic tremors deep beneath the San Andreas fault, *Science*, 307, 389, doi:10.1126/science.1107142.
- Nadeau, R.M. and A. Guilhem (2009), Nonvolcanic Tremor and the 2003 San Simeon and 2004 Parkfield, California Earthquakes, *Science*, 325, 191-193.
- Shelly, D. R., and J. L. Hardebeck (2010), Precise tremor source locations and amplitude variations along the lower-crustal central San Andreas Fault, *Geophys. Res. Lett.*, doi:10.1029/2010GL043672.
- Shelly, D. R. (2010), Migrating tremors illuminate deformation beneath the seismogenic San Andreas fault, *Nature*, 463, 648-652. doi:10.1038/nature0875.
- Thomas, A., R. M. Nadeau, and R. Bürgmann (2009), Tremor-tide correlations and near-lithostatic pore pressure on the deep San Andreas fault, *Nature*, 462, 24-31.

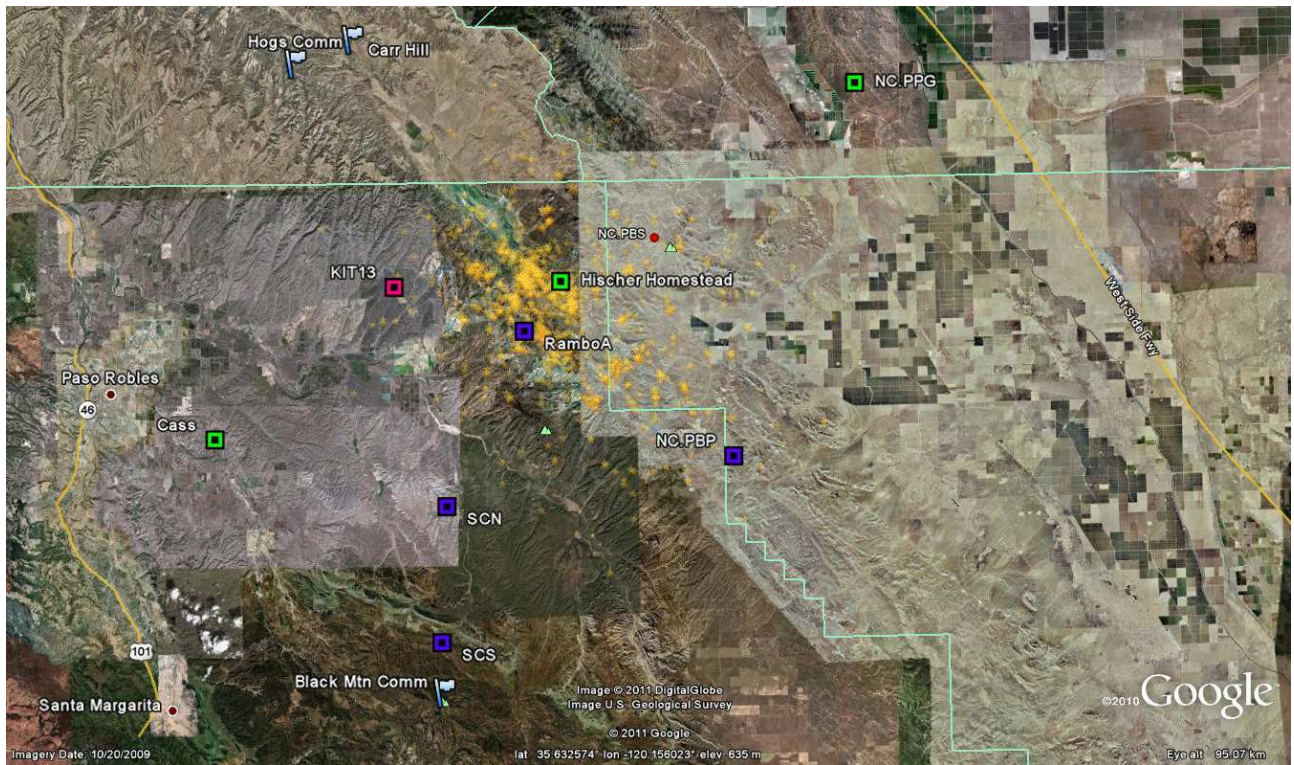


Figure 2.33: Planned locations for TremorScope stations. Gold stars: Tremor locations. Colored squares: TremorScope sites. NC.PBP and NC.PPG are currently operated by the USGS Menlo Park and have short period vertical geophones and analog telemetry. Sites Cass, SCS, NC.PBP and NC.PPG will be borehole stations. SCN and SCS are collocated with PBO GPS stations. Telemetry will go via radio to Carr Hill, Hogs Canyon Comm. or Black Mountain Comm.

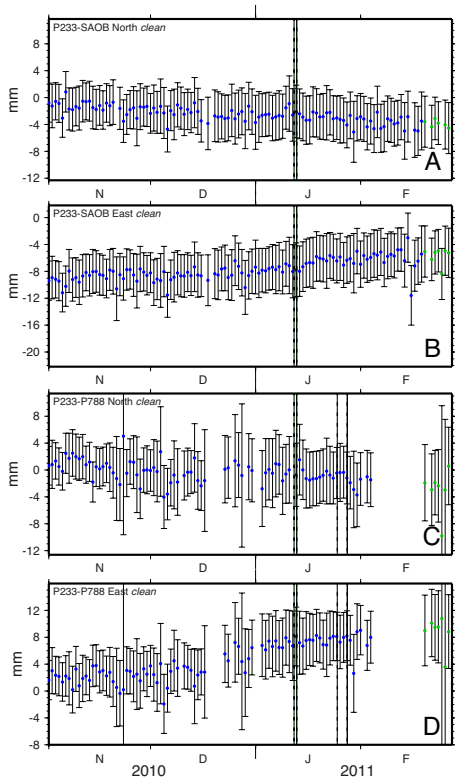


Figure 2.36: Time series of position differences for sites P233 to SAOB (A: North B: East) and sites P233 to P788 (C: North D: East). Both are fault-crossing baselines near the location of the 1/12/11 earthquake. Green points are those processed with IGS Rapid orbit files rather than Final orbits (black points). First set of black lines are the times of the two largest EQs in the SJB sequence; the second set is the creep events at XSJ3 and XHR2/CWN1.

(Figure 2.37B). This decrease and then resumption of eastward motion is also apparent in the P251 to P232 baseline, which also crosses the San Andreas fault, but has a longer distance. This suggests that the apparent motion is due to a regional process. However, from a multi-year time series, it is apparent that such a change in eastward motion occurs every year in the wintertime (Figure 2.37C). So while the motion may be consistent across several stations, it seems likely due to regional rainfall, rather than a slow slip event.

18.3 Acknowledgements

This work was supported by NSF-EarthScope Grant #EAR-0951430.

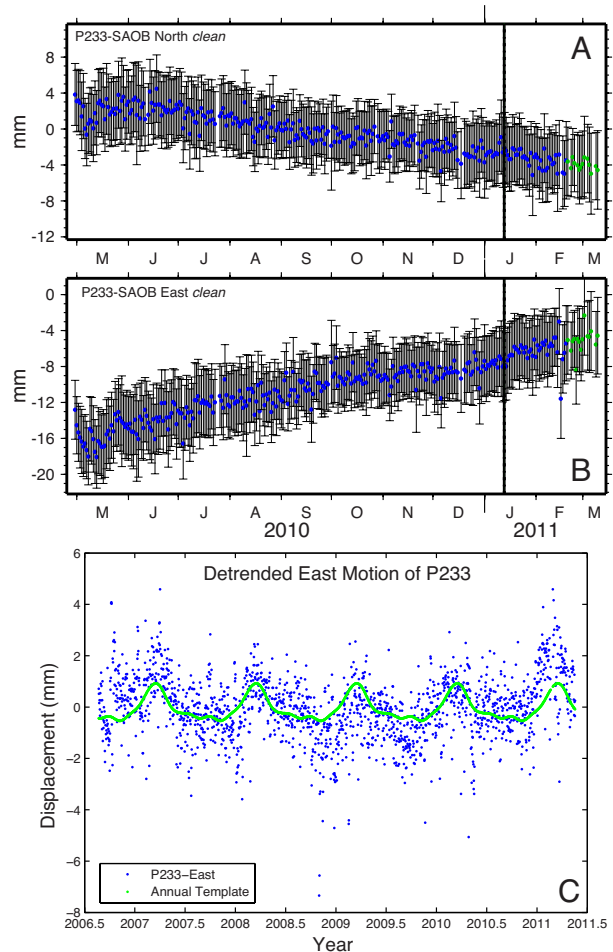


Figure 2.37: Time series of position differences for sites P233 to SAOB (A: North B: East) and C) detrended eastward motion of site P233 relative to stable North America, processed by PBO (<http://pboweb.unavco.org/shared/scripts/stations>).

18.4 References

Gwyther, R. L., C. H. Thurber, M. T. Gladwin, and M. Mee, Seismic and aseismic observations of the 12th August 1998 San Juan Bautista, California M5.3 earthquake, paper presented at *3rd San Andreas Fault Conference*, Stanford Univ., Stanford, Calif., 2000.

Uhrhammer, R., L. S. Gee, M. Murray, D. Dreger, and B. Romanowicz, The M_w 5.1 San Juan Bautista, California earthquake of 12 August 1998, *Seismol. Res. Lett.*, 70, 10-18, 1999.

19 Probing the Deep Rheology of Tibet: Constraints from 2008 M_w 7.9 Wenchuan, China Earthquake

Mong-Han Huang and Roland Bürgmann

19.1 Introduction

The 2008 M_w 7.9 earthquake occurred at Wenchuan of Sichuan Province, China, and studies of the earthquake and its postseismic relaxation give us an opportunity to examine the rheology of east Tibet. The surface motion after a large earthquake is a response to the redistribution of stresses induced by the earthquake and can be used to probe the viscous strength of the upper lithosphere. Various processes can contribute to the postseismic deformation, such as aseismic afterslip, aftershock related deformation, viscoelastic relaxation in the lower crust/upper mantle, and poroelastic rebound. In this study, we consider the viscous relaxation due to the coseismic stress redistribution that would primarily affect the middle- to far-field surface deformation.

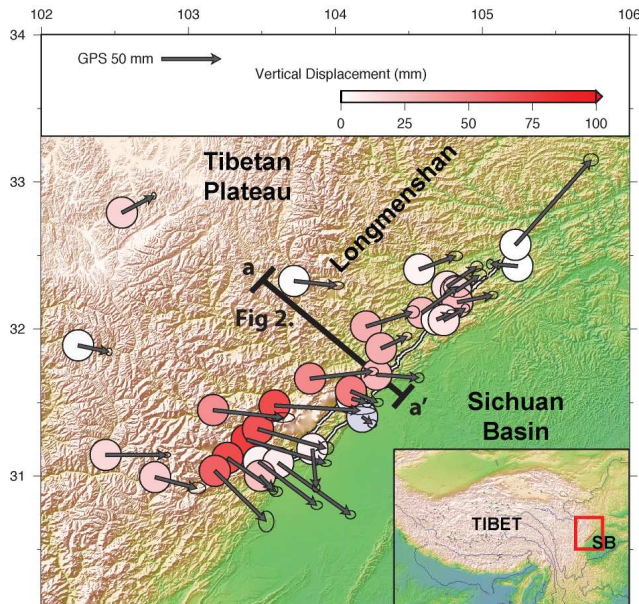


Figure 2.38: Wenchuan postseismic deformation from GPS. The arrows show horizontal motions, and colored circles are the vertical displacement (the scale is shown above). The inset shows the topographic contrasts between Tibet and the Sichuan basin (SB).

19.2 Method and Data

We apply an analytical solution (Pollitz, 1992) to calculate postseismic deformation due to viscoelastic relaxation of a layered spherical Earth, and include the effects of gravity and medium compressibility. Each layer can be represented with elastic or viscoelastic (Maxwell

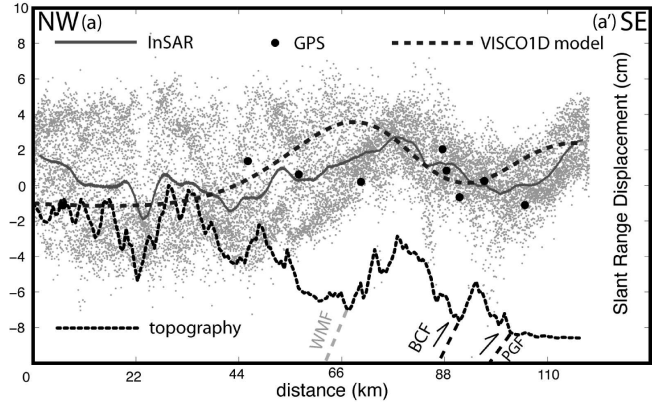


Figure 2.39: The slant range displacement along the profile in Figure 2.38. The mean SRD is the average of the dots representing extracted data from InSAR pair 2008/07/21-2009/09/08. The predicted model shows agreement with InSAR and GPS (projected to line of sight).

and Burgers) properties. In this study, the density, bulk modulus, and rigidity of each layer are based on the CRUST 2.0 model (<http://igppweb.ucsd.edu/~gabi/crust2.html>). The Wenchuan earthquake fault geometry is based on Shen *et al.*, 2009, based on geodetic inversion of coseismic deformation. Our simplified fault geometry is composed of five segments with different slip rates, extends to a depth of 20 km, and runs along the 285 km Longmenshan fault zone oriented 229° (Figure 2.38).

Thirty one cGPS stations are deployed in eastern Tibet in the hanging wall of the Longmenshan fault zone. To obtain the first-year postseismic deformation, we fit the cGPS time series in terms of a linear least square fit with the assumption of zero displacement right after the main shock (Figure 2.39). We used more than 30 ALOS PALSAR L band (23.6 cm wavelength) data sets from May 2008 to October 2010 to measure the postseismic deformation. The ALOS PALSAR data from six paths (471-476) and seven frames (590-640) cover most of the Wenchuan postseismic deformation. All PALSAR data are processed using the software ROI PAC 3.0, and the 90 m SRTM DEM is used to correct the phase due to topography.

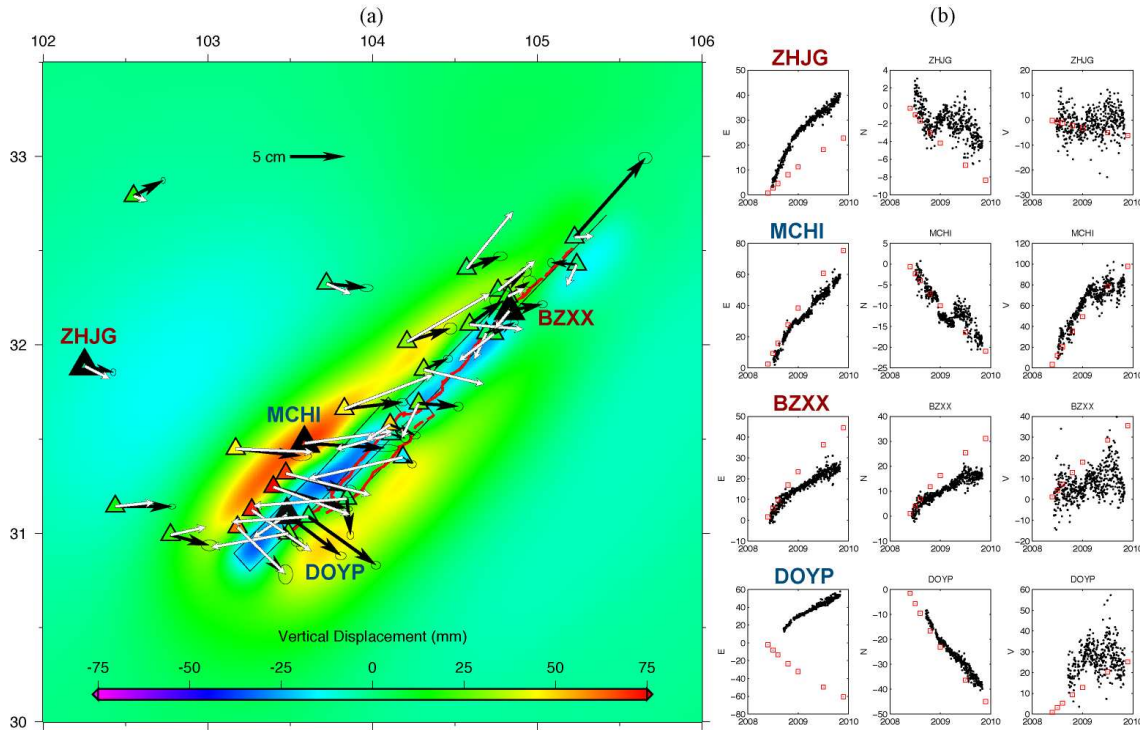


Figure 2.40: (a) The comparison of GPS and the forward model. The five fault planes that represent the Wenchuan coseismic fault geometry are shown by blue rectangles. The black arrows are the GPS horizontal measurements, and the white arrows are the model. The color in the triangles is the GPS vertical displacement, and the background color is the model uplift. (b) The cGPS time series. The black dots are the GPS and the red squares are the model.

19.3 Results

All cGPS time series data show transient displacements in the horizontal and vertical components. The 1.5-year observations (Figure 2.38) show southeastward displacement in the SW and northeastward displacement in the NE Longmenshan. Most of the interferograms have strong topographic and ionospheric correlated noise and low coherence in the mountains. The mean slant range displacement (SRD) of one 2.5-year interferogram of track 474 (Figure 2.39) shows postseismic deformation comparable with the cGPS measurements.

The best fitting forward model suggests that a Burgers body based lower crust with a steady-state viscosity of 10^{19} Pa s and a transient viscosity of 4×10^{18} Pa s, with a 20 km elastic upper crust, can represent the rheology of Longmenshan. Figures 2.39 and 2.40 show the predicted viscoelastic relaxation and the comparison with the InSAR and cGPS data, respectively. Figure 2.40b shows the temporal fitting of 4 out of 31 cGPS stations representing far-field, middle-field, and near-field deformation, respectively. The prediction is generally of the same scale as the data and better fits the middle- to far-field data. The poor fit to the near field might be because of the lateral heterogeneity in the boundary of the plateau and the basin, which is not considered in our 1D model. Neither afterslip nor poroelastic deformation, either of which

could control the near-field postseismic deformation, are considered here.

Future work will focus on a reliable 3D rheological structure of eastern Tibet and the consideration of other processes such as afterslip and poroelastic deformation. Additional ENVISAT InSAR data will be considered in order to obtain the deformation in time series following the Wenchuan mainshock.

19.4 Acknowledgements

We thank prof. Z.-K. Shen of Beijing for providing the GPS time series. This work is supported by NSF grant EAR 0738298.

19.5 References

- Pollitz, F., Postseismic relaxation theory on a spherical earth. *Bull. Seism. Soc. Am.*, 82, 1, 422-453, 1992.
- Shen, Z.K., J. Sun, P. Zhang, Y. Wan, M. Wang, R. Bürgmann, Y. Zeng, W. Gan, H. Hiao, and Q. Wang, Slip maxima at fault junctions and rupturing of barriers during the 2008 Wenchuan earthquake, *Nat. Geosci.*, 2, 718-724, doi:10.1038/NCEO636, 2009.

20 Joint Seismic and Geodetic Analysis of the 2009 Padang, Sumatra Intraslab Earthquake

Kelly Wiseman, Roland Bürgmann, Doug Dreger, Paramesh Banerjee (EOS, Singapore) and Kerry Sieh (EOS, Singapore)

20.1 Introduction

The M_w 7.6 Padang earthquake occurred on 30 September 2009 offshore of central Sumatra (Figure 2.42). Seismicity in the Sumatra region is driven by the oblique subduction of the Indian and Australian plates beneath the Burma forearc block and Sunda plate at the Sunda trench. The Sunda megathrust has been extremely active ever since the 2004 M_w 9.2 Sumatra-Andaman earthquake, with additional megathrust earthquakes in 2005, 2007, and 2010. The last remaining section of the Sunda megathrust without a modern great earthquake is the Siberut segment, which lies offshore of Padang. Thus, it is especially important to understand the fault mechanism of the 2009 Padang earthquake in order to assess how it affects the stress levels on the Siberut segment of the megathrust.

The Padang earthquake is an unusual event because it likely ruptured the subducting Australian plate. The Engdahl relocated earthquake catalog locates the earthquake at 78 km depth, \sim 250 km from the Sunda trench, where the Hayes *et al.* (2009) Sunda slab model places the interface at \sim 69 km depth. The Padang earthquake rupture mechanism is also consistent with an intraslab event. The strike is approximately perpendicular to the trench with significant left-lateral strike-slip motion. Possible candidates for the rupture plane could be subducted paleo transform faults, fractures, or ridges. We attempt to resolve the fault plane using regional broadband seismic data, GPS data, and aftershock locations.

20.2 Data and Processing

There are 7 three-component broadband stations located within 750 km of the epicenter, with useable data available on IRIS, operated by the GEOFON network, the Malaysian National Seismic Network, and the Singapore National Network. For our finite fault inversions, both the displacement waveform data and the Greens functions are bandpass filtered between 0.01 to 0.3 Hz. The maximum waveform amplitude for each component varies from about 0.5 to 1.5 cm at this frequency range. We also include data from 18 three-component permanent GPS stations, located within 380 km of the epicenter, from the SuGAR and ENS-INSU regional networks (Figure 2.42).

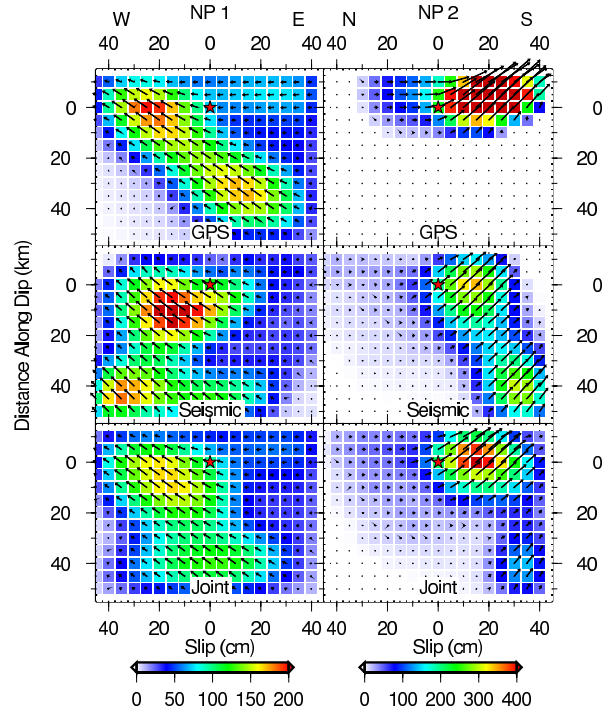


Figure 2.41: Left: Slip models for the east-west nodal plane using GPS, seismic, and joint data. Right: Slip models for the north-south nodal plane. The hypocenter is marked with a star and the arrows indicate the variable inverted rake direction.

20.3 Inversion Method

The Green's functions for our finite fault inversions are calculated using a 1D frequency-wavenumber integration method (Saikia, 1994). Our starting earth model consists of the Lange *et al.* (2010) velocity structure, PREM densities, and typical crustal attenuation values. To invert for finite fault slip, we use a least-squares inversion method that employs simultaneous smoothing and dampening (e.g. Kaverina *et al.*, 2002). We initially invert the GPS data for fault geometry, using a uniform slip model. Nodal plane (NP) 1 has a strike of 80° and dip of 57° , and NP2 has a strike of 190° and dip of 60° . Our optimal strike and dip values are very similar to the GCMT moment tensor solution geometry, and we allow variable rake in the finite fault inversions. Our fault plane extends 100 km along strike by 75 km downdip, divided into 5 x 5 km patches. The hypocenter is located in the central

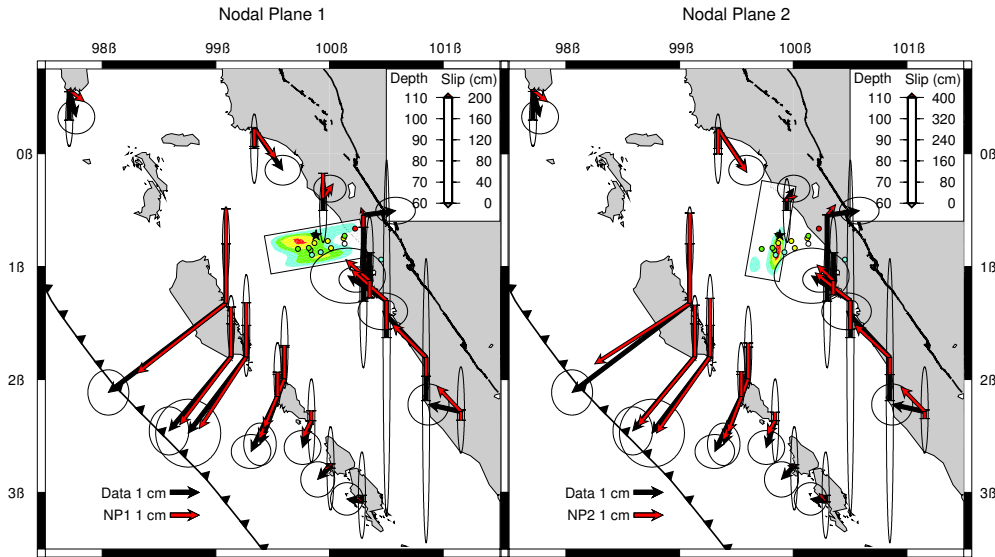


Figure 2.42: Map view of the joint inversion slip distributions (shown in Figure 2.41) with overlain GPS observation and model vectors.

position along strike and 3 patches downdip to prevent slip from propagating through the plate interface.

20.4 Inversion Results

The initial seismic finite fault inversion for both nodal plane geometries does a fairly good job of fitting the waveform amplitudes and polarities. However, all of the synthetics have significant phase shifts on the order of 10 seconds that cause the variance reductions to be negative. The highest variance reductions for each NP geometry are achieved using the Lange model with a uniform 10% increase in velocities across all depths. NP1 has a variance reduction (VR) of 56% and NP2 has a VR of 54%. For both inversions, there are two high slip regions, one near the hypocenter and the other ~ 40 km downdip (Figure 2.41).

The NP1 GPS-only inversion also has two high slip regions, although the deeper slip extends further east than the seismic-only inversion and has a VR of 79%. The NP2 GPS-only inversion has one focused high slip region, south of the hypocenter, with a VR of 80%. The NP2 model has higher peak slip values than the NP1 model, but the total moment is $\sim 20\%$ lower.

The joint inversions both have one high slip region. The east-west NP1 slip distribution is broader and extends 45 km downdip of the hypocenter, with a 40 x 55 km high slip region. The north-south NP2 slip distribution has a more focused depth range, and the high-slip region is constrained to 40 x 25 km. The seismic and GPS data are very compatible, and the joint variance reductions are within 95% of their individual inversion values.

20.5 Discussion

Our joint inversions of the Padang earthquake, using both regional seismic waveform and geodetic data, have shown that the two nodal planes have equivalent variance reductions and the total moment differs by only $\sim 10\%$, equal to M_w 7.7 events. The north-south plane has a more focused slip distribution than the east-west plane. However, the NEIC aftershock sequence better aligns with the strike and depth range of the east-west plane (Figure 2.42). Therefore our preferred fault model is slip on the east-west nodal plane, primarily southwest of the hypocenter.

20.6 Acknowledgments

This work is supported by the National Science Foundation grant EAR 0738299.

20.7 References

- Hayes et al., Advancing techniques to constrain the geometry of the seismic rupture plane on subduction interfaces a priori: Higher-order functional fits, *Geochem. Geophys. Geosys.*, *10*, 10.1029/2009GC002633, 2009.
- Kaverina et al., The combined inversion of seismic and geodetic data for the source process of the 16 October 1999 M_w 7.1 Hector Mine, California, earthquake, *Bull. Seis. Soc. Am.*, *92*, 1266-1280, 2002.
- Lange et al., The fine structure of the subducted investigator fracture zone in Western Sumatra as seen by local seismicity, *EPSL*, *298*, 47-56, 2010.
- Saikia et al., Modified frequency-wave number algorithm for regional seismograms using Filon's quadrature-modeling of L(g) waves in eastern North America, *Geophys. J. Int.*, *118*, 142-158, 1994.

21 Rapid Detection of Large Earthquakes Using Quasi-Finite-Source Green's Functions in Moment Tensor Analysis

Aurelie Guilhem and Douglas S. Dreger

21.1 Introduction

Rapid procedures (i.e. within 5 to 15 minutes) for earthquake and tsunami early warnings focus on earthquake location, depth, magnitude, and slowness, but initial tsunami early warnings are more often issued without knowing the mechanism of the earthquake. *Kawakatsu* (1998) proposed using a limited number of stations to automatically detect, locate and determine the source parameters of earthquakes occurring within a predefined region by computing moment tensors at each point of a grid from continuously streaming long-period waveform data. This method gives correct results in terms of detection and source characterization of up to M7 earthquakes offshore Japan (*Tsuruoka et al.*, 2009). For major earthquakes (M8+), we propose to improve the point-source moment tensor inversion by using QFS Green's functions (QFS GFs) that takes into account the finiteness of the rupture zone. Using a direct and single-step procedure, it becomes possible to monitor all $M_w > 3.5$ earthquakes.

21.2 Method

Kawakatsu (1998) proposed to continuously invert the long period seismic wavefield (> 10 sec) for moment tensors at grid points representing virtual sources distributed over a region. At each station, the data d are represented as the convolution of the GF tensor, G , describing the wave propagation between the source and the receiver, and the moment tensor components m of the source:

$$d = G \cdot m$$

The least-square solution for the moment tensor can be obtained:

$$M = (G^T G)^{-1} G^T d$$

where the $(G^T G)^{-1} G^T$ matrix for each point-source can be computed in advance. The multiplication of this matrix with streaming data can be performed continuously. Earthquake detection is given when the variance reduction (VR), or fit between the data and the synthetics, exceeds a detection threshold.

We set up a moment tensor grid search for the Mendocino Triple Junction (MTJ) using four BDSN stations and virtual sources located every 0.2° in latitude and longitude and every 3 km in depth (Figure 2.43). We propose to run in parallel a system for small to moderate earthquakes (inversion of 380 seconds of 20-50 second period data) and a second one for large (M8+) earthquakes along the CSZ (inversion of 480 seconds

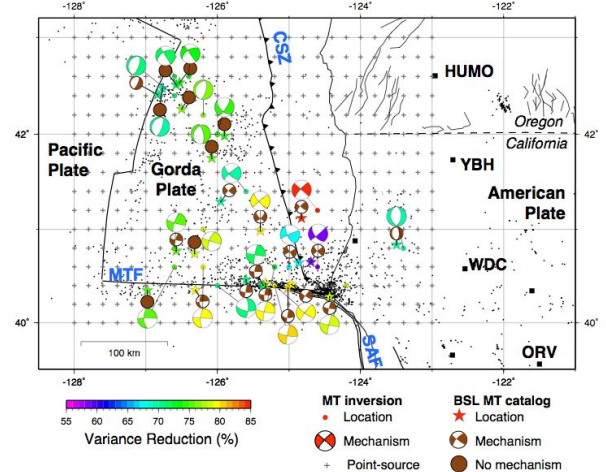


Figure 2.43: Map of the Mendocino Triple Junction region showing the grid of point sources (crosses), the four seismic stations (HUMO, ORV, WDC and YBH), the regional seismicity since 1990 (black dots), and the studied events that are shown in brown for the catalog solutions and are color-coded by the VR for the inversion solutions.

of 100-200 second period data). For large earthquakes, we also include an 84-second source time function in the GFs corresponding to the tested synthetic M 8.2 earthquake (Figure 2.44).

Because for large subduction zone earthquakes the problem grows into a near-field problem, we propose to employ quasi-finite-source adjusted GFs where GFs of n grid points are averaged in advance to generate composite GFs, G_{tot} , which take into account the source-receiver back-azimuth and by consequence the radiation patterns of each component (Figure 2.44):

$$G_{tot}(t) = \frac{\sum_{i=1}^n G_i(t)}{n}$$

Directivity can also be pre-included in the composite GFs, giving constraints on the nature of finite rupture (i.e. unilateral or bilateral) (Figure 2):

$$G_{tot} = \frac{\left[G_1(t) + \sum_{i=2}^n G_i(t) \cdot \left(\frac{\Delta_{1-n}}{v_r} \right) \right]}{n}$$

where Δ_{1-n} is the distance between Source 1 (reference source) and Source n , and v_r is the rupture velocity. The

moment tensor inversion itself is performed assuming a point-source analysis method, which maintains the computational speed.

21.3 Detection of large and potentially tsunamigenic earthquakes along the Cascadia Subduction Zone

We tested the concept on M4 to M7.1 earthquakes (Figure 2.43). The solutions obtained using a 1D velocity model (i.e. Gil7) agree well with the Berkeley moment tensor catalog solutions, confirming that this system is suitable for implementation in the MTJ region. However, because of the narrow band processing (0.02-0.05 Hz), the point-source inversion for a large M8.2 earthquake only fits a small part of the record. As a consequence, it does not recover the earthquake parameters. But we find that the 100-200 second passband gives a point-source location near the fault centroid, and the correct M_w and focal mechanism (VR= 54.6% in Figure 2.44). It is possible to improve the fit between the synthetics and the data (Figure 2.44c) after simultaneously summing the GFs of several grid points centered on the event centroid. Figure 2.44d shows that, by considering a northward rupture in the composite GFs and a rupture velocity of 3 km/sec, the corresponding earthquake solution has a larger VR and better estimates the focal parameters. Similar results are obtained for a M 8.4 synthetic seismic event, which presents an extended rupture (i.e. 480 km) and two major slip areas (Guilhem and Dreger, 2011). This method permits raising the detection level of large earthquakes and allows us to obtain more precise source parameters, by considering a range of QFS GFs for different directivity scenarios and source time durations.

21.4 Conclusion

We show that it is possible to rapidly detect and characterize the seismic activity of the MTJ region using an algorithm that performs moment tensor inversions. The QFS GFs allow more rapid detection of major events and more precise determination of their source parameters than is likely to be available using standard processing systems. Complete earthquake information is retrieved about 6 minutes after a M 4-7 earthquake and 8 minutes after a M 8+ earthquake and may allow for tens of minutes of warning in the near field.

21.5 Acknowledgements

Supported by the U.S. Geological Survey through external award G10AP00069.

21.6 References

Guilhem, A., and D. S. Dreger, Rapid detection and characterization of large earthquakes using quasi-finite-source

Green's functions in continuous moment tensor inversion, *Geophys. Res. Lett.*, 38, L13318, doi:10.1029/2011GL047550, 2011.

Kawakatsu, H., On the realtime monitoring of the long-period seismic wavefield., *Bull. Earth. Res. Inst.*, 73, 267-274, 1998.

Tsuruoka, H., H. Kawakatsu, and T. Urabe, GRiD MT (grid-based real-time determination of moment tensors) monitoring the long-period seismic wavefield, *Physics of the Earth and Planetary Interiors*, 175, 8-16, doi:10.1016/j.pepi.2008.02.014, 2009.

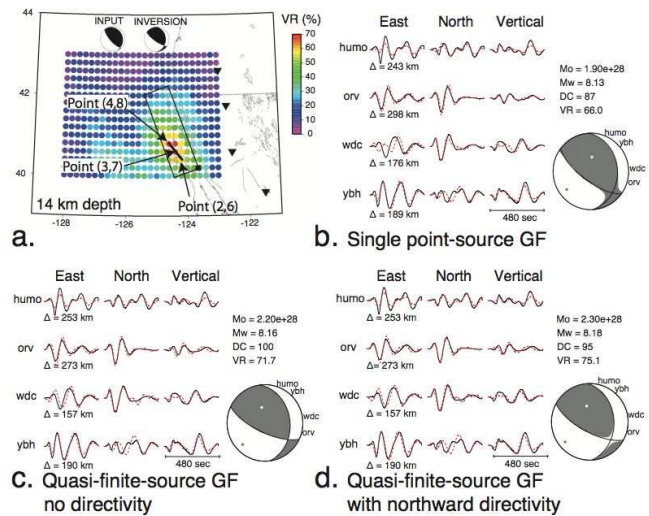


Figure 2.44: a) Map of the best VRs at 14 km depth obtained for a point-source moment tensor inversion for a synthetic M 8.2 earthquake (rectangle). The best mechanism (top, right) is compared to the input mechanism (top, left). Arrows point to the points that are considered in the multi-point source inversion. b) Best moment tensor solution obtained at Point (3,7). c) Moment tensor solution for the multi-point source inversion (no directivity). d) Moment tensor solution for the multi-point source inversion with a northward directivity.

22 Identifying Undetected Early Aftershocks Associated with the 12 August 1998 M_w 5.1 San Juan Bautista Earthquake

Taka'aki Taira, Roland Bürgmann, Robert M. Nadeau

22.1 Introduction

Aftershocks are triggered by abrupt changes of stress induced by a larger earthquake. Detailed images of spatiotemporal changes in aftershock activity help delineate the mainshock rupture area. However, large numbers of early aftershocks are not detected because they are masked by large amplitudes and long duration of seismic coda waves from the mainshock and other aftershocks. *Peng and Zhao* (2009) have demonstrated that $\sim 10,000$ aftershocks during the first three days following the 2004 M 6.0 Parkfield earthquake were undetected by the standard earthquake-detection algorithm of the Northern California Seismic Network (NCSN). We focus on the detection of uncatalogued aftershocks after the 12 August 1998 M_w 5.1 San Juan Bautista (SJB) earthquake. This event was the largest historic earthquake in the SJB area and was associated with a large slow slip event (*Uhrhammer et al.*, 1999). Additionally, *Nadeau and McEvilly* (2004) and *Templeton et al.* (2008) found accelerations in repeating microearthquake frequency accompanying the 1998 slow slip event.

22.2 Identification of Undetected Early Aftershocks

Following *Peng and Zhao* (2009), we have been identifying undetected early aftershocks with a cross-correlation based approach. We use waveforms from 248 SJB earthquakes detected by the NCSN during a 10-day period spanning the 1998 SJB earthquake (9 August through 18 August, 1998) as templates to identify additional, previously undetected earthquakes. Using continuous data recorded by the closest two seismic stations to the 1998 SJB event (BK.SAO and NC.BVY; less than 4 km from the mainshock), our preliminary analysis has detected ~ 900 individual earthquakes, with the averaged cross-correlation threshold of 0.7 (Figure 2.45). We have identified four times more aftershocks than listed in the NCSN catalog (Figure 2.46). We also searched for small foreshocks immediately preceding the mainshock (e.g., *Dodge et al.*, 1996; *Bouchon et al.*, 2011), but no events were detected during the two minutes preceding the mainshock. We currently assign the locations of the detected events to that of the template events providing the highest cross-correlation values (Figure 2.46a).

With the detected early aftershocks, we find that a highly productive burst of aftershocks started 17 hours after the mainshock (Figure 2.46b). In this aftershock episode, ~ 100 events occurred within a 3-hour period.

These aftershocks occurred in the northwest part of the rupture area (Figure 2.46b). This aftershock episode may be the result of the redistribution of stress induced by the 1998 SJB earthquake. Apparently strain and creepmeter data of the associated slow slip event do not resolve an acceleration of slip associated with this accelerated aftershock activity.

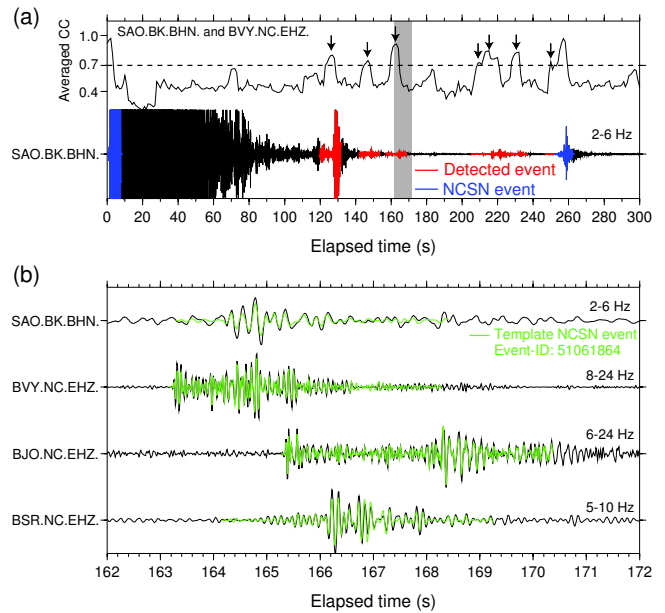


Figure 2.45: (a) Top panel shows averaged cross-correlation functions based on SAO.BK.BHN and BVY.NC.EHZ data. Highest cross-correlation values were plotted at individual time steps from cross-correlation functions for the 248 template events. Black arrows indicate identified events using the threshold with averaged cross-correlation value of 0.7 (dashed line). Bottom panel shows observed seismograms (black) recorded at BK.SAO in the N-S component with a 2-6 Hz bandpass filter. Waveforms shown in red and blue are the newly detected events and the NCSN events (the first 10-s data). (b) Detected early aftershock at ~ 160 s after the mainshock shown in grey area in Figure 2.45a using the template event nc51061864 (M 0.85) occurring ~ 4 days after the mainshock. Waveforms shown in black and green are the continuous and the template waveforms, respectively.

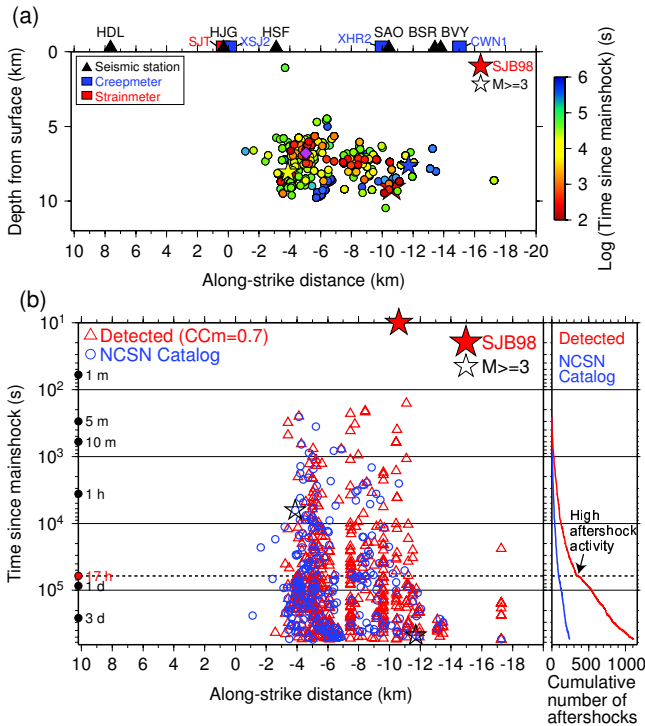


Figure 2.46: (a) Cross-section view of the newly detected and NCSN events (circles) along the San Andreas fault in the SJB area (NW to SE) color-coded by the logarithmic time after the mainshock (red star). The purple diamond is the location of the characteristically repeating earthquake sequence shown in Figure 2.47. (b) Left panel shows the occurrence times of aftershocks since the 1998 SJB mainshock as a function of the along-strike distances. The blue circles are the events listed in the NCSN catalog and the red triangles are newly detected events from the cross-correlation analysis. Right panel shows the cumulative numbers of aftershocks from the NCSN catalog (blue) and this study (red).

22.3 Characteristically Repeating Microearthquakes

As a complementary study to Nadeau and McEvilly (2004) and Templeton et al. (2008), we are identifying smaller characteristically repeating earthquakes around the rupture area of the 1998 SJB earthquake. We have analyzed $\sim 6,000$ SJB earthquakes in the NCEDC earthquake catalog between 1984 and June 2011 and found ~ 350 candidate repeating earthquake sequences. By integrating the early aftershock and repeating microearthquake catalogs, we found that some of the newly identified early aftershocks are characteristically repeating microearthquakes (Figure 2.47). We now focus on completing the repeating microearthquake catalog in the vicinity of the 1998 SJB earthquake, to better characterize the accelerated deep fault creep induced by the 1998 SJB mainshock.

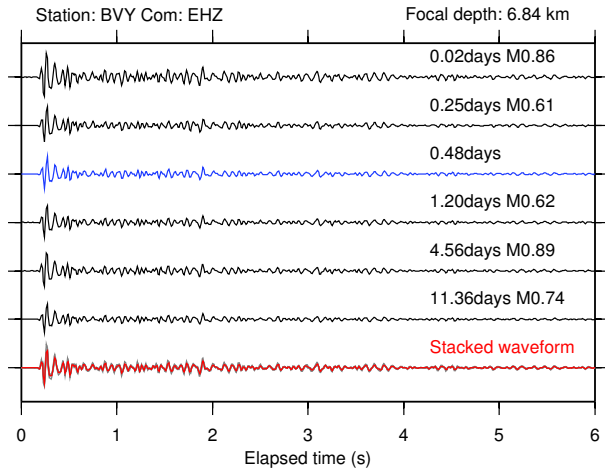


Figure 2.47: Characteristically repeating earthquakes identified from our preliminary analysis. An example of vertical seismograms recorded at station BVY. Blue waveform is from a newly identified early aftershock that is not listed in the NCEDC catalog. The bottom waveform shown in red is a stack of the six seismograms (gray in the bottom trace) for six individual repeating earthquakes shown as the first to sixth traces. Also shown are the elapsed times (days) since the 1998 SJB mainshock and the NCEDC magnitudes.

22.4 Acknowledgements

We thank R. Turner, P. Audet, and I. Johanson for discussion, and NCEDC for data collection and distribution. This work is supported by the National Science Foundation EAR-0951430.

22.5 References

- Bouchon, M., H. Karabulut, M. Aktar, S. Özalaybey, J. Schmittbuhl, and M.-P. Bouin, Extended nucleation of the 1999 Mw 7.6 Izmit earthquake, *Science*, 331, 877-880, doi:10.1126/science.1197341, 2011.
- Dodge, D.A., G.C. Beroza, and W.L. Ellsworth, Detailed observations of California foreshock sequences: Implications for the earthquake initiation process, *J. Geophys. Res.*, 101(B10), 22,371-22,392, 1996.
- Nadeau, R. M. and T.V. McEvilly, Periodic pulsing of characteristic microearthquakes on the San Andreas Fault, *Science*, 303, 220-222, 2004.
- Peng, Z. and P. Zhao, Migration of early aftershocks following the 2004 Parkfield earthquake, *Nature Geosci.*, 28, 877-881, 2009.
- Templeton, D., R.M. Nadeau, and R. Bürgmann, Behavior of repeating earthquake sequences in Central California and the implications for subsurface fault creep, *Bull. Seismol. Soc. Am.*, 98, 52-65, 2008.
- Uhrhammer, R., L.S. Gee, M. Murray, D. Dreger, and B. Romanowicz, The Mw 5.1 San Juan Bautista, California earthquake of 12 August 1998, *Seismol. Res. Lett.*, 70, 10-18, 1999.

23 Persistent Scatterer InSAR Analysis of Berkeley Hills Landslides

Ling Lei and Roland Bürgmann

23.1 Introduction

Over the past decade, InSAR has been proven to be a powerful tool for studying earth processes such as volcano deformation, tectonic deformation, and land subsidence. InSAR provides a spatially continuous observation of the change in line of sight between the satellite and the ground over the time period of an interferogram. It has the potential to resolve spatially and temporally complex deformation. But the geometrical and temporal de-correlation with atmospheric error has long been its limitation. Persistent Scatterer InSAR (PS-InSAR) has the advantage of overcoming these limiting factors. The persistent scatterer, which can keep the phase stable in the temporal series, can be used

to get surface deformation by analyzing the time-series differential phase variation. They are typically radar-bright and phase stable structures such as building corners, telephone poles and rock spars. PS-InSAR is an approach that estimates several contributions: atmospheric disturbances, orbital errors, deformation signal, and topographical errors. It is particularly well suited to monitoring deformation over urban areas, where an abundance of man-made structures results in large numbers of suitable radar-bright and phase-stable reflectors.

23.2 Study Area and Data Set

The Berkeley Hills are located in the eastern San Francisco Bay area. The active Hayward Fault (HF) bounds

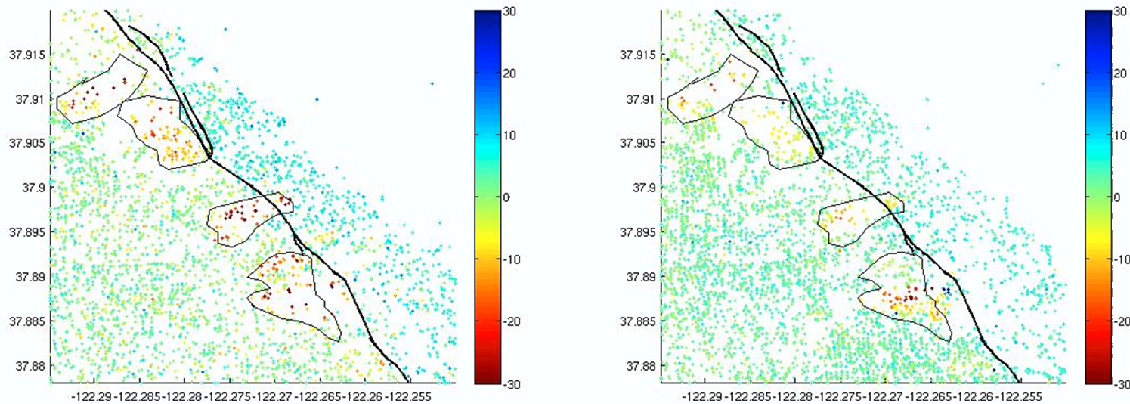


Figure 2.48: Mean LOS velocity with ERS and RST Data

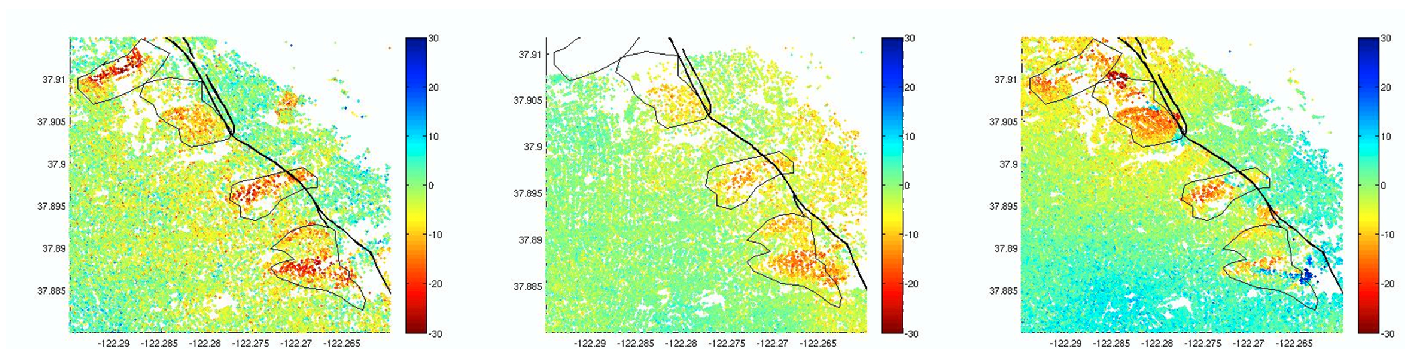


Figure 2.49: Mean LOS velocity with TSX Data

the western margin of the East Bay Hills (EBH), which rises to about 370 m above sea level. On the Berkeley Hills there are four large, slow moving, deep-seated landslides. All the landslides extend through residential areas and move on the order of cm/year, each covering an area of roughly 0.25-1.00 km². These slides are located in a rapidly uplifting zone adjacent to the Hayward fault. A lot of damage to homes, breakage of underground utility pipes, and confusion over property lines has been caused by landslides over the years, although deformation on these landslides is typically small and slow. It is currently not well understood how the landslides respond to seismic activity on the Hayward fault, but significant deformation is conceivable under wet conditions and given a moderate to large seismic event. Resolving the kinematics of landslides is a pre-requisite for improving understanding of the mechanics of these potentially hazardous features. Here we will evaluate the potential and limitations of TerraSAR-X data for monitoring deformation of landslides. The TerraSAR-X satellite operates in an 11 day repeat orbit at an altitude of 514 km. The rather short orbit repeat cycle and the electronically steerable antenna allow fast and frequent imaging of a particular site. The frequent interferometric coverage can help especially with monitoring events in shorter time scales. Fast events can be detected and atmospheric delay errors can be reduced by averaging many interferograms. The interferometric processing for the study area was performed based on three sets of TerraSAR-X Spotlight SLC images and Stripmap SLC images delivered by DLR. Table 2.2 shows their beam numbers, incidence angles and pass directions. The TerraSAR-X images were acquired over the Bay Area, particularly around the active landslides, coastal subsidence and shallow Hayward fault creep near the city of Berkeley. The data acquisition interval is from May 2009 to August 2010.

Beam No.	Inc. Angle	Track Type	No. of Data
Strip_003	21	Descending	21
Spot_038	38	Descending	17
Spot_049	49	Descending	18

Table 2.2: Data sets information

23.3 Data Processing

The processing was started from SLC data and then coregistered to the same geometry. To minimize the effect of topography on interferograms, we applied a two-pass differential interferometry approach using SRTM 1-arc-second DEM heights as a reference. The Stanford Method for Persistent Scatterers (StaMPS) was applied. It was developed in Stanford University by Andy Hooper. It is a public-domain tool of InSAR processing. All of these images were used to identify persistent and coherent pixels. The wrapped phase of the PS pixels was

selected and the improved phase unwrapping algorithm adopted.

23.4 Results and Analysis

A previous study by *Hilley et al.* used InSAR data from European Remote Sensing satellites (ERS-1,2) from 1992-2000 and Radarsat from 2001 to 2006 to image the landslides and estimate rates of motion (Figure 2.48). The Permanent Scatterer InSAR analysis was utilized. The slow-moving landslides of the Berkeley Hills are clearly indicated by the faster moving yellow and red pixels. Since all the results rates were measured in the direction of the look angle of the satellite, it was hard to compare them with different satellite data or the same satellite data with different look angles. However, assuming that most of the displacement along these landslides follows the average four degree downhill slope, we projected the LOS velocity to downslope velocity, shown in Figure 2.49. You can see that the PS density of TerraSAR-X data is much higher than ERS or Radarsat, and most of the results are consistent with southwest motion of the landslides. The negative mean LOS velocity in the landslides area is consistent with landslide motion moving away from the satellite. For future work, we hope the four beams of TerraSAR-X data from different viewing geometries will significantly improve our ability to fully characterize the kinematics and temporal patterns of the landslides.

23.5 Acknowledgements

We thank the German Aerospace Centre (DLR) for providing TerraSAR-X data for this project. We thank Andy Hooper for supporting StaMPS software.

23.6 References

- Hilley, G., R. Bürgmann, A. Ferretti, F. Novali and F. Rocca, Dynamic of slow-moving landslides from permanent scatterer analysis, *Science*, 304, 1952-1955, 2004.
- TerraSAR-X Ground Segment Basic Product Specification Document, TX-GS-DD-3302.
- TerraSAR-X Ground Segment Level 1b Product Format Specification, TX-GS-DD-3307.
- Bürgmann, R., E. Fielding, and J. Sukhatme, Slip along the Hayward fault, California, estimated from space-based synthetic aperture radar interferometry, *Geology*, 26, 559-562, 1998.
- Eineder, M., N. Adam, and R. Bamler, Spaceborne Spotlight SAR Interferometry With TerraSAR-X, *IEEE Trans. Geosci. Remote Sense.*, 5, 1524-1535, 2009.
- Hooper, A., H. Zebker, P. Segall and B. Kampes, A new method for measuring deformation on volcanoes and other natural terrains using InSAR persistent scatterers, *Geophys*, 31, 2004.

24 Toward Global Waveform Tomography with the SEM: Improving Upper-Mantle Images at Shallow Depths

Scott French, Vedran Lekic, and Barbara Romanowicz

24.1 Introduction

The SEMum upper-mantle V_S model (Lekic and Romanowicz, 2011) was developed using the spectral element method (SEM: e.g. Komatitsch and Vilotte, 1998) to invert long-period ($T \geq 60$ s) waveforms of fundamental and overtone mode surface waves. SEM global waveform inversion was made feasible partly through use of a mode-coupled SEM (Capdeville et al., 2003), combined with an innovative smooth crustal model. The 60 km crustal layer allows the SEM to take long time steps, thus speeding computation, at the expense of complicating interpretation of the shallowest upper-mantle structure.

Our goal has been to produce an updated model (SEMum2) using a more geologically-plausible fictitious Moho for the crustal layer. This update would have the immediate benefit of easing interpretation of some uppermost upper-mantle structure. In the future, we intend to include SEMum2 in the initial model for a forthcoming whole-mantle inversion, using shorter period waveform data ($T \geq 40$ s). Thus, it is advantageous to perform the update *now*, while still using the 60 s data set so that SEM simulation is comparatively inexpensive.

24.2 Crustal model development

SEM solution accuracy is strongly affected by mesh fidelity to the underlying earth model, requiring interior boundaries (Moho, 410 km, etc...) to be matched with element faces. Time-stability of the SEM is determined by the minimum ratio between spatial discretization and wave speed (the Courant-Friedrichs-Lewy, or CFL condition), with the maximum stable time-step determining the overall cost of time-integration.

In a pure global SEM (e.g. Tromp, et al., 2008), the CFL condition is dominated by high V_P in the core. If the core is replaced with a modal solution (Capdeville, et al., 2003), then small spatial discretization in the thin oceanic crust dominates - leading to a less restrictive, but still prohibitively small, time-step. As a solution, Lekic and Romanowicz (2011) developed a new crustal model: a radially-anisotropic smooth crustal layer of uniform 60 km thickness, designed to fit observed surface-wave dispersion maps (Shapiro and Ritzwoller, 2002). This scheme provides a simpler alternative to a true “homogenization” of an *a priori* crustal model (e.g. Capdeville and Marigo, 2007), while also supplying independent constraints on the effect of crustal structure on the wavefield.

For SEMum2, we adopt a more geologically plausible

laterally-varying layer thickness, at the expense of a more restrictive CFL condition. Starting from Crust2.0 Moho depth (Bassin and Masters, 2000), we restrict crustal thickness H to the interval $H \in [30, 60]$ km and filter at 2x lateral resolution of the SEM mesh. We seek “crust-equivalent” anisotropic V_S structure (e.g. Backus, 1962) that fits observed surface-wave dispersion and is parameterized with depth in Gauss-Lobatto-Legendre interpolants (GLL), as used in the SEM. The crustal layer is generated following a two-step procedure:

(1) We define a space of admissible radially-anisotropic GLL models $V_{S,iso} \in [3, 4.5] \text{ km s}^{-1}$, $V_{SH}^2/V_{SV}^2 \in [0.8, 1.2]$ from which we draw $\sim 20k$ realizations $\{\mathbf{m}_i\}$ and calculate dispersion curves for layer thickness $H \in [30, 60]$ km and bathymetry $h \in [0, 6]$ km. Group-velocity dispersion maps (25 - 60 s) are resampled on a uniform grid of knots, and dispersion curves are estimated for all $\{\mathbf{m}_i\}$ through interpolation to local seafloor and Moho topography (H, h). Best-fitting GLL models are selected for each knot, where misfit is measured in the L_1 norm to reduce sensitivity to outlier measurements common at short periods, with additional weighting by measurement uncertainty and tunable anisotropy regularization.

(2) We next perform a linearized inversion in a neighborhood surrounding the selected model using the generalized least-squares formalism (Tarantola and Valette, 1982). We use individual group-velocity kernels for each model knot, reflecting local bathymetry and fictitious Moho, which are recalculated following each iteration. Upper-mantle structure from SEMum is assumed. After 3 iterations, mean absolute misfit over all periods and model knots fell into the target range of 50 - 60 m s^{-1} . The resulting model allows a **5x** time-step prolongation over direct meshing of Crust2.0.

24.3 Preliminary update and discussion

We refer the reader to Lekic and Romanowicz (2011) for a detailed discussion of the waveform inversion scheme. The SEM is used to forward model fundamental and overtone mode surface waves ($T \geq 60s$), which are inverted for upper-mantle structure using NACT waveform sensitivity kernels following the generalized least-squares formalism. Group-velocity data ($T \leq 150s$) is included in the inversion for consistency. We follow an identical procedure, substituting the new crustal model as well as new crustal corrections for use with NACT, developed in a manner similar to that of Lekic, et al. (2010).

To date, we have performed one update iteration, and SEM simulation for the second is ongoing. We antici-

	L		T		Z	
fund	0.360	0.388	0.283	0.413	0.326	0.354
high	0.248	0.327	0.293	0.385	0.275	0.310
mixed	0.299	0.320	0.212	0.316	0.283	0.296

Table 2.3: $\|u_{obs} - u_{pred}\|^2 / \|u_{obs}\|^2$ for SEMum2 and [SEMum] by data-type and component. Values reflect 80 % of the total data set, but are considered representative.

pate two iterations will be required for the full update. Preliminary results show mantle structure highly consistent with that of SEMum. Using the East Pacific Rise as an example, Figure 2.50 demonstrates that (first-iteration) SEMum2 achieves its goal of improving shallowest upper-mantle structure, while further enhancing agreement with regional studies already exhibited by SEMum. Waveform relative square residuals are shown in Table 2.3 above for SEMum and SEMum2. These values reflect only the portion of the data set with the most recent SEM synthetics completed, or approximately 80 % thereof. We consider these values representative.

In the near future, we will complete the second update iteration, at which point we anticipate SEMum2 will have stabilized. Thereafter, we will begin data collection for the whole-mantle inversion, potentially using new ($T \geq 40$ s) SEMum2 synthetics for waveform selection.

24.4 Acknowledgements

This work was supported by the National Science Foundation (EAR-0738284). SF acknowledges support from the NSF Graduate Research Fellowship Program. SEM computations were performed at the DOE National Energy Research Scientific Computing Center (NERSC). We thank Yann Capdeville for providing us with the mode-coupled SEM implementation.

24.5 References

- Backus, G., Long-wave elastic anisotropy produced by horizontal layering, *J. Geophys. Res.*, 67, 4427-4440, 1962.
- Bassin, C.G.L. and G. Masters, The current limits of resolution for surface wave tomography in North America, *EOS, Trans. Am. Geophys. Un.*, 81, F897, 2000.
- Capdeville, Y. and Marigo, J., Second order homogenization of the elastic wave equation for non-periodic layered media, *Geophys. J. Int.*, 170(2), 823-838, 2007.
- Capdeville, Y., E. Chaljub, J.P. Vilotte, and J.P. Montagner, Coupling the spectral element method with a modal solution for elastic wave propagation in global earth models, *Geophys. J. Int.*, 152, 34-67, 2003.
- Harmon, N., D.W. Forsyth, and D.S. Weeraratne, Thickening of young Pacific lithosphere from high-resolution Rayleigh wave tomography: A test of the conductive cooling model, *Earth Planet. Sci. Lett.*, 278, 96-106, 2009.
- Komatitsch, D. and J.P. Vilotte, The spectral element method: an efficient tool to simulate the seismic response of 2D and 3D geological structures, *Bull. Seism. Soc. Am.*, 88(2), 368-392, 1998.
- Kustowski, B., G. Ekstrom, and A. Dziewonski, Anisotropic shear-wave velocity structure of the Earth's mantle: a global model, *J. Geophys. Res.*, 113, B06306, 2008.

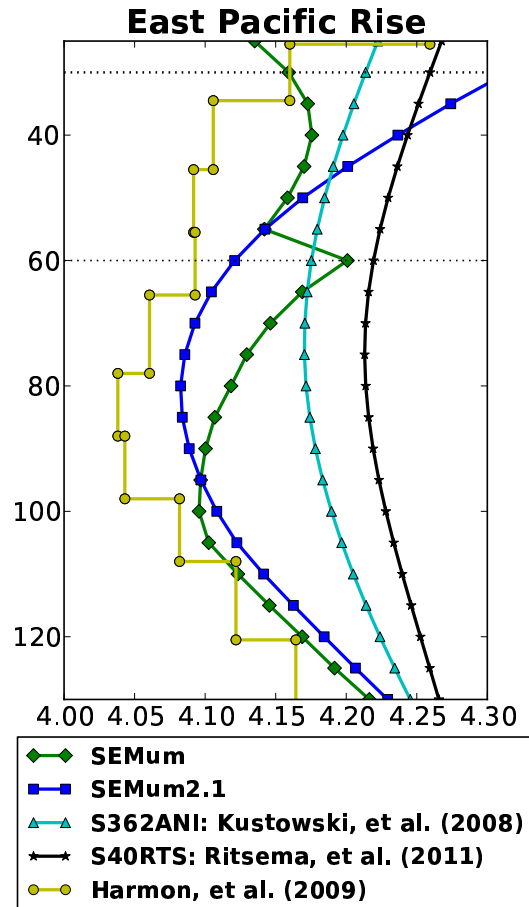


Figure 2.50: Comparison of V_S profiles at an arbitrary point beneath the EPR. Dotted lines at 30 and 60 km indicate Moho depth in the old and new crustal models. (Mean of *Harmon, et al. (2009)* regional V_{SV} model shown)

- Lekic, V. and B. Romanowicz, Inferring upper-mantle structure by full waveform tomography with the spectral element method, *Geophys. J. Int.*, 185(2), 799-831, 2011.
- Lekic, V., M. Panning, and B. Romanowicz, A simple method for improving crustal corrections in waveform tomography, *Geophys. J. Int.*, 182(1), 265-278, 2010.
- Li, X.D. and B. Romanowicz, Comparison of global waveform inversions with and without considering cross-branch modal coupling, *Geophys. J. Int.*, 121, 695-709, 1995.
- Ritsema, J., A. Deuss, H. J. van Heijst and J. H. Woodhouse, S40RTS: a degree-40 shear-velocity model for the mantle from new Rayleigh wave dispersion, teleseismic traveltime and normal-mode splitting function measurements. *Geophys. J. Int.*, 184, 1223-1236, 2011.
- Shapiro, N. and M. Ritzwoller, Monte-Carlo inversion for a global shear-velocity model of the crust and upper mantle, *Geophys. J. Int.*, 151(1), 88-105, 2002.
- Tarantola, A. and B. Valette, Generalized nonlinear inverse problems solved using the least squares criterion, *Rev. Geophys. Space Phys.*, 20, 219-232, 1982.
- Tromp, J., D. Komatitsch, and Q. Liu, Spectral-element and adjoint methods in seismology. *Comm. Comp. Phys.*, 3(1), 1-32, 2008.

25 On the Interpretation of SKS Splitting Measurements in the Presence of Several Layers of Anisotropy

Barbara Romanowicz and Huaiyu Yuan

25.1 Summary

Concerns over the validity of expressions derived by *Montagner et al.* (2000; referred to as MGL00) that link SKS splitting measurements to the variation with depth of anisotropic parameters in the upper mantle have been recently expressed (*Silver and Long, 2011*; referred to as SL11), pointing out that the long period approximations applied by these authors may not be valid for the frequency range commonly used in SKS studies, and in particular, that the anisotropy splitting parameters should depend on the order in which different anisotropy layers are arranged with depth. We show that measurements of splitting time δt and fast axis direction ψ performed at individual azimuths do depend on the order of layering; however, the expressions of MGL00 concern station averaged quantities that do not depend on the order of layers. It is therefore correct to use these expressions in joint inversions of surface waveforms and SKS station averaged splitting measurements. On the other hand, the depth-dependent sensitivity of surface waveforms naturally provides constraints on the order of layering.

We extend the expressions of MGL00 to the case of a tilted axis of symmetry and non vertical incident waves, and show that station averaged estimates of "effective" splitting parameters: splitting time, fast axis direction and tilt of the fast axis, can be related to the integral with depth of quantities which now depend not only on the local splitting time and fast axis direction, but also on the local tilt of the fast axis, thus also providing constraints also on the variation of the tilt with depth. Thus, combining body wave and surface wave observations also has the potential for constraining the variation with depth of the tilt of the fast axis of anisotropy, a geodynamically important parameter.

25.2 Two Layer Examples

We first consider a two layer case and show that the formalism of MGL00 can also lead to exactly the same derivation of azimuthal dependent individual SKS parameters as in (*Silver and Savage, 1994*). Detailed derivation is seen in *Romanowicz and Yuan (2011*; referred to as RY11). Figure 2.51 shows the two-layer anisotropic models and Figure 2.52 shows synthetic splitting parameters δt and ψ computed using Equation 12 of RY11 and the approximated terms with 1st order and 2nd order of $\omega\delta t$, where ω is the peak period of the SKS waveform and δt is the splitting time. Synthetic waveforms generated by the two-layer models (Figure 2.52) are also measured for

splitting parameters, which are also plotted for comparison. In all models, Equation 12 of RY11 gives the same azimuthal dependent variation of δt and ψ shown in SL11 (red), which is confirmed by individual event measurements of the synthetic waveforms (dashed black). Note the splitting parameters computed using expressions up to 2nd order terms (green) follow the back-azimuthal pattern, but blow up near the one-layer equivalent apparent "fast" (vertical gray line) and "slow" axis directions. Using the first terms only, Equation 12 of RY11, which is equivalent to Equations 21 and 22 in MGL00 in the two layer case, gives azimuthally invariant effective δt and ψ (solid black), which are identical to the measured station averages (dashed blue).

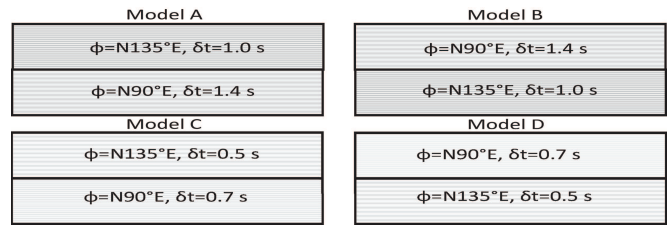


Figure 2.51: Two layer test models with ψ and δt shown for each layer. A and B have flipped layer order, and C and D are identical to A and B with only half δt .

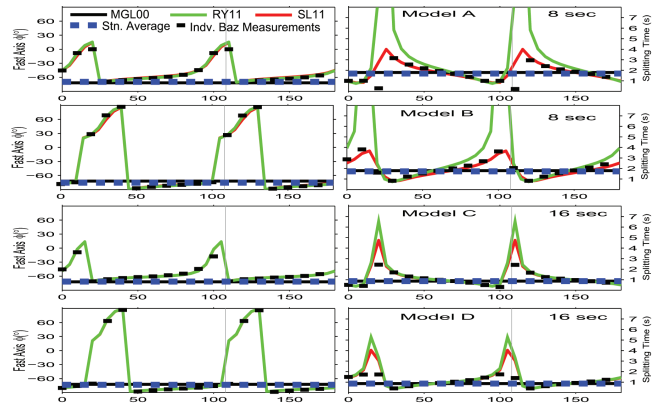


Figure 2.52: Predicted (solid) and measured (dashed) splitting parameters for model A&B at 8 s period and C&D at 16 s.

25.3 Harmonic Decomposition

Figure 2.52 also shows that individual splitting measurements tend to become singular near particular az-

imuths ψ ; therefore it is not wise to apply the long period approximation to Equation 12 in RY11. Neither MGL00 nor we use any azimuthally dependent individual event splitting data in the joint tomographic inversion. As shown in RY11, after extending to the case of multiple layers, the transverse component displacement at the top of the anisotropic model can be decomposed as $u_T^n = A \cos 2\psi + B \sin 2\psi + C$, in which ψ is event back-azimuth, A and B take the form of summation over layers of splitting time δt_i and fast axis direction ψ_i within each layer, and C is independent of the event back-azimuth ψ . Equating A and B to the one-layer effective splitting time $\delta \hat{t}$ and fast axis direction $\hat{\psi}$ (Equations 16 to 18 of RY11): $A = 0.5 \sin(2\hat{\psi}) \delta \hat{t} \dot{u}_{R_0}$ and $B = 0.5 \cos(2\hat{\psi}) \delta \hat{t} \dot{u}_{R_0}$, which eventually leads to the expression used in MGL00 and in our joint inversion (Eqn. 19 of RY11):

$$\sin(2\hat{\psi}) \frac{\delta \hat{t}}{2} = \int_0^a \frac{G(z)}{V_s(z)L(z)} \sin 2\Psi_G(z) dx$$

$$\cos(2\hat{\psi}) \frac{\delta \hat{t}}{2} = \int_0^a \frac{G(z)}{V_s(z)L(z)} \cos 2\Psi_G(z) dx$$

G and L are the anisotropic parameters of the model at depth (z) to be solved for. Noteworthy is that using tabulated values of the station averaged splitting time $\delta \hat{t}$ and fast axis direction $\hat{\psi}$ avoids instability in the individual splitting measurements and yields a robust quantity which can also be obtained from measurements of the splitting intensity (Chevrot, 2000) when measurements in a wide enough back-azimuth range are available (Figure 2.53). Note these quantities are independent of the order of layers; in the joint inversion the layering constraints come naturally from the surface waves, at least for the shallow upper mantle.

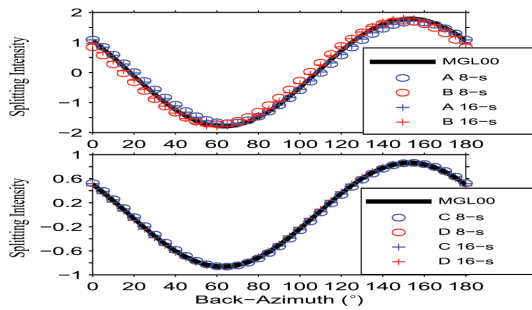


Figure 2.53: Predicted (solid line; $\sin 2(\hat{\psi} - \psi) \frac{\delta \hat{t}}{2}$) and measured (symbols) splitting intensity for models A-D at 8 s period (top) and 16 s (bottom).

25.4 Dipping symmetry axis

The formalism of RY11 can also be generalized to the case of tilted fast symmetry axis (Equations 20-32 of RY11). After the same type of analysis as for the horizontal axis of symmetry, but with Θ and Φ for the tilt from

the horizontal plane and azimuth from north, by defining $x = \cos(\pi - 2\Theta)$, the tomographic system of equations can be written as:

$$\sin(2\hat{\psi}) \frac{\delta \hat{t}}{2} \cos^2 \hat{\Theta} = \int_0^a \frac{G(z)(1-x) \sin 2\Psi_G(z)}{2V_s(z)L(z)} dx$$

$$\cos(2\hat{\psi}) \frac{\delta \hat{t}}{2} \cos^2 \hat{\Theta} = \int_0^a \frac{G(z)(1-x) \cos 2\Psi_G(z)}{2V_s(z)L(z)} dx$$

$$\sin(2\hat{\Theta}) \frac{\delta \hat{t}}{2} \sin^2 \hat{\psi} = \int_0^a \frac{G(z)\sqrt{(1-x^2)} \sin 2\Psi_G(z)}{2V_s(z)L(z)} dx$$

$$\cos(2\hat{\Theta}) \frac{\delta \hat{t}}{2} \sin^2 \hat{\psi} = \int_0^a \frac{G(z)\sqrt{(1-x^2)} \cos 2\Psi_G(z)}{2V_s(z)L(z)} dx$$

Here also the one-layer effective splitting time $\delta \hat{t}$, fast axis symmetry axis $\hat{\psi}$ and the newly introduced apparent tilt $\hat{\Theta}$ can be obtained from measurements and can be used to form the splitting intensity in the presence of a tilted symmetry axis (Equations 31 and 32 of RY11). Figure 2.54 shows that the analytic prediction of the splitting intensity agrees with the measurements of the synthetic waveforms generated by the two-layer models very well.

To conclude, the results presented here provide a framework for the extension of the joint inversion of surface waveforms and SKS splitting data to constrain the tilt of the fast axis as a function of depth.

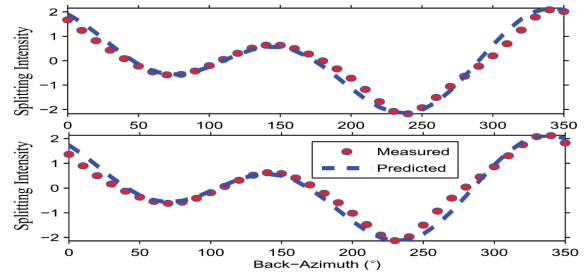


Figure 2.54: Predicted (dashed line) and measured (dots) splitting intensity for models at 8 s period (top) and 16 s (bottom). Note the break of 180° symmetry by introducing Θ .

25.5 References

- Chevrot, S., Multichannel analysis of shear wave splitting, *J. Geophys. Res.*, *105*, 21579-90, 2000.
- Montagner, J.-P., Griot-Pommeroy, D.-A., and Lave, J., How to relate body wave and surface wave anisotropy?, *J. Geophys. Res.*, *105*, 19,015-19,027, 2000.
- Romanowicz, B., and Yuan, H., On the interpretation of SKS splitting measurements in the presence of several layers of anisotropy, *Geophys. J. Int.*, submitted, 2011.
- Silver, P.G., and Long, M.D., The non-commutativity of shear wave splitting operators at low frequencies and implications for anisotropy tomography, *Geophys. J. Int.*, *184*, 1415-1427, 2011.
- Silver, P.G., and Savage, M.K., The interpretation of shear-wave splitting parameters in the presence of two anisotropic layers, *Geophys. J. Int.*, *119*, 949-963, 1994.

26 Anisotropic Stratification in the Continental Upper Mantle

Huaiyu Yuan and Barbara Romanowicz

26.1 Introduction

The Berkeley North American regional azimuthal anisotropy model reveals the presence of three anisotropic layers throughout the stable part of the North American cratonic upper mantle (*Yuan and Romanowicz, 2010*). While in the bottom asthenospheric layer the fast axis direction is parallel to the current plate motion direction, the top two lithospheric layers have distinct fast axis directions, with ancient suture zone trending directions in the top layer and a general north-south direction in the bottom layer, respectively. The boundary between the two lithospheric layers, as defined by systematic changes in the direction of azimuthal anisotropy, correlates well with the sharp mid-lithospheric negative velocity boundary found by available S-wave receiver function measurements. This spatial correlation suggests that the two boundaries, found by the surface wave inversion and receiver functions, may share a common origin, possibly during the lithosphere formation, which indicates that accretion by shallow subduction may have played an important role in the North American craton formation (*Yuan and Romanowicz, 2010; Yuan et al., 2011*).

In this study, we look for upper mantle anisotropy signatures globally. Is the anisotropy stratification observed in North America a common feature in the cratons worldwide? If so, can we infer systematic anisotropy domains in the continents' and oceans' upper mantle (i.e. lithosphere and asthenosphere)? What about the anisotropy directions within each domain? Can we see the plate shear under continents? Answers to these imminent questions would put tighter constraints on evaluating how plate tectonics works and the rules of shallow subduction versus plume underplating in early stage craton formation worldwide (e.g. *Lee, 2006; O'Reilly and Griffin, 2006*).

26.2 Global Inversion

Taking advantage of a global isotropic and radially anisotropic shear wave velocity model developed using the Spectral Element Method (SEMum; *Lekic and Romanowicz, 2011*), we expand our regional azimuthal anisotropy inversion to the globe. We start with the global dataset of *Lekic and Romanowicz (2011)*, in order to cross-validate the results in North America (developed using a different dataset that utilizes the USArray; *Yuan and Romanowicz, 2010*). Following the ray path density and azimuthal coverage, we parameterize the globe approximately in nodes of 400- and 800-km spacing in continents and oceans, respectively. The vertical node spacing varies from 30-50 km above the transition zone to 100-150 km down to 1000 km depth. We perform a

two-step inversion: in the first step both isotropic Vs and radial anisotropy $\xi = (V_{sh}/V_{sv})^2$ are allowed to vary in our new model mesh while azimuthal anisotropy remains zero, and in the second step the inverted Vs and ξ from the first step remain fixed and azimuthal anisotropy parameters Gc and Gs are inverted.

26.3 Preliminary Results

Our preliminary results indicate that globally the upper mantle is clearly stratified (Figure 2.55). The 1D depth profile of the azimuthal anisotropy strength shows that under the continents the anisotropy strength (thick blue line) peaks above 100 km in the shallow upper mantle. A secondary local maximum develops around 150 km, and the anisotropy decreases rapidly to 200-250 km depth. This layered shallow upper mantle is consistent with our previous observations in the North American craton. In fact, the mean values of the anisotropy strength in North America from this study (right panel in Figure 2.55b) are nearly identical to those of our regional study (Figure 3c in *Yuan et al., 2011*) in the upper 250 km, which are constrained by different waveforms recorded only at North American stations. The difference below 250 km is due to the enhanced depth sensitivity by the SKS dataset in the regional study (Figure 2.553a in *Yuan et al., 2011*). We will soon include the SKS dataset in the global study.

In North America, the averaged anisotropy direction (left panel in Figure 2.55b) reaches the averaged absolute plate motion (APM) direction (HS3-NUVEL 1A; *Gripp and Gordon, 2002*) at ~ 250 km. This suggests that 1) well developed plate shear occurs in the North American asthenosphere at this depth (250 km), and 2) the anisotropic domains associated with local maxima in anisotropy strength (right panel in Figure 2.55b) are within the lithosphere. These were confirmed independently in our NA regional study (*Yuan and Romanowicz, 2010*). Obviously Figure 2.55c shows the same conclusions can be drawn for the Australian plate, except that the plate shear occurs at shallower depth (~ 200 km), suggesting thinner Australian lithospheric thickness than in North America.

Another interesting feature comes from the 1D oceanic anisotropy strength profile (thin red line in Figure 2.55a). In addition to a shallow depth (60-70km) secondary peak that may be associated with the plate shear between the young oceanic lithosphere and underlying asthenosphere, the major peak of anisotropy occurs below 150 km. Close examination of the 3D global anisotropy variations (Fig-

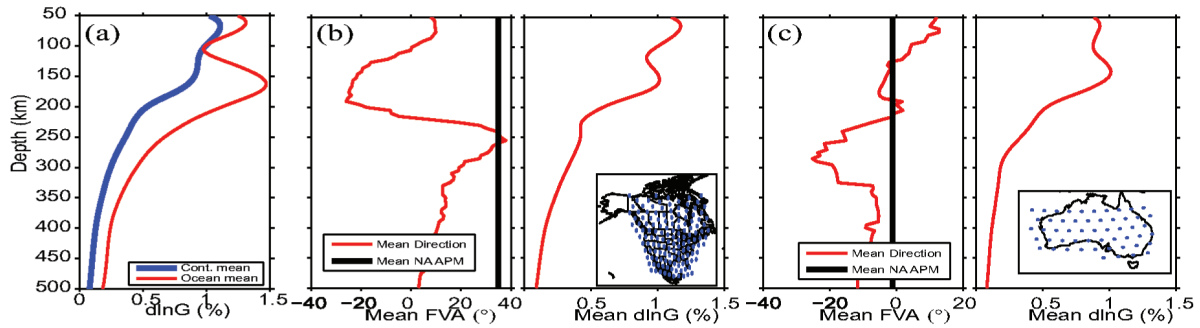


Figure 2.55: (a) Global depth profiles of azimuthal anisotropy strength ($d\ln G$) averaged for continents and oceans, respectively. (b) Regional depth profiles of anisotropy fast axis direction (North at 0; in a clockwise direction) and strength for North America averaged from model nodes shown in the inset. Vertical black line is the averaged absolute plate motion direction (HS3-NUVEL 1A) of these model points. (c) Same as (b) but for the Australian continent.

ure 2.56) shows this signature is closely related to the prominent positive radial anisotropy ξ in the Pacific and India/Australia plates.

26.4 Future Work

We are working on including a global SKS dataset, which will significantly improve the depth sensitivity to anisotropy down to the transition zone (Romanowicz and Yuan, 2011; Yuan *et al.*, 2011). In addition, the new version of the global model SEMum is available (French *et al.*, this volume), which includes a more realistic crust and will allow us to better constrain anisotropy in the uppermost upper mantle. Upon finalizing the global inversion, our results will be compared with global dynamic models.

26.5 References

Gripp, A.E. and Gordon, R.G., Young tracks of hotspots and current plate velocities, *Geophys. J. Int.*, 150, 321-361, 2002.

Lee, C.T., Geochemical/petrologic constraints on the origin of cratonic mantle. in *Archean Geodynamics and Environments*, pp. 89-114, eds. Benn, K., Mareschal, J. C. and Condie, K. C. American Geophysical Union Monograph, Washington, 2006.

Lekic, V. and Romanowicz, B., Inferring upper-mantle structure by full waveform tomography with the spectral element method, *Geophys. J. Int.*, 185, 799-831, 10.1111/j.1365-246X.2011.04969.x, 2011.

O'Reilly, S.Y. and Griffin, W.L., Imaging global chemical and thermal heterogeneity in the subcontinental lithospheric mantle with garnets and xenoliths: Geophysical implications, *Tectonophysics*, 416, 289-309, 2006.

Romanowicz, B. and Yuan, H., On the interpretation of SKS splitting measurements in the presence of several layers of anisotropy, *Geophys. J. Int.*, 2011.

Yuan, H. and Romanowicz, B., Lithospheric layering in the North American craton, *Nature*, 466, 1063-1068, 10.1038/nature09332, 2010.

Yuan, H., Romanowicz, B., Fischer, K.M. and Abt, D., 3-D shear wave radially and azimuthally anisotropic velocity model of the North American upper mantle, *Geophys. J. Int.*, 184, 1237-1260, 10.1111/j.1365-246X.2010.04901.x, 2011.

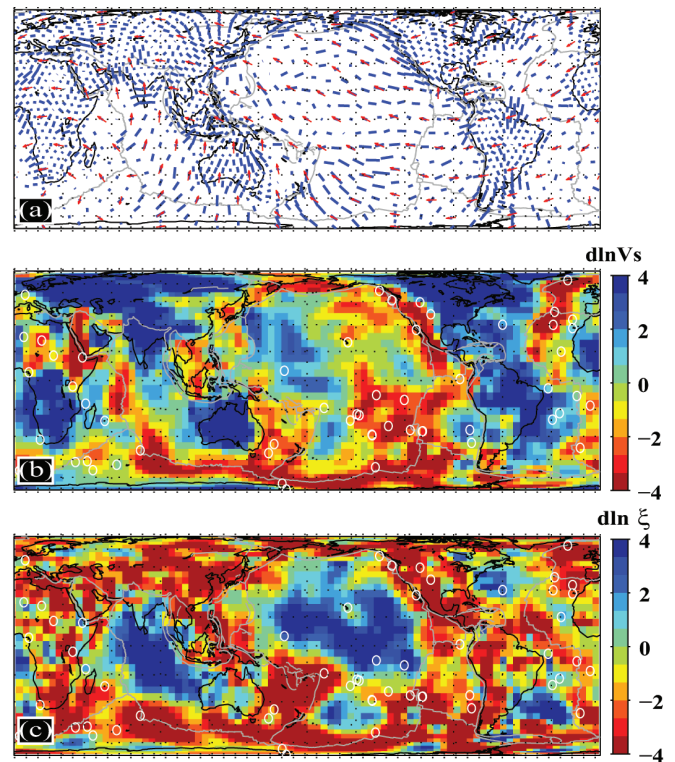


Figure 2.56: Preliminary results of our global inversion at 150 km. (a) Azimuthal anisotropy. Blue bars show the anisotropy strengths and fast axis directions. Red arrows are APM directions (HS3-NUVEL 1A). Continents are outlined in black and plate boundaries shown in gray. (b) Isotropic Vs variations. White circles are hotspots. Note at this depth thick cratons beneath North and South America, Australia, west and south Africa, India and most of Eurasia. High velocities are visible beneath the >150Ma west Pacific and north-west Atlantic regions. (c) Radial anisotropy ξ variations. Note significant positive ξ anomalies in the western-central Pacific and the Indian/western Australia plates, which correlate with the large azimuthal anisotropy strength in (a).

27 Refining the Cratonic Upper Mantle Using RegSEM

Huaiyu Yuan, Paul Cupillard and Barbara Romanowicz

27.1 Introduction

Our regional tomographic model has revealed a rapid change of anisotropic directions at middle depth in the North American craton (Yuan and Romanowicz, 2010). Intriguingly, shear wave receiver functions also report a bright negative velocity gradient in this depth range for many the cratonic stations (Abt et al., 2010; Fischer et al., 2010). This negative velocity gradient, referred to as the mid-lithospheric-discontinuity (MLD; Fischer et al., 2010) is also found in other continents (e.g., Ford et al., 2010) and may reflect a global feature associated with the shear wave velocity drop around 100 km (Thybo, 2006; Romanowicz, 2009). Further exploring the nature of this mid-lithospheric boundary, and better constraining the absolute values of shear velocities of the lithospheric layers therefore becomes a timely endeavor when the Transportable Array (TA) sweeps the continental US.

The TA coverage in the middle and eastern parts of the continent also opens up an opportunity to address a fundamental aspect of the North American continent's formation, i.e. the welding and growing processes. This portion of the continent is overall characterized by high velocities indicating less deformed cratonic upper mantle, although it was the site of very unique episodes in the history of the creation of the North American continent: e.g. the 1.92-1.77 Ga Trans-Hudson orogeny represented the plate collision between Archean Wyoming and Superior, analog to the present day Himalayas; the 1.71-1.68 Ga Yavapai and 1.70-1.65 Mazatzal Orogeny represented the accretional addition of juvenile volcanic arcs to the cratonic core (Hoffman, 1988), and to the east, the 1.1 Ga

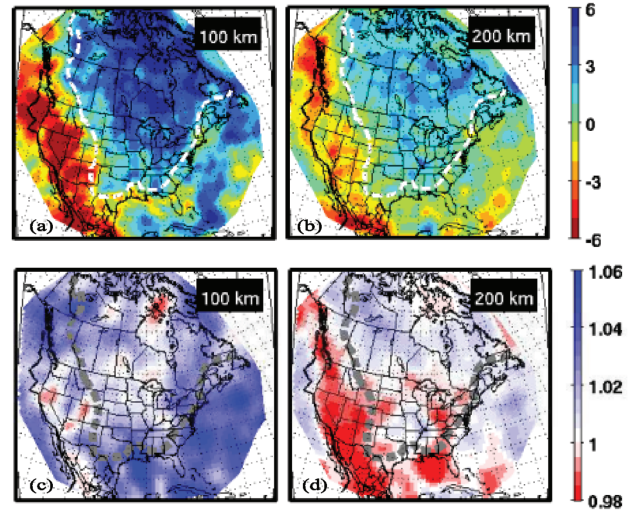


Figure 2.58: Preliminary results for the first iteration inversion for V_s and ξ . Top, isotropic velocity V_s variations with respect to SEMum global average at 100 and 200 km (a and b). White line demarcates the cratonic region. Bottom, radial anisotropy ξ variations with respect to isotropy. Craton boundary is shown in dashed gray.

Grenville and 260 Ma Appalachian Orogeny marked the formation and breakup of super continents Rodinia and Pangea (Thomas, 2006). A hypothesis to test is whether the signature of the distinct continent assembling processes may have been frozen in and well preserved in the crust and upper mantle. High resolution isotropic and anisotropic shear wave velocity tomography images may help address this question.

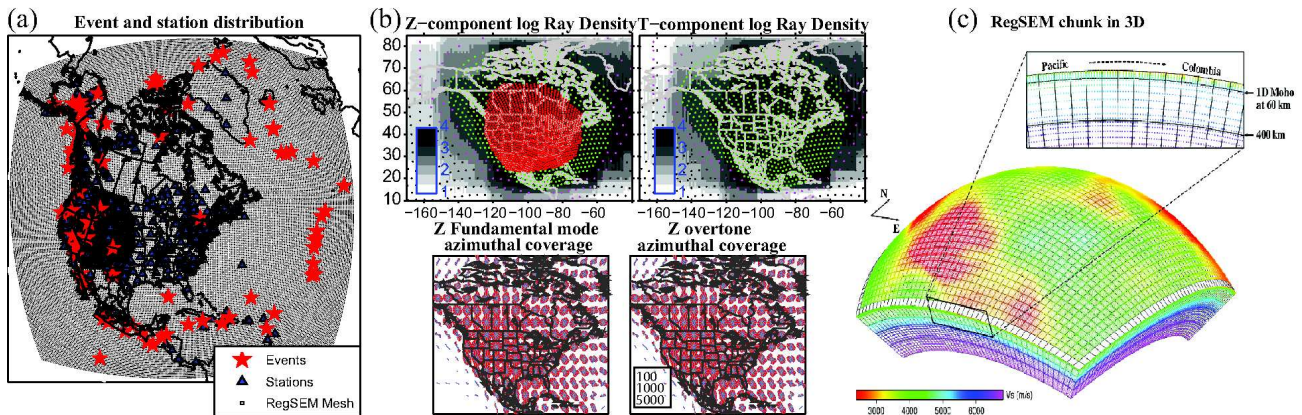


Figure 2.57: (a) RegSEM inversion setup. (a) Local and Regional events (red stars), broadband stations (black triangles) and RegSEM mesh (dotted background). (b) Ray density and azimuthal coverage for Z- and T-component and fundamental mode and overtones. (c) RegSEM mesh for 60-km crust and upper mantle used in the current inversion. The S-wave speed at each GLL point on the vertical and horizontal borders of the domain is plotted. A zoom into the upper part of the model shows the Moho and 410-km discontinuities.

27.2 RegSEM Inversion

We conduct a refined 3D tomographic inversion of the cratonic North American upper mantle. The new inversion utilizes shorter period waveforms (down to 40 s) from over 100 local and regional events (Figure 2.57) to improve both horizontal and vertical resolution, and a regional Spectral Element code, RegSEM (Cupillard *et al.*, 2011) to compute the forward synthetics. RegSEM includes ellipticity, attenuation, arbitrary anisotropy, and non-conformal mapping of discontinuities, and can accurately represent scattering and focusing/defocusing effects caused by the 3D Earth structure. We apply a hybrid iterative inversion approach that uses accurate RegSEM synthetics and approximate but computationally efficient 2D finite frequency kernels based on NACT normal model perturbation theory (Li and Romanowicz, 1995). We also test a much more time-consuming but accurate inversion scheme in which we consider Frechet kernels computed using RegSEM and the adjoint formalism.

A good crust model is essential in all SEM simulations. By combining a suite of 1D and 3D crust models with several North American upper mantle velocity models, we compare with real data the RegSEM simulations to evaluate effects of different types of crust models. Starting models are selected based on waveform fits to both Z- and T-component data waveforms. In this inversion, we choose the Berkeley global model SEMum (Lekic and Romanowicz, 2011), in which a homogenized 60-km uniform crust (thickness compensated by radial anisotropy; Backus, 1962) is used to speed up the SEM simulations.

We parameterize our model space with a range of 100-400km horizontal nodes (Figure 2.58bc) according to the ray path coverage. The inversion problem is then solved iteratively: 1) compute RegSEM synthetics; 2) compute NACT partial derivative kernels; 3) invert for isotropic Vs and radial anisotropy ξ structure; 4) repeat 2)-3) due to using approximated partial derivatives kernels; and 5) repeat 1)-4) for the next iteration. Frechet kernels computed using RegSEM and the adjoint formalism will be included after obtaining stable inversions.

27.3 Initial Results and Ongoing Work

The iteration tomographic inversion results for Vs and ξ variations are shown in Figure 2.58a-d. The isotropic Vs images confirm the thick root of the craton down to 200 km. Along the east margin of the craton, a noticeable band of low velocity structure closely follows the Grenville/Appalachian orogens down to 100 km, indicating persistent influence of orogeny boundaries deep in the lithosphere. In contrast, the northwestern Atlantic plate shows large positive velocity perturbations, consistent with the over 150 Ma age of this portion of the oceanic lithosphere.

We are currently migrating to the second version of

our global model SEMum (French *et al.*, this volume), in which in oceans the homogenized crust is 30 km thick while in continents the crust remains of realistic thickness constrained by a fundamental mode surface wave group and phase velocity dataset (Shapiro and Ritzwoller, 2002). Upon finalizing the new RegSEM inversion for Vs and ξ , we will move on to the joint inversion of azimuthal anisotropy with both surface and body waveforms (down to 20 s) and a more robust SKS dataset.

27.4 References

- Abt, D.L., Fischer, K.M., French, S.W., Ford, H.A., Yuan, H. and Romanowicz, B., North American lithospheric discontinuity structure imaged by Ps and Sp receiver functions, *J. Geophys. Res.*, 115, B09301, DOI: 10.1029/2009jb006914, 2010.
- Backus, G.E., Long-Wave Elastic Anisotropy Produced by Horizontal Layering, *J. Geophys. Res.*, 67, 4427-4440, DOI: 10.1029/JZ067i011p04427, 1962.
- Cupillard, P., Delavaud, E., Burgos, G., Festa, G., Villotte, J.-P., Capdeville, Y. and Montagner, J.P., RegSEM : a versatile code based on the Spectral Element Method to compute seismic wave propagation at the regional scale, *Geophys. J. Int.*, submitted.
- Fischer, K.M., Ford, H.A., Abt, D.L. and Rychert, C.A., The Lithosphere-Asthenosphere Boundary, *Annu. Rev. Earth Planet. Sci.*, 38, 551-575, doi:10.1146/annurev-earth-040809-152438, 2010.
- Ford, H.A., Fischer, K.M., Abt, D.L., Rychert, C.A. and Elkins-Tanton, L.T., The lithosphere-asthenosphere boundary and cratonic lithospheric layering beneath Australia from Sp wave imaging, *Earth Planet. Sci. Lett.*, 300, 299-310, DOI: 10.1016/j.epsl.2010.10.007, 2010.
- Hoffman, P.F., United Plates of America, The Birth of a Craton: Early Proterozoic Assembly and Growth of Laurentia, *Annu. Rev. Earth Planet. Sci.*, 16, 543-603, DOI: 10.1146/annurev.ea.16.050188.002551, 1988.
- Lekic, V. and Romanowicz, B., Inferring upper-mantle structure by full waveform tomography with the spectral element method, *Geophys. J. Int.*, 185, 799-831, DOI: 10.1111/j.1365-246X.2011.04969.x., 2011.
- Li, X.-D. and Romanowicz, B., Comparison of global waveform inversions with and without considering cross-branch modal coupling, *Geophys. J. Int.*, 121, 695-709, 1995.
- Romanowicz, B., The Thickness of Tectonic Plates, *Science*, 324, 474-476, DOI: 10.1126/science.1172879, 2009.
- Thomas, W.A., Tectonic inheritance at a continental margin, *GSA Today*, 16, DOI: 10.1130/1052-5173, 2006.
- Thybo, H., The heterogeneous upper mantle low velocity zone, *Tectonophysics*, 416, 53-79, 2006.
- Whitmeyer, S.J. and Karlstrom, K.E., Tectonic model for the Proterozoic growth of North America, *Geosphere*, 3, 220-259, DOI: 10.1130/ges00055.1, 2007.
- Yuan, H. and Romanowicz, B., Lithospheric layering in the North American craton, *Nature*, 466, 1063-1068, DOI: 10.1038/nature09332, 2010.

28 Investigating Upper Mantle Discontinuities Beneath Subduction Zones

Ruiqing Zhang and Barbara Romanowicz

28.1 Introduction

Subduction zones can be regarded as natural laboratories because of the wide variety of processes involved. Macquarie Island is an exposed portion of the Macquarie Ridge, and is located where the Australian plate meets the Pacific plate. To its north is the Tonga trench, where the old Pacific floor subducts at a rapid rate below the Indo-Australia plate, producing a deep slab of former oceanic lithosphere.

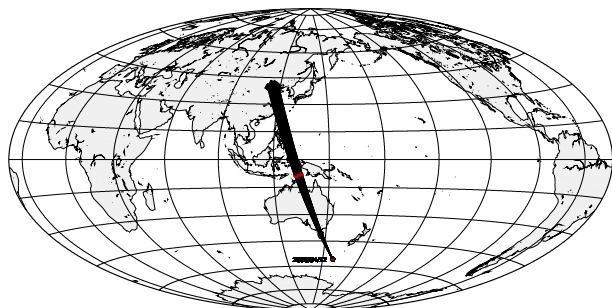


Figure 2.59: Raypath from the event to stations in the array.

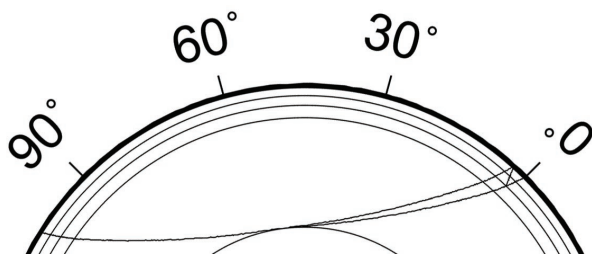


Figure 2.60: Raypaths of Sdiff and S410sSdiff.

Study of seismic velocity anomalies in the transition zone (TZ) is an approach to investigating variations in temperature or petrology. Travel time tomography shows that the Pacific plate deflects in the transition zone (between about 400 and 700km depth) before continuing into the lower mantle beneath the Tonga trench. However, beneath the Kermadec Trench, penetration into the lower mantle occurs without a link (*Van der Hilst, 1995*). Moreover, the depth observations of the 410 and 660-km discontinuities, which are sensitive to temperature, also provide a reference point for investigating properties of the transition zone. The receiver function has become a commonly used tool for constraining the depth of the

upper mantle discontinuities. However, due to the limitation of recording stations installed in the oceans, it seems difficult to constrain the depth of discontinuities beneath subduction zones.

28.2 Data and preliminary results

From 2006 to 2009, a 150 station broadband seismic array (Figure 2.59) was deployed in north China by the Institute of Geophysics, China Earthquake Administration (CEA). Figure 2.61 is a high quality seismic profile of a shallow event (16 km depth) with a magnitude of M_w 7.2 which occurred in Macquarie Ridge, recorded by the CEA array. The epicentral distance is from about $99\sim 105^\circ$.

In the distance range larger than 100° , SS precursors should be observed. Considering the location of the event and seismic array shown in Figure 1, the corresponding SS bounce points mainly sample the Arafura Basin between Papua New Guinea and the Australian Gulf of Carpentaria. It is common to map discontinuity topography by constraining the relative travel time between the S660S (S410S) and the reference SS phase. Because precursor phases have amplitudes that are typically $\sim 5\text{-}10\%$ (or less) of the amplitude of the SS phase, stacking of data is required to bring the precursors out of the background noise (*Schemerr, 2006*).

Figure 2.61 is a seismic profile of SS precursors (band-pass filtered between $20\sim 100$ s), in which the maximum amplitude of SS in each record has been normalized and the timing of the peak is defined with a reference time of zero. From Figure 2.61, it can be seen that precursors of S660S (-200 s) and S410S (-150 s) are relatively difficult to identify, compared with the S210S (-70 s) precursor.

It should be noted that in Figure 2.61, there is a phase in the time window of about -250 s, with a relatively high signal-to-noise ratio and which can be clearly observed across the whole seismic profile. It is suggested by Taup that this is the S410sSdiff phase. The S410sSdiff phase is the upside reflection from the 410km discontinuity beneath the source region (Figure 2.60). It is surprising that S410sSdiff is so clearly observed.

28.3 Future work

1. Stacking methods – enhancing the signals of S660S (S410S): How to increase the signal of the precursors of interest is a challenge. In future research, we want to use a phase weighted stack (*Schimmel, 1997*).

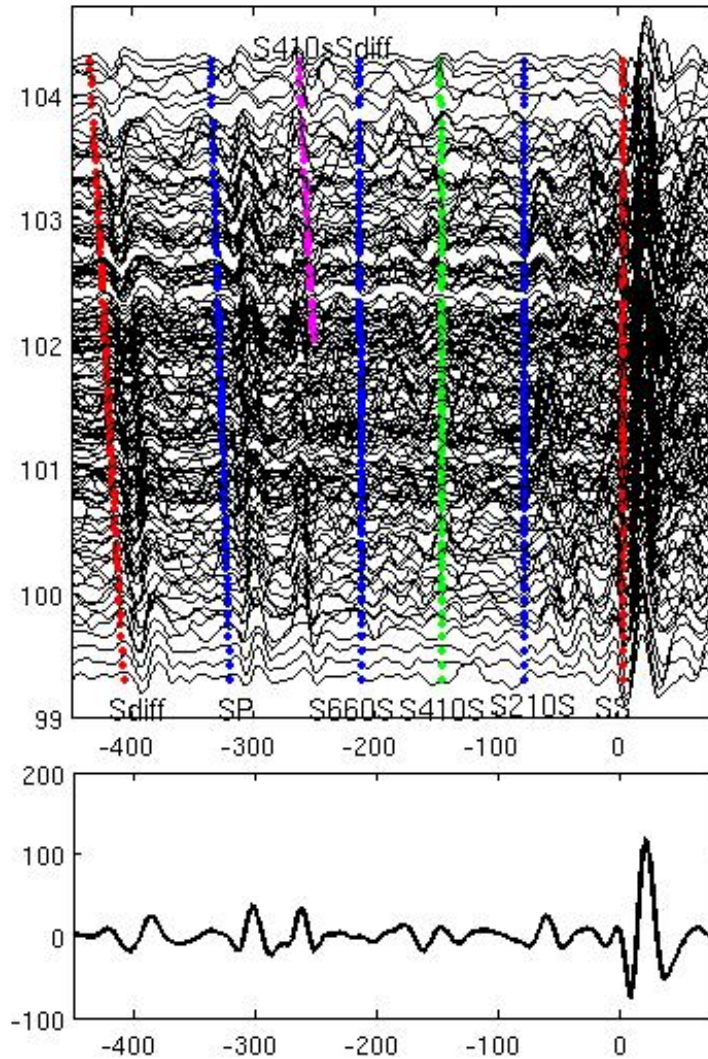


Figure 2.61: Top: Seismic profile of SS precursors with predicted traveltimes of the IASP91. Bottom: Stacked data using the SS phase as a reference.

2. Mapping the 410-km discontinuity beneath Macquarie Ridge: In the future, we will focus on how to use the relative time difference between the Sdiff and S410sSdiff to constrain the depth of 410-km discontinuity beneath Macquarie trench.

28.4 References

Schmerr, N., and E. Garnero, Investigation of upper mantle discontinuity structure beneath the central Pacific using SS precursors, *J. Geophys. Res.*, **111**, doi:10.1029/2005JB004197, 2006

Van der Hilst, R.D, Complex morphology of subducted lithosphere in the mantle beneath the Tonga trench, *Nature J.*, **374**, 154-157, 1995.

Schimmel, M. and Paulssen, H. Noise reduction and detection of weak, coherent signals through phase-weighted stacks. *Geophys. J. Int.*, **130**, 497-505, 1997

29 Small-scale Variation of SS Precursors Observed by US Transportable Array

Zhao Zheng and Barbara Romanowicz

29.1 Introduction

SS precursors are the underside reflections from the upper mantle discontinuities (400 and 670 primarily) at half distance. They have almost identical ray paths as SS except in the vicinity of the bounce point; therefore their differential travel times (with reference to SS) and amplitudes provide ideal constraints on the discontinuity topography and the impedance contrast across it. They have been extensively used to investigate the discontinuities, mainly on the global scale (for a review, see *Deuss, 2009*) but also in regional studies if there is enough coverage (e.g. *Schmerr and Garnero, 2006; Cao et al., 2011*).

SS precursors are usually at or below noise level. Therefore, they are difficult to identify on individual seismograms. In most previous studies, stacking (including non-linear) techniques are employed to bring out a clear phase, which results in robust travel time measurements. The amplitude information, however, is usually distorted or lost after stacking. In addition, constrained by data

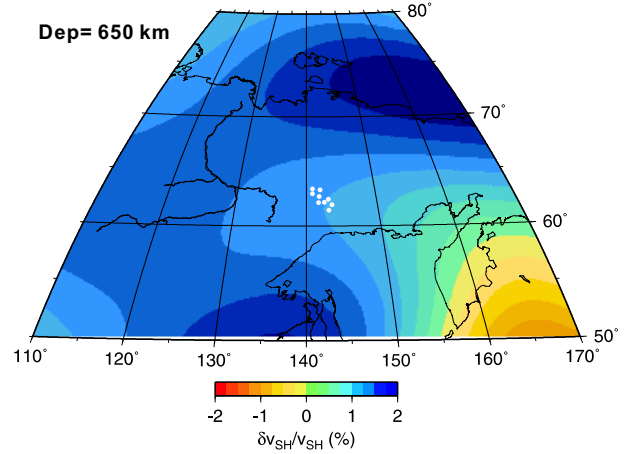


Figure 2.63: A map view of the 3D model S362ANI (*Kustowski et al., 2008*) in the study region at a depth of 650 km. V_{SH} is plotted as relative perturbation to the 1D reference model STW105 (*Kustowski et al., 2008*). The white circles represent the locations of precursor bounce points of the stations shown in Figure 2.62.

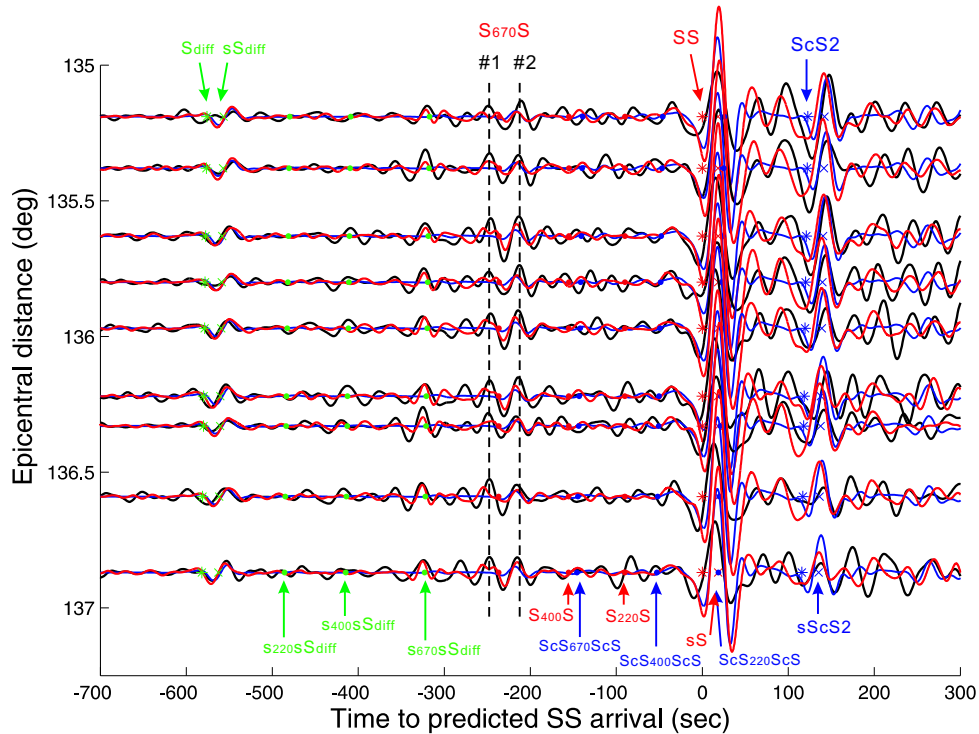


Figure 2.62: Transverse component waveforms of stations with azimuth i20-23° and distance in 135-137°: data (black lines), 1D (blue) and 3D synthetics (red). All traces are normalized to a common factor. PREM predicted arrivals are labeled with colored arrows. The two phases associated with S670S are marked out by dash lines.

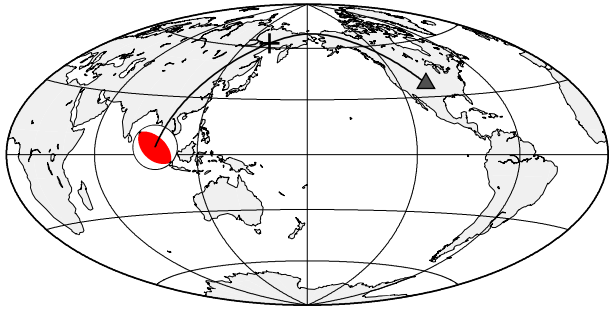


Figure 2.64: SS ray path from a shallow event (m_b 6.7; depth 38 km) to a station (T28A) in the US Transportable Array. The location of the bounce point is denoted by a cross.

coverage, the bin size for stacking is usually 10 or 5° in radius at best, putting a limit on the resolution.

29.2 Data

Owing to the high quality recordings from the US Transportable Array (TA), it is now feasible to identify clear and coherent SS precursors on individual seismograms across a distance profile, allowing resolution for small-scale lateral variations in discontinuity characteristics. As a rule of thumb, if the station interval in the array is ~ 70 km, the interval between bounce points is half of that, i.e. ~ 35 km.

In this study, we show the observation from an m_b 6.7 event that occurred in Northern Sumatra, whose SS bounce points of the TA stations sample the northern coast of Okhotsk Sea (Figure 2.64), a previously understudied location. A tomographic study of this region has revealed two subducted slabs sinking into the transition zone and ponding at the 670 discontinuity (Gorbatov *et al.*, 2000). For this event, we collect broadband waveforms from the IRIS data center, rotate (here we look at transverse component only), remove instrument response, integrate to displacement, bandpass filter 20-100 seconds (shorter periods are also tried), and visually inspect trace by trace to exclude the noisy waveforms. We then bin the array data by azimuth and epicentral distance of 2-3°. Within each bin, there are approximately 10 traces of high quality. Figure 2.62 shows the record section (observed traces plotted in black lines) of one such bin. It is not possible to discuss all the interesting observations in this short report; here we focus on S670S. The most striking feature is the large amplitude (on the order of the main phases) of this precursor throughout the profile. In addition, two pulses can be identified around the predicted S670S arrival time.

29.3 Modeling

We try to model the observations with synthetic seismograms from 1D and 3D earth models. The 1D synthetics are computed for PREM (Dziewonski and Anderson, 1981) by normal mode summation, accurate at periods >10 seconds. The 3D synthetics are made available from the Global ShakeMovie project of Princeton University (<http://global.shakemovie.princeton.edu>). In that simulation, the Earth model is S362ANI (Kustowski *et al.*, 2008) for the mantle plus Crust2.0 (Bassin *et al.*, 2000); the Spectral Element Method (SEM) is used; and the synthetics are accurate between 17 and 500 seconds (Tromp *et al.*, 2010).

Figure 2.62 shows the 1D (blue) and 3D (red) synthetics plotted against observations (black), with emphasis on S670S. The 1D synthetics fail by far to reproduce the precursor observations. In particular, they fail to model the first one of the two S670S arrivals. The 3D synthetics, on the other hand, are able to model the precursor waveforms much better. However, even the 3D synthetics are unable to fully reproduce the large S670S amplitude observed. To explain the remaining discrepancy may require focusing effects caused by complex geometry of the slab interacting with the 670 discontinuity. A map of V_{SH} perturbation at 650 km is shown in Figure 2.63. It is interesting to notice that the precursor bounce points of these stations fall in a "valley" between two strong high velocity anomalies, which might serve to focus the precursor energy. A thorough investigation of the 3D model is necessary in order to fully understand what structure enables the improvement with respect to the 1D model in fitting the precursor observations.

29.4 References

- Bassin, C., G. Laske and G. Masters, The current limits of resolution for surface wave tomography in North America, *EOS, Trans. Am. Geophys. Un.*, **F897**, 81, 2000.
- Cao, Q. et al., Seismic Imaging of Transition Zone Discontinuities Suggests Hot Mantle West of Hawaii, *Science*, **332**, 1068, 2011.
- Deuss, A., Global observations of mantle discontinuities using SS and PP precursors, *Surv. Geophys.*, **30**, 301-326, 2005.
- Dziewonski, A. and D. Anderson, Preliminary reference Earth model, *Phys. Earth Planet. Inter.*, **25**, 297-356, 1981.
- Gorbatov, A. et al., Signature of remnant slabs in the North Pacific from P-wave tomography, *Geophys. J. Int.*, **142**, 27-36, 2000.
- Kustowski, B., G. Ekstrom, and A. Dziewonski, Anisotropic shear-wave velocity structure of the Earth's mantle: a global model, *J. Geophys. Res.*, **113**, 2008.
- Tromp, J. et al., Near real-time simulations of global CMT earthquakes, *Geophys. J. Int.*, **183**, 381-389, 2010.

30 Investigation of Cascadia Segmentation with Ambient Noise Tomography

Robert W. Porritt and Richard M. Allen

30.1 Introduction

Several lines of evidence suggest that simple subduction with one downgoing and one overriding plate is an insufficient model of the Cascadia Subduction Zone. Instead, the subduction zone and arc are segmented, exhibiting variations in multiple characteristics along strike. One line of evidence comes from the analysis of seismicity. The subduction zone is atypical everywhere in that the Wadati-Benioff zone is sparsely defined and shallow. There are a few subduction interface events deeper than the continental crust at the northern and southern ends of the subduction zone in Washington and California, but only to 75km depth. However, there are almost no sub-crustal (>30km depth) earthquakes beneath Oregon. In contrast, Episodic Tremor and Slip (ETS) events have been mapped throughout the subduction zone (*Brudzinski and Allen, 2007*). The recurrence rate of ETS, consisting of many non-volcanic (or tectonic) tremors at the same time as geodetically measured back-slip, varies along strike with similar segment boundaries as observed by the variation in seismicity and topography.

Other evidence for segmentation along the arc comes from the composition of arc volcanism. Detailed analysis of primitive basalt families in the main volcanic arc reveals variable mantle domains and melting regimes attributed to the effects of the slab window to the south, impingement of the Basin and Range terrain, and interaction with the Siletzia Terrane (*Schmidt et al., 2008*). In addition, measurements of total heat production from volcanic fumaroles, thermal springs, and slightly thermal springs (*Ingebritsen and Mariner, 2010*) show significantly higher total heat production in the southern part of the arc where Basin and Range extension is thought to create permeable zones in the crust (*Ingebritsen and Mariner, 2010*).

30.2 Data Processing

Our dataset focuses on two Flexible Array experiments, FlexArray along Cascadia Experiment for Segmentation (FACES) and the Flexible Array Mendocino Experiment (Mendocino), while also including data from the Berkeley BDSN, Canadian Seismic Network, USArray Transportable Array, and the Advanced National Seismic System (ANSS) backbone seismic network. The dataset extends temporally from July 2007 through September 2010. While we focus on the Pacific Northwest, the dataset extends spatially throughout the entire

United States with some coverage in Canada.

Detailed processing flow for computing phase velocity maps can be found in *Benson et al. (2007)* and the updates applied here are described in *Porritt et al. (in press)*.

30.3 Implications for tremor

Brudzinski and Allen (2007) identify a variation in the recurrence interval of ETS along the arc with a recurrence interval of 14 months in the north, 20 months in the center, and 11 months in the south. The cross section in Figure 2.65 is constructed by extracting the velocity values along a profile aligned to the 30 km slab contour from *Audet et al. (2010)*, which is thought to represent the up-dip limit of ETS. Superimposed on this image are the long-term ETS segmentation boundaries at 43°N and 46.7°N (*Brudzinski and Allen, 2007*). These boundaries, based on the recurrence interval for ETS events, are aligned with both the location of the high velocity Siletzia Terrane in the mid-crust (15 km depth) and also the deeper three-way segmentation in the subducting oceanic lithosphere between the Gorda, Southern Juan de Fuca, and Northern Juan de Fuca at 60-120 km depth. Thus the segmentation of ETS is aligned with structural boundaries in both the continental crust and the subducting oceanic lithosphere.

30.4 Implications for volcanic activity

Figure 2.66 shows a set of observations along the axis of the Cascades volcanic range. Figure 2.66a is modified from *Ingebritsen and Mariner (2010)* showing cumulative heat production from the north to the south. Comparing this to PNW10-S shows a strong correlation between the high heat production south of 45°N and a large zone of low velocities between 40.5°N and 45°N. The extension of the Basin and Range, and the associated clockwise rotation of the Cascadia margin, could explain the lower velocities in the southern half of the subduction zone at all depths (Figure 2.66c; anomalies SM1, SM2, and SM5). The rotation leads to extension at the southern end, which promotes melting and results in the larger low velocity zone. The center of this low velocity zone is also located at the slab segmentation boundary (at 43°N, Figure 2.66c, anomaly SM5) associated with the continuation of the Blanco Fracture Zone separating the Gorda and Juan de Fuca portions of the plate.

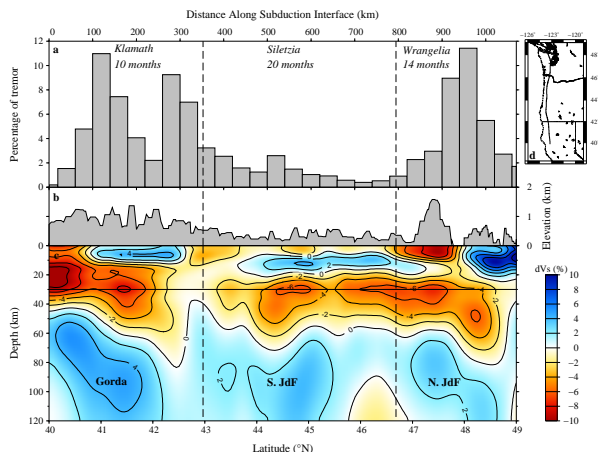


Figure 2.65: Fence diagram along the 30km slab contour as defined by *Audet et al.*, 2010. Panel (a) is the distribution of tremor from *Boyarko and Brudzinski*, 2010. Panel (b) is the topography along the profile. Panel (c) is the relative velocity extracted from PNW10-S and panel (d) gives the location in map view. Panel (a) labels the 3 segmented zones based on the tremor recurrence with their given recurrence interval. Panel (c) labels the high velocity centers of the Gorda, Southern Juan de Fuca, and Northern Juan de Fuca slabs.

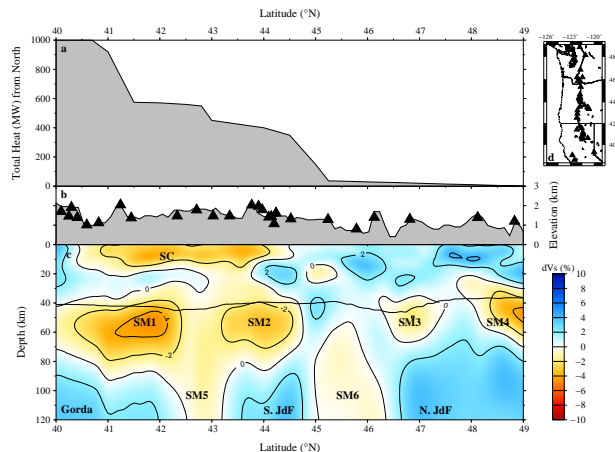


Figure 2.66: Fence diagram comparing PNW10-S with heat production measured in *Ingebritsen and Mariner*, 2010. Panel (a) is cumulative heat production from north, panel (b) shows the topography with volcanic centers (black triangles), panel (c) is the structure along the arc, and panel (d) gives a reference location for the profile. Thick black line in (c) is the Moho. Major anomalies are labeled as: SC- slow crust; SM1-6 - low velocity mantle anomalies; Gorda - Gorda plate; S. JdF and N. JdF - south and north Juan de Fuca plates, respectively.

30.5 Acknowledgements

We would like to acknowledge our co-PIs and collaborators on the flexible array experiments. The Mendo-

cino Broadband Experiment was made possible through NSF grants EAR0643392 and EAR0745934, with help from Gene Humphreys, Leland O’Driscoll, Alan Levander, and Yongbo Zhao for fieldwork and discussions. The FlexArray Along Cascadia was funded through NSF grant EAR0643007 with co-PI Mike Brudzinski and his students Devin Boyarko and Stefany Sit.

Data from this study came from the Earthscope US-Array/Transportable Array, the Canadian National Seismic Network through the AutoDRM system, the Berkeley Digital Seismic Network, and the Southern California Earthquake Center.

This work has been made possible with the resources available through the PASSCAL instrument center at New Mexico Tech.

30.6 References

Audet, P., Bostock, M. G., Boyarko, D. C., Brudzinski, M. R., and Allen, R. M., Slab morphology in the Cascadia forearc and its relation to episodic tremor and slip, *Journal of Geophysical Research*, *115*, B00A16, 2010.

Benson, G.D., Ritzwoller, M.H., Barmin, M.P., Levshin, A.L., Lin, F., Moschetti, M. P., Shapiro, N.M., Yang, Y., Processing seismic ambient noise data to obtain reliable broadband surface wave dispersion measurements. *Geophysical Journal International*, *169*, 1239-1260, 2007.

Boyarko, D. C. and Brudzinski, M. R., Spatial and temporal patterns of nonvolcanic tremor along the southern Cascadia subduction zone. *J. Geophys. Res.*, *115*, B00A22, DOI:10.1029/2008JB006064, 2010.

Brudzinski, M. and Allen, R. M., Segmentation in Episodic Tremor and Slip All Along Cascadia. *Geology*, *35*(10) 907-910, 2007.

Ingebritsen, S. E., and Mariner, R. H., Hydrothermal heat discharge in the Cascade Range, northwestern United States, *Journal of Volcanology and Geothermal Research*, *196*(3-4), 208-218, 2010.

Levander, A., Niu, F., Miller, M.S., Zhai, Y. and Liu, K., USArray Receiver Function Images of the Lithosphere in the Western U.S., *EOS Trans. AGU* *82*(52), Fall Meet. Suppl., Abstract S44B-01, 2007.

Obrebski, M., Allen, R. M., Xue, M., Hung, S-H., Slab-plume interaction beneath the Pacific Northwest, *Geophys. Res. Letters*, *37*, 114305, 2010.

Porritt, R. W., Allen, R. M., Boyarko, D. C., and Brudzinski, M. R., Investigation of Cascadia Segmentation with Ambient Noise Tomography, *EPSL*, accepted, 2011.

Pollitz, F. F., Observations and interpretation of fundamental mode Rayleigh wave-fields recorded by the Transportable Array (USArray), *J. Geophys. Res.*, *113*, B10311, 2008.

Schmidt, M. E., Grunder, A.L., and Rowe, M., Segmentation of the Cascades Arc as indicated by Sr and Nd isotopic variation among primitive basalts, *Earth and Planetary Science Letters*, *266*, 166-181, 2008.

31 Characterization of the Pacific Superplume Boundary

Sanne Cottaar and Barbara Romanowicz

31.1 Introduction

The lowermost lower mantle, also called the D^{''}, is a thermo-chemical boundary layer, exposing many intriguing observations. Global tomography of shear velocities show strong degree 2 and 3, dominated by two large low shear velocity provinces (LLSVP): one under Africa and one under the Pacific. Local studies show that the boundaries of these superplumes are sharp, sharper than can be explained by temperature variations. Another complication of the D^{''} is the occurrence of localized ultra-low velocity zones (ULVZ), suggesting the possible presence of partial melt and/or iron enrichment.

31.2 Data and observations

Data is collected for recent events in Southeast Asia towards the Transportable Array in the USA. The main event studied is a M_w 6.6 and 414 km deep event on the 20th of March 2010 in New Ireland Region, Papua New Guinea. Paths of this event towards the Transportable Array and other arrays in the USA travel on both sides of the Pacific LLSVP boundary. The radiation pattern of the main event is opportune, with strong non-nodal SH amplitudes in the azimuthal direction covered here. Amplitudes in the favorable radiation pattern decrease slightly towards the south, but less significantly than the data shows. The strong decrease in amplitude and wave broadening occurs as the paths to the south cross into the Pacific mantle plume. Center points for ScS and Sdiff for all events are plotted in Figure 2.67 and for some waveforms in Figure 2.68.

The striking observation is the occurrence of a post-cursor, most visible for periods between 10 and 20 seconds. The post-cursors are delayed by more than 30 seconds for the southernmost stations and move out to almost 50 seconds for stations around the plume boundary, as can be seen in the waveforms in Figure 2.68. The occurrence and move-out of the phase is mainly a function of azimuth, and there is little variation in timing with distance. The ratio in amplitude between post-cursor and main phase does increase with distance. For the further diffracted phases, the post-cursor becomes stronger than the main phase. Two additional events with less coverage but similar features can be found in *Toh et al.*, 2011.

Additionally, the SVdiff waveforms are stronger outside of the superplume. Future work will concentrate on constraining anisotropic behavior across the superplume boundary to explain these observations. The P-wave arrivals also show delay and wave broadening towards the south, although this is less significant. This can constrain

the V_p/V_s ratios across the boundary, and will be part of future work.

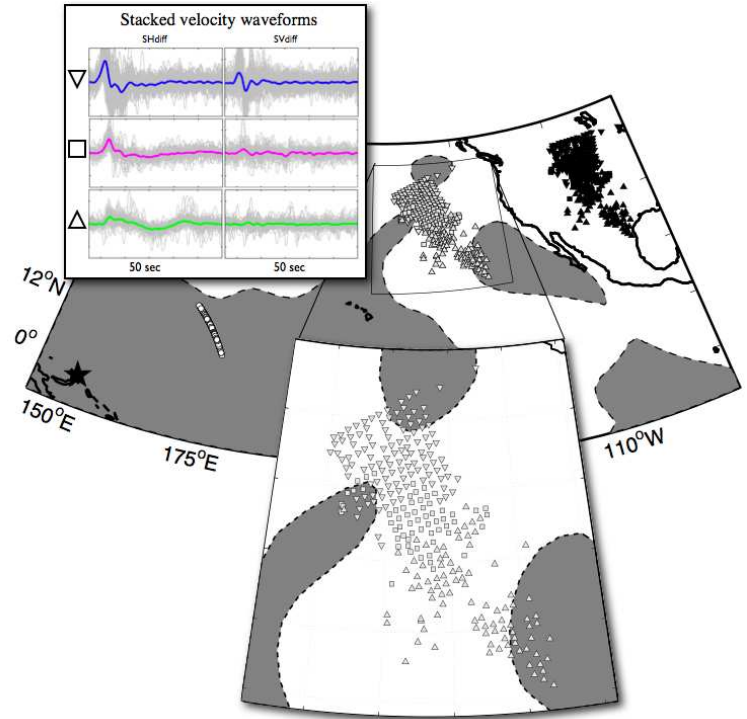


Figure 2.67: Location of clusters and stacked waveforms for each cluster.

31.3 Clustering

Clustering the waveforms provides an objective way to bin the data. We choose a 60 s window around the predicted arrival time of Sdiff for PREM. The measure of coherence is the correlation between the two waveforms. We apply hierarchical clustering with complete linkage (see Matlab manual). Initially, each waveform is considered a single cluster, which is then combined stepwise for the highest correlation. For each new cluster, the correlation to other clusters is defined by the minimum correlation between two waveforms from each cluster. This is repeated until three significant clusters remain. Results for the clustering are shown by the symbols in Figure 2.67. Clear clusters that vary with azimuth also result for ScS, sSdiff and Pdiff waveforms for the same event. This method has also proven to work for rays traveling parallel to the African plume boundary, while waveforms

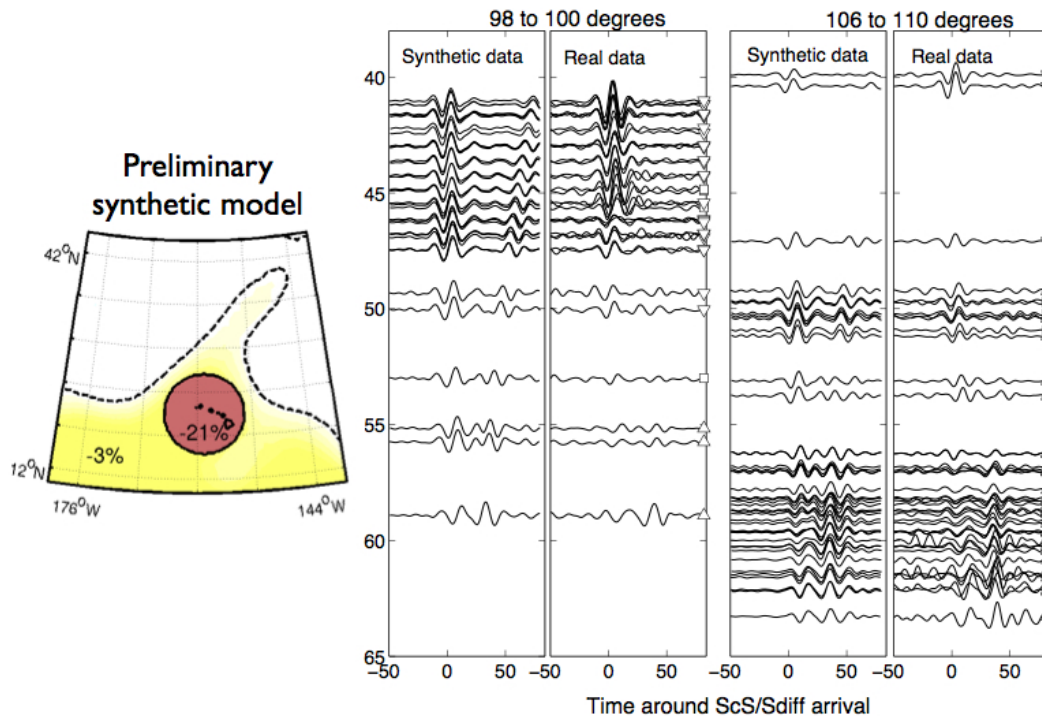


Figure 2.68: Preferred ULVZ input model, and synthetic data next to real data, filtered between 10 and 22 seconds. Symbols next to the real waveforms denote the clusters shown in Figure 2.67

cluster as a function of distance for rays that travel solely outside of the superplume.

31.4 Forward modeling

Synthetic data are forward modeled using a sandwiched version of CSEM (Coupled Spectral Element Method, *Capdeville et al.*, 2003). This method is computationally effective, solving only for the full 3D model, which can include sharp boundaries and anisotropy, in the lowermost part of the mantle and coupling to a normal mode solution for a 1D model in the rest of the Earth. The data can constrain the best fitting model by comparing observed and synthetic full waveforms. Based on the move-out of the postcursors, we rule out that the main boundary of the superplume, as defined by global S tomographic models, can be the cause. A ULVZ with a sharp velocity decrease within the superplume is required. However, with the many possible parameters and their different trade-offs, we cannot claim to find a unique solution. Waveforms for one of our (preliminary) preferred models are shown in Figure 2.68, alongside the real data. This model contains a circular ULVZ with a radius of 600 km and a shear wave velocity reduction of -21%. The height is poorly constrained.

31.5 Summary

Here we present a data set with several striking features. The rays from this event in Southeast Asia travel parallel to the northern boundary of the Pacific superplume up to stations in North America, making it ideal for mapping changes across the boundary. We illustrate this by objective clustering of the waveforms. SHdiff and SVdiff waveforms indicate changes in velocity, attenuation and anisotropy across the plume. Secondly, there are postcursors with a clear move-out, indicating the presence of an ULVZ on the superplume side. The superplume boundary itself is not sharp enough to cause postcursors.

31.6 Acknowledgements

This project is funded by NSF's CSEDI program under grant number NSF EAR-0757608.

31.7 References

- Capdeville, Y., B. Romanowicz, and A. To, Coupling spectral elements and modes in a spherical earth: an extension to the "sandwich" case, *Geophys. J. Int.*, 154, 44-57, 2003
- To, A., Fukao, Y., Tsuboi, S., Evidence for a thick and localized ultra low shear velocity zone at the base of the mantle beneath the central Pacific, *Earth Plan. Sci. Lett.*, 184, 119-133, 2011

32 An Automated Despiking Algorithm for Seismic Normal Mode Data

Shan Dou and Barbara Romanowicz

32.1 Introduction

The normal modes spectra of the Earth's free oscillations contain valuable information on the longest wavelength three dimensional structure of the Earth's interior. *Dahlen* (1982) first showed that the optimum record length for measuring eigenfrequencies and decay rates of normal modes using a Hanning taper is 1.1 Q cycles. Since typical modal Q values lie in the range 10^2 of to 10^3 , optimum window lengths are on the order of days to weeks. However, it is difficult even today to retrieve clean continuous time series spanning days or weeks following a large earthquake: in addition to aftershocks and other seismic events, data spikes due to transient disturbances at the station or temporary data storage failures are often unavoidable. Therefore, it is necessary to edit seismograms prior to the spectral analysis. Spikes are usually difficult to identify by existing algorithms because they have features which often are quite similar to those of real earthquake signals. The majority of conventional despiking algorithms require empirical tuning of associated parameters. The required parameter tuning often degrades the efficiency of automated algorithms, which in the end do not save much time and effort when compared with manual approaches. Hence, most despiking is done by direct manual editing, which can be a rather monotonous task, especially when one deals with a large dataset. Ideally, to be helpful, an automated despiking algorithm should not require users to manually intervene.

In this report, we describe a 3D phase space thresholding despiking algorithm which was first developed in the hydraulic engineering community and which we have adapted to our needs. The method was originally used to remove spikes from acoustic Doppler velocimeter data. It makes use of several ideas: (1) Differentiating a signal can enhance the high-frequency components (e.g. *Roy et al.*, 1999); (2) The Universal Threshold (*Donoho and Johnstone*, 1994; *Katul and Vodakovic*, 1998) provides the maximum of a white noise sequence; (3) Valid data tend to cluster into a dense cloud in a three-dimensional Poincar map and data points lying outside that cloud should be suspected as spikes (e.g. *Abarbanel*, 1995; *Addison*, 1997). In this study, we examine the validity of the 3D phase space thresholding despiking algorithm for preparing long seismic time series for normal mode analysis. Synthetic tests shown below demonstrated that spikes can be successfully detected and removed by the 3D phase space thresholding despiking algorithm.

32.2 Description of the Algorithm

The process of removing spikes comprises two steps: detection and replacement. In principle, these two parts are independent of each other, but the method described here is iterative and thus a proper spike replacing approach is also important for spike detection in the subsequent iterations.

(a) Universal Threshold:

As mentioned in the last section, Donoho and Johnstone (1994b) introduced the Universal Threshold, which is given by

$$\lambda^U = \sigma\sqrt{2\log n}$$

where σ is the standard deviation of the noise sequence and n is the number of data points.

(b) Differentiating and Calculating the Correlation Coefficients:

We calculate first and second derivatives of the original time series Δu_i and $\Delta^2 u_i$ and the associated three sets of standard deviations σ_u , $\sigma_{\Delta u}$ and $\sigma_{\Delta^2 u}$. The correlation coefficients between $u - \Delta u$, $u - \Delta^2 u$ and $\Delta u - \Delta^2 u$ are calculated as follows:

$$\alpha_{u-\Delta u} = \tan^{-1}\left(\frac{\sum u_i \Delta u_i}{\sum u_i^2}\right) = 0;$$

$$\alpha_{u-\Delta^2 u} = \tan^{-1}\left(\frac{\sum u_i \Delta^2 u_i}{\sum u_i^2}\right);$$

$$\alpha_{\Delta u-\Delta^2 u} = \tan^{-1}\left(\frac{\sum \Delta u_i \Delta^2 u_i}{\sum (\Delta u_i)^2}\right) = 0;$$

(c) 3D Phase-Space Map:

Each set of three variables $\{u_i, \Delta u_i, \Delta^2 u_i\}$ determines a point $\{\rho, \theta, \phi\}$ in spherical coordinates, where $\rho_i^2 = u_i^2 + (\sum u_i)^2 + (\sum^2 u_i)^2$. For each pair of θ, ϕ , we can then calculate a threshold ellipsoid determined by:

$$\frac{1}{\rho_0^2} = \frac{(\sin\phi\cos\theta\cos\alpha + \cos\phi\sin\alpha)^2}{a^2} + \frac{(\sin\phi\cos\theta\cos\alpha - \cos\phi\cos\alpha)^2}{b^2} + \frac{(\sin\phi\sin\theta)^2}{c^2}$$

Where $a = \lambda_u^U = \sigma_u\sqrt{2\log n}$, $b = \lambda_{\Delta^2 u}^U = \sigma_{\Delta^2 u}\sqrt{2\log n}$, $c = \lambda_{\Delta u}^U = \sigma_{\Delta u}\sqrt{2\log n}$ and α is the rotation angle calculated from the correlation coefficient of $\alpha_{u-\Delta^2 u}$. The valid data points will then cluster inside of the threshold ellipsoids, while the data points that fall outside of the ellipsoids will be suspected as spikes.

The 3D phase-space map has been used broadly in fractal geometry and chaotic dynamics studies. In phase-space, the transient high frequency component of the time series, which is much less random, can be separated from the chaotic regime that is featured as a compact cluster that is associated with chaotic oscillations. Because the time series needs to appear random for the Universal Threshold approach to be valid, the despiking procedure is not applied to the portion of data that are recorded within the first 21 hours after the origin time of the target event, during which strong coherent energy would not have the needed apparent randomness.

(d) Replacement:

Windows containing spikes can be considered as having gaps in the data stream. As one can already see, the shape of the threshold ellipsoid will vary when spikes are removed from a given segment of time series. Therefore, the entire despiking procedure needs to be repeated for several iterations until the number of detected spikes goes to zero. To ensure that the data cleaning procedure is complete and avoid introducing biases, it is important to develop a replacing strategy that can preserve the low frequency mode information contained in the time series.

The Discrete Fourier Transform (DFT) can be used to interpolate any data set that exhibits a periodic behavior. It consists of dividing the input signal into its major frequencies, determining the DFT coefficients (weights of each major frequency component), and then using the DFT coefficients and the associated frequencies to re-compose the signal. This is the same process as is used for transmitting signals over telephone lines.

32.3 Application Examples

To explore the effectiveness of the automated despiking procedure while verifying that no significant bias is introduced during despiking, a set of spikes extracted from a noisy record is added to a raw time series free of spikes. The automated despiking algorithm is then applied on the artificially contaminated time series. We then compare the originally clean record with that obtained after applying the despiking procedure both in the time and frequency domain so as to check the preservation of the valid signal. Figure 2.69 shows the associated power spectra: The contaminated spectra (thick black line) and the post-despiking spectra (solid grey line) are plotted together. The striking effect of the added spikes is the severely elevated baseline level in the pre-despiking spectra. In Figure 2.69b, we compare the original uncontaminated power spectra (black dashed line) and the power spectra generated from the post-despiking time series (solid grey line). The fact that they are indistinguish-

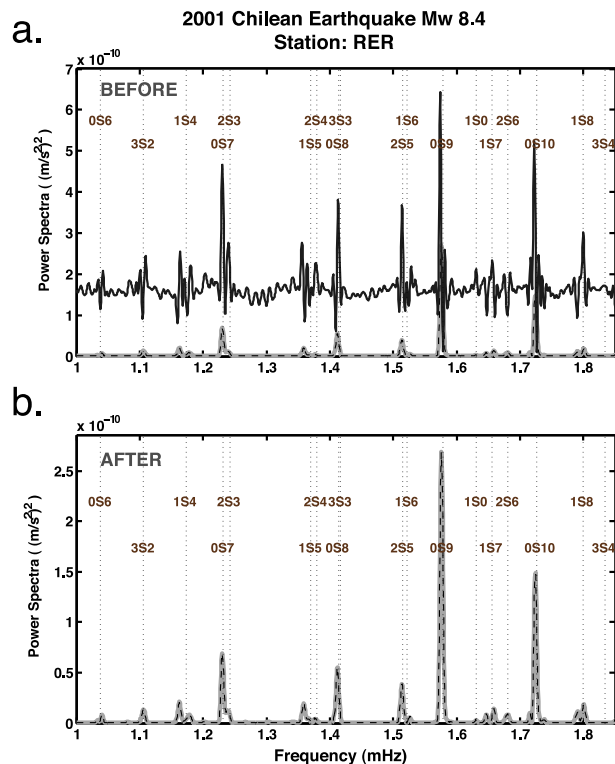


Figure 2.69: Frequency domain illustration of the effect of despiking algorithm. Panel a: The spectra shown in solid black line are generated from an artificially contaminated seismogram (i.e. clean seismogram + spikes extracted from another noisy record). Panel b: To examine whether any significant biases could be caused by the despiking algorithm, the original spectra associated with the clean seismogram are plotted (black dash line) on top of the post-despiking spectra (solid light grey line). The consistency of the two spectra indicates that valid information of the data is well maintained by the despiking algorithm. A noticeable feature is the scale differences between the two panels due to the high noise floor in Panel a.

able confirms that the despiking procedure is working well.

32.4 References

Donoho, D. L and Johnston, I. M., Ideal spatial adaptation by wavelet shrinkage, *Biometrika*, 81, 425-455, 1994.
 Roy, M., Kumar, V. R., Kulkarni, B. D., Sanderson, J., Rhodes, M. and van der Stappen, M., Simple denoising algorithm using wavelet transform, *J. Am. Ins. Chem. Eng.*, 45, 2461 - 2466, 1999.
 Abarbanel, H. D. I., *Analysis of Observed Chaotic Data*, Springer, New York, 1995.
 Dahlen, F. A., The effect of data windows on the estimation of free oscillation parameters, *Geophys. J. R. astr. Soc.*, 69, 537-549, 1982.

33 Seismic Imaging of the San Andreas Fault in Northern California using Receiver Functions

Pascal Audet

33.1 Introduction

Scattering of teleseismic body waves is conventionally used to investigate crustal and mantle structure using the so-called “receiver function” technique. This approach makes use of the fact that teleseismic events have near-vertical incidence upon horizontally layered structure, ensuring minimum phase, and assumes that source-time functions can be approximated by energy on the P component of motion. This approach has been successful in countless applications, including the characterization of layered crust and mantle, anisotropy and dipping structure.

Results from a recent application of the receiver function method near Parkfield in Northern California suggest that crustal structure is highly anisotropic with some indication of shallow offset in crustal discontinuities across the San Andreas Fault (SAF) (Ozacar and Zandt, 2009). Here we use receiver functions to analyze crustal structure around the SAF near San Juan Bautista in Northern California by decomposing radial and transverse signals into first order harmonic modes. Variations of energy of the different modes with depth are then used to characterize teleseismic wave scattering from velocity contrasts across the San Andreas Fault.

33.2 Data and method

We use data from the broadband station SAO, located 3 km from the surface trace of the SAF. Three-component seismograms are collected for all events with $M > 5.5$ in the epicentral distance range 30° - 100° . Vertical and horizontal (both radial and transverse) components of motion are decomposed into upgoing P , S_V (radial) and S_H (transverse) wave components. Individual single-event seismograms are processed using the receiver function method, which employs the P component as an estimate of the source to deconvolve the S_V and S_H components using a modified Wiener spectral deconvolution technique and recover receiver-side S velocity structure (Audet, 2010).

Resulting S_V and S_H receiver functions represent mostly forward-scattered P_S waves from planar discontinuities in physical properties. For horizontal layering, timing and amplitude of each converted phase constrain overlying velocity structure (depth and V_P/V_S of the overlying column) and velocity contrasts at discontinuities, respectively. For isotropic, horizontal layering, no energy is converted onto the S_H component; any energy observed on this component must therefore repre-

sent either structural heterogeneity (e.g., dipping interface), anisotropy, or both. In either case, periodic polarity reversals of converted S_H phase amplitude with back-azimuth are expected; a plane dipping layer will produce a $1-\theta$ periodicity, whereas anisotropy may produce more complicated patterns with higher order harmonics due to various degrees of symmetry of the elastic tensor and its orientation in space.

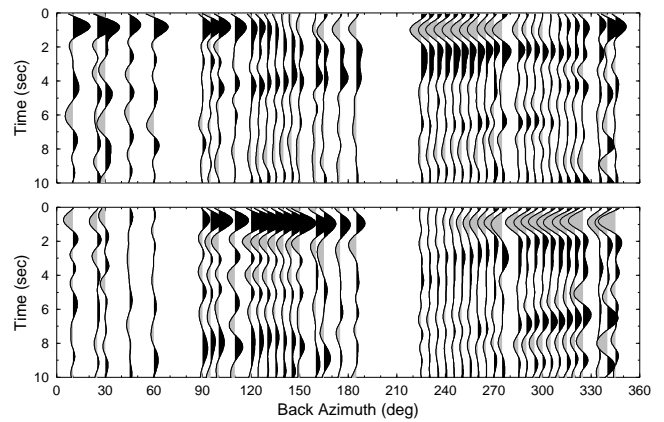


Figure 2.70: Receiver functions from station SAO near San Juan Bautista, Northern California. S_V (top) and S_H (bottom) components sorted by back-azimuth of incoming wavefield. Black is positive and grey is negative.

Results are shown in Figure 33.2. A number of features can be readily identified:

- S_V signals at 1-2 seconds show strong $1-\theta$ back-azimuthal variations in amplitude, with polarity reversals at 130° and 310° , which cannot be explained by simple, horizontal isotropic layering and must involve shallow anisotropy and/or a dipping structure.
- Corresponding S_H waves at 1-2 seconds also show similar $1-\theta$ back-azimuthal variations, with polarity reversals shifted by 90 degrees.
- Typical crust-mantle (Moho) conversions, normally appearing at 3-5 seconds as strong positive arrivals on the S_V component of motion, are lacking, indicating that the Moho may be invisible to high-frequency waves, or that it is highly complex.

These first-order observations can be further refined by decomposing the amplitude of migrated S_V and S_H signals at each depth increment as a function of back-azimuth using the equation

$$S_{V,H}(z, \phi) = A_{V,H}(z) + B_{V,H}(z) \cos(\phi + C_{V,H}(z)). \quad (2.2)$$

For S_V , energy on the A component should reflect bulk, isotropic velocity contrasts. Any signal on the B component represents dipping or anisotropic structure, and is seen on both S_V and S_H . Higher order harmonics (not analyzed here) are diagnostic of anisotropy. The C component represents the phase of the fitted cosine function. Results are shown in Figure 33.2. The fit appears to be best between 2-6 km depth, where the A component is close to 0 on the S_V component and negligible on the S_H component. The energy arises from the purely sinusoidal terms (B and C) on both components. Amplitudes are very high (<-0.5), and components are 90° out of phase, with maximum S_V signal from back-azimuths perpendicular to strike of the SAF (128° or 308°). Absence of energy on the A component strongly suggests that structure other than horizontal layering is responsible. Anisotropy is also unable to explain the absence of energy on the A component, especially at the large amplitude of the B component. Instead, these signals can be easily explained by near-vertical velocity contrast of the San Andreas Fault.

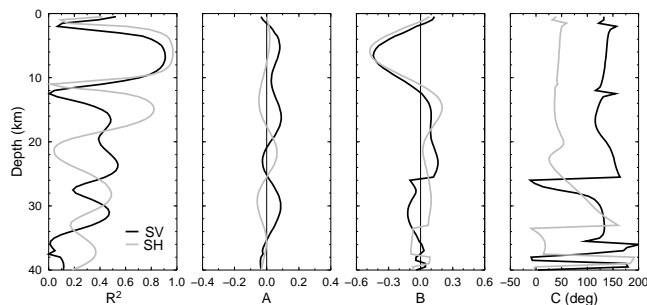


Figure 2.71: First order harmonic decomposition of receiver function amplitude as a function of inferred depth (Equation 2.2). Results for S_V and S_H are shown in black and grey, respectively. R^2 shows the fit to Equation (2.2). The A component represents a constant amplitude term. B and C are amplitude and phase of a fitted cosine term.

33.3 Discussion and conclusion

Receiver functions for station SAO near San Juan Bautista show signals related to scattering from a near-vertical SAF. These signals indicate strong velocity contrasts, possibly related to major structural differences across the fault, or to the presence of a low-velocity zone

caused by fault damage and/or elevated pore-fluid pressure. Future work will involve modeling of these fault-scattered waves using a finite-difference technique (e.g., Levin *et al.*, 2007). In addition, the method presented here will allow characterization of time variations in fault scattering structure by analyzing residuals of the fitted Equation 2.2 as a function of time. This technique could prove to be a powerful tool for the analysis of transient fault properties following major earthquakes.

33.4 Acknowledgements

This work was funded by the Miller Institute for Basic Research in Science (UC Berkeley).

33.5 References

- Audet, P, Temporal variations in crustal velocity structure near Parkfield, California, using receiver functions, *Bull. Seism. Soc. Am.*, 100, 1356-1362, 2010.
- Levin, V., D. Okaya, and J. Park, Shear wave birefringence in wedge-shaped anisotropic regions, *Geophys. J. Int.*, 168, 275-286, 2007.
- Ozacar A. A., and G. Zandt, Crustal structure and seismic anisotropy near the San Andreas fault at Parkfield, California, *Geophys. J. Int.*, 178, 1098-1104, 2009.

Chapter 3

BSL Operations

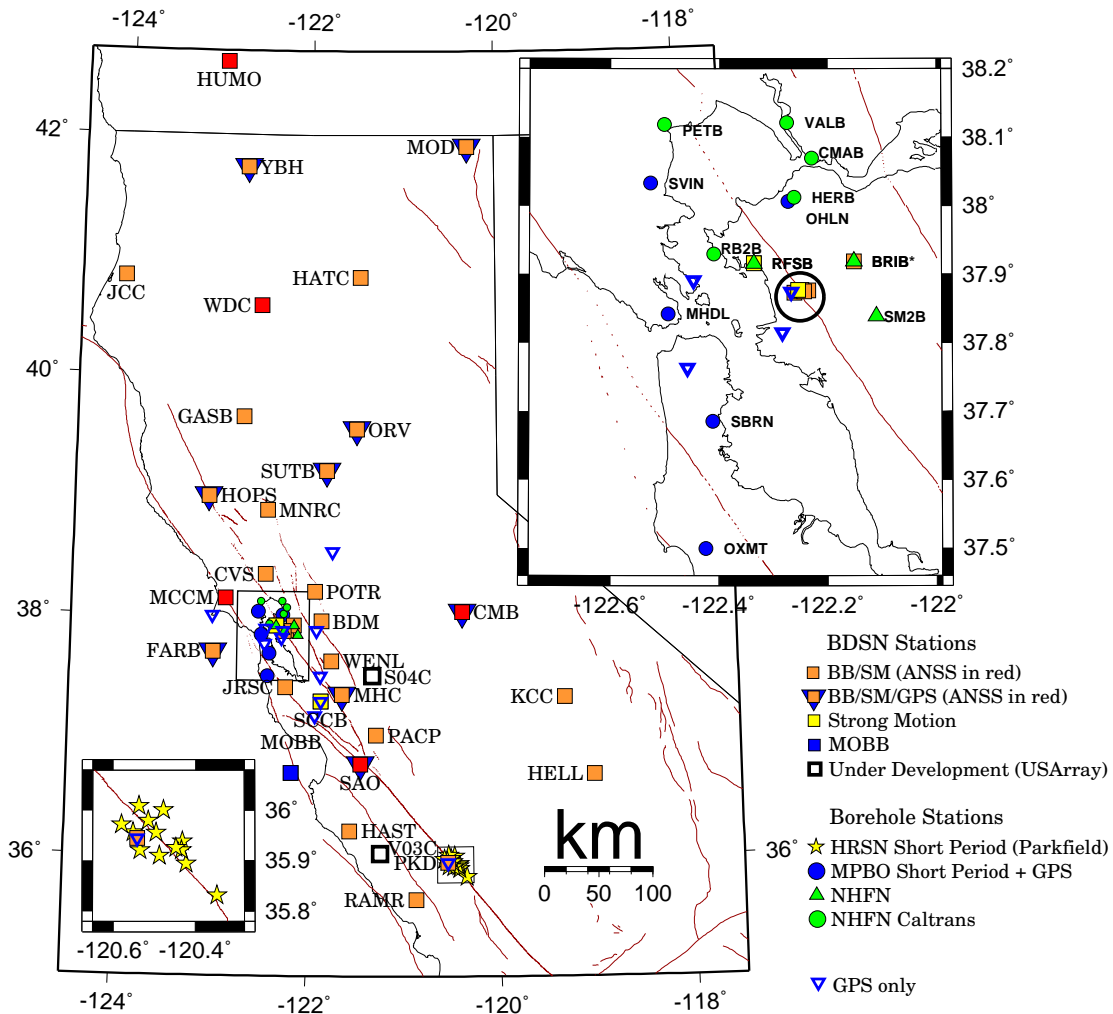


Figure 3.1: Map illustrating the distribution of BSL networks in Northern and Central California. UCGS and CalEMA contribute to operating these stations. ANSS backbone stations are shown in red. In the inset map, the shown stations in the circle include BRK, BKS, CMSB, VAK, BL88, and BL67. * Station BRIB is also a GPS and mPBO site. Abbreviations: BB/SM - Broadband/Strong Motion; BB/SM/GPS - Broadband/Strong Motion/GPS

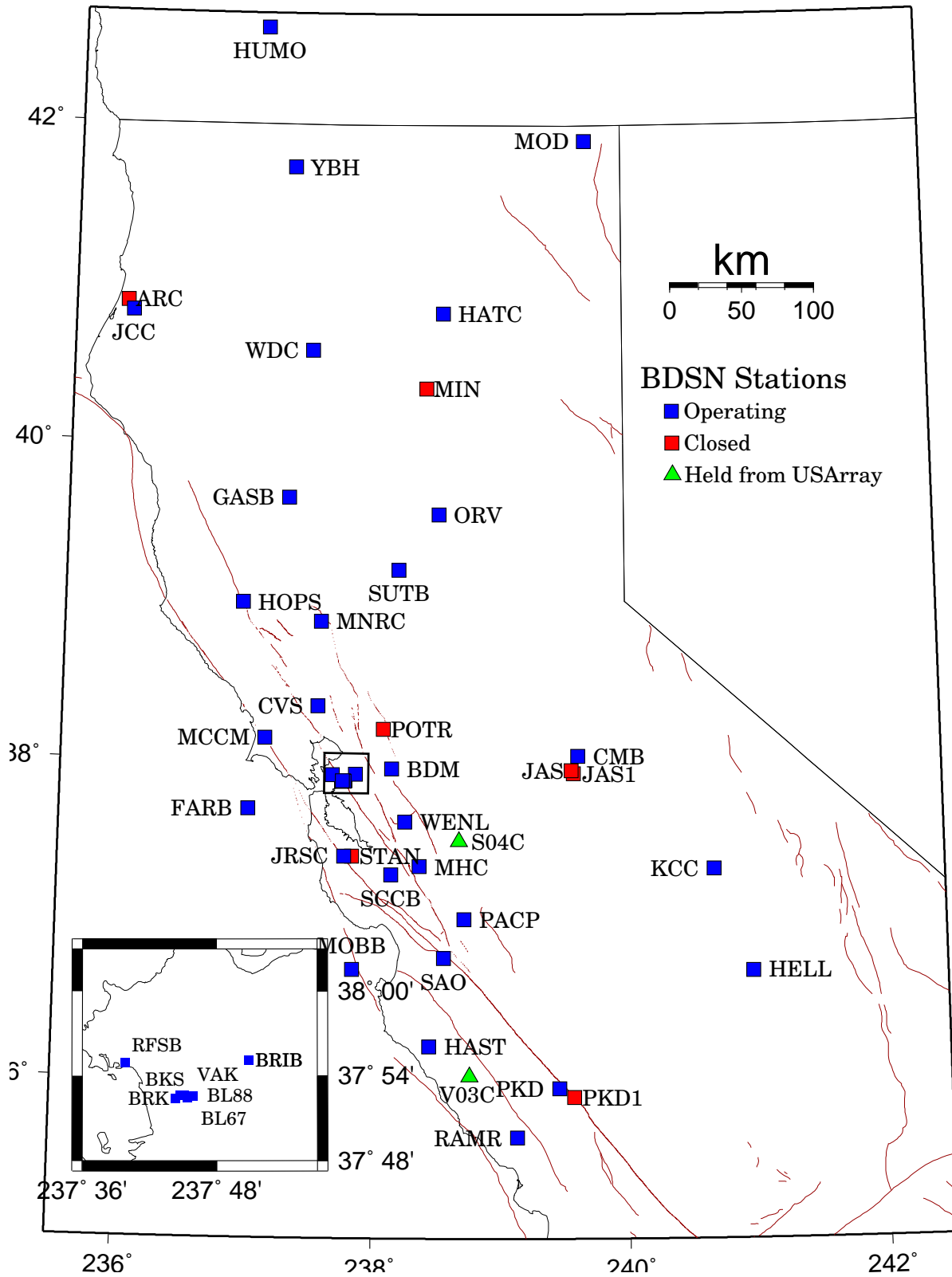


Figure 3.2: Map illustrating the distribution of BDSN stations in Northern and Central California. In the inset map, the order of the stations from left to right is: RFSB, BRK, BL88, VAK, BL67, BKS, BRIB.

1 Berkeley Digital Seismic Network

1.1 Introduction

The Berkeley Digital Seismic Network (BDSN) is a regional network of very broadband and strong motion seismic stations spanning Northern California and linked to UC Berkeley through continuous telemetry (Figure 3.2 and Table 3.1). The network is designed to monitor regional seismic activity as well as to provide high quality data for research in regional and global broadband seismology.

Since 1991, the BDSN has grown from the original three broadband stations installed in 1986-87 (BKS, SAO, MHC) to 35 stations, including an ocean-bottom seismometer in Monterey Bay (MOBB). We take particular pride in high quality installations, which often involve lengthy searches for appropriate sites away from sources of low-frequency noise as well as continuous improvements in installation procedures and careful monitoring of noise conditions and problems. This year, most of the field and operation efforts have been directed toward station upgrades, thanks to the American Recovery and Reinvestment Act (ARRA). Engineering and research efforts were also devoted to several projects to develop and test new instrumentation (see Operational Section 7). We have tested the Quanterra environmental add-on, the QEP. In addition, the BSL is part of a team that is developing and testing a newly designed very broadband (VBB) sensor to replace the STS-1 seismometer.

The expansion of our network to increase the density of state-of-the-art strong motion/broadband seismic stations and improve the joint earthquake notification system in this seismically hazardous region, one of BSL's long term goals, must be coordinated with other institutions and is contingent on the availability of funding. In the past year, in cooperation with and with support from the Lawrence Berkeley National Laboratory (LBNL), we installed and are collecting data from three sites on the LBNL Campus (VAK, BL88 and BL67). We also received funds from the Gordon and Betty Moore Foundation for TremorScope (see Section 17). As part of this exciting project for monitoring non-volcanic tremor sources along the San Andreas Fault south of Parkfield, the BDSN will be augmented by a network of four high-quality borehole stations and four surface stations.

Data quality and the integrity of the established network are just as important as network growth, so existing network stations must be preserved. The first generation of broadband seismometers installed by the BSL has been operating for almost 25 years. At the same time, the first generation of broadband data loggers have completed their 19th year of service. Fortunately, be-

tween September 2009 and September 2011, we received funding and equipment from the ARRA to replace data loggers at the 25 stations where older models were still installed. The upgrade of the last remaining station to have an old Quanterra data logger was completed in June 2011. We continue to exercise vigilance and to commit time and resources to repairs and upgrades as necessary.

1.2 BDSN Overview

Thirty one of the BDSN sites are equipped with three-component broadband seismometers and strong-motion accelerometers, and with 24- or 26-bit digital data acquisition systems or data loggers. Three additional sites (BL88, RFSB and SCCB) consist of a strong-motion accelerometer and a 24-bit digital data logger. The ocean-bottom station MOBB is equipped with a three component broadband seismometer with integrated digitizer and a differential pressure gauge (DPG). Data from all BDSN stations are transmitted to UC Berkeley using continuous telemetry. Continuous telemetry from MOBB was implemented early in 2009. Unfortunately, the underwater cable was trawled and damaged several times, until it failed in late February 2010. The cable was finally replaced in June 2011. In order to avoid data loss during utility disruptions, each site has batteries to supply power for three days; many are accessible via a dialup phone line. The combination of high-dynamic range sensors and digital data loggers ensures that the BDSN has the capability to record the full range of earthquake motion required for source and structure studies. Table 3.2 lists the instrumentation at each site.

Most BDSN stations have Streckeisen STS-1 or STS-2 three-component broadband sensors (*Wielandt and Streckeisen, 1982; Wielandt and Steim, 1986*). A Guralp CMG-3T broadband sensor contributed by LLNL is deployed in a post-hole installation at BRIB. A Guralp CMG-1T is deployed at MOBB. As part of the ARRA upgrade, all remaining Kinemetrics FBA-23 accelerometers in the network were replaced. Now all stations have either Kinemetrics FBA-ES-T or Metrozet TSA-1 accelerometers with ± 2 g dynamic range. By the end of June 2011, old data loggers systems at all BDSN sites except MOBB had been replaced. There are no longer any Q680, Q730, or Q4120 Quanterra data loggers in the network, only Q330, Q330HR or Q330S data loggers. The Quanterra data loggers employ FIR filters to extract data streams at a variety of sampling rates. With the data logger upgrade, several conventions changed: All sites received SEED location codes, with the data logger for the broadband and strong motion sensors having the location code "00," and accelerometer channels are now

Code	Net	Latitude	Longitude	Elev (m)	Over (m)	Date	Location
BDM	BK	37.9540	-121.8655	219.8	34.7	1998/11 -	Black Diamond Mines, Antioch
BKS	BK	37.8762	-122.2356	243.9	25.6	1988/01 -	Byerly Vault, Berkeley
BL67	BK	37.8749	-122.2543	736.18	0	2011/04 -	LBNL Building 67, Berkeley
BL88	BK	37.8772	-122.2543	602.21	0	2011/01 -	LBNL Building 88, Berkeley
BRIB	BK	37.9189	-122.1518	219.7	2.5	1995/06 -	Briones Reservation, Orinda
BRK	BK	37.8735	-122.2610	49.4	2.7	1994/03 -	Haviland Hall, Berkeley
CMB	BK	38.0346	-120.3865	697.0	2	1986/10 -	Columbia College, Columbia
CVS	BK	38.3453	-122.4584	295.1	23.2	1997/10 -	Carmenet Vineyard, Sonoma
FARB	BK	37.6978	-123.0011	-18.5	0	1997/03 -	Farallon Island
GASB	BK	39.6547	-122.716	1354.8	2	2005/09 -	Alder Springs
HAST	BK	36.3887	-121.5514	542.0	3	2006/02 -	Carmel Valley
HATC	BK	40.8161	-121.4612	1009.3	3	2005/05 -	Hat Creek
HELL	BK	36.6801	-119.0228	1140.0	3	2005/04 -	Miramonte
HOPS	BK	38.9935	-123.0723	299.1	3	1994/10 -	Hopland Field Stat., Hopland
HUMO	BK	42.6071	-122.9567	554.9	50	2002/06 -	Hull Mountain, Oregon
JCC	BK	40.8175	-124.0296	27.2	0	2001/04 -	Jacoby Creek
JRSC	BK	37.4037	-122.2387	70.5	0	1994/07 -	Jasper Ridge, Stanford
KCC	BK	37.3236	-119.3187	888.1	87.3	1995/11 -	Kaiser Creek
MCCM	BK	38.1448	-122.8802	-7.7	2	2006/02 -	Marconi Conference Center, Marshall
MHC	BK	37.3416	-121.6426	1250.4	0	1987/10 -	Lick Obs., Mt. Hamilton
MNRC	BK	38.8787	-122.4428	704.8	3	2003/06 -	McLaughlin Mine, Lower Lake
MOBB	BK	36.6907	-122.1660	-1036.5	1	2002/04 -	Monterey Bay
MOD	BK	41.9025	-120.3029	1554.5	5	1999/10 -	Modoc Plateau
ORV	BK	39.5545	-121.5004	334.7	0	1992/07 -	Oroville
PACP	BK	37.0080	-121.2870	844	0	2003/06 -	Pacheco Peak
PKD	BK	35.9452	-120.5416	583.0	3	1996/08 -	Bear Valley Ranch, Parkfield
RAMR	BK	37.9161	-122.3361	416.8	3	2004/11 -	Ramage Ranch
RFSB	BK	37.9161	-122.3361	-26.7	0	2001/02 -	RFS, Richmond
SAO	BK	36.7640	-121.4472	317.2	3	1988/01 -	San Andreas Obs., Hollister
SCCB	BK	37.2874	-121.8642	98	0	2000/04 -	SCC Comm., Santa Clara
SUTB	BK	39.2291	-121.7861	252.0	3	2005/10 -	Sutter Buttes
VAK	BK	37.8775	-122.2489	266.0	10	2010/08 -	LBNL Building 46, Berkeley
WDC	BK	40.5799	-122.5411	268.3	75	1992/07 -	Whiskeytown
WENL	BK	37.6221	-121.7570	138.9	30.3	1997/06 -	Wente Vineyards, Livermore
YBH	BK	41.7320	-122.7104	1059.7	60.4	1993/07 -	Yreka Blue Horn Mine, Yreka

Table 3.1: Stations of the Berkeley Digital Seismic Network currently in operation. Each BDSN station is listed with its station code, network id, location, operational dates, and site description. The latitude and longitude (in degrees) are given in the WGS84 reference frame, and the elevation (in meters) is relative to the WGS84 reference ellipsoid. The elevation is either the elevation of the pier (for stations sited on the surface or in mining drifts) or the elevation of the well head (for stations sited in boreholes). The overburden is given in meters. The date indicates either the upgrade or installation time.

Code	Broadband	Strong-motion	Data logger	GPS	Other	Telemetry	Dial-up
BDM	STS-2	FBA-ES-T	Q330HR			FR	
BKS	STS-1	FBA-ES-T	Q330HR		E300, Baseplates	FR	X
BL67	CMG-3T	FBA-ES-T	Q330S			LAN	
BL88		FBA-ES-T	Q330S			R	
BRIB	CMG-3T	FBA-ES-T	Q330HR	X	Strainmeter, EM	FR	X
BRK	STS-2	FBA-ES-T	Q330HR			LAN	
CMB	STS-1	FBA-ES-T	Q330HR	X	E300, Baseplates	FR	X
CVS	STS-2	FBA-ES-T	Q330HR			FR	
FARB	STS-2	FBA-ES-T	Q330HR	X		R-FR/R	
GASB	STS-2	FBA-ES-T	Q330HR	X		R-FR	
HAST	STS-2	FBA-ES-T	Q330HR			R-Sat	
HATC	STS-2	FBA-ES-T	Q330HR			T1	
HELL	STS-2	FBA-ES-T	Q330			R-Sat	
HOPS	STS-1	FBA-ES-T	Q330HR	X	E300, Baseplates	FR	X
HUMO	STS-2	FBA-ES-T	Q330HR			VSAT	X
JCC	STS-2	FBA-ES-T	Q330HR			FR	X
JRSC	STS-2	TSA-100S	Q330HR			Mi-LAN	X
KCC	STS-1	FBA-ES-T	Q330HR		E300, Baseplates	R-Mi-FR	X
MCCM	STS-2	FBA-ES-T	Q330HR			VSAT	
MHC	STS-1	FBA-ES-T	Q330HR	X		FR	X
MNRC	STS-2	FBA-ES-T	Q330HR	X		Sat	X
MOBB	CMG-1T		DM24		OCM, DPG	LAN	
MOD	STS-1*	FBA-ES-T	Q330HR	X	Baseplates	VSAT	X
ORV	STS-1	FBA-ES-T	Q330HR	X	Baseplates	FR	X
PACP	STS-2	FBA-ES-T	Q330HR			Mi/FR	
PKD	STS-2	FBA-ES-T	Q330HR	X	EM	R-Mi-T1	X
RAMR	STS-2	FBA-ES-T	Q330			R-FR	X
RFSB		FBA-ES-T	Q330HR			FR	
SAO	STS-1	FBA-ES-T	Q330HR	X	Baseplates, EM	FR	X
SCCB		TSA-100S	Q330HR	X		FR	
SUTB	STS-2	FBA-ES-T	Q330HR	X		R-FR	
VAK	CMG-3T	FBA-ES-T	Q330S			R	
WDC	STS-2	FBA-ES-T	Q330HR	X		FR	X
WENL	STS-2	FBA-ES-T	Q330HR			FR	
YBH	STS-1,STS-2	FBA-ES-T	Q330HR, Q330**	X	E300, Baseplates	FR	X

Table 3.2: Instrumentation of the BDSN as of 06/30/2011. Except for BL88, RFSB, SCCB, and MOBB, each BDSN station consists of collocated broadband and strong-motion sensors, with a 24-bit Quanterra data logger and GPS timing. The stations BL88, RFSB, and SCCB are strong-motion only, while MOBB has only a broadband sensor. Additional columns indicate collocated GPS receivers as part of the BARD network (GPS) and additional equipment (Other), such as warpless baseplates, new STS-1 electronics (E300) or electromagnetic sensors (EM). The OBS station MOBB also has a ocean current meter (OCM) and differential pressure gauge (DPG). The main and alternate telemetry paths are summarized for each station. FR - frame relay circuit, LAN - ethernet, Mi - microwave, R - radio, Sat - Commercial Satellite, T1 - T1 line, VSAT - USGS ANSS satellite link. An entry like R-Mi-FR indicates telemetry over several links, in this case, radio to microwave to frame relay. (*) During 2010-2011, the STS-1 at this station was replaced by an STS-2. (**) YBH is CTBT auxiliary seismic station AS-109. It has a high-gain STS-2. After the ARRA upgrade of the data logger there, a new Q330 will be installed to collect data from the STS-2.

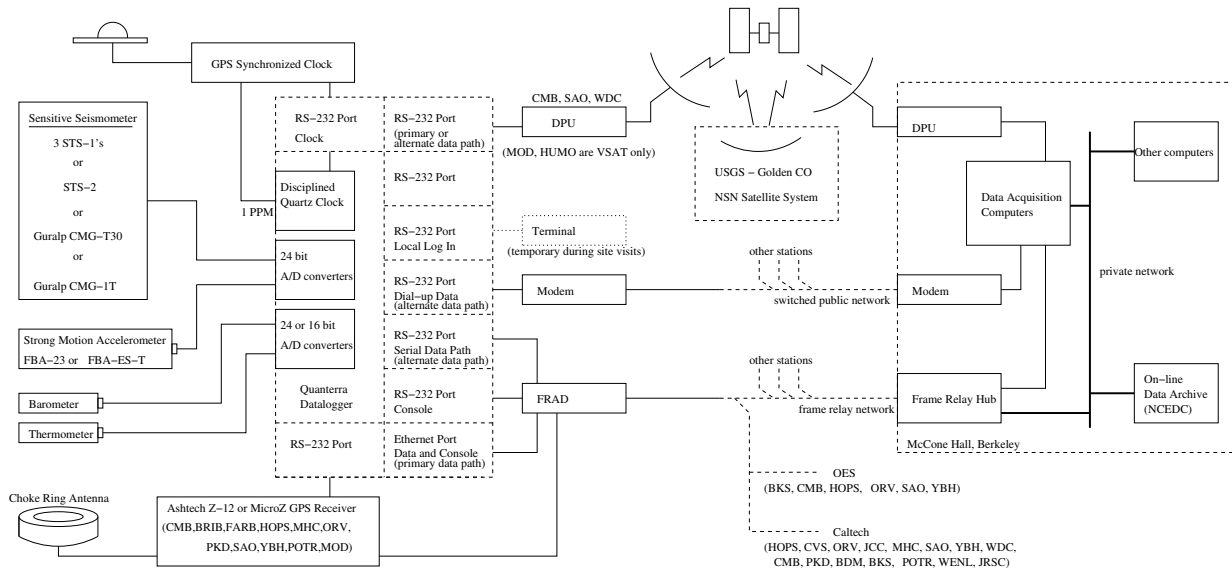


Figure 3.3: Schematic diagram showing the flow of data from the sensors through the data loggers to the central acquisition facilities of the BSL.

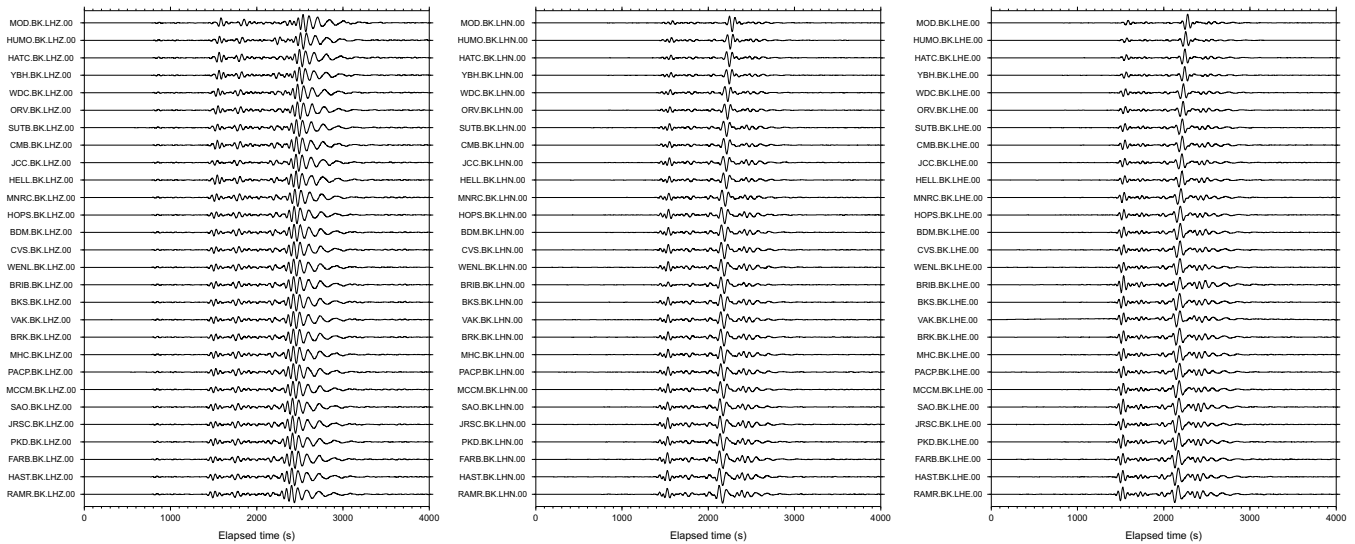


Figure 3.4: Long period (50-200 s period) waveforms recorded across BDSN from the M_w 7.6 teleseism which occurred on July 6, 2011, in Kermadec Islands region (650 km north of New Zealand) at 29.312 S, 176.204 W. This is the first large teleseism for which all the data loggers of the BDSN’s stations had been upgraded to Q330 or Q330HR units. The traces are deconvolved to ground velocity, scaled by their maximum values, and ordered from bottom to top by distance from the epicenter. The highly similar waveforms recorded across the BDSN provide evidence that the broadband sensors are operating within their nominal specifications. Data from MOBB and KCC were not available for this earthquake.

designated with “HN?” rather than “HL?”. In addition, the BDSN stations now record continuous data at 0.1, 1.0, 40, and 100 samples per second (Table 3.3). In the past, other sample rates may have been available (see

past annual reports).

When the broadband network was upgraded during the 1990s, a grant from the CalREN Foundation (California Research and Education Network) in 1994 enabled the

BSL to convert data telemetry from analog leased lines to digital frame relay. The frame-relay network uses digital phone circuits which support 56 Kbit/s to 1.5 Mbit/s throughput. Today, 22 of the BDSN sites use frame-relay telemetry for all or part of their communications system. Other stations send their data to the data center via satellite, Internet, microwave, and/or radio (see Table 3.2).

As described in Operational Section 7, data from the BDSN are acquired centrally at the BSL. These data are used for rapid earthquake reporting as well as for routine earthquake analysis (Operational Sections 2 and 8). As part of routine quality control (Operational Section 7), power spectral density (PSD) analyses are performed continuously and are available on the Internet (<http://www.ncedc.org/ncedc/PDF/>). The occurrence of a significant teleseism also provides the opportunity to review station health and calibration. Figure 3.4 displays BDSN waveforms for the M_w 7.6 earthquake that occurred in the Kermadec Islands on July 6, 2011, shortly after the last data logger had been upgraded.

BDSN data are archived and available at the Northern California Earthquake Data Center. This is described in detail in Operational Section 6.

Sensor	Channel	Rate (sps)	Mode	FIR
BB	VH?	0.1	C	Ac
BB	LH?	1	C	Ac
BB	BH?	40	C	Ac
BB	HH?	80/100	C	Ca
SM	LN?	1	C	Ac
SM	BN?	20/40	C	Ac
SM	HN?	80/100	C	Ca

Table 3.3: Typical data streams currently acquired at BDSN stations, with channel name, sampling rate, sampling mode, and the FIR filter type. BB indicates broadband; SM indicates strong-motion; C continuous; Ac acausal; Ca causal. The LN and BN strong-motion channels are not transmitted over the continuous telemetry but are available on the Quanterra disk system if needed. The HH and HN channels are now all recorded and telemetered continuously at 100 sps and have causal filtering. During the past two years, the SM channels have been renamed from HL? (BL?, LL?) to HN? (BN?, LN?). For past sampling rates, see earlier annual reports.

Electromagnetic Observatories

In 1995, in collaboration with Dr. Frank Morrison, the BSL installed two well-characterized electric and magnetic field measuring systems at two sites along the San Andreas Fault which are part of the Berkeley Digital Seismic Network. Since then, magnetotelluric (MT) data

have been continuously recorded at 40 Hz and 1 Hz and archived at the NCEDC (Table 3.4). At least one set of orthogonal electric dipoles measures the vector horizontal electric field, E, and three orthogonal magnetic sensors measure the vector magnetic field, B. These reference sites, now referred to as electromagnetic (EM) observatories, are collocated with seismometer sites so that the field data share the same time base, data acquisition, telemetry, and archiving system as the seismometer outputs.

Sensor	Channel	Rate (sps)	Mode	FIR
Magnetic	VT?	0.1	C	Ac
Magnetic	LT?	1	C	Ac
Magnetic	BT?	40	C	Ac
Electric	VQ?	0.1	C	Ac
Electric	LQ?	1	C	Ac
Electric	BQ?	40	C	Ac

Table 3.4: Typical MT data streams acquired at SAO, PKD, BRIB, and JRSC with channel name, sampling rate, sampling mode, and FIR filter type. C indicates continuous; Ac acausal. Data loggers for these systems have not been upgraded/replaced.

The MT observatories are located at Parkfield (PKD1, PKD), 300 km south of the San Francisco Bay Area, and Hollister (SAO), halfway between San Francisco and Parkfield (Figure 3.2). In 1995, initial sites were established at PKD1 and SAO, separated by a distance of 150 km, and equipped with three induction coils and two 100 m electric dipoles. PKD1 was established as a temporary seismic site, and when a permanent site (PKD) was found, a third MT observatory was installed in 1999 with three induction coils, two 100 m electric dipoles, and two 200 m electric dipoles. PKD and PKD1 ran in parallel for one month in 1999, and then the MT observatory at PKD1 was closed. Starting in 2004, new electromagnetic instrumentation was installed at various Bay Area sites in cooperation with Simon Klemperer at Stanford University. Sensors are installed at JRSC (2004), MHDL (2006) and BRIB (2006/2007).

Data at the MT sites are fed to Quanterra data loggers, shared with the collocated BDSN stations, synchronized in time by GPS, and sent to the BSL via dedicated communication links.

In October 2009, the EM coils at SAO were found to be not working. They were removed and returned to the manufacturer (EMI Schlumberger). They have not yet been reinstalled at SAO. EM/MT equipment at PKD was evaluated in August of 2008. There, the data logger was removed from the PKD EM/MT system and has not yet been returned.

Since it began in 1995, the EM/MT effort has suffered from minimal funding.

1.3 2010-2011 Activities

Station Upgrades, Maintenance, and Repairs

Given the remoteness of the off-campus stations, BDSN data acquisition equipment and systems are designed, configured, and installed so that they are both cost effective and reliable. As a result, there is little need for regular station visits. Nonetheless, many of the broadband seismometers installed by BSL are from the first generation and are about 25 years old. Concurrently, the first generation of broadband data loggers is now 19 years old. Computer systems are retired long before this age, yet the electronics that form these data acquisition systems are expected to perform without interruption.

In the summer of 2009, the USGS received ARRA funds, among other things, to upgrade and improve seismic stations operated as part of the Advanced National Seismic System (ANSS). The BSL is benefitting from those funds. We have received the new model of Quanterra data logger, the Q330HR, as government-furnished equipment (GFE) to replace the old Quanterras at 25 of the BDSN seismic stations. By the end of this fiscal year, data loggers had been replaced at all stations except KCC. There, the data logger had been upgraded to a Q330HR in December 2009, before we received the ARRA data loggers. According to the station's host, Southern California Edison, we will have to remove our equipment in 2012, as they will be renovating the tunnel. When we redeploy, we will install the ARRA data logger. In addition to replacing the data loggers, all remaining Kinemetrics FBA-23 accelerometers have been replaced with Kinemetrics' newer, lower noise model, the FBA-ES-T.

In addition to the equipment upgrades, we have used support from the ARRA project to implement alternative, and less expensive, telemetry options at two stations. At JRSC, on Stanford University's Jasper Ridge Biological Preserve, we took advantage of the opportunity to replace the frame relay service by using the new microwave Internet link installed between the Preserve and Stanford's campus. At MNRC, on UC Davis's McLaughlin Reserve, we installed a Wild Blue satellite Internet system. The radio-to-frame relay service through CAL FIRE's communications towers on Mt. St. Helena was always fraught with problems. In addition, the rent was due to increase on July 1, 2011.

Finally, some ARRA money has been used to purchase Quanterra Environmental Packages (QEP) and SETRA pressure sensors for several of our quietest sites. Over the years the environmental sensors (pressure, temperature, humidity) installed at many of the sites had died. In addition, the Q330 has only 6 input channels, which we use for the seismometer and accelerometer components. The QEP offer additional digitizing capacity as well as rudimentary environmental sensors (pressure, temperature, humidity). To ensure high quality pressure measure-

ments for reducing long period noise in the very broadband recordings, we have purchased and will also install the SETRA pressure sensors.

In addition, over the past two years, we have been able to purchase and install new electronics for five of our STS-1 sites, KCC, HOPS, BKS, CMB and YBH. Funds for this equipment have come from our IRIS/GSN grant and from our funding from the California Emergency Management Agency (CalEMA).

As always, some of the BSL's technical efforts were directed toward maintaining and repairing existing instrumentation, stations, and infrastructure. While expanding the network continues to be a long term goal of BSL, it is equally important to assure the integrity of the established network and preserve data quality.

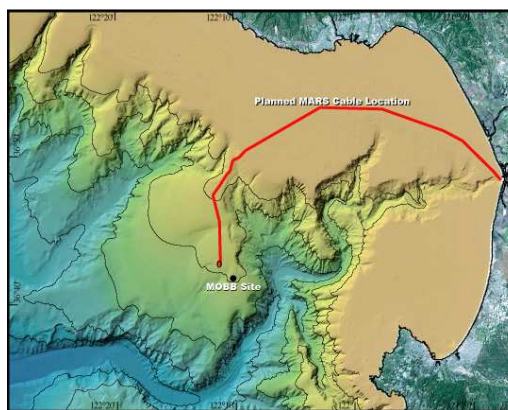


Figure 3.5: Location of the MOBB station in Monterey Bay, California, against seafloor and land topography. The path of the MARS cable is indicated by the solid line.

The Monterey Bay Ocean Bottom Seismic Observatory (MOBB)

The Monterey Ocean Bottom Broadband observatory (MOBB) is a collaborative project between the Monterey Bay Aquarium Research Institute (MBARI) and the BSL. Supported by funds from the Packard Foundation to MBARI, NSF/OCE funds, and UC Berkeley funds to the BSL, its goal has been to install and operate a long-term seafloor broadband station as a first step toward extending the onshore broadband seismic network in Northern California to the seaward side of the North-America/Pacific plate boundary, providing better azimuthal coverage for regional earthquake and structure studies. It also serves the important goal of evaluating background noise in near-shore buried ocean floor seismic systems, such as may be installed as part of temporary deployments of "leap-frogging" arrays (e.g. Ocean Mantle Dynamics Workshop, September 2002). The project has been described in detail in BSL annual reports since

2002 and in several publications (e.g. *Romanowicz et al., 2003, 2006*).

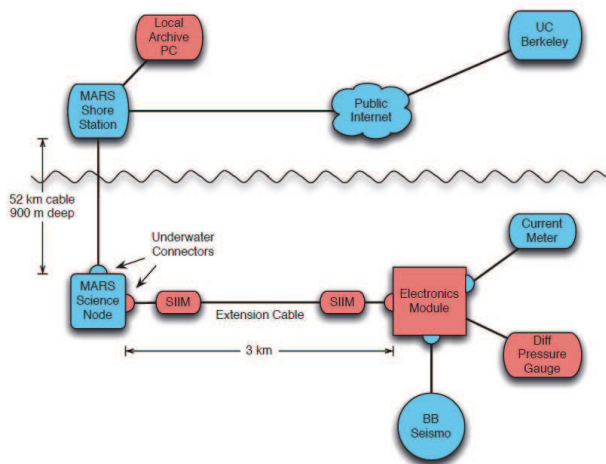


Figure 3.6: Components of the cabled observatory: the MOBB system integrated into the MARS network. MARS-provided components are shown in blue, and components installed or modified by the MOBB team are shown in pink.

The MARS (Monterey Accelerated Research System) observatory (Figure 3.5, <http://www.mbari.org/mars/>) comprises a 52 km electro-optical cable that extends from a shore facility in Moss Landing out to a seafloor node in Monterey Bay (Figure 3.5). The cable was deployed in the spring of 2007, and node installation was completed in November 2008. It now can provide power and data to as many as eight science experiments through underwater electrical connectors. MOBB, located ~ 3 km from the node, is one of the first instruments to be connected to the cable. The connection was established on February 28, 2009, through an extension cable installed by the ROV *Ventana*, with the help of a cable-laying toolsled. The data interface at the MARS node is 10/100 Mbit/s Ethernet, which can directly support cables of no more than 100 m in length. To send data over the required 3 km distance, the signals pass through a Science Instrument Interface Module (SIIM) at each end of the extension cable (Figure 3.6). The SIIMs convert the MARS Ethernet signals to Digital Subscriber Line (DSL) signals, which are converted back to Ethernet signals close to the MOBB system. Power from the MARS node is sent over the extension cable at 375 VDC, and then converted to 28 VDC in the distal SIIM for use by the MOBB system. The connection to the MARS node eliminates the need for periodic exchange of the battery and data package using ROV and ship. At the same time, it allows us to acquire seismic data from the seafloor in real time (*Romanowicz et al., 2009*).

The electronics module in the MOBB system has been

refurbished to support the connection to the MARS observatory. The low-power autonomous data logger has been replaced with a PC/104 computer stack running embedded Linux. This new computer runs an Object Ring Buffer (ORB), whose function is to collect data from the various MOBB sensors and forward it to another ORB running on a computer at the MARS shore station. There, the data are archived and then forwarded to a third ORB running at the UC Berkeley Seismological Laboratory. The Linux system acquires data from the various systems on the sea floor: from the Guralp digitizer included in the seismometer package (via RS232) and from a Q330 Quanterra 24 bit A/D converter which digitizes data from the DPG (via Ethernet). It also polls and receives data (via RS232) from the current meter. The data are available through the NCEDC. Procedures to include the MOBB data in the Northern California real time earthquake processing are under development.

After one year of continuous operation, the MOBB real-time telemetry ceased abruptly as a result of repeated trawling of the extension cable, which was not buried, even though the observatory is located in a protected zone. We obtained funds from NSF/OCE to replace the 3.2 km cable in late 2010, and decided to “go the extra mile” to bury the cable to protect it better from such future occurrences. The MBARI team built a custom-made basket for the ROV *Ventana* to carry and lay the cable out, while burying it. The cable was laid out on June 22, 2012 from the *Western Flyer* and plugged into the MARS system. The next day, the team dropped and installed the datalogger package and the MOBB data came back on-line. Figure 3.7 shows the cable sled with the new cable (red) being mounted under the ROV *Ventana* prior to installation. Hanging from the sled, one can see the “cutter” that would be used to dig a narrow trench in order to bury the cable in the seafloor. Figure 3.8 shows data from MOBB after the new cable was installed and buried. Traces from the three components of the MOBB broadband sensor are compared with corresponding traces for the nearby land broadband stations MHC and SAO.

1.4 Acknowledgements

Under Barbara Romanowicz’s general supervision, Peggy Hellweg and Doug Neuhauser oversee the BDSN data acquisition operations, and Bill Karavas heads the engineering team. Aaron Enright, John Friday, Jarrett Gardner, Rick Lellinger, Joshua Miller, Taka’aki Taira, and Bob Uhrhammer contribute to the operation of the BDSN. The network upgrades and improvements are funded through the ARRA (American Recovery and Reinvestment Act), under USGS award number G09AC00487. The new STS-1 electronics, E300s, installed at five of our stations, were purchased with funds from an IRIS/GSN grant and from CalEMA.

MOBB is a collaboration between the BSL and MBARI, involving Barbara Romanowicz, Taka'aki Taira, and Doug Neuhauser from the BSL, and Paul McGill from MBARI. The MBARI team also has included Steve Etchemendy (Director of Marine Operations), Jon Erickson, John Ferreira, Tony Ramirez, and Craig Dawe. The MOBB effort at the BSL is supported by UC Berkeley funds. MBARI supports the dives and data recovery. The MOBB seismometer package was funded by NSF/OCE grant #9911392. The development of the interface for connection to the MARS cable is funded by NSF/OCE grant #0648302.

Taka'aki Taira, and Peggy Hellweg contributed to the preparation of this section.

1.5 References

Cox, C., T. Deaton and S. Webb, A deep-sea differential pressure gauge, *J. Atm. Ocean. Tech.*, 1, 237-245, 1984.

Crawford W. C., and S. C. Webb, Identifying and removing tilt noise from low-frequency (<0.1 Hz) seafloor vertical seismic data, *Bull. Seis. Soc. Am.*, 90, 952-963, 2000.

Murdock, J., and C. Hutt, A new event detector designed for the Seismic Research Observatories, *USGS Open-File-Report 83-0785*, 39 pp., 1983.

Romanowicz, B., D. Stakes, R. Uhrhammer, P. McGill, D. Neuhauser, T. Ramirez, and D. Dolenc, The MOBB experiment: a prototype permanent off-shore ocean bottom broadband station, *EOS Trans. AGU*, Aug 28 issue, 2003.

Romanowicz, B., D. Stakes, D. Dolenc, D. Neuhauser, P. McGill, R. Uhrhammer, and T. Ramirez, The Monterey Bay Broadband Ocean bottom seismic observatory, *Ann. Geophys.*, 49, 607-623, 2006.

Romanowicz, B., P. McGill, D. Neuhauser and D. Dolenc, Acquiring real time data from the broadband ocean bottom seismic observatory at Monterey Bay (MOBB), *Seismol. Res. Lett.*, 80, 197-202, 2009.

Wielandt, E., and J. Steim, A digital very broadband seismograph, *Ann. Geophys.*, 4, 227-232, 1986.

Wielandt, E., and G. Streckeisen, The leaf spring seismometer: design and performance, *Bull. Seis. Soc. Am.*, 72, 2349-2367, 1982.

Zürn, W., and R. Widmer, On noise reduction in vertical seismic records below 2 mHz using local barometric pressure, *Geophys. Res. Lett.*, 22, 3537-3540, 1995.



Figure 3.7: This figure shows the cable laying tool, with the red cable wrapped inside it, as it is being mounted on the bottom of the ROV Ventana prior to installation. The sharp metal "edge" hanging from the middle of the sled was used to dig a narrow trench in the seafloor as the cable was laid down, so as to bury it and protect it from trawling,. Courtesy of Paul McGill, MBARI.

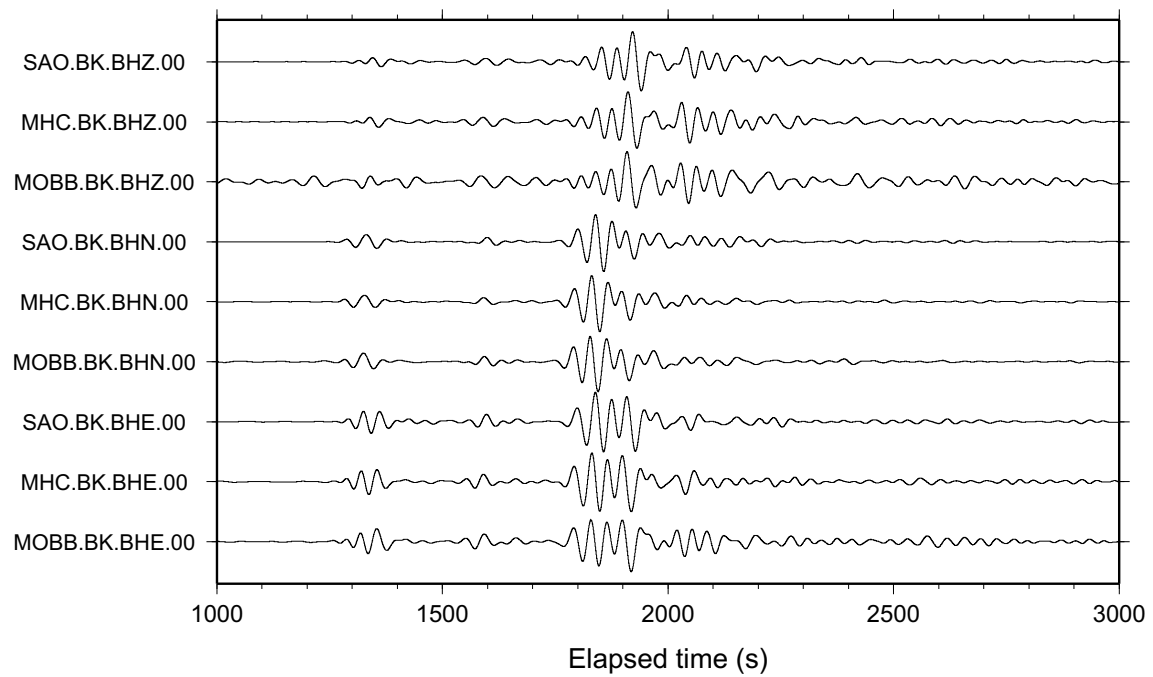


Figure 3.8: This figure shows MOBB broadband data along with traces from SAO and MHC for the M7.0 earthquake off the east coast of Honshu, Japan (2011/07/10 00:57:12 UTC). A 0.01-0.03 Hz BP filter was applied. They are in ground velocity and are normalized by their maximum amplitudes.

2 California Integrated Seismic Network

2.1 Introduction

Advances in technology have made it possible to integrate separate earthquake monitoring networks into a single seismic system as well as to unify earthquake monitoring instrumentation. In California, this effort began in the south with the TriNet Project. There, Caltech, the California Geological Survey (CGS), and the USGS created a unified seismic system for Southern California. With major funding provided by the Federal Emergency Management Agency (FEMA), the California Governor's Emergency Management Agency (CalEMA), and the USGS, monitoring infrastructure was upgraded and expanded, combining resources in a federal, state and university partnership. In 2000, the integration effort expanded to the entire state with the formation of the California Integrated Seismic Network (CISN, see 2000-2001 Annual Report). To this end, UC Berkeley and the USGS Menlo Park and Pasadena offices joined forces with Caltech and the CGS. The CISN is now in the eleventh year of collaboration and its tenth year of funding from CalEMA.

2.2 CISN Background

Organization

The organizational goals, products, management, and responsibilities of the CISN member organizations are described in the founding memorandum of understanding and in the strategic and implementation plans. To facilitate activities among institutions, the CISN has three management centers:

- Southern California Earthquake Management Center: Caltech/USGS Pasadena
- Northern California Earthquake Management Center: UC Berkeley/USGS Menlo Park
- Engineering Strong Motion Data Center: California Geological Survey/USGS National Strong Motion Program

The Northern and Southern California Earthquake Management Centers operate as twin statewide earthquake processing centers, serving information on current earthquake activities, while the Engineering Strong Motion Data Center is responsible for producing engineering data products and distributing them to the engineering community.

The Steering Committee, made up of two representatives from each core institution and a representative from CalEMA, oversees CISN projects. The position of chair

rotates among the institutions; Ken Hudnut took over as chair of the Steering Committee in December 2010 from Barbara Romanowicz.

An external Advisory Committee represents the interests of structural engineers, seismologists, emergency managers, industry, government, and utilities, and provides review and oversight. The Advisory Committee is chaired by Loren Turner of Pacific Gas and Electric Company. It last met in October 2010. Agendas from the meetings and the resulting reports may be accessed through the CISN website (<http://www.cisn.org/advisory>).

The Steering Committee has commissioned other committees, including a Program Management Group to address planning and coordination and a Standards Committee to resolve technical design and implementation issues.

In addition to the core members, other organizations contribute data that enhance the capabilities of the CISN. Contributing members include: University of California, Santa Barbara; University of California, San Diego; University of Nevada, Reno; University of Washington; California Department of Water Resources; Lawrence Livermore National Lab; and Pacific Gas and Electric Company.

CISN and ANSS

The USGS Advanced National Seismic System (ANSS) has developed along a regionalized model. Eight regions have been organized, with the CISN representing California. David Oppenheimer of the USGS represents the CISN on the ANSS National Implementation Committee (NIC).

This year, the CISN is benefiting from the American Recovery and Reinvestment Act (ARRA). The ANSS has received funds from the ARRA to improve seismic monitoring throughout the nation and the world. In California, these funds are being directed toward replacing old data loggers in both Northern and Southern California, as well as improving installations at individual stations and adding strong motion sites in the form of NetQuakes sensors. The BSL's ARRA-funded activities are described in Operational Sections 1, 4 and 3.

As the ANSS moves forward, committees and working groups are established to address issues of interest. BSL faculty and staff have been involved in several working groups of the Technical Integration Committee, including Doug Dreger, Peggy Hellweg, Pete Lombard, Doug Neuhauser, Bob Uhrhammer, and Stephane Zuzlewski.

CISN and CalEMA

CalEMA has long had an interest in coordinated earthquake monitoring. The historical separation between Northern and Southern California and between strong-motion and weak-motion networks resulted in a complicated situation for earthquake response. Thus, CalEMA has been an advocate of increased coordination and collaboration in California earthquake monitoring and encouraged the development of the CISN. In FY 01-02, Governor Gray Davis requested support for the CISN, to be administered through CalEMA. Funding for the California Geological Survey, Caltech and UC Berkeley was made available in spring 2002, officially launching the statewide coordination efforts. Following the first year of funding, CalEMA support led to the establishment of 3-year contracts to UC Berkeley, Caltech, and the California Geological Survey for CISN activities. We have just completed the third year of the third three-year contract (2008-2011). Past CISN-related activities are described in previous annual reports.

2.3 2010-2011 Activities

We have just completed the second full year of operation in the NCEMC (Northern California Earthquake Management Center) with the new suite of earthquake monitoring software. In the past, we have called this system the CISN software. In 2008, it was adopted by the ANSS as the system to be used by the regional networks for their operations and earthquake reporting, and it is now called the ANSS Quake Monitoring System, or AQMS. As AQMS is rolled out to other regional networks, BSL staff members are providing information and software support to the operators of those networks. The NCEMC made the switch to the AQMS software package in June 2009, and the software is now operating at the BSL and in Menlo Park. CISN funding from CalEMA contributed to this transition, and has supported a number of other activities at the BSL during the past year as well.

Northern California Earthquake Management Center

As part of their effort within the CISN, the BSL and the USGS Menlo Park are operating the AQMS software as the Northern California joint earthquake information system. Operational Section 8 describes the operation of this system and reports on implementation progress.

For monitoring earthquakes in Northern California, the USGS Menlo Park and BSL have improved their communications infrastructure. The BSL and the USGS Menlo Park are currently connected by two dedicated T1 circuits. One circuit is a component of the CISN ring, while the second circuit was installed in 2004-2005 (Figure 3.11) to support dedicated traffic between Berkeley

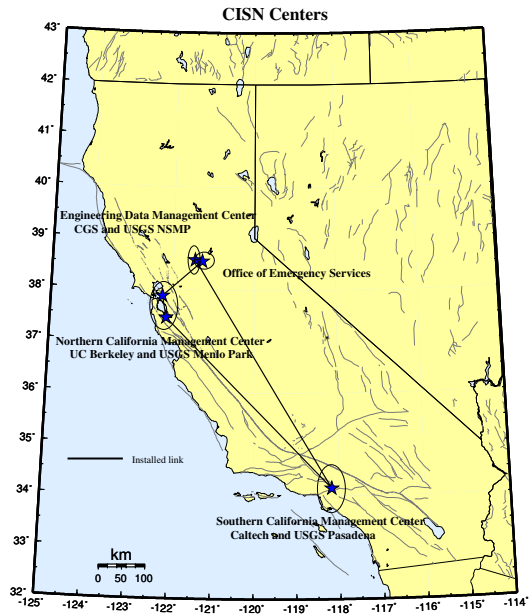


Figure 3.9: Map showing the geographical distribution of the CISN partners and centers. The communications “ring” is shown schematically with installed links (solid lines).

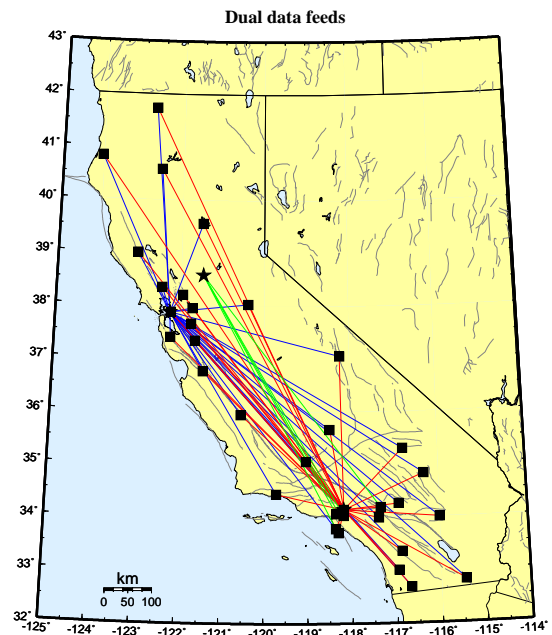


Figure 3.10: Map showing the 30 stations selected to send data directly to the Northern and Southern California processing centers, and the 5 stations that send data directly to the Engineering Data Center and the Southern California processing center.

and Menlo Park above and beyond that associated with the CISN.

The installation of the second dedicated T1 between Berkeley and Menlo Park freed up a frame-relay connection deployed by the BSL as part of the CalREN project in mid-1990s. The BSL now uses this frame-relay circuit as a second data acquisition link. BDSN data acquisition is distributed between two frame-relay T1 circuits, eliminating what had been a single point of failure. An additional Permanent Virtual Circuit (PVC) has also been implemented at each BDSN site so that each station has connections to both T1s. This has improved the robustness of data acquisition at the BSL by providing redundancy in the incoming circuit.

In the long term, the BSL and USGS Menlo Park hope to be connected by high-bandwidth microwave or satellite service. Unfortunately, we have not yet been able to obtain funding for such an additional communication link.

Statewide Integration

Despite the fact that AQMS software is now operating in both Northern and Southern California, efforts toward statewide integration continue. BSL staff are involved in many elements of these efforts. The Standards Committee, chaired by Doug Neuhauser, continues to define and prioritize projects important to the ongoing development and operation of the statewide earthquake processing system and to establish working groups to address them (see minutes from meetings and conference calls at <http://www.cisn.org/standards/meetings.html>).

Dual Station Feeds: Early in the existence of CISN, “dual station feeds” were established for 30 stations (15 in Northern California and 15 in Southern California) (Figure 3.10). Because of decreases in funding and other issues, Northern California now sends data from 13 stations to Southern California in real time, and Southern California sends data from 12 to Northern California. The Northern California Earthquake Management Center (NCEMC) is using data from the Southern California stations to estimate magnitudes on a routine basis. In addition, some of the stations are used in moment tensor inversions, a computation that is sensitive to the background noise level.

Data Exchange: Part of the AQMS software allows reduced amplitude timeseries to be produced and exchanged. Currently, these timeseries are being exchanged at the NCEMC, but not yet statewide. Using a common format, the CISN partners continue to exchange observations of peak ground motion with one another following an event or a trigger. This step increases the robustness of generating products such as ShakeMap, since all CISN partners now exchange data directly with one another. This also improves the quality of ShakeMaps for events on the boundary between Northern and Southern California, such as the San Simeon earthquake, by allowing all data to be combined in a single map. Finally, this is

a necessary step toward the goal of generating statewide ShakeMaps.

The Software Calibration & Standardization: CISN partners have calibrated and standardized much of the software used for automatic earthquake processing and earthquake review, now the AQMS software. The AQMS software now serves as the real-time system operating in the NCEMC. The transition was made in June 2009.

Local Magnitudes: Since the transition to the AQMS software in Northern California in June 2009, local magnitudes are calculated throughout the state using the new $\log A_o$ function and the associated station-specific corrections for broadband/strong motion stations, and also for strong-motion only stations. We are now focusing magnitude development on adding vertical components, whether short period or broadband, and short period horizontal components to the new local magnitude system. A final component of the magnitude efforts is the determination of a magnitude reporting hierarchy. For the near future, each region will continue to use its own preferences for magnitude reporting.

ShakeMap: At present, ShakeMaps are generated on five systems within the CISN. Two systems in Pasadena generate “SoCal” Shakemaps; two systems in the Bay area generate “NoCal” Shakemaps; and one system in Sacramento generates ShakeMaps for all of California. The Sacramento system uses EIDS (Earthquake Information Distribution System) to collect the authoritative event information for Northern and Southern California. In the CISN, we evaluated the new release of the program, ShakeMap 3.5. In early June, 2011, we finally made the transition to using ShakeMap 3.5 in production. We are now preparing to recalculate ShakeMaps for all events in the catalog.

A second goal is to improve the robustness of ShakeMap generation and delivery by taking advantage of the fact that ShakeMaps are generated in the Bay Area, Pasadena, and Sacramento.

Moment Tensor Analysis: We have implemented an upgraded version of the complete waveform moment tensor code. This version allows the calculation of full moment tensor solutions, including an isotropic element. In the real time system, only deviatoric solutions will be allowed, but a reviewer may “turn on” the capability to allow full solutions. Using this new package, we are recalculating moment tensors for earthquakes in the Geysers and Long Valley regions, which appeared anomalous using the deviatoric code (see Research Section 12).

Location Codes: The CISN adopted a standard for the use of “location” codes (part of the Standard for the Exchange of Earthquake Data [SEED] nomenclature to describe a timeseries based on station-network-channel-location) in the late fall of 2003. USGS and UC Berkeley developers modified the Earthworm software to support their use. After the transition at USGS Menlo Park away

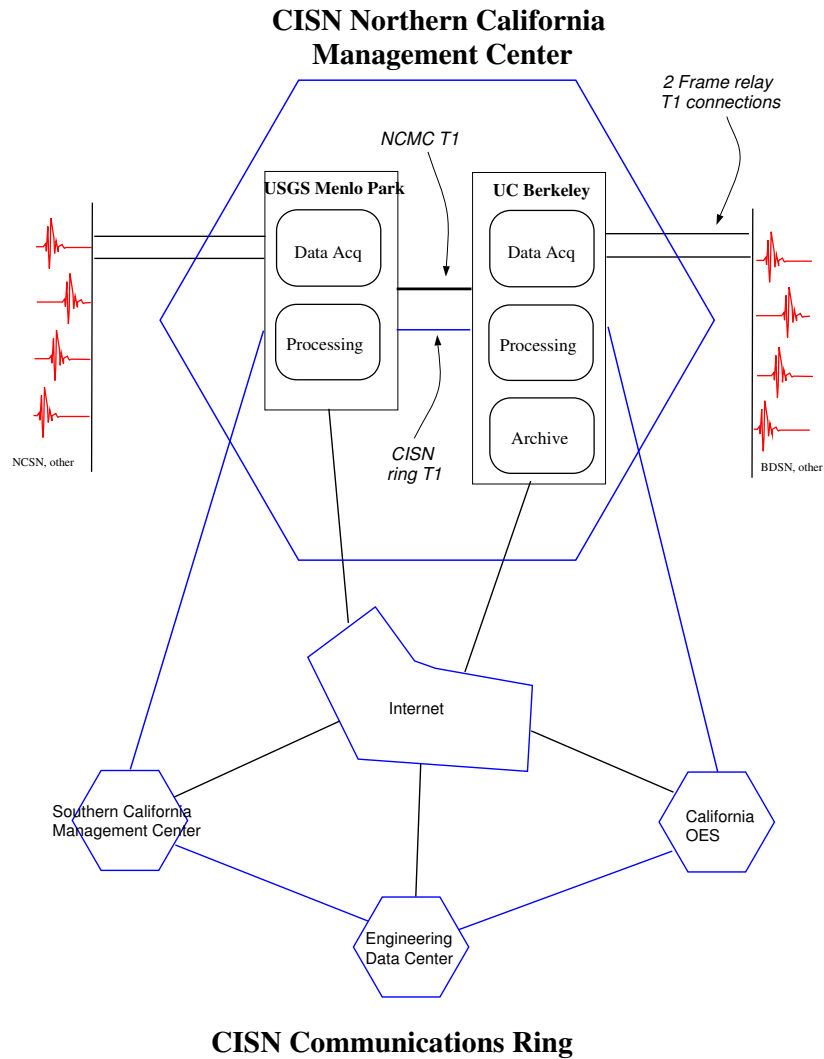


Figure 3.11: Schematic diagram illustrating the connectivity between the real-time processing systems at the USGS Menlo Park and UC Berkeley, forming the Northern California Management Center, and with other elements of the CISN.

from the CUSP analysis system to *Jiggle* in late November 2006, all networks in the CISN implemented location codes in their systems. During the past two years, as we deploy new data loggers using ARRA funding, we have begun the transition to non-blank location codes for the BDSN stations. When the data logger at a station is replaced with an ARRA-funded data logger, it receives the location code “00.” Borehole seismic stations will have the location code “40.”

Metadata Exchange: Correct metadata are vital to CISN activities, as they are necessary to ensure valid interpretation of data. CISN is working on issues related to their reliable and timely exchange. The CISN Metadata

Working Group compiled a list of metadata necessary for data processing and developed a model for their exchange. In this model, each CISN member is responsible for the metadata for its stations and for other stations that enter into CISN processing through it. For example, Menlo Park is responsible for the NSMP, Tremor, and PG&E stations, while Caltech is responsible for the Anza data. At the present time, dataless SEED volumes are used to exchange metadata between the NCEMC and the SCEMC. The Metadata Working Group is developing a Station XML format for metadata exchange. This vehicle is expandable, and will probably allow exchange of a more comprehensive set of metadata than dataless

SEED volumes, some of which may be necessary for other systems, for example in V0 formatted data.

Standardization: The CISN's focus on standardization of software continues. The complete system is now implemented and providing real-time earthquake information in the NCEMC (see Operational Section 8). The software is currently being implemented at other regional networks of the ANSS.

Earthquake Early Warning: Caltech, the BSL and the ETH Zurich have been using CISN data in real time to test earthquake early warning algorithms and to develop a prototype earthquake early warning system (see sections 1 and 2; see also <http://www.cisn.org/eew>). In the past year, we finally achieved end-to-end processing, with events being published to a user display.

CISN Display

CISN Display is an integrated Web-enabled earthquake notification system designed to provide earthquake information for emergency response at 24/7 operations centers. First responders, organizations with critical lifelines and infrastructure, and emergency responders are invited to register for an account at <http://www.cisn.org/software/cisndisplay.htm>.

The application provides users with maps of real-time seismicity and automatically provides access to Web-related earthquake products such as ShakeMaps. CISN Display also offers an open source GIS mapping tool that allows users to plot freely available layers of public highways, roads and bridges, as well as private layers of organizational-specific infrastructure and facilities information. The current version of CISN Display is 1.4. Its primary enhancement over the previous version is the development of a kiosk mode for public display purposes.

Earthquake Information Distribution

The USGS hosted a workshop in October 2004 to develop plans for the installation and use of the EIDS software. Doug Neuhauser and Pete Lombard participated in this workshop, which resulted in a document outlining the steps necessary for the installation and migration of the earthquake notification system from the current Quake Data Distribution Services (QDDS) to EIDS. The NCEMC uses the EIDS system for publishing earthquake information. In the meantime, the USGS has developed a new tool, the Product Distribution Layer (PDL), for transferring so-called add-on information, such as ShakeMaps. The BSL has had a test PDL system running for several months. In June, 2011, it became the production means of transferring ShakeMaps from Northern California to the USGS.

Outreach

Since FY 05-06, the CISN website (www.cisn.org) has been supported by two servers located at Berkeley and Caltech. The Web servers were set up so that the load could be distributed between them, providing improved access during times of high demand. With these servers, the CISN provided access to certain earthquake products directly from www.cisn.org. For example, ShakeMaps are now served directly from the CISN website, in addition to being available from several USGS Web servers and the CGS. The design and content of <http://www.cisn.org> continues to evolve. The website is an important tool for CISN outreach as well as for communication and documentation among the CISN partners.

The CISN supports a dedicated website for emergency managers. This website provides personalized access to earthquake information. Known as "myCISN," the website is available at eoc.cisn.org. To provide highly reliable access, the website is limited to registered users.

As part of the CISN, the BSL contributes each year to efforts to raise awareness of earthquakes and earthquake preparedness. The BSL is a member of the Earthquake Country Alliance, a state-wide organization of people, institutions and agencies associated with earthquake response and research. In the past year, we publicized the state-wide ShakeOut on October 21, 2010 and participated in it. We are now working toward the statewide California ShakeOut on October 20, 2011 at 10:20 (see <http://www.shakeout.org> for more information and to sign up).

2.4 Acknowledgements

CISN activities at the BSL are supported by funding from the California Emergency Management Agency, CalEMA.

Barbara Romanowicz and Peggy Hellweg are members of the CISN Steering Committee. Peggy Hellweg is a member of the CISN Program Management Group, and she leads the CISN project at the BSL with support from Doug Neuhauser. Doug Neuhauser is chair of the CISN Standards Committee, which includes Peggy Hellweg, Pete Lombard, Taka'aki Taira, and Stephane Zuzulewski as members.

Because of the breadth of the CISN project, many BSL staff members have been involved, including: Aaron Enright, John Friday, Jarrett Gardner, Peggy Hellweg, Ivan Henson, Bill Karavas, Oleg Khainovski, Rick Lellinger, Pete Lombard, Joshua Miller, Doug Neuhauser, Charley Paffenbarger, Taka'aki Taira, Stephen Thompson, Bob Uhrhammer, and Stephane Zuzulewski. Peggy Hellweg contributed to this section. Additional information about the CISN is available through reports from the Program Management Group.

3 Northern Hayward Fault Network

3.1 Introduction

Complementary to the regional surface broadband and short-period networks, the Hayward Fault Network (HFN) (Figure 3.12 and Table 3.5) is a deployment of borehole-installed, wide-dynamic range seismographic stations along the Hayward Fault and throughout the San Francisco Bay toll bridges system. Development of the HFN initiated through a cooperative effort between the BSL (Berkeley Seismological Laboratory) and the USGS, with support from the USGS, Caltrans, EPRI, the University of California Campus/Laboratory Collaboration (CLC) program, LLNL (Lawrence Livermore National Laboratory), and LBNL (Lawrence Berkeley National Laboratory). The project's objectives included an initial characterization phase followed by a longer-term monitoring effort using a backbone of stations from among the initial characterization station set. Subsequent funding from Caltrans, however, has in the past allowed for some continued expansion of the backbone station set for additional coverage in critical locations.

The HFN consists of two components. The Northern Hayward Fault Network (NHFN), operated by the BSL, consists of 29 stations in various stages of development and operation. These include stations located on Bay Area bridges, at free-field locations, and now at sites of the Mini-PBO (mPBO) project (installed with support from NSF and the member institutions of the mPBO project). The NHFN is considered part of the Berkeley Digital Seismic Network (BDSN) and uses the network code BK. The Southern Hayward Fault Network (SHFN) is operated by the USGS and currently consists of 5 stations. This network is considered part of the Northern California Seismic Network (NCSN) and uses the network code NC. The purpose of the HFN is fourfold: 1) to contribute operational data to California real-time seismic monitoring for response applications and the collection of basic data for long-term hazards mitigation; 2) to increase substantially the sensitivity of seismic data to low amplitude seismic signals; 3) to increase the recorded bandwidth for seismic events along the Hayward fault; and 4) to obtain deep bedrock ground motion signals at the bridges from more frequent, small to moderate sized earthquakes.

In addition to the NHFN's contribution to real-time seismic monitoring in California, the mix of deep NHFN sites at near- and far- field sites and the high-sensitivity (high signal to noise), high-frequency broadband velocity and acceleration data recorded by the NHFN also contributes significantly to a variety of scientific objectives, including: a) investigating bridge responses to deep strong ground motion signals from real earthquakes; b)

obtaining a significantly lower detection threshold for microearthquakes and possible non-volcanic tremor signals in a noisy urban environment; c) increasing the resolution of the fault-zone seismic structure (e.g., in the vicinity of the Rodgers Creek/Hayward Fault step over); d) improving monitoring of spatial and temporal evolution of background and repeating seismicity (to magnitudes below $M \sim 0.0$) that may signal behavior indicative of the nucleation of large, damaging earthquakes and to infer regions and rates of deep fault slip and slip deficit accumulation; e) investigating earthquake scaling, physics, and related fault processes; f) improving working models for the Hayward fault; and g) using these models to make source-specific response calculations for estimating strong ground shaking throughout the Bay Area.

Below, we focus primarily on activities associated with BSL operations of the NHFN component of the HFN.

3.2 NHFN Overview

The initial characterization period of HFN development ended in 1997. During that period, the NHFN sensors initially provided signals to on-site, stand-alone Quanterra Q730 and RefTek 72A-07 data loggers, and manual retrieval and download of data tapes was required. Also during the characterization period, the long-term monitoring phase of the project began involving the gradual transition of backbone monitoring sites to 24-bit data acquisition and communication platforms and data telemetry to the BSL.

Over the years, Caltrans has provided additional support for the upgrade of some non-backbone sites to backbone operational status and for the addition of several entirely new sites into the monitoring backbone. Efforts at continued expansion are ongoing. In February of 2007, the stations of the mPBO project were also folded into the NHFN monitoring scheme, increasing the NHFN by five sites.

Of the 29 stations considered part of the NHFN history, none (E17B, E07B, YBAB, W05B, SAFB, SM1B, DB1B, DB2B, DB3B) are non-backbone stations and were not originally envisioned as long-term monitoring stations. Because the borehole sensor packages at these sites could not be retrieved (having been grouted in downhole), the sites were mothballed for possible future reactivation. Support for reactivation of two of these mothballed sites (W05B and E07B) was eventually forthcoming and their reactivation is currently in progress. Efforts at acquiring funds for reactivation/upgrade of additional mothballed sites are ongoing.

Fifteen of the remaining 20 stations are currently operational (VALB, PETB, CMAB, HERB, BRIB, RFSB, CMSB, SM2B, W02B, RB2B, SVIN, OHLN, MHDL,

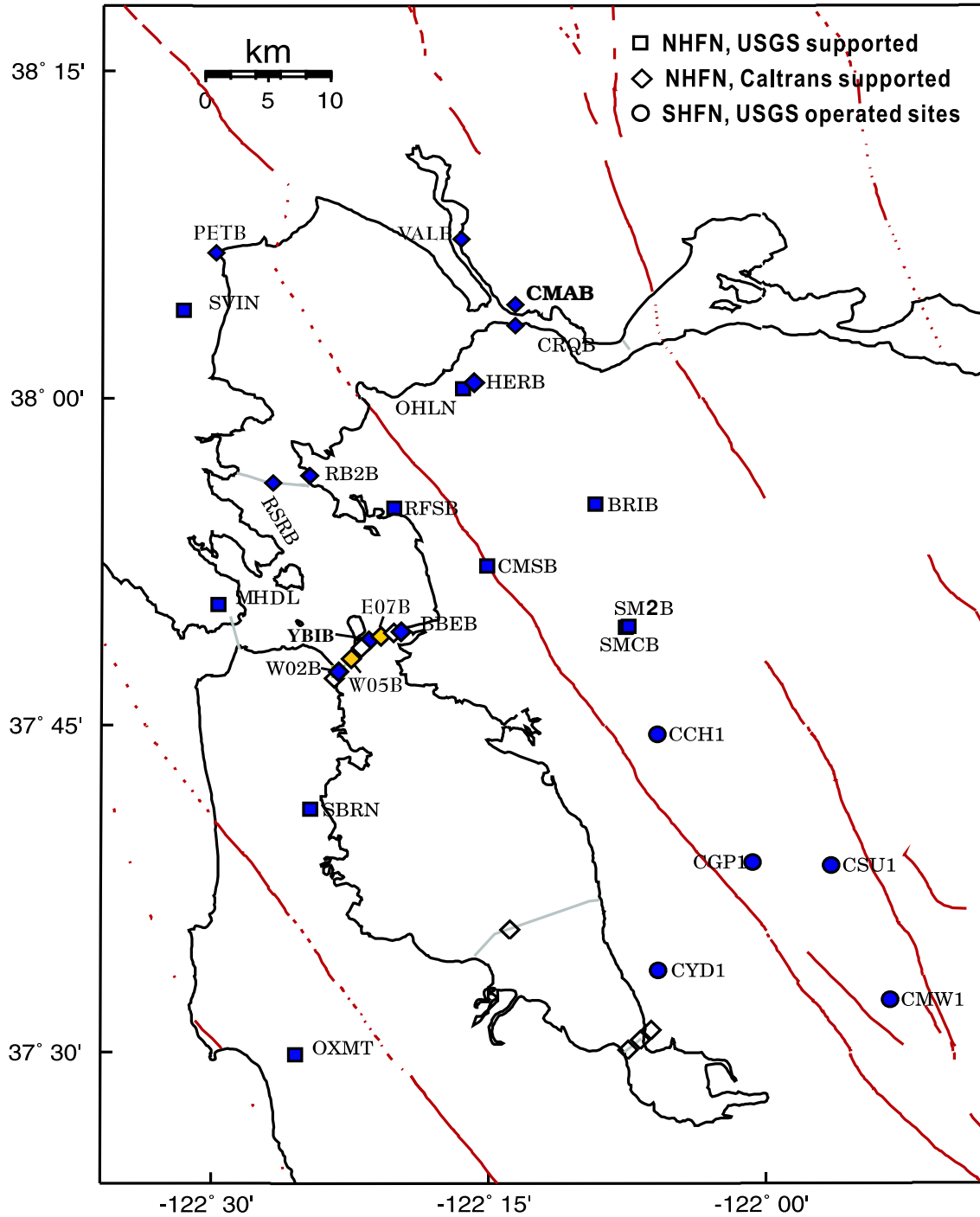


Figure 3.12: Map showing the locations of the HFN stations operated by the BSL (NHFN - squares and diamonds) and the USGS (SHFN - circles). Current and previously active NHFN and SHFN monitoring sites (i.e., those with data archived at the NCEDC) are filled blue/black. Sites CRQB and SMCB have been decommissioned in favor of replacement sites (CMAB and SM2B, respectively) with higher quality data. Previously recorded data at sites RSRB, BBEB (resulting from retrofit work on the Richmond-San Rafael and Bay bridges) and YBIB is also available at the NCEDC. Sites in progress (E07B and W05B) are yellow/grey. Other instrumented but currently non-operational boreholes are indicated as open symbols. Currently, station BBEB operates only as a telemetry repeater site because access to the borehole was cut off during seismic retrofit work on the eastern span of the Bay Bridge.

Sensor	Channel	Rate (sps)	Mode	FIR
Accelerometer	CL?	500.0	T	Ca
Accelerometer	CN?	500.0	T	Ca
Accelerometer	HL?	200.0	C	Ca
Accelerometer	HL?	100.0	C	Ca
Accelerometer	HN?	200.0	C	Ca
Accelerometer	BL?	20.0	C	Ac
Accelerometer	BN?	20.0	C	Ac
Accelerometer	LL?	1.0	C	Ac
Accelerometer	LN?	1.0	C	Ac
Geophone	DP?	500.0	T,C	Ca
Geophone	EP?	200.0	C	Ca
Geophone	EP?	100.0	C	Ca
Geophone	BP?	20.0	C	Ac
Geophone	SP?	20.0	C	Ac
Geophone	LP?	1.0	C	Ac

Table 3.7: Typical data streams acquired at NHFN sites, with channel name, sampling rate, sampling mode, and FIR filter type. C indicates continuous, T triggered, Ca causal, and Ac acausal. Typically, the DP1 continuous channel is archived and the remaining high sample rate data (i.e., CL?, CN?, DP2 and DP3 channels) are archived as triggered snippets. As telemetry options improve, progress is being made towards archiving higher sample rate and continuous data on more channels. Prior to September 2004, only triggered data was archived for all high sample rate channels. Of the stations that are currently operational, CMAB, HERB, BRIB, RFSB, CMSB, SM2B, W02B, and RB2B record at maximum sample rates of 500 Hz; VALB and PETB at maximum 200 Hz and mPBO sites (SVIN, OHLN, MHDL, SBRN, OXMT) at maximum 100 Hz.

SBRN, OXMT), though operation of one of the sites (CMSB) has been temporarily suspended pending completion of construction at U.C. Berkeley’s Cal Memorial Stadium. These include the five stations folded in from the mPBO project. These 15 sites telemeter seismic data streams continuously into the BSL’s BDSN processing stream with subsequent archival in the Northern California Earthquake Data Center (NCEDC).

The five remaining stations have been decommissioned for various reasons ranging from the sites’ replacement with near-by higher quality installations (SMCB, CRQB, RSRB) to irreparable site damage by outside influences such as bridge retrofit activity and construction (BBEB, YBIB). Station BBEB, however, continues to operate as a telemetry relay site.

Installation/Instrumentation: The NHFN Sensor packages are generally installed at depths ranging between 100 and 200 m, the non-backbone, non-operational Dumbarton bridge sites being exceptions with sensors at

multiple depths (Table 3.5).

The five former mPBO sites that are now part of the NHFN have 3-component borehole geophone packages. Velocity measurements for the mPBO sites are provided by Mark Products L-22 2 Hz geophones (Table 3.6). All the remaining backbone and non-backbone NHFN sites have six-component borehole sensor packages. The six-component packages were designed and fabricated at LBNL’s Geophysical Measurement Facility and have three channels of acceleration, provided by Wilcoxon 731A piezoelectric accelerometers, and three channels of velocity, provided by Oyo HS-1 4.5 Hz geophones.

The 0.1-400 Hz Wilcoxon accelerometers have lower self-noise than the geophones above about 25-30 Hz, and remain on scale and linear to 0.5 g. In tests performed in the Byerly vault at UC Berkeley, the Wilcoxon is considerably quieter than the FBA-23 at all periods, and is almost as quiet as the STS-2 between 1 and 50 Hz.

Currently seven of the currently operational NHFN backbone sites have Quanterra data loggers, and eight of the operational sites have been upgraded with BASALT data loggers this year. All 15 of these sites telemeter continuously to the BSL, with the exception of CMSB which is temporarily off-line. Signals from these stations are digitized at a variety of data rates up to 500 Hz at 24-bit resolution (Table 3.7). The data loggers employ causal FIR filters at high data rates and acausal FIR filters at lower data rates (see: Table 3.5).

Data Rates and Channels: Because of limitations in telemetry bandwidth and local disk storage, 7 of the 10 (excluding CMAB, VALB and PETB) six-component NHFN stations transmit maximum 500 Hz data continuously on only 1 channel of geophone data (i.e., when operational, their vertical geophone channel). Triggered 500 Hz data for 3 additional channels with 180 second snippets are also transmitted. Station VALB also transmits data from only four channels; however, continuous data for all four channels are transmitted at a maximum of 200 Hz sampling. PETB transmits maximum 200 Hz data continuously on all six channels (three geophone, three accelerometer), and CMAB transmits maximum 500 Hz data continuously on all six channels. Continuous data for the channels of all 10 of these stations are also transmitted to the BSL at reduced sampling rates (20 and 1 sps). A Murdock, Hutt, and Halbert (MHH) event detection algorithm (Murdock and Hutt, 1983) is operated independently at each station on 500 sps data for trigger determinations. Because the accelerometer data is generally quieter, the MHH detections are made locally using data from the Wilcoxon accelerometers when possible. However, there is a tendency for these powered sensors to fail, and, in such cases, geophone channels are substituted for the

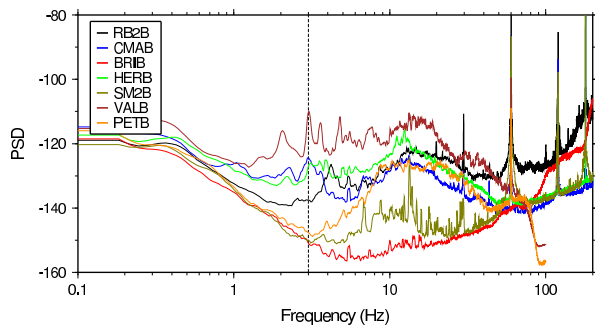


Figure 3.13: See caption for Figure 3.14.

failed accelerometers. The five mPBO-originated sites all transmit their three-component continuous geophone data streams to the BSL at 100, 20, and 1 sps.

Integration with the NCSS, SeisNetWatch, and SeismicQuery: The NHFN is primarily a research network that complements regional surface networks by providing downhole recordings of very low amplitude seismic signals (e.g., from micro-earthquakes or non-volcanic tremor) at high gain and low noise. Nonetheless, data streams from the NHFN are also integrated into the Northern California Seismic System (NCSS) real-time/automated processing stream for response applications and collection of basic data for long-term hazards mitigation. The NCSS is a joint USGS (Menlo Park) and Berkeley Seismological Laboratory (BSL) entity with earthquake reporting responsibility for Northern California, and data from networks operated by both institutions are processed jointly to fulfill this responsibility.

Through this integration, the NHFN picks, waveforms, and NCSS event locations and magnitudes are automatically entered into a database where they are immediately available to the public through the NCEDC and its DART (Data Available in Real Time) buffer. The capability for monitoring state of health information for all NHFN stations using SeisNetWatch has also now been added, and up-to-date dataless SEED formatted metadata is now made available by the NCEDC with the SeismicQuery software tool.

Station Maintenance

Ongoing network maintenance involves regular inspection of the collected seismic waveform data and spectra of nearby seismic events, and also of noise samples. Other common problems include changes to background noise levels due to ground loops and failing preamps, as well as power and telemetry issues. Troubleshooting and remediation of problems often benefit from a coordinated

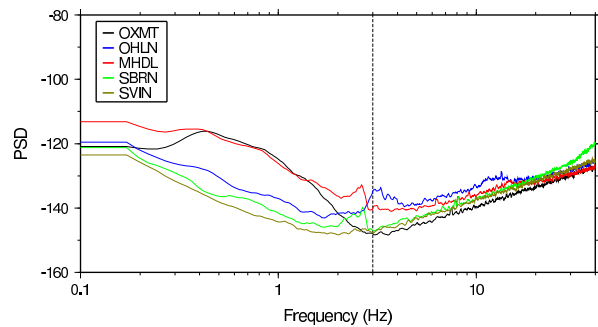


Figure 3.14: Plot showing typically observed background noise PSD for the vertical DP1 channels of the NHFN borehole stations as a function of frequency. The data are for a 1000 sec period on January 1, 2011 beginning at 01:00 (AM) local time. The PSD ranking (lowest to highest) of the non-mPBO stations (top panel) in operation at the time given at 3 Hz (near minimum PSD for most NHFN stations) is:

BRIB.BK.DP1 -150.774
 SM2B.BK.DP1 -150.110
 PETB.BK.EP1 -147.577
 RB2B.BK.DP1 -137.457
 HERB.BK.DP1 -127.471
 CMAB.BK.DP1 -124.355
 VALB.BK.EP1 -110.195

PSD ranking (lowest to highest) for the EP1 channels of the 5 mPBO stations (lower panel) at the time given at 3 Hz) is:

OXMT.BK.EP1 -148.042
 SVIN.BK.EP1 -147.730
 SBRN.BK.EP1 -146.937
 MHDL.BK.EP1 -140.137
 OHLN.BK.EP1 -134.722

Note that there is considerable variation in the general level and structure of the individual station background noise PSD estimates. For example the signals from many of the non-mPBO stations have 60 Hz noise (sometimes accompanied by 120 and 180 Hz harmonics), which is indicative of the presence of ground loops that need to be addressed. If noise spikes at the mPBO stations exist, it is not recorded due to the lower sampling rate of these data. Variations in PSD noise among the stations are also sometimes attributable to the stations' proximity to different cultural noise sources such as freeways or train-tracks, differences in depth of sensor installation, or to differences in local geologic conditions.

effort, with a technician at the BSL examining seismic waveforms and spectra while the field technicians are still on site. BSL technicians and researchers regularly review data and assist in troubleshooting.

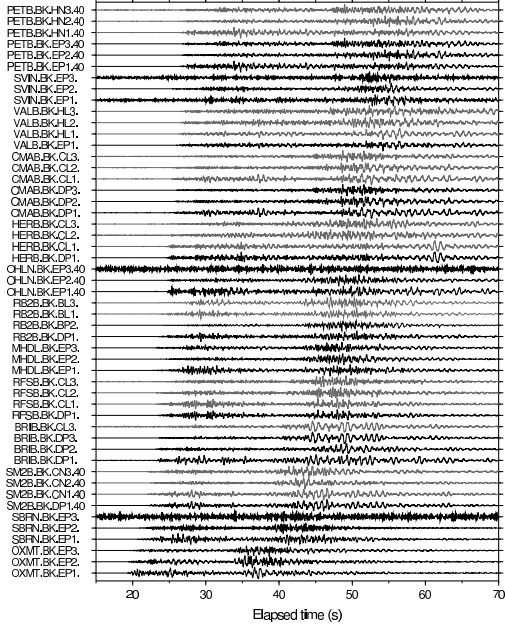


Figure 3.15: Plot of ground accelerations recorded on the geophones (black lines) and accelerometers (gray lines) of the 13 NHFN borehole stations in operation at the time of a recent Bay Area earthquake (12 January 2011, M_w 4.5 near San Juan Bautista, CA). The traces are filtered with a 1-8 Hz bandpass filter, scaled by their maximum values, and ordered from bottom to top by distance from the epicenter.

The NHFN station hardware has proven to be relatively reliable. Nonetheless, numerous maintenance and performance enhancement measures are still carried out. In particular, when a new station is added to the backbone, extensive testing and correction for sources of instrumental noise (e.g., grounding related issues) and telemetry through-put are carried out to optimize the sensitivity of the station. Examples of maintenance and enhancement measures that are typically performed include: 1) testing of radio links to ascertain reasons for unusually large numbers of dropped packets; 2) troubleshooting sporadic problems with numerous frame relay telemetry dropouts; 3) manual power recycle and testing of hung Quanterra data loggers; 4) replacing blown fuses or other problems relating to dead channels identified through remote monitoring at the BSL; 5) repairing frame relay and power supply problems when they arise; and 6) correcting problems that arise due to various causes, such as weather or cultural activity.

Quality Control

Power Spectral Density Analyses: One commonly used quality check on the performance of the borehole installed network includes assessment of the power spectral density (PSD) distributions of background noise. Figures

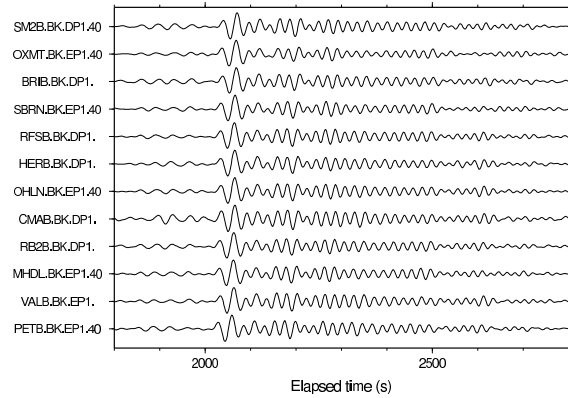


Figure 3.16: Plot of surface wave seismograms of the teleseismic M_w 9.0 earthquake near the east coast of Honshu, Japan (Lat.: 38.322N; Lon.: 142.369E; depth 32 km) occurring on March 11, 2011 at 05:46:23 (UTC) recorded on the DP1/EP1 (vertical) channels of the 12 NHFN and mPBO borehole stations in operation at the time. Here, vertical component geophone (velocity) data have been 0.02-0.05 Hz bandpass filtered and normalized by their maximum amplitudes.

3.13 and 3.14 show PSDs of background noise for vertical geophone components of the 12 NHFN stations operating at the time.

By periodically generating such plots, we can rapidly evaluate the network's recording of seismic signals across the wide high-frequency spectrum of the borehole NHFN sensors. Changes in the responses often indicate problems with the power, telemetry, or acquisition systems or with changing conditions in the vicinity of station installations that are adversely affecting the quality of the recorded seismograms. In general, background noise levels of the borehole NHFN stations are more variable and generally higher than those of the Parkfield HRSN borehole stations (see Parkfield Borehole Network section). This is due in large part to the significantly greater cultural noise in the Bay Area and the siting of several near-field NHFN sites in proximity to bridges.

On average, the mPBO component of the NHFN sites is more consistent and somewhat quieter. This is due in large part to the greater average depth of the mPBO sensors, the locations of mPBO stations in regions with generally less industrial and other cultural noise sources, and possibly to the absence of powered sensors (i.e. accelerometers) in their borehole sensor packages.

One of the most pervasive problems at NHFN stations is power line noise (60 Hz and its harmonics at 120 and 180 Hz). This noise reduces the sensitivity of the MHH detectors and can corrupt research based on full waveform analyses. When NHFN stations are visited, the engineer at the site and a seismologist at the BSL frequently

work together to identify and correct ground-loop problems, which often generate 60, 120, and 180 Hz contamination from inductively coupled power line signals.

Real Event Displays: Another method for rapid assessment of network performance is to generate and evaluate the seismograms from moderate local and large teleseismic earthquakes recorded by the NHFN stations. This is an essential component of NHFN operations because the seismic data from local, regional, and teleseismic events is telemetered directly to the BSL and made available to the Northern California Seismic System (NCSS) real-time/automated processing stream for seismic response applications within a few seconds of being recorded by the NHFN.

Shown in Figure 3.15 is an example display of NHFN geophone and accelerometer channels for a recent local Bay Area earthquake (12 January 2011, M_w 4.5 near San Juan Bautista, CA). It is immediately apparent from this simple display that the some components of stations OHLN, SVIN, and SBRN were in need of attention by field personnel.

Figure 3.16 shows seismograms of the recent teleseismic M_w 9.0 earthquake of March 11, 2011 05:46:23 (UTC) occurring offshore near the east coast of Honshu, Japan (Lat.: 38.322N; Lon.: 142.369E; Depth 32 km). On this date and for this frequency band (0.02-0.05 Hz), network performance appears good for the vertical (DP1 and EP1) channels of the 12 stations in operation at the time; however, an additional four sites did not record this event, for various reasons, and had to be visited by field personnel. Figures 3.15 and 3.16 serve to illustrate the value of routine evaluation of both local (higher frequency) and teleseismic (lower frequency) events when monitoring the state of health of the NHFN.

Owing to their near similar source-receiver paths, signals from teleseismic events also serve as a good source for examining the relative responses of the BK borehole network station/components to seismic ground motion, after correction for differences in instrument response among the stations. By rapidly generating such plots (particularly with correction for instrument response) following large teleseismic events, quick assessment of the NHFN seismometer responses to real events is easily done and corrective measures implemented with relatively little delay.

3.3 2010-2011 Activities

As in every year, routine maintenance, operations, quality control, and data collection have played an important part in our activities. In addition this year, we are fortunate to have received funds and government furnished equipment (GFE) data loggers to update equipment and improve station infrastructure from an American Recovery and Reinvestment Act award from the USGS. So far this year the equipment has been used

to upgrade data loggers at eight stations, including the mPBO stations. In addition, some maintenance activities were also funded by the award.

Other NHFN project activities have included: a) efforts to obtain additional funds for future upgrade and expansion of the network; b) leveraging NHFN activities through partnerships with various institutions outside of BSL; c) network adaptations to compensate for changing conditions associated with retrofit work on Bay Area bridges; and d) new station additions and network expansion efforts.

Additional Funding

Operation of this Bay Area borehole network is funded by the Advanced National Seismic System (ANSS) and through a partnership with the California Department of Transportation (Caltrans). ANSS provides operations and maintenance (O&M) support for a fixed subset of nine operational stations that were initiated as part of previous projects in which the USGS was a participant. Caltrans has in the past provided support for development and O&M for the remaining stations that have been added to the network Caltrans partnership grants. Caltrans has also provided additional support for upgrade and expansion when possible.

Due to the State budget crisis, Caltrans has been reviewing and modifying its financial commitments and its accounting practices relating to its funding of external projects, such as the NHFN project. Over the past two years, this has severely complicated efforts to receive previously approved NHFN funding from Caltrans, and has imposed many additional administrative road-blocks to acquiring additional Caltrans support. In June of last year, our team held two meetings at Berkeley with our Caltrans contact and made a presentation at Caltrans in Sacramento to argue against O&M funding reductions and for further upgrade and expansion of the NHFN. These efforts resulted in a request by Caltrans for a proposal to install surface instruments at up to six of our borehole installations and to reactivate three currently mothballed NHFN sites. We submitted our proposal in September of 2010. Subsequently, a reduction in the Caltrans budget for external support resulted in a request from Caltrans for us to reduce the scope of the proposal we submitted. We promptly responded to this request and tentative approval was promised. Funding was held up for several months, however, by bureaucratic concerns and haggling between the University of California and Caltrans over proper/acceptable formats for budgets and proposal documentation. At this time, these roadblocks have apparently been worked out, the reformatted documentation has been submitted, and we are expecting formal approval for future funding in the near future.

Unfortunately, these delays have put on hold much of our work at maintaining, improving and expanding

the Caltrans supported component of the NHFN, so that progress in this area this year has been limited.

Partnerships

The NHFN is heavily leveraged through partnerships with various institutions, and we have continued to nurture and expand these relationships. Over the past year, we have continued our collaborative partnerships with the USGS, St. Mary's College, and the Cal Maritime Academy, and we have continued to strive for ongoing collaboration with Caltrans. In addition, we and the BSL more generally have continued to coordinate with Lawrence Berkeley National Laboratory (LBNL) in their project to develop an LBNL array of borehole stations that have placement with our existing NHFN borehole stations.

3.4 Acknowledgments

Thomas V. McEvelly, who passed away in February 2002, was instrumental in developing the Hayward Fault Network, and, without his dedication and hard work, the creation and continued operation of the NHFN would not have been possible.

Under Robert Nadeau's and Doug Dreger's general supervision, Bill Karavas, Doug Neuhauser, Bob Uhrhammer, John Friday, and Taka'aki Taira, all contribute to the operation of the NHFN. Robert Nadeau prepared this section with help from Taka'aki Taira.

Support for the NHFN this year was provided by the USGS through the cooperative networks grant program (grant number G10AC00093). The ARRA award to support maintenance and equipment upgrades at the USGS-supported NHFN stations is USGS grant number G09AC00487. Over the years, Pat Hipley of Caltrans has been instrumental in the effort to continue to upgrade and expand the network. Larry Hutchings and William Foxall of LLNL have also been important collaborators on the project in past years.

3.5 References

Rodgers, P.W., A.J. Martin, M.C. Robertson, M.M. Hsu, and D.B. Harris, Signal-Coil Calibration of Electromagnetic Seismometers, *Bull. Seism. Soc. Am.*, 85(3), 845-850, 1995.

Murdock, J. and C. Hutt, A new event detector designed for the Seismic Research Observatories, *USGS Open-File-Report 83-0785*, 39 pages, 1983.

Code	Net	Latitude	Longitude	Elev (m)	Over (m)	Date	Location
VALB	BK	38.12150	-122.27530	-24.5	155.8	2005/11 - current	Napa River Bridge
PETB	BK	38.11890	-122.50110	-30.0	113.0	2010/09 - current	Petaluma River Bridge
CMAB	BK	38.06892	-122.22914	0.0	142.2	2009/12 - current	Cal Maritime Academy
CRQB	BK	38.05578	-122.22487	-25.0	38.4	1996/07 - 2010/05	CB
HERB	BK	38.01239	-122.26217	-18.0	217.0	2001/09 - current	Hercules
BRIB	BK	37.91886	-122.15179	222.2	108.8	1995/07 - current	BR, Orinda
RFSB	BK	37.91608	-122.33610	-27.3	91.4	1996/02 - current	RFS, Richmond
CMSB	BK	37.87195	-122.25168	94.7	167.6	1995/06 - current	CMS, Berkeley
SMCB	BK	37.83881	-122.11159	180.9	3.4	1998/02 - 2007/06	SMC, Moraga
SM2B	BK	37.83874	-122.11022	200.0	150.9	2007/06 - current	SMC, Moraga
SVIN	BK	38.03318	-122.52632	-27.5	152.4	2003/08 - current	mPBO, St. Vincent's school
OHLN	BK	38.00625	-122.27299	-0.5	196.7	2001/11 - current	mPBO, Ohlone Park
MHDL	BK	37.84232	-122.49431	94.5	151.9	2006/05 - current	mPBO, Marin Headlands
SBRN	BK	37.68561	-122.41127	4.0	161.5	2002/08 - current	mPBO, San Bruno Mtn.
OXMT	BK	37.49936	-122.42431	209.1	194.3	2003/12 - current	mPBO, Ox Mtn.
BBEB	BK	37.82160	-122.32975	-30.8	182.9	2002/09 - 2007/11	BB, Pier E23
E17B	BK	37.82086	-122.33534	TBD	160.0	1995/08 - unknown *	BB, Pier E17
E07B	BK	37.81847	-122.34688	TBD	134.0	1996/02 - unknown +	BB, Pier E7
YBIB	BK	37.81420	-122.35923	-27.0	61.0	1996/07 - 2000/08	BB, Pier E2
YBAB	BK	37.80940	-122.36450	TBD	3.0	1998/06 - unknown *	BB, YB Anchorage
W05B	BK	37.80100	-122.37370	TBD	36.3	1997/10 - unknown +	BB, Pier W5
W02B	BK	37.79112	-122.38632	-45.0	57.6	2003/06 - current	BB, Pier W2
SFAB	BK	37.78610	-122.38930	TBD	0.0	1998/06 - unknown *	BB, SF Anchorage
RSRB	BK	37.93575	-122.44648	-48.0	109.0	1997/06 - 2001/04	RSRB, Pier 34
RB2B	BK	37.93335	-122.40314	-18.0	133.5	2009/12 - current	RSRB, Pier 58
SM1B	BK	37.59403	-122.23242	TBD	298.0	not recorded *	SMB, Pier 343
DB3B	BK	37.51295	-122.10857	TBD	1.5	1994/09 - 1994/11 *	DB, Pier 44
					62.5	1994/09 - 1994/09 *	
					157.9	1994/07 - unknown *	
DB2B	BK	37.50687	-122.11566	TBD		1994/07 - unknown *	DB, Pier 27
					189.2	1992/07 - 1992/11 *	
DB1B	BK	37.49947	-122.12755	TBD	0.0	1994/07 - 1994/09 *	DB, Pier 1
					1.5	1994/09 - 1994/09 *	
					71.6	1994/09 - 1994/09 *	
					228.0	1993/08 - unknown *	
CCH1	NC	37.74332	-122.09657	345.0	119.0	1995/06 - current	Chabot
CGP1	NC	37.64545	-122.01128	461.0	121.0	1995/06 - current	Garin Park
CSU1	NC	37.64303	-121.94020	623.0	124.0	1995/11 - current	Sunol
CYD1	NC	37.56289	-122.09670	114.0	137.0	1996/11 - current	Coyote
CMW1	NC	37.54053	-121.88743	498.0	155.0	1995/06 - current	Mill Creek

Table 3.5: Stations of the Hayward Fault Network. Each HFN station is listed with its station code, network id, location, period of available monitoring data, and site description. For entries with "*" and "+" in the date column, no monitoring data is available. For these sites, dates indicate periods of operation during which data was downloaded manually. The manually retrieved data from these stations are not available at the NCEDC, but may be available upon request from Larry Hutchings (now at LBNL). The latitude and longitude (in degrees) are given in the WGS84 reference frame. The elevation of the well head (in meters) is relative to the WGS84 reference ellipsoid. The overburden (depth of sensor package below surface) is given in meters. Abbreviations are: TBD - to be determined; BB - Bay Bridge; BR - Briones Reserve; CMS - Cal Memorial Stadium; CB - Carquinez Bridge; DB - Dumbarton Bridge; mPBO - Mini-Plate Boundary Observatory; RFS - Richmond Field Station; RSRB - Richmond-San Rafael Bridge; SF - San Francisco; SMB - San Mateo Bridge; SMC - St. Mary's College; and YB - Yerba Buena. At the end of the initial characterization phase of the HFN project, the stations labeled with "*" were mothballed with their borehole sensors remaining cemented in place. Incorporation of the "+" stations into the NHFN monitoring backbone is work in progress. A proposal submitted to Caltrans requesting support to bring several more of the mothballed sites into the NHFN backbone is pending. Note that due to Bay Bridge retrofit work, station BBEB no longer records seismic data but continues to operate as a telemetry relay station. Data collection at site CMSB has also been suspended temporarily this year to accommodate construction at Cal Memorial Stadium on the UC Berkeley campus.

Site	Geophone	Accelerometer	Z	H1	H2	data logger	Notes	Telem.
VALB	Oyo HS-1	Wilcoxon 731A	-90	336	246	Q330		FR
PETB	Oyo HS-1	Wilcoxon 731A	-90	TBD	TBD	Q330		FR/Rad.
CMAB	Oyo HS-1	Wilcoxon 731A	-90	161	251	Q4120		Rad./VPN
CRQB	Oyo HS-1	Wilcoxon 731A	-90	68	338	None at Present		FR
HERB	Oyo HS-1	Wilcoxon 731A	-90	160	70	Q4120		FR
BRIB	Oyo HS-1	Wilcoxon 731A	-90	79	169	BASALT	Acc. failed, Dilat.	FR
RFSB	Oyo HS-1	Wilcoxon 731A	-90	346	256	BASALT		FR
CMSB	Oyo HS-1	Wilcoxon 731A	-90	19	109	Q4120		FR
SMCB	Oyo HS-1	Wilcoxon 731A	-90	76	166	None at present	Posthole	FR
SM2B	Oyo HS-1	Wilcoxon 731A	-90	TBD	TBD	BASALT		FR
SVIN	Mark L-22		-90	319	49	BASALT	Tensor.	FR/Rad.
OHLN	Mark L-22		-90	300	30	BASALT	Tensor.	FR
MHDL	Mark L-22		-90	64	154	BASALT	Tensor.	FR
SBRN	Mark L-22		-90	6	96	BASALT	Tensor.	FR
OXMT	Mark L-22		-90	120	210	BASALT	Tensor.	FR
BBEB	Oyo HS-1	Wilcoxon 731A	-90	19	109	None at present	Acc. failed	Radio
E17B	Oyo HS-1	Wilcoxon 731A	-90	TBD	TBD	None at present		
E07B	Oyo HS-1	Wilcoxon 731A	-90	TBD	TBD	None at present		
YBIB	Oyo HS-1	Wilcoxon 731A	-90	257	347	None at present	Z geop. failed	FR/Rad.
YBAB	Oyo HS-1	Wilcoxon 731A	-90	TBD	TBD	None at present		
W05B	Oyo HS-1	Wilcoxon 731A	-90	TBD	TBD	None at present		
W02B	Oyo HS-1	Wilcoxon 731A	-90	TBD	TBD	Q4120		Radio
SFAB	None	LLNL S-6000	TBD	TBD	TBD	None at present	Posthole	
RSRB	Oyo HS-1	Wilcoxon 731A	-90	50	140	None at present	2 acc. failed	FR
RB2B	Oyo HS-1	Wilcoxon 731A	-90	252	162	Q4120	1 acc. failed	FR
SM1B	Oyo HS-1	Wilcoxon 731A	-90	TBD	TBD	None at present		
DB3B	Oyo HS-1	Wilcoxon 731A	-90	TBD	TBD	None at present	Acc. failed	
DB2B	Oyo HS-1	Wilcoxon 731A	-90	TBD	TBD	None at present		
DB1B	Oyo HS-1	Wilcoxon 731A	-90	TBD	TBD	None at present	Acc. failed	
CCH1	Oyo HS-1	Wilcoxon 731A	-90	TBD	TBD	Nanometrics HRD24	Dilat.	Radio
CGP1	Oyo HS-1	Wilcoxon 731A	-90	TBD	TBD	Nanometrics HRD24	Dilat.	Radio
CSU1	Oyo HS-1	Wilcoxon 731A	-90	TBD	TBD	Nanometrics HRD24	Dilat.	Radio
CYD1	Oyo HS-1	Wilcoxon 731A	-90	TBD	TBD	Nanometrics HRD24	Dilat.	Radio
CMW1	Oyo HS-1	Wilcoxon 731A	-90	TBD	TBD	Nanometrics HRD24	Dilat.	Radio

Table 3.6: Instrumentation of the HFN as of 06/30/2011. Every HFN downhole package consists of collocated 3-component geophones and accelerometers, with the exception of mPBO sites which have only 3-component geophones and are also collecting tensor strainmeter data. Six HFN sites (five of the SHFN and one of the NHFN) also have dilatometers (Dilat.). The five SHFN sites have Nanometrics data loggers with radio telemetry to the USGS and eventually from there to the NCEDC for archiving. Currently, seven NHFN sites have Quanterra data loggers and eight have been upgraded with ARRA funds to BASALT data loggers with local storage capacity. Of these 15 sites, 14 are currently telemetering continuous data to the BSL for archiving at the NCEDC, and 1 site (CMSB) is temporarily shutdown due to construction at the Cal Memorial stadium on the U.C. Berkeley Campus. Five additional backbone sites have been decommissioned for reasons ranging from the sites' replacement with nearby higher quality installations (SMCB, CRQB, RSRB) to irreparable site damage by outside influences such as bridge retrofit activity and construction (BBEB, YBIB). Station BBEB, however, continues to operate as a telemetry relay site. The component orientation of the sensors (vertical (Z): -90 \Rightarrow positive counts up; horizontals (H1 and H2): azimuthal direction of positive counts in degrees clockwise from north) are given when known or labeled as TBD if they are yet to be determined. VPN is Virtual Private Network.

4 Parkfield Borehole Network (HRSN)

4.1 Introduction

The operation of the High Resolution Seismic Network (HRSN) at Parkfield, California began in 1987, as part of the United States Geological Survey (USGS) initiative known as the Parkfield Prediction Experiment (PPE) (*Bakun and Lindh, 1985*).

Figure 3.17 shows the location of the network, its relationship to the San Andreas fault, sites of significance from previous and ongoing experiments using the HRSN, clusters of repeating earthquakes being monitored by the network, nonvolcanic tremors recorded by the network and located using a new station-pair double-difference method (*Zhang et al., 2010*), and the epicenters of the 1966 and 2004 M6 earthquakes that motivated much of the research. The HRSN records exceptionally high-quality data, owing to its 13 closely-spaced three-component borehole sensors (generally emplaced in the extremely low attenuation and background noise environment at 200 to 300 m depth [Table 3.8], its high-frequency, wide bandwidth recordings (0-100 Hz; 250 sps), and its sensitivity to very low amplitude seismic signals (e.g., recording signals from micro-earthquakes and non-volcanic tremors with equivalent magnitudes below $0.0 M_L$).

Several aspects of the Parkfield region make it ideal for the study of small earthquakes and nonvolcanic tremors and their relationship to tectonic processes and large earthquakes. These include the fact that the network spans the SAFOD (San Andreas Fault Observatory at Depth) experimental zone, the nucleation region of earlier repeating magnitude 6 events and a significant portion of the transition from locked to creeping behavior on the San Andreas fault; the availability of three-dimensional P and S velocity models (*Michelini and McEvilly, 1991; Thurber et al., 2006*); a long-term HRSN seismicity catalog (complete to very low magnitudes and that includes over half of the M6 seismic cycle); a well-defined and relatively simple fault segment; the existence of deep nonvolcanic tremor (NVT) activity; and a relatively homogeneous mode of seismic energy release as indicated by the earthquake source mechanisms (over 90% right-lateral strike-slip).

In a series of journal articles and Ph.D. theses, the cumulative, often unexpected, results of research by UC Berkeley and others using HRSN data trace the evolution of a new and exciting picture of the San Andreas fault zone responding to its plate-boundary loading, and they are forcing new thinking on the dynamic processes and conditions within the seismogenic fault zone (upper ~ 15 km) at the sites of recurring small earthquakes and to much greater sub-seismogenic depths (~ 30 -35 km)

where recently discovered nonvolcanic tremors are occurring (*Nadeau and Dolenc, 2005*).

Parkfield has also become the focus of a major component of NSF's EarthScope (<http://www.earthscope.org>) project, known as the San Andreas Fault Observatory at Depth (SAFOD) (<http://www.earthscope.org/observatories/safod>). The SAFOD project is a comprehensive effort whose objectives include drilling into the hypocentral zone of repeating M ~ 2 earthquakes on the San Andreas Fault at a depth of about 3 km and establishing a multi-stage geophysical observatory in the immediate proximity of these events. The purpose of such an observatory is to carry out a comprehensive suite of down-hole measurements in order to study the physical and chemical conditions under which earthquakes nucleate and rupture (*Hickman et al., 2004*). In these efforts, the HRSN plays a vital support role by recording seismic data used to directly constrain seismic signals recorded in the SAFOD main hole and by recording seismic events in the surrounding region to provide information on the larger scale fault zone processes that give rise to any changes observed in the main hole.

4.2 HRSN Overview

Installation of the HRSN deep (200-300 m) borehole sensors initiated in late 1986, and recording of triggered 500 sps earthquake data began in 1987. The HRSN sensors are 3-component geophones in a mutually orthogonal gimbaled package. This ensures that the sensor corresponding to channel DP1 is aligned vertically and that the others are aligned horizontally. The sensors are also cemented permanently in place, ensuring maximum repeatability of the sensors' responses to identical sources, and allowing for precise relative measurements with minimal need for corrections and assumptions associated with moving the sensors. Originally a 10 station network, fully operational by January 1988, the HRSN was expanded to 13 borehole stations in late July 2001, and the original recording systems (see previous Berkeley Seismological Laboratory [BSL] Annual Reports) were upgraded to 24 bit acquisition (Quanterra 730s) and 56K frame relay telemetry to UCB. As part of funding from the American Recovery and Reinvestment Act (ARRA), an additional replacement/upgrade of the Quanterra 730 acquisition systems to 24-bit BASALT acquisition systems is underway in 2010-2011 that is allowing for local site storage and later retrieval of data during periods of sporadic telemetry failures. Properties of the sensors are summarized in Table 3.9.

The three newest borehole stations (CCRB, LCCB, and SCYB) were added, with NSF support, at the north-

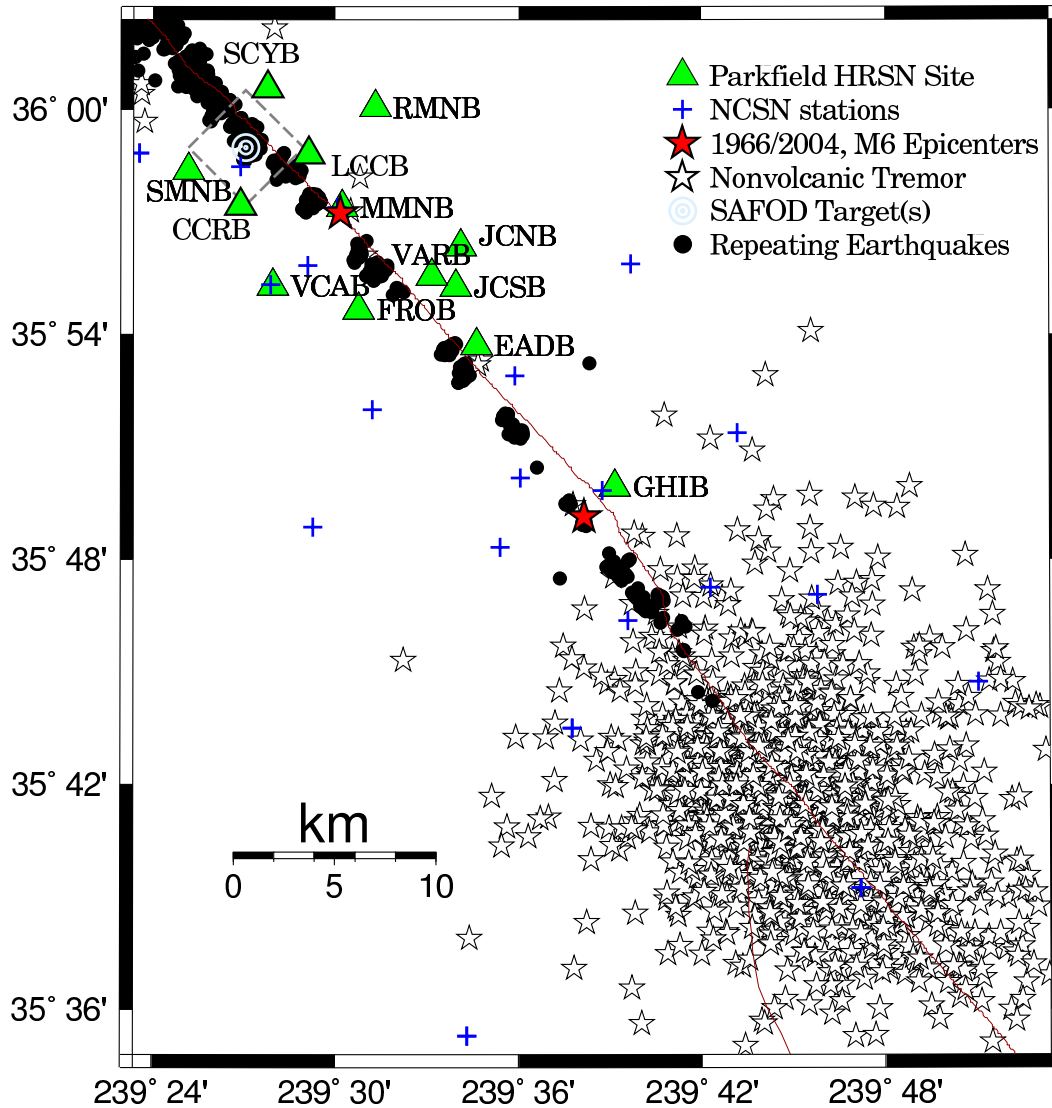


Figure 3.17: Map showing the San Andreas Fault trace and locations of the 13 Parkfield HRSN stations, the repeating M2 SAFOD targets (a 4 km by 4 km dashed box surrounds the SAFOD zone), and the epicenters of the 1966 and 2004 M6 Parkfield mainshocks. Also shown are locations (stars) of nonvolcanic tremors in the Cholame, CA area relocated using a new station-pair double-difference method (*Zhang et al., 2010*), and routine locations of clusters of repeating earthquakes processed by the integrated HRSN and NCSN networks.

Site	Net	Latitude	Longitude	Surf. (m)	Depth (m)	Date	Location
EADB	BP	35.89525	-120.42286	466	245	01/1987 -	Eade Ranch
FROB	BP	35.91078	-120.48722	509	284	01/1987 -	Froelich Ranch
GHIB	BP	35.83236	-120.34774	400	63	01/1987 -	Gold Hill
JCNB	BP	35.93911	-120.43083	527	224	01/1987 - 02/18/2008	Joaquin Canyon North
JCNB*	BP	35.93911	-120.43083	527	4	07/2011 -	Joaquin Canyon North
JCSB	BP	35.92120	-120.43408	455	155	01/1987 -	Joaquin Canyon South
MMNB	BP	35.95654	-120.49586	698	221	01/1987 -	Middle Mountain
RMNB	BP	36.00086	-120.47772	1165	73	01/1987 -	Gastro Peak
SMNB	BP	35.97292	-120.58009	699	282	01/1987 -	Stockdale Mountain
VARB	BP	35.92614	-120.44707	478	572	01/1987 - 08/19/2003	Varian Well
VARB	BP	35.92614	-120.44707	478	298	08/25/2003 -	Varian Well
VCAB	BP	35.92177	-120.53424	758	200	01/1987 -	Vineyard Canyon
CCRB	BP	35.95718	-120.55158	595	251	05/2001 -	Cholame Creek
LCCB	BP	35.98005	-120.51424	640	252	08/2001 -	Little Cholame Creek
SCYB	BP	36.00938	-120.53660	945	252	08/2001 -	Stone Canyon

Table 3.8: Stations of the Parkfield HRSN. Each HRSN station is listed with its station code, network id, location, operation period, and site description. The latitude and longitude (in degrees) are given in the WGS84 reference frame. The surface elevation (in meters) is relative to mean sea level, and the depth to the sensor (in meters) below the surface is also given. Coordinates and station names for the three new SAFOD sites are given at the bottom. Note two entries for JCNB, which failed in February of 2008 and is being replaced with a post-hole installation '**' with ARRA funds.

Site	Sensor	Z	H1	H2	RefTek 24	Quanterra 730	BASALT
EADB	Mark Products L22	-90	170	260	01/1987 - 06/1998	03/2001 -	pending
FROB	Mark Products L22	-90	338	248	01/1987 - 06/1998	03/2001 - 11/2010	11/2010 -
GHIB	Mark Products L22	90	failed	unk	01/1987 - 06/1998	03/2001 -	pending
JCNB	Mark Products L22	-90	0	270	01/1987 - 06/1998	03/2001 - 02/2008	-
JCNB*	replacement pending	tdb	tdb	tdb	-	-	pending
JCSB	Geospace HS1	90	300	210	01/1987 - 06/1998	03/2001 - 04/2011	04/2011 -
MMNB	Mark Products L22	-90	175	265	01/1987 - 06/1998	03/2001 - 12/2010	12/2010 -
RMNB	Mark Products L22	-90	310	40	01/1987 - 06/1998	03/2001 -	pending
SMNB	Mark Products L22	-90	120	210	01/1987 - 06/1998	03/2001 - 04/2011	04/2011 -
VARB	Litton 1023	90	15	285	01/1987 - 06/1998	03/2001 - 04/2011	04/2011 -
VCAB	Mark Products L22	-90	200	290	01/1987 - 06/1998	03/2001 - 04/2011	04/2011 -
CCRB	Mark Products L22	-90	N45W	N45E	-	05/2001 -	pending
LCCB	Mark Products L22	-90	N45W	N45E	-	08/2001 -	pending
SCYB	Mark Products L22	-90	N45W	N45E	-	08/2001 -	pending

Table 3.9: Instrumentation of the Parkfield HRSN. Most HRSN sites have L22 sensors and were originally digitized with a RefTek 24 system. The WESCOMP recording system failed in mid-1998, and after an approximate three year hiatus the network was upgraded and recording was replaced with a new 4-channel system. The new system, recording since July 27, 2001, uses a Quanterra 730 4-channel acquisition. Three new stations were also added during the network upgrade period (bottom) with horizontal orientations that are approximately N45W and N45E. More accurate determinations of these orientations will be made as available field time permits. In 2010-2011, with ARRA funding, additional replacement/upgrade to 24-bit BASALT acquisition with station-local data storage is underway. Note, 2 entries for JCNB which failed in February of 2008 and is being replaced with a post-hole installation '**', also with ARRA support.

Sensor	Channel	Rate (sps)	Mode	FIR
Geophone	DP?	250.0	C	Ca
Geophone	BP?	20.0	C	Ac

Table 3.10: Data streams currently being acquired at operational HRSN sites. Sensor type, channel name, sampling rate, sampling mode, and type of FIR filter are given. C indicates continuous; Ac acausal; Ca causal. “?” indicates orthogonal, vertical, and two horizontal components.

west end of the network as part of the SAFOD project to improve resolution of the structure, kinematics, and monitoring capabilities in the SAFOD drill-path and target zones. Figure 3.17 illustrates the location of the drill site and the new borehole sites, as well as locations of earthquakes recorded by the initial and upgraded/expanded HRSN.

These three new stations have a similar configuration to the original upgraded 10 station network and include an additional channel for electrical signals. Station descriptions and instrument properties are summarized in Tables 3.8 and 3.9. All the HRSN data loggers employ FIR filters and extract data at 250 Hz (causal) and 20 Hz (acausal). (Table 3.10).

The remoteness of the SAFOD drill site and supporting HRSN stations required an installation of an intermediate data collection point at Gastro Peak, with a microwave link to our CDF facility. Prior to June, 2008, six of the HRSN sites transmitted directly to the CDF, and the other seven sites transmitting to a router at Gastro Peak, where the data was aggregated and transmitted to the CDF. However, due to disproportionately increasing landowner fees for access to the Gastro Peak site, we reduced our dependence on that site in the summer and fall of 2008 (in cooperation with the USGS) by re-routing telemetry of five of the sites previously telemetered through Gastro Peak through an alternative site at Hogs Canyon (HOGS).

Continuous 20 and 250 Hz data from all HRSN channels are recorded to disk at our central site data collection facility on the California Department of Forestry’s (CDF) property in Parkfield. From there the data is radio telemetered to the USGS site at Carr Hill and then telemetered over a dedicated T1 circuit to the USGS where it is incorporated into the USGS earthquake detection system and to the Northern California Earthquake Center (NCEDC) at U.C. Berkeley for archiving and online access by the community. The HRSN system also generates autonomous event trigger associations which are also archived at the NCEDC.

The HRSN’s telemetry system also provides remote access of the local site data acquisition systems for state of health monitoring and control.

Another feature of the HRSN system that has been particularly useful both for routine maintenance and for pathology identification has been the Internet connectivity of the central site processing computer and the individual stations’ data acquisition systems. Through this connectivity, locally generated warning messages from the central site processor are sent directly to the BSL for evaluation by project personnel. If, upon these evaluations, more detailed information on the HRSN’s performance is required, additional information can also be remotely accessed from the central site processing computer and generally from the individual site data loggers as well. Analysis of this remotely acquired information has been extremely useful for trouble shooting by allowing field personnel to schedule and plan the details of maintenance visits to Parkfield. The connectivity also allows for local site acquisition shut-downs and restarts and for remote implementation of data acquisition parameter changes when needed.

The network connectivity and seamless data flow to U.C. Berkeley also provide near-real-time monitoring capabilities that are useful for rapid evaluation of significant events as well as the network’s general state of health. For example, shown in Figure 3.18 are surface wave seismograms of the teleseismic M_w 9.0 earthquake near the east coast of Honshu, Japan (Lat.: 38.322N; Lon.: 142.369E; depth 32 km) occurring on March 11, 2011 05:46:23 (UTC) recorded on the BP1/SP1 (vertical) channels of the 11 HRSN borehole stations in operation at the time. The seismic data from the quake was telemetered to Berkeley and available for analysis by the Northern California Seismic System (NCSS) real-time/automated processing stream within a few seconds of being recorded by the HRSN.

This is a good signal source for examining the relative responses of the BP borehole network station/components to seismic ground motion. In this case, for the large amplitude surface waves, the vertical channels all appear to be working well and with proper polarities. Closer inspection of the unfiltered pre-event noise for these channels and for their corresponding horizontal (DP2 and DP3 channels) indicated that on a finer scale, the following channels were not entirely responding normally to seismic ground motions at the time of this event:

- FROB.BP.DP1 - Strong 60 Hz noise
- LCCB.BP.DP2 - anomalously low signal level
- SCYB.BP.DP3 - excessive 60 Hz noise
- VARB.BP.DP1 - large wander/offsets, numerous glitches
- VARB.BP.DP2 - large DC offset
- VARB.BP.DP3 - large DC offset
- JCSB.BP.DP1 - no seismic response, power failure
- JCSB.BP.DP2 - no seismic response, power failure
- JCSB.BP.DP3 - no seismic response, power failure
- JCNB.BP.DP1 - no seismic response, signal cable cut
- JCNB.BP.DP2 - no seismic response, signal cable cut

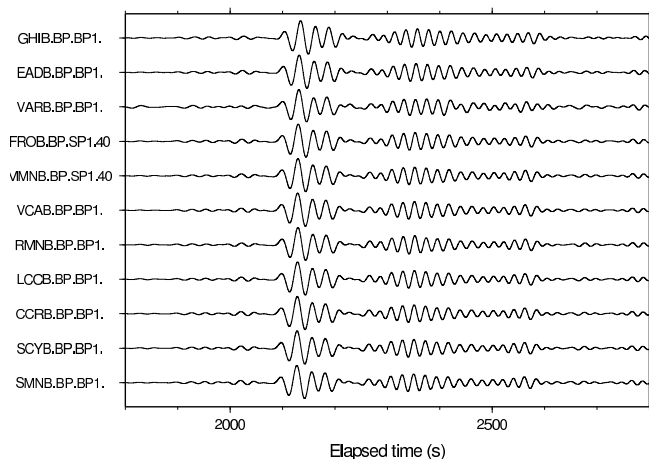


Figure 3.18: Plot of surface wave seismograms of the teleseismic M_w 9.0 earthquake near the east coast of Honshu, Japan (Lat.: 38.322N; Lon.: 142.69E; depth 32 km) occurring on March 11, 2011 05:46:23 (UTC) recorded on the BP1/SP1 (vertical) channels of the 11 HRSN borehole stations in operation at the time. Here, vertical component geophone (velocity) data have been 0.02-0.05 Hz bandpass filtered and normalized by the maximum amplitude for each trace.

JCNB.BP.DP3 - no seismic response, signal cable cut
 By rapidly generating such plots following large teleseismic events, quick assessment of the HRSN seismometer responses to real events is easily done and corrective measures implemented with relatively little delay.

Data Flow

Initial Processing Scheme. Continuous data streams on all HRSN components are recorded at 20 and 250 sps on disk on the local HRSN computer at the CDF facility. These continuous data are transmitted in near-real-time to the Berkeley Seismological Laboratory (BSL) over a T1 link and then archived at the NCEDC. In addition, the near-real-time data are being transmitted over the T1 circuit to the USGS at Menlo Park, CA, where they are integrated into the Northern California Seismic System (NCSS) real-time/automated processing stream. This integration has also significantly increased the sensitivity of the NCSN catalog at lower magnitudes, effectively doubling the number of small earthquake detections in the critical SAFOD zone.

Shortly after being recorded to disk on the central site HRSN computer, event triggers for the individual stations are also determined, and a multi-station trigger association routine then processes the station triggers and generates a list of HRSN specific potential earth-

quakes. For each potential earthquake that is detected, a unique event identification number (compatible with the NCEDC classification scheme) is also assigned. Prior to the San Simeon earthquake of December 22, 2003, 30 second waveform segments were then collected for all stations and components and saved to local disk as an event gather, and event gathers were then periodically telemetered to BSL and included directly into the NCEDC earthquake database (DBMS) for analysis and processing.

Because of its mandate to record very low amplitude seismic signals and microearthquakes in the Parkfield area, the HRSN was designed to operate at very high sensitivity levels. To some degree, this comes at the expense of dynamic range for the larger events (above ~ 3.5), but high sensitivity is also achieved by recording in the low noise borehole environment (200-300m) and by exhaustive efforts at knocking down extraneous noise sources that arise in the electronics of the recording, power, and telemetry systems or from interference from cultural or scientific noise sources near the stations. As a consequence of the network's high sensitivity, the HRSN also records above its noise floor numerous signals from regional events and relatively distant and small amplitude nonvolcanic tremor events. For example, spot checks of aftershocks following the M 6.5 San Simeon earthquake of December 22, 2003 using continuous data and HRSN event detection listings revealed that the overwhelming majority of HRSN generated detections following San Simeon resulted from seismic signals generated by San Simeon's aftershocks, despite the HRSN's ~ 50 km distance from the events. Data from the California Integrated Seismic Network (CISN) show that there were $\sim 1,150$ San Simeon aftershocks with magnitudes > 1.8 in the week following San Simeon, and during this same period, the number of HRSN event detections was $\sim 10,500$ (compared to an average weekly rate before San Simeon of 115 HRSN detections). This suggests that, despite the ~ 50 km distance, the HRSN is detecting San Simeon aftershocks well below magnitude 1.

Current Processing. Since the beginning of the network's data collection in 1987, and up until 2002, the local and regional events were discriminated based on analyst assessment of S-P times, and only local events with S-P times less than ~ 2.5 s at the first arriving station were picked and located as part of the HRSN routine catalog. However, because of the network's extreme sensitivity to the large swarm of aftershocks from the 2003 San Simeon and 2004 Parkfield M6 earthquakes (e.g., in the first five months following the San Simeon mainshock, over 70,000 event detections were made by the HRSN system, compared to an average five month detection rate of 2500 prior to San Simeon) and because of ever declining funding levels, analyst review of individual microearthquakes had to be abandoned.

In addition, the dramatic increase in event detections following the San Simeon and Parkfield earthquakes vastly exceeded the HRSN's capacity to process and telemeter both continuous and triggered event waveform data. To prevent the loss of seismic waveform coverage, processing of the triggered waveform data was discontinued to allow the telemetry and archival of the 20 and 250 sps continuous data to continue uninterrupted. Subsequent funding limitations have since precluded reactivation of the triggered event processing. Cataloging of associated event triggers from the modified REDI real-time system algorithm continues, however, and both the continuous waveform data and trigger times are telemetered to and archived at the NCEDC, for access by the research community.

Because funding to generate catalogs of local micro-events from the tens of thousands of San Simeon and Parkfield aftershocks has not been forthcoming, major changes in our approach to cataloging events have had to be implemented. For example, HRSN data flow has now been integrated into NCSN automated event detection, picking, and catalog processing (with no analyst review). In addition, we have implemented a high resolution cross-correlation (pattern matching) based procedure to automatically detect, pick, locate, double-difference relocate, and determine magnitudes for select similar and repeating earthquake families down to very low magnitudes (i.e., below $-1.0M_L$). These new schemes are discussed in more detail in the activities section below.

4.3 2010-2011 Activities

This year, routine operation and maintenance of the HRSN (California's first and longest operating borehole seismic network) have been augmented by funding through the USGS from the American Recovery and Reinvestment Act (ARRA). This funding is directed toward upgrading the data loggers at all sites with government furnished equipment (GFE) data loggers, and with improving and upgrading telemetry and power infrastructure at the sites. Many of the routine maintenance activities described below were also carried out with ARRA support.

In addition to routine operations and maintenance, project activities this year include: a) processing of ongoing similar and repeating very low magnitude seismicity; b) implementing the ARRA upgrades and identifying needed corrections to the upgrades using repeating events; c) supporting SAFOD activities with the repeating and similar event seismicity catalogs; and d) monitoring non-volcanic tremor activity in the Parkfield-Cholame area.

Routine Operations and Maintenance

Routine maintenance tasks required this year to keep the HRSN in operation include cleaning and replacing

corroded electrical connections; grounding adjustments; cleaning solar panels; testing and replacing failing batteries; ventilating battery and data logger housings to address problems with low power during hot weather, and repairing and realigning repeater sites and antennas.

Remote monitoring of the network's health using the Berkeley Seismological Laboratory's internally developed and SeisNetWatch software is also performed to identify both problems that can be resolved over the Internet (e.g. rebooting of data acquisition systems due to clock lockups) and more serious problems requiring field visits. Over the years, such efforts have paid off handsomely by providing exceptionally low noise recordings of very low amplitude seismic signals produced by microearthquakes (below $0.0M_L$) and nonvolcanic tremors.

The network connectivity over the T1 circuit also allows remote monitoring of various measures of the state of health (SOH) of the network in near-real-time using waveforms directly. For example, background noise levels can be rapidly evaluated. Shown in Figure 3.19 are power spectral density (PSD) plots of background noise for the 12 vertical HRSN channels in operation at the time (beginning 01:00 AM local time on day 12/01/2010) over a 1000 second period. By periodically generating such plots, we can rapidly evaluate, through comparison with previously generated plots, changes in the network's station response to seismic signals across the wide band high-frequency spectrum of the borehole HRSN sensors. Changes in the responses often indicate problems with the power, telemetry, or acquisition systems, or with changing conditions in the vicinity of station installations that are adversely affecting the quality of the recorded seismograms. Once state of health issues are identified with the PSD analyses, further remote tests can be made to more specifically determine possible causes for the problem, and corrective measures can then be planned in advance of field deployment within a relatively short period of time.

Similar and Repeating Event Catalogs

The increased microseismicity (thousands of events) resulting from the San Simeon M6.5 (SS) and Parkfield M6 (PF) events, the lack of funds available to process and catalog the increased number of micro-earthquakes, and the increased interest in using the micro-quakes in repeating earthquake and SAFOD research have required new thinking on how to detect and catalog microearthquakes recorded by the HRSN.

One action taken to help address this problem has been to integrate HRSN data streams into the NCSN event detection and automated cataloging process. This approach has been successful at detecting and locating a significantly greater number of micro-earthquakes over the previous NCSN detection and location rate (essentially doubling the number of events processed by the NCSN).

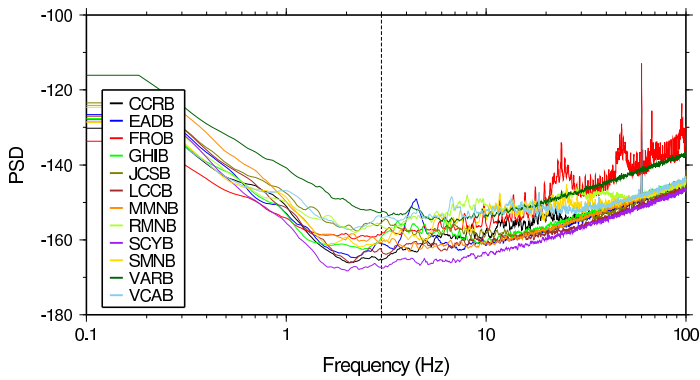


Figure 3.19: Background noise Power Spectral Density (PSD) levels as a function of frequency for the twelve 250 sps vertical component channels (DP1) of the HRSN borehole stations in operation during the 1000 second period analyzed, beginning 01:00 AM local time on day 12/01/2010. The approximate 2 Hz minimum of the PSD levels occurs because of the 2 Hz sensors used at these sites. Below 2 Hz, noise levels rise rapidly. The PSD (dB) ranking (lowest to highest) at 3 Hz (intersection with vertical line) for the vertical channels is:

- SCYB.BP.DP1 -167.377
- CCRB.BP.DP1 -165.256
- LCCB.BP.DP1 -162.697
- EADB.BP.DP1 -160.999
- MMNB.BP.DP1 -160.754
- SMNB.BP.DP1 -159.789
- GHIB.BP.DP1 -159.294
- FROB.BP.DP1 -158.343
- RMNB.BP.DP1 -156.325
- JCSB.BP.DP1 -155.427
- VCAB.BP.DP1 -154.052
- VARB.BP.DP1 -152.552

However, the HRSN sensitized NCSN catalog is still only catching about half the number of local events previously cataloged by the HRSN using the old, HRSN-centric processing approach. Furthermore, triggered waveforms for the additional small NCSN-processed events are often not reviewed by an analyst, nor do these smaller events generally have NCSN magnitude determinations associated with them.

These limitations can severely hamper research efforts relying on the more numerous similar and characteristically repeating micro-events (e.g., earthquake scaling studies, SAFOD-related research, deep fault slip rate estimation, and the compilation of recurrence interval statistics for time-dependent earthquake forecast models). They also reduce the efficacy of using frequently recurring micro-events as a tool for monitoring the network state-of-health (SOH).

To help overcome these limitations, we continued this

year to implement our semi-automated similar event cataloging scheme based on pattern matching (match filter) scans using cross-correlation of the continuous HRSN data. The method uses a library of reference event (pattern) waveforms, picks, locations, and magnitudes that have been accurately determined, to automatically detect, pick, locate, and determine magnitudes for events similar to the reference event with a level of accuracy and precision that only relative event analysis can bring.

The similar event detection is also remarkably insensitive to the magnitude of the reference event used, allowing similar micro-events ranging over about 3 magnitude units to be fully cataloged using a single reference event, and it does a remarkably good job at discriminating and fully processing multiple superposed events.

Once a cluster of similar events has been processed, an additional level of resolution can then be achieved through the identification and classification of characteristically repeating microearthquakes (i.e., near identical earthquakes) occurring within the similar event family (Figure 3.20). The pattern scanning approach also ensures optimal completeness of repeating sequences owing to scans of the matching pattern through “all” available continuous data (critical for applications relying on recurrence interval information). For example, only about half of the magnitude 0.25 events shown in Figure 3.20 were picked up by the NCSN-HRSN integrated network.

Figure 3.20 also shows how stable the performance of the borehole VCAB.BP.DP1 channel has remained over the ~5 year period shown. Due to station malfunctions or human error during field maintenance, this would not necessarily be the case. Because repeating events can generally be identified using any combination of 4 of the HRSN’s 38 channels, assessment of the channel responses for channels not in the 4 channel combination can be carried out. This can be carried out repeatedly through time as additional repeats are identified with time resolutions depending on the number of repeating sequences used and the frequency of their repeats. Repeating sequences of this magnitude typically repeat every 1 to 2 years, and we are in the process of expanding our similar event monitoring capability to 61 of these sequences. Hence, on average, evaluations of this type can be possible approximately 10 days on an automated basis. However, there are on the order of 200 such sequences known in the Parkfield area, and if one is willing to include even more frequently occurring similar but non-identical events into the equation, near-daily automated SOH analyses are a possibility.

Armed with this type of information, technicians and field engineers can quickly identify and address major problems. In addition to a visual assessment, the high similarity of the events lends itself to the application of differencing techniques in the time and frequency domains to automatically identify even subtle SOH issues.

For other networks recording continuously in the Parkfield area (e.g., NCSN, BDSN) it is also a relatively simple process to extend the SOH analysis using characteristic repeating events to their stations. Furthermore, numerous repeating and similar event sequences are also known to exist in the San Francisco Bay and San Juan Bautista areas, where continuous recording takes place. Hence, application of the repeating event SOH technique to these zones should also be feasible.

This year we have worked at adapting our cataloging codes to take advantage of faster computing now available. We have expanded the library of reference event patterns and plan to retroactively scan these patterns through previously recorded and ongoing data to capture and catalog an ever growing body of similar and repeating earthquakes for research purposes, in support of SAFOD and for SOH monitoring (including the use of repeaters to identify and correct problems associated with the ARRA upgrade of the HRSN).

Progress on ARRA upgrades

This year, funding through the USGS from the American Recovery and Reinvestment Act (ARRA) was used to begin upgrade of data loggers at all sites with government furnished equipment (GFE) data loggers, and for improving and upgrading telemetry and power infrastructure at the sites. Because of increased use of pattern-match scanning techniques through continuous seismograms to detect and process repeating and Low Frequency Events (LFEs), care is being taken in our upgrade efforts to maintain the response characteristics of the HRSN's continuous data. At the time of this report, six of the HRSN stations (FROB, MMNB, JCSB, VCAB, VARB and SMNB) have had new BASALT data loggers installed, with corresponding power and telemetry infrastructure upgrades. A seventh site (JCNB), whose connection to its downhole sensor (cemented in place) was severed, has now had a new sensor emplaced at 4 m depth and is awaiting final radio and BASALT installation. BASALTS and radios for the remaining six sites have only recently been received and final upgrades are planned for July and August.

The repeating and similar event data we are compiling provide nearly ideal natural sources for ensuring the stability of the HRSN station's response characteristics across the transition to ARRA upgrade electronics. In comparing waveforms from repeating events before and after the the first two BASALT installations (i.e. at FROB and MMNB), it became immediately apparent that the nominal polarities of the BASALT data loggers were of the opposite sign to those of their predecessors (Q730s). In subsequent installations, this was taken into account. We were also immediately able to recognize in the repeating event waveforms that the horizontal channel assignments were switched in about half of the cases

(i.e., DP2 mapped to DP3 and DP3 mapped to DP2). Whether this was due to incorrect cable preparation or to incorrect documentation is still not known, but subsequent site visits and analyses of ongoing repeat event waveforms are being used to correct and confirm appropriate channel assignments and polarities.

In a particularly bizarre twist, the repeating earthquake data also revealed that the upgrade of the site FROB resulted in the superposition of horizontal channels DP2 and DP3 being mapped to channel DP3 and an identical but polarity flipped version of that waveform being mapped to channel DP2. The repeating earthquake data shows this clearly in Figure 3.21. In this figure, horizontal channels of station FROB from the four most recent repeats of the repeating SAFOD target sequence (Hawaii, HI) are shown. The first (top) and second trace are the raw DP2 and DP3 channels (respectively) from the HI sequence's September 4, 2005 repeat, and the third, fourth, fifth, and 6th traces are from the sequence's August 11, 2006 and August 30, 2008 repeats (respectively).

The bottom two traces show the DP2 and DP3 channel responses to the most recent repeat of the HI sequence on May 15 of 2011 (determined independently from other station data), and show that the DP2 and DP3 channels are polarity flipped versions of each other. Adding (superposing) the DP2 and DP3 channels from the 2008 event generates a waveform nearly identical to the DP3 trace.

The GFE BASALT data logger was installed at FROB on November 10, 2010. It is clear from Figure 3.21 that sometime between the 2008 and 2011 repeats of HI (i.e., spanning the date of BASALT installation) the response of the DP2 and DP3 channels was seriously compromised. To more precisely bracket the time of the response change in order to help track down the cause of the change, we used a series of repeating sequences, and we were able to back-out the following history of response changes at FROB and implement corrections to restore its original response:

2010/08/03: response o.k.
 2010/08/11: SITE VISIT, cable resplice
 2010/10/29: polarities flipped, DP2, DP3 channels swapped
 2010/11/10: SITE VISIT, BASALT installed
 2010/11/16: polarities correct, DP2, DP3 still swapped
 2010/12/02: same as 2010/11/16
 2010/12/08: SITE VISIT, splice corrected
 2011/01/31: polarities flipped, DP2-3 still swapped
 2011/04/07: SITE VISIT, install new cable to correct polarities
 2011/04/29: DP1 polarity correct, DP3 superposed signals, DP2 inverted copy of DP3
 2011/05/15: same as 2011/04/29
 2011/05/26: SITE VISIT, correct superposition (crossed-

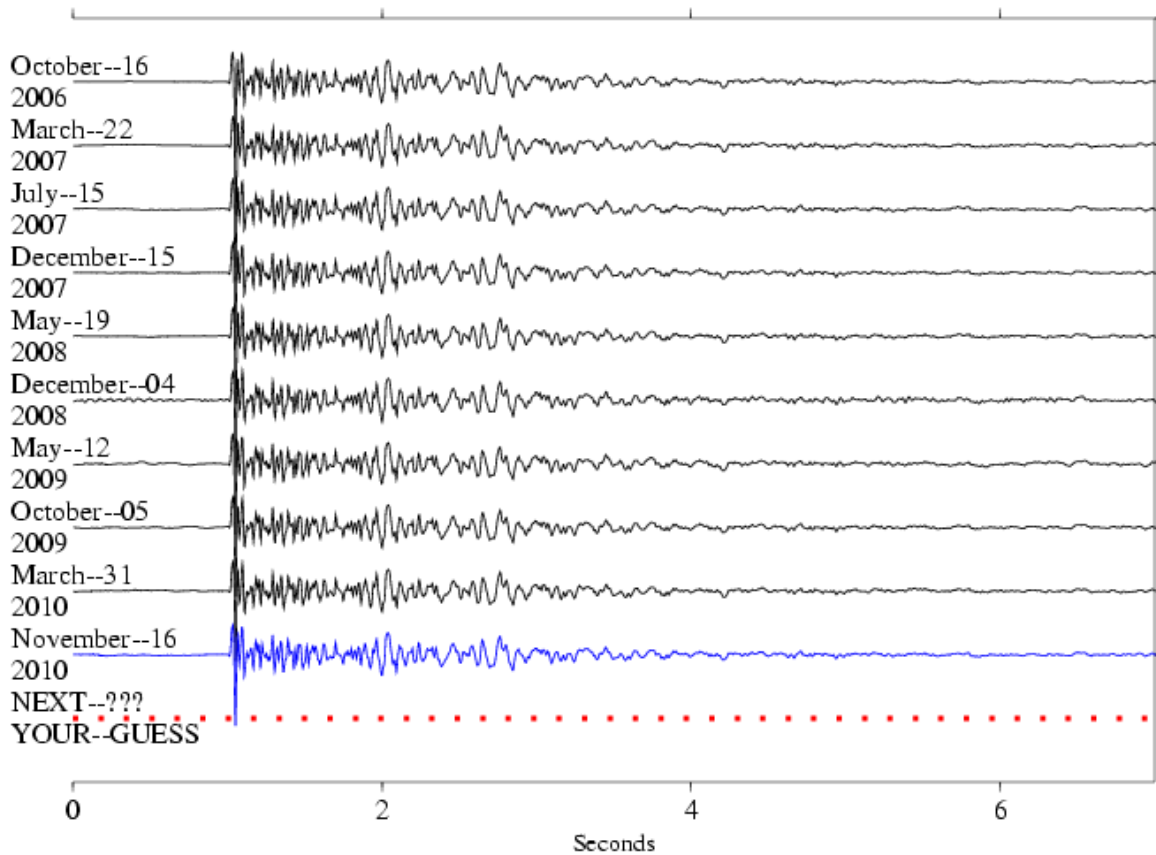


Figure 3.20: Ten most recent repeats of a characteristic sequence of repeating magnitude 0.25 (M_p , USGS preferred magnitude) microearthquakes recorded by vertical (DP1) channel of HRSN station VCAB. Waveform amplitudes are absolute scaled to the reference event (top), showing how small the variations in magnitudes of these naturally occurring events really are. High-precision location and magnitude estimates of these events show they are extremely similar in waveform (typically 0.95 cross-correlation or better), nearly collocated (to within 5-10 m) and of essentially the same magnitude ($\pm 0.13 M_p$ units). The dashed line labeled “NEXT” serves to illustrate that events in these types of sequences continue to repeat and that they can therefore be used for monitoring ongoing channel response relative to past performance. The last five Recurrence intervals in this sequence range from about six to eight months, suggesting the next repeat will take place sometime in May through July of 2011.

pairs) of DP2, DP3
 2011/06/04: DP1 polarity correct, superposition gone,
 DP2, DP3 swapped, polarities flipped
 2011/07/..: SITE VISIT scheduled

As one can see, just about all that could go wrong did go wrong with the upgrade and maintenance of FROB. Though this is atypical, the example illustrates well the utility of using repeating earthquake analysis for identifying and tracking maintenance issues that need to be addressed.

The repeating earthquake analyses have also shown that, absent the polarity flips, channel swaps and superposed signals, preservation of the the waveform and spectral shapes and spectral phasing relative the Q730

predecessors is very good. However, the analyses do reveal a significant ($\sim 15\text{-}20\%$) drop in the amplitude of the BASALT signals relative to the Q730s. At this time it appears this could involve an impedance matching issue at the interface of the BASALT with the other components of the HRSN stations. This is currently being investigated further, and corrective measures are being considered.

Tremor Monitoring

The HRSN played an essential role in the initial discovery of nonvolcanic tremors (NVT) and associated Low Frequency Events (LFE) along the San Andreas Fault (SAF) below Cholame, CA (*Nadeau and Dolenc, 2005*;

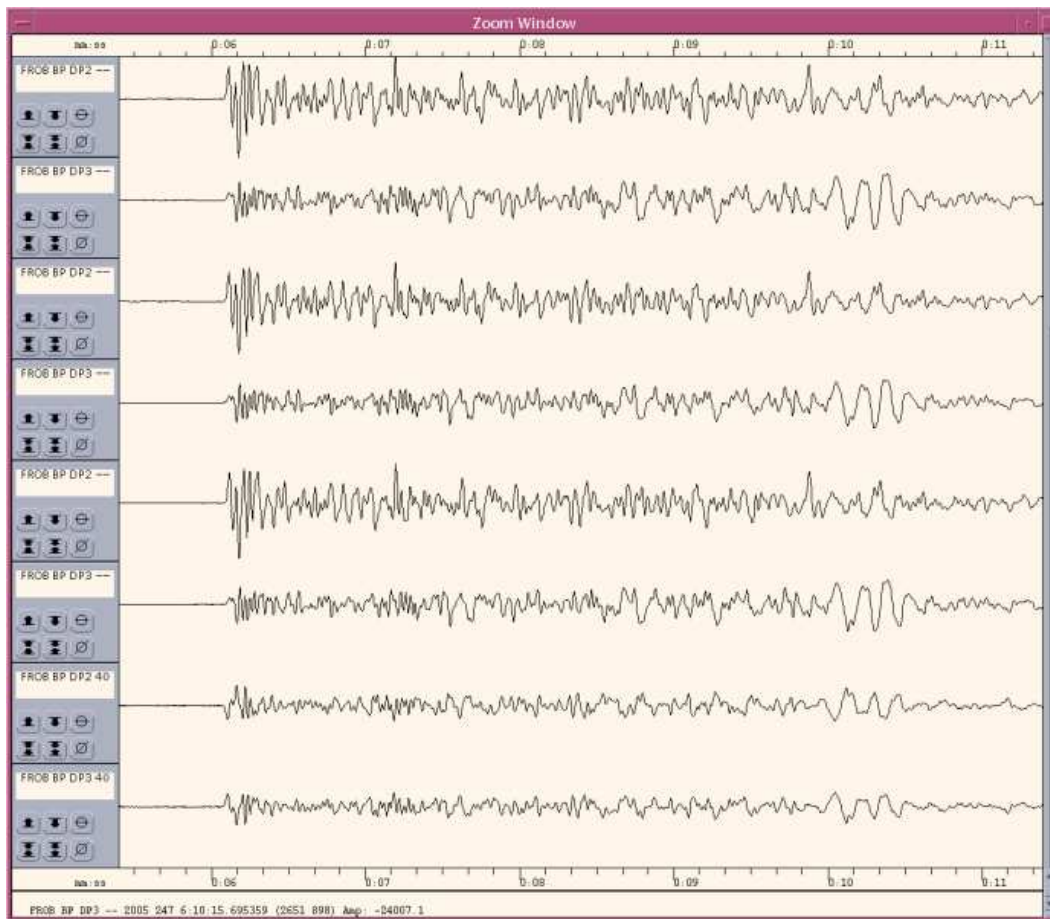


Figure 3.21: Figure of repeating earthquake data showing an example of problematic channel responses that sometimes results from ARRA upgrade efforts. Horizontal channels of station FROB from the four most recent repeats of the repeating SAFOD target sequence (Hawaii, HI) are shown. The first (top) and second trace are the raw DP2 and DP3 channels (respectively) from the HI sequence’s September 4, 2005 repeat, and the third, fourth, fifth, and sixth traces are from the sequence’s August 11, 2006 and August 30, 2008 repeats (respectively). The bottom two traces show the DP2 and DP3 channel responses to the most recent repeat of the HI sequence on May 15 of 2011 (determined independently from other station data). The ARRA upgrade effort at this site (occurring between the 2008 and 2011 events) resulted in the superposition of horizontal channels DP2 and DP3 being mapped into channel DP3 and an identical but polarity-flipped version of that waveform being mapped into channel DP2.

(Shelly *et al.*, 2009), and continues to play a vital role in ongoing NVT research. The Cholame tremors occupy a critical location between the smaller Parkfield ($\sim M6$) and much larger Ft. Tejon ($\sim M8$) rupture zones of the SAF (Figure 3.17). Because the time-varying nature of tremor activity is believed to reflect time-varying deep deformation and presumably episodes of accelerated stressing of faults, because anomalous changes in Cholame area NVT activity preceded the 2004 Parkfield M6 earthquake, and because elevated tremor activity has continued since the 2004 Parkfield event, we are continuing to monitor the tremor activity observable by the HRSN to look for additional anomalous behavior that may signal an increased likelihood of another large SAF event in the region. To

date, over 2800 NVT events have been identified and cataloged, and regular updates of the NVT catalog continue on a biweekly basis.

Efforts in Support of SAFOD

An intensive and ongoing effort by the EarthScope component called SAFOD (San Andreas Fault Observatory at Depth) is underway to drill through, sample, and monitor the active San Andreas Fault at seismogenic depths and in very close proximity (within a few tens of kilometers or less) to a repeating magnitude 2 earthquake site. The HRSN data plays a key role in these efforts by providing low noise and high sensitivity seismic waveforms from active and passive sources, and by providing

a backbone of very small earthquake detections and continuous waveform data.

As of early September 2007, SAFOD drilling had penetrated the fault near the HI repeating target sequence and collected core samples in the fault region that presumably creeps and surrounds the repeatedly rupturing HI patch. Unfortunately, due to complications during drilling, penetration and sampling of the fault patch involved in repeating rupture was not possible, though core sampling and installation of seismic instrumentation in the region adjacent to the repeating patch was achieved. Current efforts are focused on long-term monitoring of the ongoing chemical, physical, seismological, and deformational properties in the zone (particularly any signals that might be associated with the next repeat of the SAFOD repeating sequences).

HRSN activities this year have contributed in three principal ways to these and longer-term SAFOD monitoring efforts:

- 1) Processing of integrated HRSN and USGS data streams in the Parkfield area continues, effectively doubling the number of small events available for monitoring seismicity in the SAFOD target zone and for constraining relative locations of the ongoing seismic activity.

- 2) Telemetry of all HRSN channels (both 20 and 250 sps data streams) continues to flow directly from Parkfield, through the USGS Parkfield T1 and the Northern California Earthquake Management Center (NCEMC) T1, to the USGS and the BSL for near real-time processing, catalog processing, and data archiving on the Web-based NCEDC. This also provides near-real-time access of the HRSN data to the SAFOD community without the week- or month-long delay associated with the previous procedure of having to transport DLT tapes to Berkeley to upload and quality check the data.

- 3) Continued monitoring and expansion of our repeating (characteristic and similar event sequences) catalog has taken place this year, with particular focus on expansion and refinement of repeating event data within the 1.5 cubic km volume centered on the SAFOD target zone. This year, we expanded the number of repeating sequence reference patterns in this zone from 3 to 18 and have cataloged (detected, double-difference relocated, and determined magnitudes for) over 1200 earthquakes within this small volume. The pattern matching approach to detection is prone to identifying the same event from more than one reference earthquake, so a procedure was also developed this year to remove redundant events from the over-all catalog. A procedure was also developed to integrate arrival time information from the redundant pattern matches to improve connectivity of events from different similar event sequences in the double-difference relocations.

4.4 Acknowledgments

Under Robert Nadeau's and Doug Dreger's general supervision, Bill Karavas, Taka'aki Taira, Doug Neuhauser, and Peter Lombard all contribute to the operation of the HRSN. Robert Nadeau prepared this section with help from Taka'aki Taira. During this reporting period, operation, maintenance, and data processing for the HRSN project was supported by the USGS, through grant G10AC00093. Additional improvements in the power and telemetry systems were funded under the USGS ARRA grant G09AC00487.

4.5 References

- Bakun, W. H., and A. G. Lindh, The Parkfield, California, prediction experiment, *Earthq. Predict. Res.*, *3*, 285-304, 1985.
- Hickman, S., M.D. Zoback and W. Ellsworth, Introduction to special section: Preparing for the San Andreas Fault Observatory at Depth, *Geophys. Res. Lett.*, *31*, L12S01, doi:10.1029/2004GL020688, 2004.
- Michellini, A. and T.V. McEvilly, Seismological studies at Parkfield: I. Simultaneous inversion for velocity structure and hypocenters using B-splines parameterization, *Bull. Seismol. Soc. Am.*, *81*, 524-552, 1991.
- Nadeau, R.M. and D. Dolenc, Nonvolcanic Tremors Deep Beneath the San Andreas Fault, *SCIENCE*, *307*, 389, 2005.
- Shelly, D.R., W.L. Ellsworth, T. Ryberg, C. Haberland, G.S. Fuis, J. Murphy, R.M. Nadeau and R. Bürgmann, Precise location of San Andreas Fault Tremors near Cholame, California using seismometer clusters: Slip on the deep extension of the fault?, *Geophys. Res. Lett.*, *36*, L01303, doi:10.1029/2008GL036367, 2009.
- Thurber, C., H. Zhang, F. Waldhauser, J. Hardebeck and A. Michael, Three-dimensional compressional wavespeed model, earthquake relocations, and focal mechanisms for the Parkfield, California region, *Bull. Seismol. Soc. Am.*, *96*, S38-S49, doi:10.1785/0120050825, 2006.
- Zhang, H., R.M. Nadeau and M.N. Toksoz, Locating non-volcanic tremors beneath the San Andreas Fault using a station-pair double-difference location method, *Geophys. Res. Lett.*, *37*, L13304, doi:10.1029/2010GL043577, 2010.

5 Bay Area Regional Deformation Network

5.1 Background

The Bay Area Regional Deformation (BARD) network is a collection of permanent, continuously operating GPS receivers that monitors crustal deformation in the San Francisco Bay Area (SFBA) and Northern California. Started in 1991 with two stations spanning the Hayward Fault, BARD has been a collaborative effort of the Berkeley Seismological Laboratory (BSL), the USGS at Menlo Park (USGS/MP), and several other academic, commercial, and governmental institutions. The BARD network is designed to study the distribution of deformation in Northern California across the Pacific-North America plate boundary and interseismic strain accumulation along the San Andreas fault system in the Bay Area for seismic hazard assessment, and to monitor hazardous faults and volcanoes for emergency response management. The BSL maintains and/or has direct continuous telemetry from 29 stations comprising the BARD Backbone (Table 3.11), while additional stations operated by the USGS, US Coast Guard and others fill out the extended BARD network. Fifteen BARD Backbone sites are collocated with broadband seismic stations of the BDSN, with which they share continuous telemetry to UC Berkeley (Table 3.11). Four additional sites, all collocated with BDSN stations, are scheduled to be installed in the next several months, under ARRA funding.

With the completion of major construction on the Plate Boundary Observatory (PBO) portion of EarthScope, the number of GPS stations in Northern California has expanded to over 250 (Figure 3.22), and a number of BARD stations were folded into the PBO network. Together, PBO and BARD stations provide valuable information on the spatial complexity of deformation in the SFBA and Northern California, while the BARD network has the infrastructure and flexibility to additionally provide information on its temporal complexity over a wide range of time scales and in real time. Many of the GPS stations in the BARD network are collocated with BDSN seismic instrumentation or are close to active faults where reliable access to real-time information could be critical following an earthquake.

The BSL received funding through the American Recovery and Reinvestment Act (ARRA) to upgrade 16 BARD sites with modern receivers (Topcon Net-3GA) that provide BINEX data streams with 1 Hz sampling over TCP/IP. The new receivers are also capable of recording L5 data in addition to L1 and L2; L5 is a third frequency that will be added to GPS satellites in the coming years. The BSL also received ARRA funding to install seven new stations at existing BDSN stations (Table 3.11), thereby taking advantage of shared telemetry.

Three of these stations (GASB, MNRC, WDCB) have already been installed, while four (HAST, HELL, JRSC, MCCM) will be constructed in the next couple of months.

All BARD Backbone stations now collect data at 1 Hz sampling frequency (Table 3.11). The data are collected continuously, as opposed to on a triggered basis, and transmitted to the BSL. The effort to expand the high-rate data collection was helped by upgrades over the past several years at 13 stations to Trimble NetRS receivers and to ARRA-funded Topcon Net-3GA receivers at an additional 12. The NetRS receivers feature a compact data stream, which has allowed us to collect high-rate data from locations with limited bandwidth telemetry. Furthermore, IP connectivity on the NetRS and Net-3GA facilitates streaming of data over a Ntrip server to other agencies and the general public. Data streams from NetRS and Net-3GA equipped BARD stations are currently available (<http://seismo.berkeley.edu/bard/realtime>).

5.2 BARD overview

BARD station configuration

Thirteen BARD stations are currently equipped with high performance Trimble NetRS receivers, which have sufficient internal buffering to allow robust real-time telemetry at 1 Hz. Recent upgrades include stations SUTB in March 2010 and MHCB in October 2010. Twelve additional stations have been upgraded in the last year from older Ashtech Z-12 (A-Z12) or Ashtech MicroZ-CGRS (A-UZ) receivers to Topcon Net-G3As as part of the ARRA program. The new receivers replaced ones which were connected directly via serial connection and were thus susceptible to data loss during telemetry outages. With the upgraded receivers, we are more able to provide complete daily data. We are also able to finally upgrade the last two low-rate stations to high data collection rate (LUTZ, SODB), such that the entire BARD network now streams, collects and archives data at 1 Hz.

All BARD stations are continuously telemetered to the BSL. Many use frame relay technology, either alone or in combination with radio telemetry. Other methods include a direct radio link to Berkeley (TIBB, EBMD) and satellite telemetry. At MODB, we are able to telemeter 1 Hz data using the USGS VSAT system that collects seismic broadband data as part of the National Seismic Network (NSN). We also changed our data strategy by allowing some data to be transferred by web-based telemetry (ADSL lines). This will reduce our communication operational costs and, we hope, will not affect our ability to react in a large event.

BARD station monumentations broadly fall into three

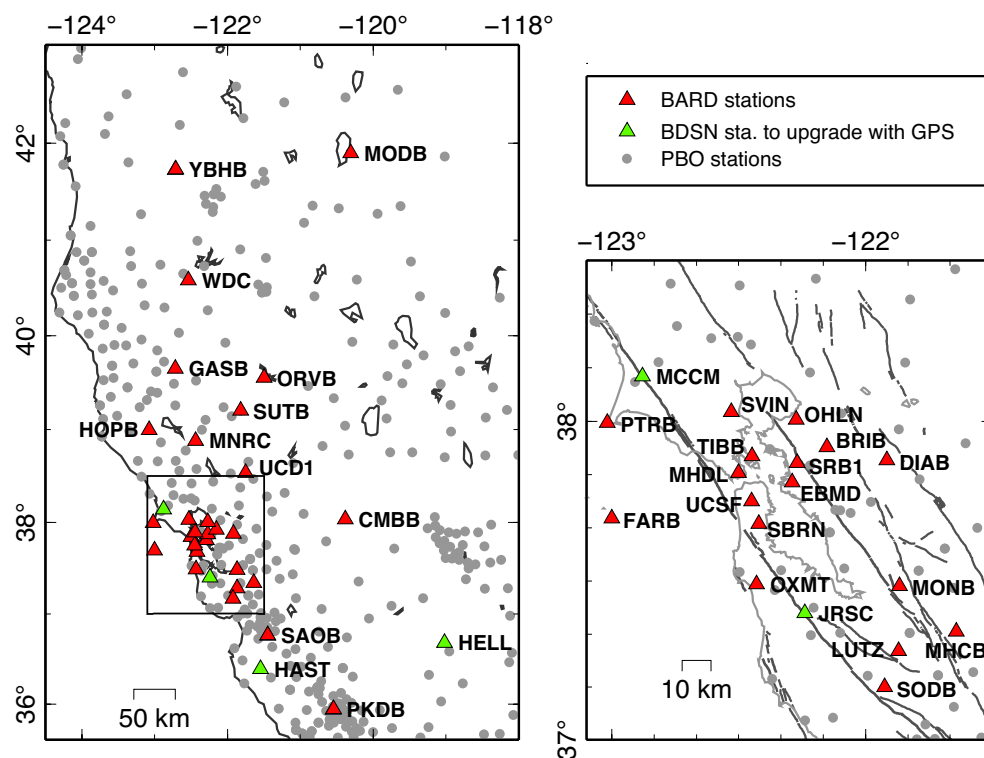


Figure 3.22: Map of the BARD Backbone network and surrounding PBO sites in Northern California.

types. Most are anchored into bedrock, either directly or via a steel-reinforced concrete cylinder. The five “mini-PBO” stations that are still operated by the BSL are collocated with USGS strainmeters and the GPS antennas are bolted onto the borehole casing using an experimental mount developed at the BSL, which has since been adopted by PBO for their strainmeter sites. Four sites (UCD1, SRB1, UCSF, SBRB) are located on the roofs of buildings. Most of the last type have been installed in the past three years, and their stability over long periods of time is yet to be evaluated.

Most BARD stations use a radome-equipped, low-multipath choke-ring antenna, designed to provide security and protection from weather and other natural phenomena, and to minimize differential radio propagation delays. Two stations are equipped with Trimble Zephyr Geodetic antennas, though these are scheduled to be upgraded to choke-rings under ARRA funding. A low-loss antenna cable is used to minimize signal degradation on the longer cable setups that normally would require signal amplification. Low-voltage cutoff devices are installed to improve receiver performance following power outages.

Data Archival

Raw and RINEX data files from the 29 BARD backbone stations and several other stations run by BARD collaborators are archived at the Northern California Earthquake Data Center (NCEDC). The data are

checked to verify their integrity, quality, completeness, and conformance to the RINEX standard, and are then made accessible, usually within 2 hours of the end of the UTC day, to all BARD participants and other members of the GPS community through the Internet, both by anonymous FTP and through the World Wide Web (<http://ncedc.org/>). BARD data are also available to the community through GPS Seamless Archive Centers (GSAC), such as that hosted by the Scripps Orbit and Permanent Array Center (SOPAC, <http://gsac.ucsd.edu>). High-rate raw data are also decimated to create 15 s RINEX data files. 1 Hz RINEX files are available for all BARD Backbone sites after May 2010.

As part of the activities funded by the USGS through the BARD network, the NCEDC has established an archive of the 10,000+ survey-mode occupations collected by the USGS since 1992. The NCEDC continues to archive non-continuous survey GPS data. The initial dataset archived is the survey GPS data collected by the USGS Menlo Park for Northern California and other locations. The NCEDC is the principal archive for this dataset. Quality control efforts were implemented by the NCEDC to ensure that raw data, scanned site log sheets, and RINEX data are archived for each survey. All of the USGS/MP GPS data has been transferred to the NCEDC, and virtually all of the data from 1992 to the present has been archived and is available for distribution. These survey-mode data are used together with

	Sites	Lat. (deg.)	Lon. (deg)	Receiver	Telem.	Sampling rate	Collocated Network	Location
1	BRIB	37.91	-122.15	NETRS	T1	1 Hz	BDSN	Briones Reservation, Orinda
2	CMBB	38.03	-120.39	NET-G3A	FR	1 Hz	BDSN	Columbia College, Columbia
3	DIAB	37.87	-121.92	NETRS	FR	1 Hz		Mt. Diablo
4	EBMD	37.81	-122.28	T-5700	R	1 Hz		East Bay Mud Headquarters
5	FARB	37.69	-123.00	NETRS	R-FR/R	1 Hz	BDSN	Farallon Island
6	GASB	39.65	-122.72	NET-G3A	FR	1 Hz	BDSN	Alder Springs, CA
7	HOPB	38.99	-123.07	T-SSI	FR	1 Hz	BDSN	Hopland Field Stat., Hopland
8	LUTZ	37.28	-121.87	NET-G3A	FR	1 Hz	BDSN	SCC Comm., Santa Clara
9	MHCB	37.34	-121.64	NETRS	FR	1 Hz	BDSN	Lick Obs., Mt. Hamilton
10	MHDL	37.84	-122.49	NETRS	FR	1 Hz	mini-PBO	Marin Headlands
11	MNRC	38.88	-122.44	NET-G3A	FR	1 Hz	BDSN	McLaughlin Mine, CA
12	MODB	41.90	-120.30	NETRS	VSAT	1 Hz	BDSN	Modoc Plateau
13	MONB	37.48	-121.87	A-Z12	FR	1 Hz		Monument Peak, Milpitas
14	OHLN	38.00	-122.27	NET-G3A	FR	1 Hz	mini-PBO	Ohlone Park, Hercules
15	ORVB	39.55	-121.50	NETRS	FR	1 Hz	BDSN	Oroville
16	OXMT	37.49	-122.42	NET-G3A	FR	1 Hz	mini-PBO	Ox Mountain
17	PKDB	35.94	-120.54	NETRS	FR	1 Hz	BDSN	Bear Valley Ranch, Parkfield
18	PTRB	37.99	-123.01	NET-G3A	R-FR	1 Hz		Point Reyes Lighthouse
19	SAOB	36.76	-121.45	NETRS	FR	1 Hz	BDSN	San Andreas Obs., Hollister
20	SBRN	37.69	-122.41	A-Z12	FR	1 Hz	mini-PBO	San Bruno
20	SBRB	37.69	-122.41	NET-G3A	FR	1 Hz	mini-PBO	San Bruno Replacement
21	SODB	37.17	-121.93	NET-G3A	R-FR	1 Hz		Soda Springs, Los Gatos
22	SRB1	37.87	-122.27	NET-G3A	FR	1 Hz		Seismic Replace. Bldg., Berkeley
23	SUTB	39.20	-121.82	NETRS	R-FR	1 Hz	BDSN	Sutter Buttes
24	SVIN	38.03	-122.53	NET-G3A	R-FR	1 Hz	mini-PBO	St. Vincents
25	TIBB	37.89	-122.45	A-UZ12	R	1 Hz		Tiburon
26	UCD1	38.53	-121.75	NETRS	WEB	1 Hz		UC Davis, Davis
27	UCSF	37.75	-122.46	NETRS	FR	1 Hz		UC San Francisco, San Francisco
28	WDC	40.58	-122.54	NET-G3A	FR	1 Hz	BDSN	Whiskeytown Dam, Whiskeytown
29	YBHB	41.73	-122.71	NETRS	FR	1 Hz	BDSN	Yreka Blue Horn Mine, Yreka
30	HAST	36.39	-121.55				BDSN	UC Hastings Preserve
31	HELL	36.68	-119.02				BDSN	Rademacher Property, Miramonte
32	JRSC	37.4	-122.24				BDSN	Jasper Ridge Biol. Preserve
33	MCCM	38.14	-122.88				BDSN	Marconi Conference Center

Table 3.11: List of BARD stations maintained by the BSL. Six models of receiver are operating now: Trimble NetRS, (NETRS), Topcon Net-G3A (NET-G3A), Ashtech Z12 (A-Z12), and Ashtech Micro Z (A-UZ12), Trimble 4000 SSI (T-SSI), Trimble 5700 (T-5700). The telemetry types are listed in column 6: FR = Frame Relay, R = Radio, VSAT= Satellite, WEB = DSL line. Some sites are transmitting data over several legs with different telemetry. Sites 30 to 33 will be installed before 12/31/11 under ARRA funding. Site SBRN is listed above, but has been replaced by site SBRB.

data from BARD and PBO stations to produce BAVU (Bay Area Velocity Unification), a united set of continuous and survey data from the wider San Francisco Bay Area, processed under identical conditions using GAMIT (*d'Alessio et al.*, 2005).

Data from five of our sites (HOPB, MHCB, CMBB, OHLN, and YBHB) are sent to the National Geodetic Survey (NGS) in the framework of the CORS (Continuous Operating Reference Stations) project (<http://www.ngs.noaa.gov/CORS/>). The data from these five sites are also distributed to the public through the CORS FTP site.

Real-time streaming

By 12/31/2010, all BARD stations will be available in real time with 1 Hz data sampling; a step toward our goal of integrating GPS with the Northern California Seismic System (NCSS) for use in hazard assessment and emergency response. The streams are available in BINEX and RTCM formats from a Ntrip caster operated by the BSL (<http://seismo.berkeley.edu/bard/realtime>) As each station has been upgraded to a Net-G3A receiver over the past year, its data stream has been added to the Ntrip caster, with the result that we are currently short only 3 stations. At the end of the ARRA

program, all BARD stations will be streaming data to the public in real time.

Data Processing

Average station coordinates are estimated from 24 hours of observations for BARD stations and other nearby continuous GPS sites using the GAMIT/GLOBK software developed at MIT and SIO (King and Bock, 1999, Herring, 2005). GAMIT uses double-difference phase observations to determine baseline distances and orientations between ground-based GPS receivers. Ambiguities are fixed using the widelane combination followed by the narrowlane, with the final position based on the ionospheric free linear combination (LC or L3). Baseline solutions are loosely constrained until they are combined together. GAMIT produces solutions as H-files, which include the covariance parameters describing the geometry of the network for a given day and summarize information about the sites.

We combine daily, ambiguity-fixed, loosely constrained H-files using the Kalman filter approach implemented by GLOBK (Herring, 2005). They are combined with solutions from the IGS global network and PBO and stabilized in an ITRF2005 reference frame. The estimated relative baseline determinations typically have 2-4 mm long-term scatter in the horizontal components and 10-20 mm scatter in the vertical. The most recent velocity solutions (Houlié and Romanowicz, in press, Figure 3.23) are in good agreement with previous work (e.g. d'Alessio et al., 2005).

ARRA activities

A major activity of the last year has been work performed under the ARRA program to upgrade BARD infrastructure, including upgraded equipment at nearly half the BARD network stations. The receivers at twelve BARD stations have been upgraded with Topcon Net-G3A receivers and are now both collecting and streaming data at 1 Hz sampling rate. During the course of the upgrades, site SBRN was decommissioned and has been officially replaced by site SBRB. SBRB was installed after vandalism at SBRN caused an extended data outage and has been running in tandem with SBRN for over a year. BSL engineers have also installed three new stations (WDCB, GASB, MNRC); all collocated with BDSN seismometers and now collecting and streaming data at 1 Hz. WDCB, near Whiskeytown in Northern California (Figure 3.22) is a short-brace monument anchored 10 feet into the substrate, and GASB and MNRC are both mounted on top of BDSN seismic vaults. The vaults are constructed by excavating to bedrock, installing a strong frame (overturned shipping container) and cementing the frame to the surrounding rock. The GPS antennas are installed on posts embedded in the vault walls at the time of construction (Figure 3.24).

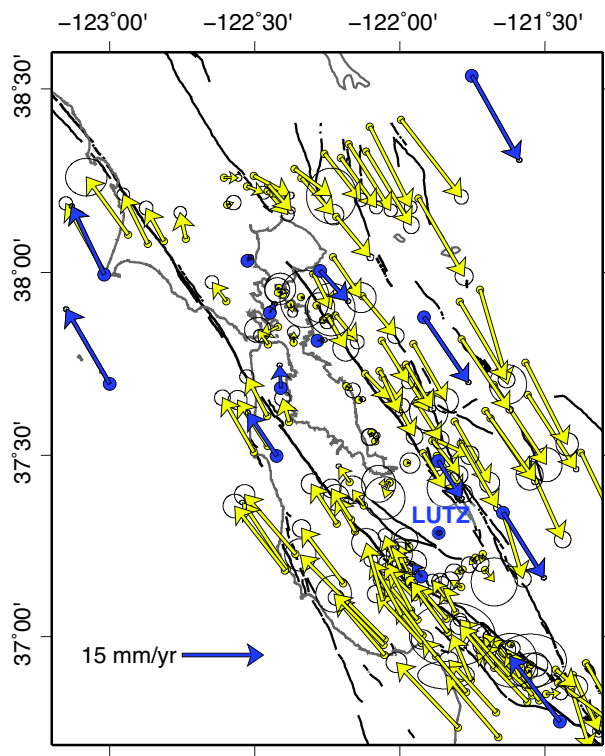


Figure 3.23: Site velocities from BAVU2 within the SFBA, including BARD (in blue), PBO and campaign stations. Shown relative to station LUTZ. BAVU website: <http://seismo.berkeley.edu/~burgmann/RESEARCH/BAVU/>

In addition to the equipment upgrades, the ARRA program also funded the re-establishment of daily processing and time-series generation for BARD backbone stations and upgrades to the BARD website. Daily processing ensures that bad data is caught quickly and problems can be fixed in a timely manner. Each day of data is processed twice, first with IGS Rapid orbit files within 24 hours of collection and again after IGS Final orbit files are available, using within 2-3 weeks. BARD rapid solutions are used to generate a new data point in the station displacement series right away and IGS global solutions and PBO network solutions are combined in when they are available and provide improved constraints to the time series. Final time series displacements are held until BARD final solutions, IGS, and PBO final network solutions are all available.

Figure 3.25 shows the time series for station FARB on the Farallon Islands, in the ITRF2005 reference frame, for 11/1/2010 through 7/26/2011, as produced on 7/27/2011. The time series has been cleaned by removing common mode errors, which were determined using all BARD backbone and extended stations. Overall scatter is very low, as would be expected for a time period with no major or moderate events, with root mean square



Figure 3.24: Site GASB in Alder Springs, CA. Left: Wide view showing seismic vault, which is cemented to bedrock. Right: Close-up of monument during pouring of stabilizing cement; the central support mast was embedded in the wall of the seismic vault during construction.

(RMS) values of 1.1 mm, 0.9 mm, and 4.3 mm for the North, East and Up directions, respectively. The scatter in the data is not dramatically affected by being processed with ISG rapid orbit files (green points) or when not combined with PBO solutions, though the calculated error bars are affected.

The BARD webpage (<http://seismo.berkeley.edu/bard>) has also been redesigned and upgraded to provide more information on individual stations. In addition to daily-updated plots of raw, cleaned and detrended station displacements, the web pages also include plots of data completeness (how many epochs are present in the data files) and estimated multipath for the L1 and L2 signals. These are also updated daily and provide a measure of the antenna and telemetry performance and of the effect of the surroundings on the data quality. Changes to these values correspond to equipment changes, equipment failure and changes to the environment surrounding the site. The last is particularly important, as changes such as construction or tree removal can occur near a station without the BSL's knowledge.

5.3 Acknowledgements

The BARD program is overseen by Barbara Romanowicz and Ingrid Johanson. Rich Clymer, Bill Karavas, Rick Lellinger, John Friday, Joshua Miller, Doug Neuhauser, Mario Aranha and Jennifer Taggart contributed to the operation of the BARD network in 2010-11. Operation of the BARD network is partially supported by funding from the USGS/NEHRP program grant #G10AC00141 and infrastructure upgrades were made possible by funding from the ARRA grant #G10AC00079.

5.4 References

d'Alessio, M. A., I. A. Johanson, R. Bürgmann, D. A. Schmidt, and M. H. Murray, Slicing up the San Francisco Bay Area: Block kinematics from GPS-derived surface velocities,

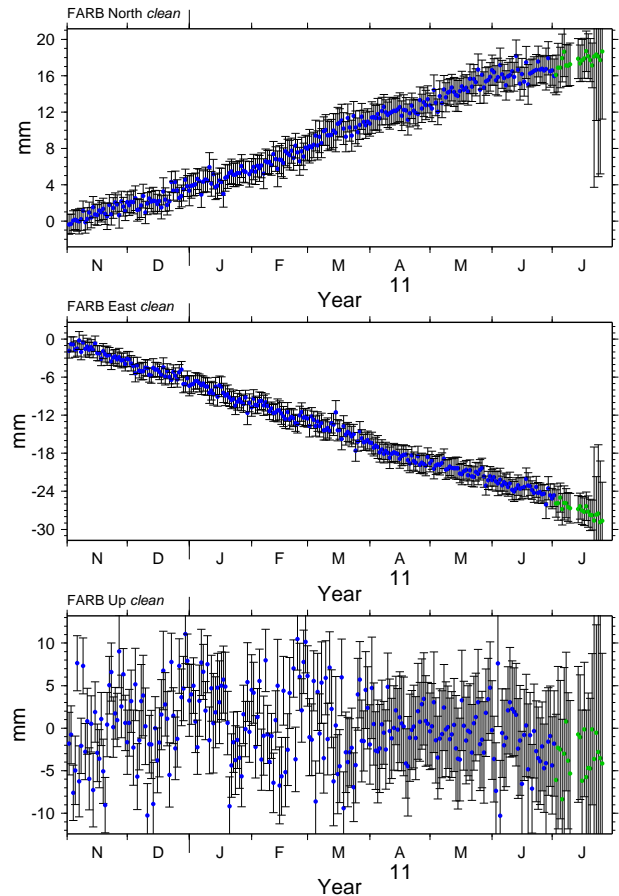


Figure 3.25: Station displacements for station FARB (on the Pacific plate) in the ITRF2005 reference frame, for November 2010-July 2011. Time series are cleaned by removing outliers and applying a common mode filter constructed from all BARD stations. Green points are those determine from processing with Rapid orbit files; large error bars in the latest days indicate that IGS and/or PBO solutions have not yet been included in the GLOBK combination. Black points are fully processed, with final orbits and all combined solutions.

J. Geophys. Res., 110, B06403, doi:10.1029/2004JB003496, 2005.

Herring, T., GLOBK: Global Kalman Filter: VLBI and GPS Analysis Program, version 10.2, 2005.

Houlié, N. and Romanowicz, B., Asymmetric deformation across the San Francisco Bay Area faults from GPS observations in northern California, *Phys. Earth Planet. In.*, in press.

King, R., and Y. Bock, Documentation of the GAMIT software, MIT/SIO, 1999.

6 Northern California Earthquake Data Center

6.1 Introduction

The Northern California Earthquake Data Center (NCEDC), a joint project of the Berkeley Seismological Laboratory (BSL) and the U.S. Geological Survey at Menlo Park, serves as an online archive and distribution center for various types of digital data relating to earthquakes in Central and Northern California. The NCEDC is located at the Berkeley Seismological Laboratory, and has been accessible to users via the Internet since mid-1992.

The primary goal of the NCEDC is to provide a stable and permanent archival and distribution center of digital geophysical data for networks in Northern and Central California. These data include seismic waveforms, electromagnetic data, GPS data, strain, creep, and earthquake parameters. The seismic data comes principally from the Berkeley Digital Seismic Network (BDSN) operated by the Berkeley Seismological Laboratory, the Northern California Seismic Network (NCSN) operated by the USGS, the Berkeley High Resolution Seismic Network (HRSN) at Parkfield, the EarthScope USArray Transportable Array stations in Northern California, the various Geysers networks, and selected stations from adjacent networks such as the University of Nevada, Reno network and the Southern California Seismic Network (SCSN). GPS data are primarily from the Bay Area Regional Deformation (BARD) GPS network, the USGS Cascade Volcano Observatory (CVO) in Long Valley, and the USGS/Menlo Park GPS surveys. The collection of NCSN digital waveforms dates from 1984 to the present, the BDSN digital waveforms date from 1987 to the present, and the BARD GPS data date from 1993 to the present. The BDSN includes stations that form the specialized Northern Hayward Fault Network (NHFN) and the MiniPBO (mPBO) borehole seismic and strain stations in the San Francisco Bay Region. Additional seismic and strain data from the EarthScope Plate Boundary Observatory (PBO) and the San Andreas Fault Observatory at Depth (SAFOD) are also archived at the NCEDC. Figure 3.28 shows the total data volume by year, as itemized in Table 3.12.

The NCEDC also provides support for earthquake processing and archiving activities of the Northern California Earthquake Management Center (NCEMC), a component of the California Integrated Seismic Network (CISN). The CISN is the California regional organization of the Advanced National Seismic System (ANSS).

Figure 3.27 shows the location of stations archived at the NCEDC (excluding EarthScope stations located outside of CA).

6.2 2010-2011 Activities

By its nature, data archiving is an ongoing activity. In 2010-2011, the NCEDC continued to expand its data holdings and enhance access to the data. Projects and activities of particular note include:

- Distributed over 5,550 GB of waveform data to external users.
- Announced and provided users with the Simple Waveform Client *swc* for interactively or programmatically retrieving waveform data from the Simple Waveform Servers *sws* for the DART and NCEDC Data Archive.
- Started developing and testing Web services for the distribution of station metadata using Station XML.
- Began streaming and providing access to real-time 1 Hz GPS data from 42 stations in Northern California.
- Received grant and began work on a DOE funded project through LBNL to archive and distribute event parameters and time series under the DOE Geothermal Monitoring Program.
- Continued the process of reading and archiving continuous NCSN seismograms from tapes for 1995-2000.
- Continued to support the NCEMC earthquake analysis by providing real-time access to earthquake parameters and waveforms from the NCEDC for the CISN *Jiggle* earthquake review software.
- Continued work with the NCSN and USGS National Strong Motion Program (NSMP) to house the metadata and build dataless SEED volumes for all NSMP dialup stations.

6.3 BDSN/NHFN/mPBO Seismic Data

The BDSN (Operational Section 1), NHFN (Operational Section 3), and Mini-PBO (Operational Section 3) stations (all network code BK) telemeter data from 50 seismic data loggers in real time to the BSL. These data are written to disk files, used for CISN real-time earthquake processing and earthquake early warning (EEW) development, and delivered in real time to the DART (Data Available in Real Time) system at the NCEDC, where they are immediately available to anyone on the

Data Type	GBytes
BDSN/NHFN/mPBO (broadband, electric and magnetic field, strain) waveforms	8,203
NCSN seismograms	30,118
Parkfield HRSN seismograms	3,877
GPS (RINEX and raw data)	2,933
UNR Nevada seismograms	1,580
SCSN seismograms	2,791
Calpine/Unocal Geysers region seismograms	38
EarthScope SAFOD seismograms	2,119
EarthScope USArray seismograms	281
EarthScope PBO strain and seismic waveforms	2,949
PG&E seismograms	688
USGS low frequency geophysical waveforms	3
Misc data	3,245
Total size of archived data	58,825

Table 3.12: Volume of Data Archived at the NCEDC by network.

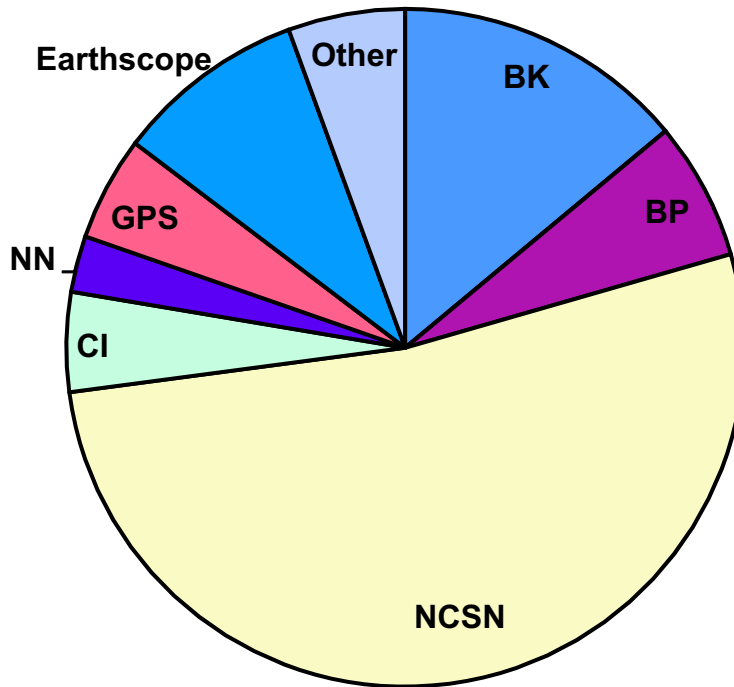


Figure 3.26: Chart showing the relative proportion of each data set at the NCEDC. (BK - Berkeley Digital Seismic Network; BP - Berkeley High-resolution Seismic Network in Parkfield; NC - Northern California Seismic Network and collaborators; CI - Southern California Seismic Network; NN - University of Nevada, Reno Seismic Network; GPS - various GPS datasets, including BARD; EarthScope - data from various EarthScope activities; Other - various small data sets.

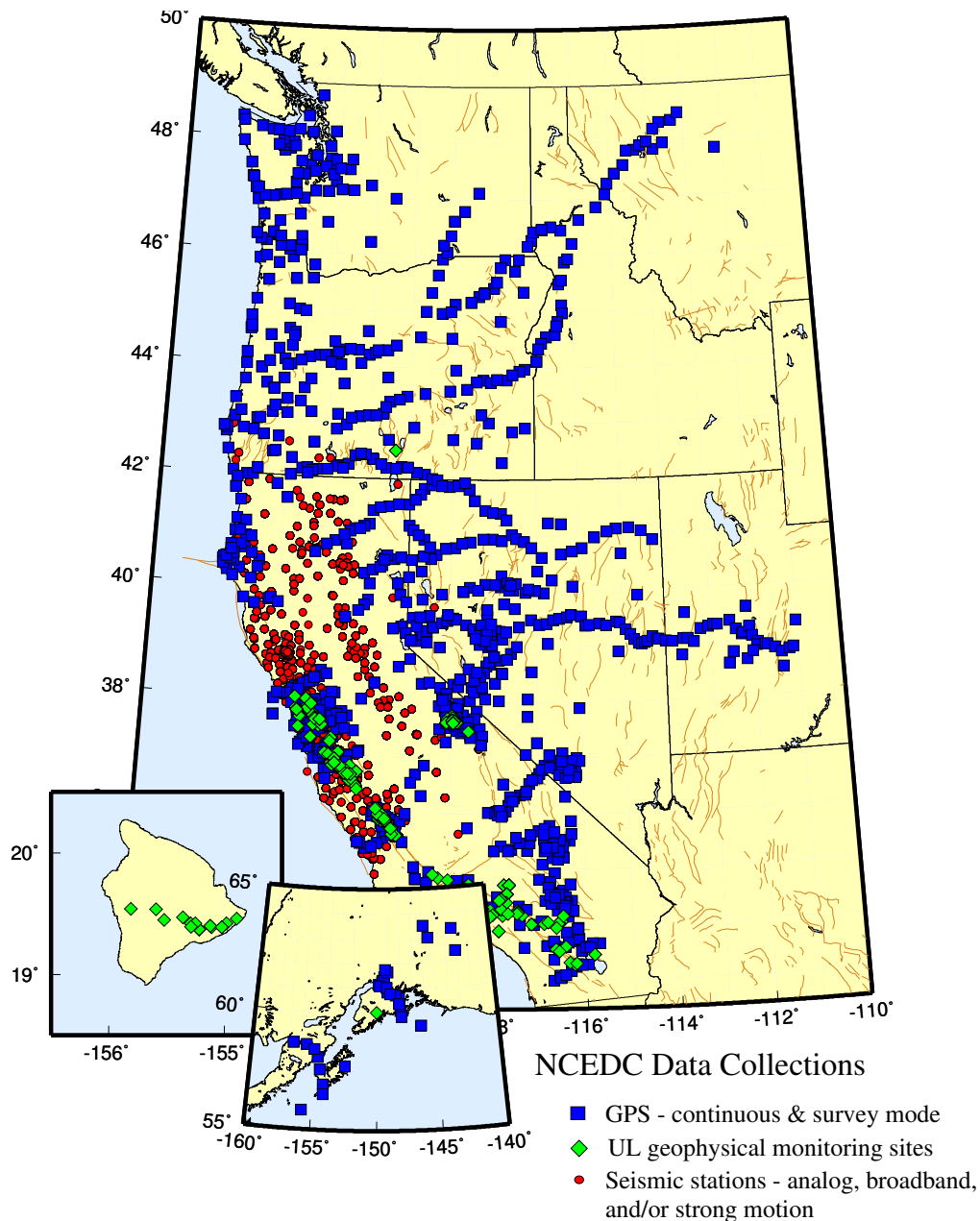


Figure 3.27: Map showing the location of stations whose data are archived at the NCEDC. Circles are seismic sites, squares are GPS sites, and diamonds are the locations of USGS low-frequency experiments.

Internet. Continuous high-rate data (200 - 500 samples/second) are now available for most of the NHFN borehole seismic data channels. All timeseries data from the Berkeley networks continue to be processed and archived by an NCEDC analyst using *calqc* in order to provide the highest quality and most complete data stream to the NCEDC.

NCSN Seismic Data

NCSN continuous waveform data are transmitted from USGS/Menlo Park in real time to the NCEDC via the Internet, converted to MiniSEED, and made available to users immediately through the NCEDC DART. NCSN event waveform data, as well as data from all other real-time BSL and collaborating networks, are automatically collected by the NCEMC waveform archiver and stored at the NCEDC for event review and analysis and for

distribution to users. All NCSN and NCEMC data are archived in MiniSEED format.

The NCEDC also maintains a list of historic teleseismic events recorded by the NCSN, since these events do not appear in the NCSN catalog.

A description of the successive improvements in the acquisition of NCSN data, leading to the acquisition of complete NCSN waveform data in early 2006, can be found in the 2005-06 BSL Annual Report. We finished the first phase of the NCSN continuous waveform archiving project by reading, converting and archiving NCSN seismograms from all available NCSN tapes for mid-2001 through early 2006. We are continuing this project by processing and archiving NCSN tape data from 1995 through 2000.

Parkfield High Resolution Seismic Network Data

The history of upgrades to the acquisition and archival of HRSN data can be found in the 2005-06 BSL Annual Report. We continue to archive continuous 250 and 20 sample-per-second data from the HRSN stations.

EarthScope Plate Boundary Observatory (PBO) Strain Data

The NCEDC is one of two funded archives for PBO EarthScope borehole and laser strain data. Strain data are collected from all of the PBO strain sites and are processed by UNAVCO. MiniSEED data are delivered to the NCEDC using SeedLink, and raw and XML processed data are delivered to the NCEDC using Unidata's Local Data Manager (LDM). The MiniSEED data are inserted into the NCEDC DART and are subsequently archived from the DART. UNAVCO provides EarthScope funding to the NCEDC to help cover the processing, archiving, and distribution costs for these data. In early 2010, the NCEDC began receiving and archiving all of the continuous seismic waveform data from the PBO network to complement the PBO strain data. The seismic data are received from an Antelope ORB server at UNAVCO and converted from their native format to MiniSEED on a data import computer. The data are then transferred via the SEEDLink protocol to the NCEDC, inserted into the NCEDC DART for immediate Internet access, and subsequently archived from the DART.

EarthScope SAFOD

The NCEDC is an archive center for the SAFOD event data and has also processed the continuous SAFOD data. Starting with the initial data in July 2002 from the SAFOD Pilot Hole, and later data from the SAFOD Main Hole, the NCEDC converted data from the original SEG-2 format data files to MiniSEED, and developed the SEED instrument responses for this data set. Continuous 4 KHz data from SAFOD written to tape

at SAFOD were periodically sent to the BSL to be converted, archived, and forwarded to the IRIS DMC (IRIS Data Management Center). SAFOD EarthScope funding to the NCEDC is to cover the processing, archiving, and distribution costs for these data. A small subset of the continuous SAFOD data channels are also incorporated into the NCSN, are available in real-time from the NCEDC DART, are archived at the NCEDC, and are forwarded to the IRIS DMC. After the failure of the SAFOD permanent instrument in September 2008, the USGS deployed a temporary network in the Main Hole, and the NCEDC continued to process and archive these data. Both the permanent and temporary seismic instruments were removed in mid-2010 in order to analyze the failure of the permanent SAFOD instrument packet, but the temporary seismic instruments were reinstalled in late 2010 and continue to send data for distribution and archiving to the NCEDC.

UNR Broadband Data

The University of Reno in Nevada (UNR) operates several broadband stations in western Nevada and eastern California that are important for Northern California earthquake processing and analysis. Starting in August 2000, the NCEDC has been receiving and archiving continuous broadband data from four UNR stations. The data are transmitted in real time from UNR to UC Berkeley, where they are made available for CISN real-time earthquake processing and for archiving. Initially, some of the stations were sampled at 20 Hz, but all stations are now sampled and archived continuously at 100 Hz.

The NCEDC installed Simple Wave Server (SWS) software at UNR, which provides an interface to UNR's recent collection of waveforms. The SWS is used by the NCEDC to retrieve waveforms from UNR that were missing at the NCEDC due to real-time telemetry outages between UNR and UC Berkeley.

In early 2006, the NCEDC started to archive continuous data from the UNR short-period stations that are contributed to the NCSN. Both the broadband and short-period UNR stations contributed to the CISN are available in real-time through the NCEDC DART.

Electro-Magnetic Data

The NCEDC continues to archive and process electric and magnetic field data acquired at several UC Berkeley sites. The BSL operates both magnetic and electric field sensors at SAO. However, most of these channels have been down for repair during the 2010-2011 year. Through a collaboration with Dr. Simon Klemperer at Stanford University, we acquire magnetic and electric field channels at BSL sites JRSC and BRIB, and magnetic field channels at site MHDL. The three magnetic field channels and either two or four electric field channels are

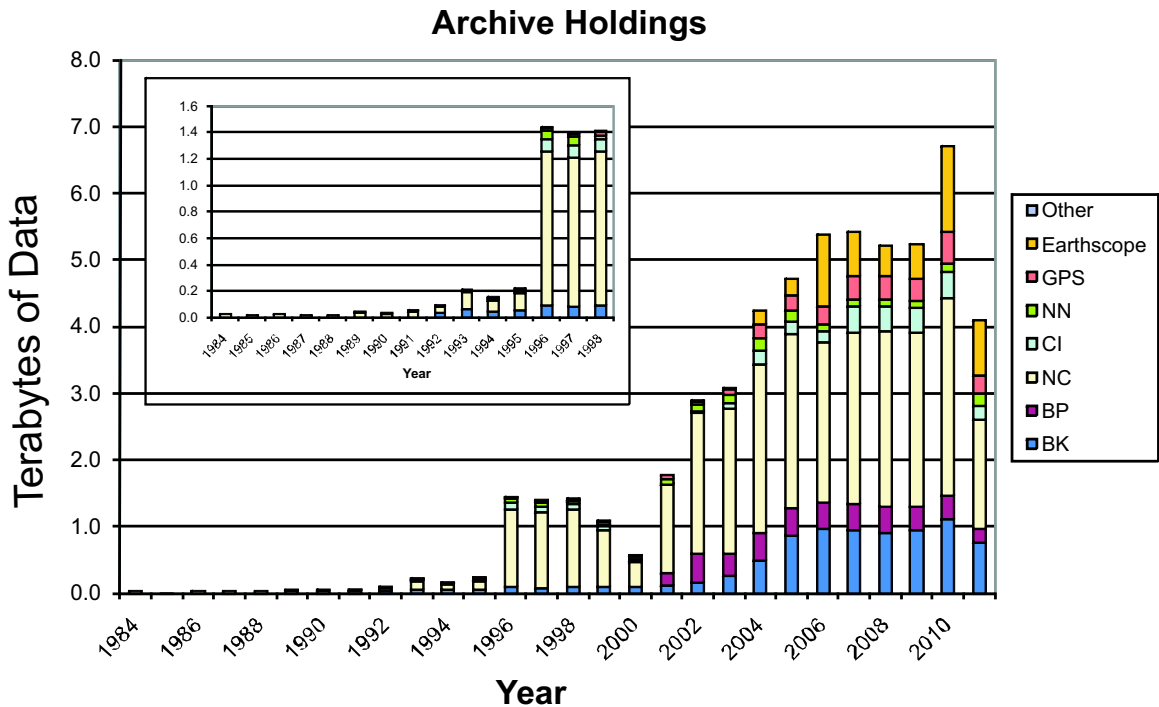


Figure 3.28: Figure showing the total volume of data archived at the NCEDC, broken down by data year.

digitized at 40 Hz, 1 Hz, and 0.1 Hz, and are telemetered in real-time along with seismic data to the Berkeley Seismological Laboratory, where they are processed and archived at the NCEDC in a similar fashion to the seismic data.

GPS Data

The NCEDC continues to archive GPS data through the BARD (Bay Area Regional Deformation) network of continuously monitored GPS receivers in Northern California (Operational Section 5). The NCEDC GPS daily archive now includes 67 continuous sites in Northern California. Of these, there are ~ 31 core BARD sites owned and operated by UC Berkeley, USGS (Menlo Park and Cascade Volcano Observatory), LLNL, UC Davis, UC Santa Cruz, Trimble Navigation, and Stanford. Data are also archived from sites operated by other agencies, including the East Bay Municipal Utilities District, the City of Modesto, the National Geodetic Survey, and the Jet Propulsion Laboratory.

In addition to the standard 15 second continuous GPS data files, the NCEDC is now archiving and distributing high-rate 1 Hz continuous GPS data from all of the BSL-operated BARD stations. In collaboration with UC San Diego/Scripps Institution of Oceanography (UCSD/SIO), USGS/Pasadena and USGS/MP, the BSL is now streaming real-time 1 Hz continuous data from 42 sites, including all BSL sites and the 13 PBO stations in Parkfield to the BSL, where it makes the data available to researchers in real time through an Ntripcaster.

The NCEDC also archives non-continuous survey GPS data. The initial dataset archived is the survey GPS data collected by the USGS Menlo Park for Northern California and other locations. The NCEDC is the principal archive for this dataset. Significant quality control efforts were implemented by the NCEDC to ensure that the raw data, scanned site log sheets, and RINEX data are archived for each survey.

Geysers Seismic Data

The Calpine Corporation operated a micro-seismic monitoring network in the Geysers region of Northern California. Prior to 1999, this network was operated by Unocal. Through various agreements, both Unocal and Calpine have released triggered event waveform data from 1989 through 2000 along with preliminary event catalogs for the same time period for archiving and distribution through the NCEDC. This dataset represents over 296,000 events that were recorded by the Calpine/Unocal Geysers network and are available via research accounts at the NCEDC.

The Lawrence Berkeley National Laboratory (LBNL), with funding from the California Energy Commission, currently operates a 22 station network in the Geysers region with an emphasis on monitoring seismicity related to well water injection. The earthquake locations and waveforms from this network are sent to the NCEDC, and the locations are forwarded to the NCSN so that they can be merged into the NCSN earthquake catalog. In August 2007, the NCSN installed an Earthworm system at

the Geysers to receive continuous LBNL Geysers data, and this system provides event waveforms for events detected by the NCEMC real-time earthquake monitoring and processing system and the corresponding event data archive at the NCEDC. The event data from LBNL Geysers event waveforms collected from April 2004 to August 2007 will be associated with events from the NCSN catalog and will be included with the existing waveforms for these events.

6.4 DOE Geothermal Monitoring Data

Starting in 2010-2011, BSL was funded to archive and disseminate seismic event parameters and corresponding waveform timeseries from monitoring networks operated under the auspices of the US Department of Energy Geothermal Monitoring Program. We are currently working on the first portion of this task, collecting, verifying and managing the metadata required to describe the waveforms and event parameters, and populating the data into the database. The timeseries data, when archived, will be available via our suite of data delivery methods, and the event and parametric information will be available via new web catalog interfaces.

USGS Low Frequency Data

Over the last 35 years, the USGS at Menlo Park, in collaboration with other principal investigators, has collected an extensive low-frequency geophysical data set that contains over 1300 channels of tilt, tensor strain, dilatational strain, creep, magnetic field, and water level as well as auxiliary channels such as temperature, pore pressure, rain and snow accumulation, and wind speed. In collaboration with the USGS, we assembled the requisite information for the hardware representation of the stations and the instrument responses for many channels of this diverse dataset, and developed the required programs to populate and update the hardware database and generate the instrument responses. We developed the programs and procedures to automate the process of importing the raw waveform data and converting it to MiniSEED format. Since these data are delivered to the NCEDC on a daily basis and immediately archived, these data are not inserted into the NCEDC DART.

We have currently archived timeseries data from 887 data channels from 167 sites, and have instrument response information for 542 channels at 139 sites. The waveform archive is updated on a daily basis with data from 350 currently operating data channels. We will augment the raw data archive as additional instrument response information is assembled by the USGS for the channels, and will work with the USGS to clearly define the attributes of the “processed” data channels.

SCSN/Statewide Seismic Data

In 2004, the NCEDC started to archive broadband and strong motion data from 15 SCSN (network CI) stations that are telemetered to the Northern California Management Center (NCEMC) of the California Integrated Seismic Network (CISN). These data are used in the prototype real-time state-wide earthquake processing system and also provide increased coverage for Northern California events. Since the data are telemetered directly from the stations in real time to both the SCSN and to the NCEMC, the NCEDC archives the NCEMC’s copy of the data to ensure that at least one copy of the data will be preserved. Due to reduced state funding, the SCSN has gradually reduced the number of telemetered stations to 12.

In early 2006, the NCEDC started to continuously archive all of the selected SCSN short-period stations that are contributed to the NCSN. All of these data are also available in real time from the NCEDC DART. In 2009, the NCEMC started incorporating data from ~ 25 additional SCSN stations near the southern border of the NCEMC monitoring area in its event waveform collection to provide better azimuthal coverage of events in that area. In 2009-2010, the NCEMC also started retrieving event waveform data from the SCSN for other SCSN stations that are expected to receive signals from Northern California earthquakes. All of these event waveforms are also archived at the NCEDC.

Earthquake Catalogs

Northern California: The NCEDC provides searchable access to both the USGS and BSL earthquake catalogs for Northern and Central California. The “official” UC Berkeley earthquake catalog begins in 1910 and runs through 2003, and the “official” USGS catalog begins in 1966. Both of these catalogs are archived and available through the NCEDC, but the existence of two catalogs has caused confusion among both researchers and the public.

In late 2006, the NCEMC began archiving and distributing a single unified Northern California earthquake catalog in real time to the NCEDC through database replication from the NCEMC’s real-time systems. The NCEDC developed and tested the required programs used to enter all previous NCSN catalog data into the NCEDC database. In 2008, we migrated all of the historic NCSN catalog, phase, and amplitude data from 1967 through 2006 into the NCEMC catalog. In addition, we spent considerable effort addressing the mapping of phase data in the BSL catalog to SEED channel names. We plan to merge the BSL catalog with the NCEMC catalog to form a single unified Northern California catalog from 1910 to the present. The BSL and the USGS have spent considerable effort over the past years to define procedures for merging the data from the

two catalogs into a single Northern and Central California earthquake catalog in order to present a unified view of Northern California seismicity. The differences in time period, variations in data availability, and mismatches in regions of coverage all complicate the task.

Worldwide: The NCEDC, in conjunction with the Council of the National Seismic System (CNSS), produced and distributed a world-wide composite catalog of earthquakes based on the catalogs of the national and various U.S. regional networks for several years. Each network updates their earthquake catalog on a daily basis at the NCEDC, and the NCEDC constructs a composite world-wide earthquake catalog by combining the data, removing duplicate entries that may occur from multiple networks recording an event, and giving priority to the data from each network's *authoritative region*. The catalog, which includes data from 14 regional and national networks, is searchable using a Web interface at the NCEDC. The catalog is also freely available to anyone via FTP over the Internet.

With the demise of the CNSS and the development of the Advanced National Seismic System (ANSS), the NCEDC was asked to update its Web pages to present the composite catalog as a product of the ANSS. This conversion was completed in the fall of 2002. We continue to create, house, distribute, and provide a searchable Web interface to the ANSS composite catalog, and to aid the regional networks in submitting data to the catalog.

6.5 NCEDC Operations

In 2005, the NCEDC relocated its archive and distribution system from McCone Hall to a new state-of-the-art computer facility in a new seismically braced building on the Berkeley campus. The facility provides seismically braced equipment racks, gigabit Ethernet network, air conditioning, and power conditioning. The entire facility is powered by a UPS with generator backup.

The currently installed NCEDC facilities consist of a mass storage environment hosted by a 8-core Sun X4150 computer, a 100 slot LTO3 tape library with two tape drives and a 20 TByte capacity, and 60 TBytes of RAID storage, all managed with the SAM-FS hierarchical storage management (HSM) software. Four additional 8-core Sun computers host the DART data import and distribution servers, the email-based data distribution systems (*NetDC*, *BREQ_FAST*, *EVT_FAST*), and the program and web-based request servers for *FISSURES*, *STP*, and *SWS*, and the *calqc* data quality control processing. Additional SPARC servers are used for the Probability Density Function (PDF) plots for the bulk of the NCEMC waveforms.

In 2008-2009, the tape library was upgraded from LTO2 to LTO3 drives, and all online tape data was re-archived on LTO3 tapes. A DLT tape libraries are used

to read NCSN continuous data tapes. Two 64-bit Linux systems host redundant Oracle databases.

The SAMFS hierarchical storage management (HSM) software used by the NCEDC is configured to automatically create multiple copies of each data file in the archive. The NCEDC creates one copy of each file on an online RAID, a second copy on LTO3 tape (of which the most recent data are stored online in the tape library), and a third copy on LTO2 tape which is stored offline and off-site. All NCEDC data are stored online and are rapidly accessible by users.

The NCEDC operates two instances of its Oracle database, one for internal operations and one for external use for user data queries and data distribution programs, and communicates with a third identical database operated offsite by the USGS in Menlo Park. These three databases are synchronized using multi-master replication.

Data Quality Control

The NCEDC developed a GUI-based state-driven system *calqc* to facilitate the quality control processing that is applied to the continuously archived data sets at the NCEDC.

The quality control procedures for these datasets include the following tasks:

- data extraction of a full day of data,
- quickcheck program to summarize the quality and stability of the stations' clocks,
- determination if there is missing data for any data channel,
- provided procedures to retrieve missing data from the stations and incorporate it into the day's data,
- optional creation of multi-day timeseries plots for state-of-health data channels,
- optional timing corrections for data,
- optional extraction of event-based waveforms from continuous data channels,
- optional repacking of MiniSEED data,
- creating waveform inventory entries in the NCEDC database,
- publishing the data for remote access on the NCEDC.

Calqc uses previously developed programs to perform each function, but it provides a graphical point-and-click interface to automate these procedures, and to provide the analyst with a record of when each process was started, whether it executed correctly, and whether the analyst has indicated that a step has been completed. *Calqc* is used to process all data from the BDSN network, and all continuous broadband data from the NCSN, UNR, SCSN, and HRSN networks that are archived by the NCEDC. The remainder of the continuously archived data are automatically archived without any analyst interaction.

The NCEDC is developing programs and procedures to replace waveforms collected for event analysis in near real-time with QC-ed waveforms from the UCB QC-ed waveform archive. This procedure will also be used to augment the NCSN event-based waveform collection from 1991 to 2006 with the appropriate waveforms from the UCB seismic networks.

6.6 Database Activity

The NCEDC continues to support the Northern California Earthquake Management Center (NCEMC) by providing information and resources vital to the NCEMC's role of rapid earthquake analysis and data dissemination. The NCEDC receives earthquake parametric data in real time from the NCEMC real-time systems and provides real-time access to the NCEDC database for *jiggle*, the CISN event analysis tool. The NCEMC continues to support the maintenance and distribution of the hardware configurations and instrument responses of the UCB, USGS/MP NCSN, and other seismic stations used by the NCEMC. BSL staff currently chairs the CISN Schema Change working group, which coordinates all database schema changes and enhancements within the CISN.

The NCEDC instrument response schema represents full multi-stage instrument responses (including filter coefficients) for the broadband data loggers. The hardware tracking schema represents the interconnection of instruments, amplifiers, filters, and data loggers over time, and is used to describe all of the UC Berkeley and USGS stations and channels archived at the NCEDC.

Database developments in the 2010-2011 year include new sets for associating strong ground motion observations with events, merging of channel table tables for real-time and post-processing applications, and adding additional event types to describe a wider range of earth motions.

Full details on the database schema used at the NCEDC may be found at <http://www.ncedc.org/db>

6.7 Data Distribution

The NCEDC continues to use the Internet as the interface for users to request, search for, and receive data

from the NCEDC. In fall 2005, the NCEDC acquired the domain name *ncedc.org*. The NCEDC's Web address is now <http://www.ncedc.org/> In the 12 months from July 2009 through June 2010, the NCEDC distributed over 5520 GB (5.5 TB) of waveform data to external users.

Earthquake Catalogs

The NCEDC provides users with searchable access to Northern California earthquake catalogs and to the ANSS world-wide catalog via the Web. Users can search the catalogs by time, magnitude, and geographic region, and can retrieve either hypocenter and magnitude information or a full set of earthquake parameters including phase readings, amplitudes, and codas. Moment tensor and first motion mechanisms have been added to the NCEMC California earthquake catalog and are searchable from the NCEDC Web catalog search page.

Station Metadata

In addition to the metadata returned through the various data request methods, the NCEDC provides dataless SEED volumes and SEED RESP files for all data channels archived at the NCEDC. The NCEDC currently has full SEED instrument responses for 17,985 data channels from 2,155 stations in 20 networks. This includes stations from the California Geological Survey (CGS) strong motion network that will contribute seismic waveform data for significant earthquakes to the NCEDC and SCEDC. In collaboration with the USGS NCSN and the NSMP (National Strong Motion Program), the NCEDC is building the metadata and dataless SEED volumes for over 300 stations and 2000 data channels of the NSMP dialup stations.

The NCEDC is also beginning to develop Web services as a new method of distributing data. We are currently testing a station metadata service that provides station and channel information, and is compatible with IRIS's Web service. StationXML is an XML (Extensible Markup Language) schema designed for sharing station metadata. StationXML was originally designed at the SCEDC and is now maintained in collaboration with NCEDC, IRIS, and NEIC. Documentation on StationXML is available at <http://www.data.scec.org/xml/station/>

SeismiQuery

The NCEDC ported and installed the IRIS *SeismiQuery* program at the NCEDC, which provides a web interface to query network, station, and channel attributes and query the availability of archived timeseries data.

DART (Data Available in Real Time)

The DART (Data Available in Real Time) represents the first step in the NCEDC's effort to make current and recent timeseries data from all networks, stations, and channels available to users in real time. The NCEDC developed DART in December 2005 to provide a mechanism for users to obtain access to real-time data from the NCEDC. All real-time timeseries data streams delivered to the NCEDC are placed in MiniSEED files in a Web-accessible directory structure. The DART waveforms can be accessed by Web browsers or http command-line programs such as *wget*, a *FISSURES* waveform server, and a Berkeley-developed Simple Wave Server (SWS) which provides programmatic access to the DART data by specified SEED channel and time interval. We will be providing users with a client program to retrieve data from the SWS in the near future. The DART currently provides access to the most recent 35 days of data.

We use both the Freeorb software, an enhanced version of the open-source orb software developed by the IRIS-funded Joint Seismic Project (JSP), and the IRIS-developed ringserver as the primary methods for delivering real-time data to the NCEDC and into the DART. Both the freeorb and ringserver packages implement an object ring buffer (ORB) and server which provides a reliable storage ring buffer and an interface for client programs to read, write, and query the orbserver. Clients running at the NCEDC computer connect to remote servers at the BSL and USGS/Menlo Park, retrieve the MiniSEED timeseries data records, and write them to daily channel files in the NCEDC DART. Strain data from the EarthScope PBO network are delivered to the NCEDC using SeedLink and are inserted into the DART using a similar SeedLink client program.

The NCEDC developed an automated data archiving system to archive data from the DART on a daily basis. It allows us to specify which stations should be automatically archived, and which stations should be handled by the NCEDC's Quality Control program *calqc*, which allows an analyst to review the waveforms, retrieve missing data from stations or waveservers that may have late-arriving, out-of-order data, and perform timing corrections on the waveform data. The majority of data channels are currently archived automatically from the DART.

NetDC

In a collaborative project with the IRIS DMC and other worldwide datacenters, the NCEDC helped develop and implement *NetDC*, a protocol which will provide a seamless user interface to multiple datacenters for geophysical network and station inventory, instrument responses, and data retrieval requests. *NetDC* builds upon the foundation and concepts of the IRIS *BREQ_FAST* data request system. The *NetDC* system

was put into production in January 2000 and is currently operational at several datacenters worldwide, including NCEDC, IRIS DMC, ORFEUS, Geoscope, and SCEDC. The *NetDC* system receives user requests via email, automatically routes the appropriate portion of the requests to the appropriate datacenter, optionally aggregates the responses from the various datacenters, and delivers the data (or FTP pointers to the data) to the users via email.

STP

In 2002, the NCEDC wrote a collaborative proposal with the SCEDC to the Southern California Earthquake Center, with the goal of unifying data access between the two data centers. As part of this project, the NCEDC and SCEDC are working to support a common set of 3 tools for accessing waveform and parametric data: *SeisQuery*, *NetDC*, and *STP*.

The *Seismogram Transfer Program* or *STP* is a simple client-server program, developed at the SCEDC. Access to *STP* is either through a simple direct interface that is available for Sun or Linux platforms, or through a GUI Web interface. With the direct interface, the data are placed directly on a user's computer in several possible formats, with the byte-swap conversion performed automatically. With the Web interface, the selected and converted data are retrieved with a single FTP command. The *STP* interface also allows rapid access to parametric data such as hypocenters and phases.

The NCEDC has continued work on *STP*, working with the SCEDC on extensions and needed additions. We added support for the full SEED channel name (Station, Network, Channel, and Location), and are now able to return event-associated waveforms from the NCSN waveform archive.

EVT_FAST

In order to provide Web access to the NCSN waveforms before the SEED conversion and instrument response for the NCSN has been completed, the NCEDC implemented *EVT_FAST*, an interim email-based waveform request system similar to the *BREQ_FAST* email request system. Users email *EVT_FAST* requests to the NCEDC and request NCSN waveform data based on the NCSN event ID. *EVT_FAST* event waveforms can be delivered in either MiniSEED or SAC format, and are now named with their SEED channel names.

FISSURES

The *FISSURES* project developed from an initiative by IRIS to improve earth scientists' efficiency by developing a unified environment that can provide interactive or programmatic access to waveform data and the corresponding metadata for instrument response, as well as station and channel inventory information. *FISSURES*

was developed using CORBA (Common Object Request Broker Architecture) as the architecture to implement a system-independent method for the exchange of this binary data. The IRIS DMC developed a series of services, referred to as the *Data Handling Interface (DHI)*, using the *FISSURES* architecture to provide waveform and metadata from the IRIS DMC.

The NCEDC has implemented the *FISSURES Data Handling Interface (DHI)* services at the NCEDC, which involves interfacing the DHI servers with the NCEDC database schema. These services interact with the NCEDC database and data storage system and can deliver NCEDC channel metadata as well as waveforms using the *FISSURES* interfaces. We have separate *FISSURES DHI* waveform servers to serve archived and DART data streams. Our *FISSURES* servers are registered with the IRIS *FISSURES naming services*, which ensures that all *FISSURES* users have transparent access to data from the NCEDC.

6.8 SWC and SWS

UC Berkeley developed the Simple Wave Server *swc* and Simple Wave Client *sws* programs to provide access to its MiniSEED data from the DART and the NCEDC archive. It currently operates a separate server for each of the above services. The *swc* program is a command-line client program written in perl that runs under Linux, Unix, and MacOS and allows users to easily retrieve waveform data in MiniSEED format by channel and time window or by NCEMC event gathers. The program is packaged for easy user installation and can be downloaded from the NCEDC web site.

GSAC

Since 1997, the NCEDC has collaborated with UNAVCO and other members of the GPS community on the development of the *GPS Seamless Archive Centers (GSAC)* project. This project allows a user to access the most current version of GPS data and metadata from distributed archive locations. The NCEDC is participating at several levels in the *GSAC* project: as a primary provider of data collected from core BARD stations and USGS MP surveys, and as a wholesale collection point for other data collected in Northern California. We helped to define database schema and file formats for the *GSAC* project and have produced complete and incremental monumentation and data holdings files describing the data sets that are produced by the BARD project or archived at the NCEDC so that other members of the *GSAC* community can provide up-to-date information about our holdings. Currently, the NCEDC is the primary provider for over 138,000 data files from over 1400 continuous and survey-mode monuments. The data holdings records for these data have been incorporated

into the *GSAC* retailer system, which became publicly available in late 2002.

The NCEDC now archives and distributes high-rate 1 Hz GPS data from BSL-operated BARD stations in addition to the normally sampled 15 second data. These high-rate data do not have GSAD data holding records due to limitations in the GSAC specification, but are publicly available to download from the NCEDC archive.

6.9 Acknowledgements

The NCEDC is a joint project of the BSL and the USGS Menlo Park and is funded primarily by BSL and USGS Cooperative Agreements 07HQAG0013 and G10AC00093. Additional funding for the processing and archiving of the EarthScope PBO and SAFOD data were provided by EarthScope subawards EAR0732947-07-06 through UNAVCO.

Doug Neuhauser is the manager of the NCEDC. Stephane Zuzlewski, Mario Aranha, Ingrid Johanson, Taka'aki Taira, Jennifer Taggart, Tom Weldon, and Peggy Hellweg of the BSL and David Oppenheimer, Hal Macbeth, Lynn Dietz, and Fred Klein of the USGS Menlo Park contribute to the operation of the NCEDC. Doug Neuhauser, Peggy Hellweg, and Mario Aranha contributed to the preparation of this section.

7 Data Acquisition and Quality Control

7.1 Introduction

Stations from the networks operated by the BSL transmit data continuously to the BSL facilities on the UC Berkeley campus for analysis and archival. In this section, we describe activities and facilities which pertain to the individual networks described in Operational Sections 1, 3, and 4, including procedures for data acquisition and quality control, and sensor testing capabilities and procedures. Some of these activities are continuous from year to year and have been described in prior BSL annual reports. In this section, we describe changes or activities which are specific to 2010-2011.

7.2 Data Acquisition Facilities

The computers and the associated telemetry equipment are located in the campus computer facility in Warren Hall at 2195 Hearst Avenue. This building was constructed to current “emergency grade” seismic codes and is expected to be operational even after a M 7 earthquake on the nearby Hayward Fault. The hardened campus computer facility within was designed with special attention for post-earthquake operations. The computer center contains state-of-the art seismic bracing, UPS power and air conditioning with generator backup, and extensive security and equipment monitoring.

7.3 Data Acquisition

Central-site data acquisition for data from the BDSN/HRSN/NHFN/mPBO networks is performed by two computer systems in the Warren Hall data center (Figure 3.29). These acquisition systems also collect data from the Parkfield-Hollister electromagnetic array and the BARD network. A third system is used primarily for data exchange. It transmits data to the U.S. National Seismograph Network (USNSN) from HOPS, CMB, SAO, WDC, HUMO, JCC, MOD, MCCM, ORV and YBH. Data from various subsets of stations also go to the Pacific and Alaska Tsunami Warning Centers, to the University of Washington and to the University of Reno, Nevada. In addition, the Southern California Earthquake Management Center has access to our wavepools for retrieving waveform data to include in its event gathers. Data for all channels of the HRSN are now telemetered continuously from Parkfield to the BSL over the USGS T1 from Parkfield to Menlo Park, and over the NCEMC T1 from Menlo Park to Warren Hall.

The BSL uses the programs `comserv` and `qmaserv` developed by Quanterra for central data acquisition. These programs receive data from remote Quanterra data loggers and redistribute it to one or more client programs.

The clients include `datalog`, which writes the data to disk files for archival purposes, `wdafill`, which writes the data to the shared memory region for processing with the network services routines, and other programs such as the seismic alarm process, the DAC480 system, and the feed for the Memento Mori Web page.

The two computers performing data acquisition are also “network services” computers that reduce waveforms for processing with the CISN software (Figure 3.30). To facilitate processing, each system maintains a shared memory region containing the most recent 30 minutes of data for each channel.

BDSN data loggers which use frame relay telemetry are configured to enable data transmission simultaneously to two different computers over two different frame relay T1 circuits to UCB. Normally, only one of these circuits is enabled. The `comserv/qmaserv` client program `cs2m` receives data and multicasts it over a private ethernet. The program `mcast`, a modified version of Quanterra’s `comserv` program, receives the multicast data from `cs2m`, and provides a `comserv`-like interface to local `comserv` clients. Thus, each network services computer has a `comserv/qmaserv` server for every station, and each of the two systems has a complete copy of all waveform data.

We have extended the multicasting approach to handle data received from other networks such as the NCSN and UNR (University of Nevada, Reno). These data are received by Earthworm data exchange programs and are then converted to MiniSEED and multicast in the same manner as the BSL data. We use `mserv` on both network services computers to receive the multicast data and handle it in the same way as the BSL MiniSEED data.

In 2006, the BSL established a real-time data feed of all BSL waveforms between the BSL acquisition systems and the NCEDC computers using the open source Freeorb software. This allows the NCEDC to provide near-real-time access to all BSL waveform data through the NCEDC DART (Data Available in Real Time) system.

We monitor seismic stations and telemetry using the program `seisnetwatch`. This program extracts current information such as time quality, mass positions, and battery voltage and allows it to be displayed. If the parameter departs from the nominal range, the station is marked with yellow or red to indicate a possible problem.

7.4 Seismic Noise Analysis

BSL seismic data are routinely monitored for state of health. An automated analysis is computed regularly to characterize the seismic noise level recorded by each broadband seismometer.

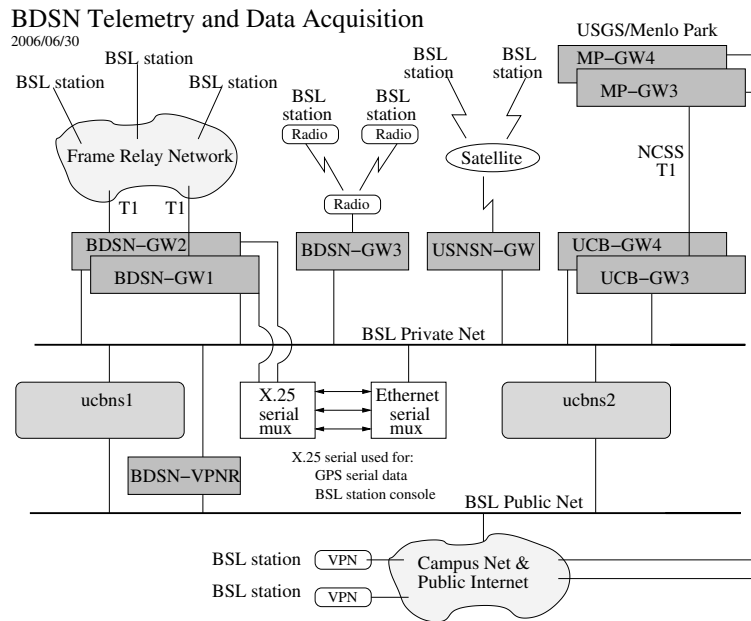


Figure 3.29: Data flow from the BDSN, NHFN, mPBO, HRSN, and BARD networks into the BSL central processing facility.

PSD Noise Analysis

The estimation of the Power Spectral Density (PSD) of the ground motion recorded at a seismic station, as documented in the 2000-2001 BSL annual report (http://seismo.berkeley.edu/annual_report/) provides an objective measure of background seismic noise characteristics over a wide range of frequencies. It also provides an objective measure of seasonal variation in noise characteristics and supports early diagnoses of instrumental problems. In the early 1990s, a PSD estimation algorithm was developed at the BSL for characterizing the background seismic noise and as a tool for quality control. The algorithm generates a bar graph output in which all the BDSN broadband stations can be compared by component. We also use the weekly PSD results to monitor trends in the noise level at each station. Cumulative PSD plots are generated for each station and show the noise level in 5 frequency bands for the broadband channels. The plots make it easier to spot certain problems, such as failure of a sensor. In addition to the station-based plots, a summary plot is produced for each channel. The figures are presented as part of a noise analysis of the BDSN on the web at <http://www.seismo.berkeley.edu/seismo/bdsn/psd/>.

PDF PSD Noise Analysis

In addition to the PSD analysis developed by Bob Uhrhammer, the BSL has implemented the Ambient Noise Probability Density Function (PDF) analysis system developed by *McNamara and Buland* (2004). This system performs its noise analysis over all the data of a given time period (week or year), including earthquakes,

calibration pulses, and cultural noise. This is in contrast to Bob Uhrhammer's PSD analysis, which looks at only the quietest portion of data within a day or week. Pete Lombard of the BSL extended the McNamara code to cover a larger frequency range and support the many different types of sensors employed by the BSL. Besides the originally supported broadband sensors, our PDF analysis now includes surface and borehole geophones and accelerometers, strain meters, and electric and magnetic field sensors. These enhancements to the PDF code, plus a number of bug fixes, were provided back to the McNamara team for incorporation in their work. The results of the PDF analysis are presented on the web at <http://www.ncedc.org/ncedc/PDF/>. One difficulty with using these plots for review of station quality is that it is necessary to look at data from each component separately. To provide an overview, we have developed summary figures for all components in two spectral bands, 32 - 128 s and 0.125 - 0.25 s (Figure 3.31). The figures are also available on the web at <http://www.ncedc.org/ncedc/PDF/>.

7.5 Sensor Testing Facility

The BSL has an Instrumentation Test Facility in the Byerly Seismographic Vault where the characteristics of up to eight sensors can be systematically determined and compared. The test equipment consists of an eight-channel Quanterra Q4120 high-resolution data logger and a custom interconnect panel. The panel provides isolated power and preamplification, when required, to facilitate the connection and routing of signals from the sensors to the data logger with shielded signal lines. The vault also

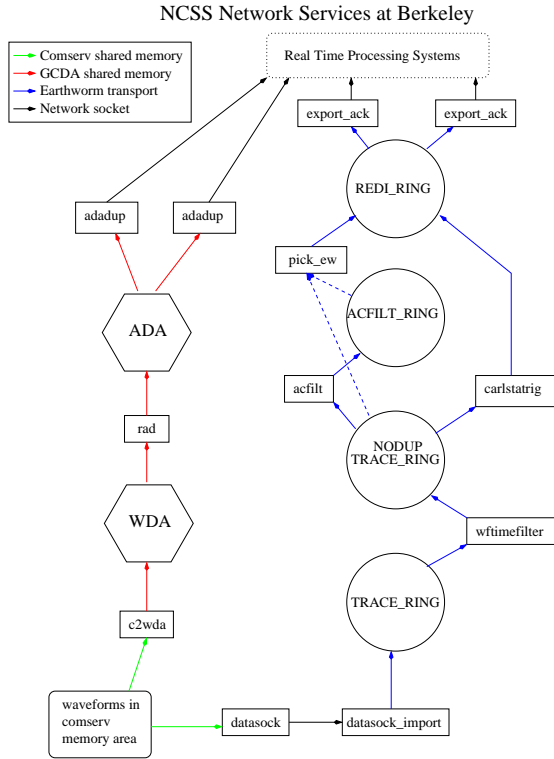


Figure 3.30: Flow of data from `comserv/qmaserv` areas through network services processing. One stream of the network services provides picks (and currently still provides codas) determined using the programs shown in the right flow path. Every 5 seconds, ground motion parameters are also determined, including PGA, PGV, PGD, and ML100 (left flow column). Parameters from the network services are available to the CISON software for event detection and characterization. Data are also logged to disk (via `dataalog`), distributed to other computers (`mserv`), and spooled into a trace ring for export.

has a GPS rebroadcaster, so that all data loggers in the Byerly vault operate on the same time base. Upon acquisition of data at up to 200 sps from the instruments under test, PSD analysis, coherence analysis, and other analysis algorithms are used to characterize and compare the sensor performance. Tilt tests and seismic signals with a sufficient signal level above the background seismic noise are also used to verify the absolute calibration of the sensors. A simple vertical shake table is used to assess the linearity of a seismic sensor. The sensor testing facility of the BSL is described in detail in the 2001-2002 Annual Report (<http://www.seismo.berkeley.edu/>).

Borehole Geophone Calibration Analysis

Introduction: Determination and verification of the response of geophones that have been permanently installed in the BK and BP network borehole stations is

accomplished by measuring their response to a current step induced into the geophone's signal coil. BSL engineering staff have constructed a calibration box which implements the methodology described in *Rodgers et al., 1995*. We show as an example the measured response of the geophones installed in the BK.PETB (Petaluma Bridge) borehole.

Theory and Method: *Rodgers et al., 1995* show that a geophone may be easily and accurately calibrated by removing a known current step from its signal coil and simultaneously switching the signal coil to a data logger to capture the resulting response. They show that the resonant frequency w_s , fraction of critical damping h_s and generator constant G_{sig} of a geophone can be uniquely determined from its measured response to the current step and that only the seismometer mass (M) and the applied current I_{sig} need be known for a complete calibration.

The geophone inertial mass (M) is obtained from the factory specification sheet and the applied current step I_{sig} is measured *insitu*. The natural frequency (w_s) and fraction of critical damping (h_s) are then determined by a grid search algorithm which determines the w_s and h_s values that maximize the variance reduction between the observed and calculated response to the current step I_{sig} , where K is the calculated signal scaling factor required to match the observed signal level.

From *Rodgers et al., 1995*, the theory is:

$$K = S_d * G_d * G_{sig} * I_{sig} / M$$

and:

$$G_d = R_d * G_{sig} / (R_c + R_d)$$

where:

S_d = data logger sensitivity (419430 counts/Volt)

G_d = damped generator constant

G_{sig} = signal coil generator constant

I_{sig} = current step

M = seismometer mass

R_d = damping resistance and

R_c = signal coil resistance.

Solving for G_{sig} :

$$G_{sig} = \sqrt{(R_d + R_c) * M * K / (S_d * R_d * I_{sig})}$$

If $R_d \gg R_c$ this simplifies to:

$$G_{sig} = \sqrt{M * K / (S_d * I_{sig})}$$

OYO Geospace HS-1 Geophone Specifications:

The values from the factory specification sheet (<http://www.geospace1p.com/>) for the OYO Geospace HS-1 geophone are:

$$R_c = 1250 \pm 62 \text{ ohms}$$

BDSN HHZ component (20–40 s period) (2010.182 – 2011.181)

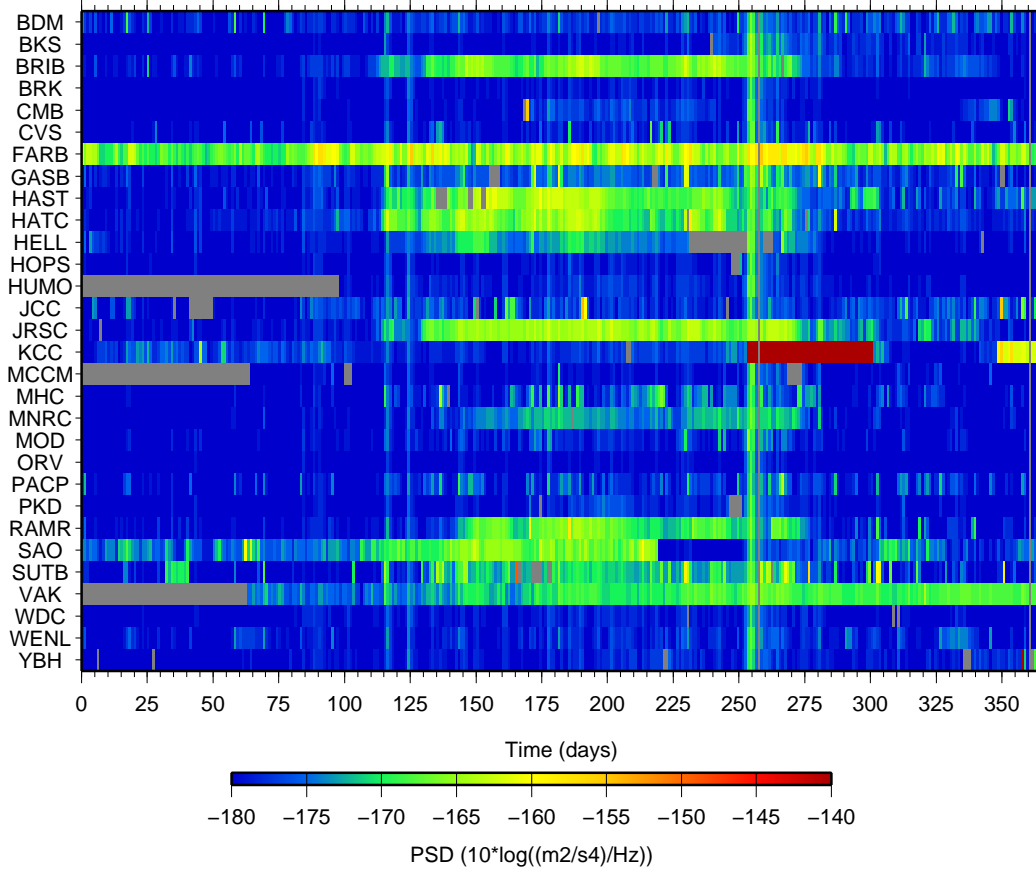


Figure 3.31: Annual summary of noise on all components of the broadband sensors of the BDSN for the band from 32 s to 128 s.

$$G_{sig} = 45.3 \pm 10\% \text{ (V/(m/s))}$$

$$w_s = 4.5 \pm 0.75 \text{ Hz}$$

$$h_s = 0.28 \pm 20\% \text{ (open circuit damping)}$$

$$M = 28 \pm 5\% \text{ grams}$$

Calibration of the PETB Geophones:

The geophones installed in the PETB (Petaluma Bridge) borehole are OYO Geospace HS-1 geophones with a 0.028 kg inertial mass (M). The calibration current (I_{sig}) is 0.5195 mA and the results are shown in Table 3.13.

Comp	w_s (Hz)	h_s (crit)	K	G V/(m/s)
Z	3.920	0.2426	20485471	51.3
H1	3.754	0.2561	20164289	50.9
H2	3.894	0.2741	25935875	57.7

Table 3.13: Calibration Results for the PETB Geophones

The measured w_s , h_s and G_{sig} for all three geophones installed at PETB are consistent (within the stated un-

certainties) with the values given on the factory specification sheet. The uncertainty in the measured sensitivity is $\sim 3\%$ and it is limited by the 5% uncertainty in the geophone inertial mass.

7.6 STS-1/E300 Calibration Analysis

Introduction

During the past year, the BSL has continued to test and install new Metrozet E300 electronics as replacements for the aging and problematic factory feedback electronics connected to the Streckeisen STS-1 very broadband seismometers.

The original tests at remote stations were done at the BDSN stations HOPS and KCC with prototype E300 electronics, and the tests during this year were done with production E300 electronics that BSL purchased using ARRA funding. To date, production E300 electronics packages have been installed at BDSN stations CMB, BKS and YBH.

Metrozet STS-1/E300 Very Broadband Seismometer Electronics

The Metrozet STS-1/E300 is an advanced electronics package that is a direct replacement for the original Streckeisen feedback electronics boxes. It matches the analog performance of the original electronics and provides a number of enhancements to facilitate the installation and operation of the STS1 seismometers in a modern seismic network. In particular, it provides digital control of all seismometer parameters, recentering, and state of health parameters, and it has auxiliary analog and digital input lines. All the control and diagnostic functions can be controlled either locally or remotely via ethernet.

The frequency response of the STS-1/E300 seismometer system is accomplished via: 1) analysis of the sensor response to a low-frequency (40-100 sec) sweep stimulus applied to the calibration coil to determine the seismometer natural period T_s and fraction of critical damping h_s and; 2) analysis of the sensor response to a high-frequency (0.5-40 Hz) stepped-sine to determine the frequency f_g and fraction of critical damping h_g of the high-frequency corner. The Metrozet Scale Factor Calculator V1.20 Applet is used to determine the sensitivity of the STS-1/E300 seismometer system given the values of critical feedback components in the Streckeisen electronics boxes and the Streckeisen determined very-broadband sensitivity in V/(m/s).

The accuracy of the Applet determined STS-1/E300 sensitivity can be checked via: 1) comparison of the inferred ground motion with a co-sited reference broadband seismometer (typically a temporarily deployed STS-2 with known calibration); 2) comparison of the inferred ground motion with the co-sited Kinometrics ES-T strong-motion accelerometer (given a local/regional earthquake with adequate ground motions), and/or; 3) measuring the response to known displacement steps. The first method requires that a reference seismometer be co-sited on the seismic pier next to the STS-1/E300 for a day or more to determine the sensitivity by comparison of the inferred signal levels. The second method requires waiting for a local/regional earthquake to occur which has adequate signal-to-noise (SNR) levels on both the STS-1/E300 and the strong motion accelerometer to determine the sensitivity by comparison of the inferred signal levels in an appropriate passband where both sensors have adequate SNR levels. The third method requires that the calibration be done in the BSL engineering lab. Of the three methods for verifying the accuracy of the STS-1/E300 sensitivity, the first method is considered the most accurate but it requires a second visit to the remote BDSN stations to retrieve the reference broadband sensor and data logger, the second method requires waiting an indeterminant length of time for an appropriate earthquake to occur and, the third method is not viable because it requires that the STS-1 sensors

(which typically have been deployed at BDSN stations for many years) be returned to BSL for testing.

Calibration of the STS-1/E300 System

The frequency response of each component of the STS-1/E300 seismometer system is determined via analysis of known calibration stimuli and the corresponding sensitivity is determined using the Metrozet Scale Factor Calculator Applet V1.20.

The low-frequency response is determined using a low-frequency (~ 40 -1100 seconds period) sweep stimuli and the high-frequency response is determined using a stepped sine (0.5-40 Hz) stimuli. The seismometer natural period (T_s) and fraction of critical damping (h_s) are determined via a grid search algorithm that finds the solution that minimizes the variance between the observed and calculated responses to the low-frequency swept sine stimuli.

The high-frequency response is determined using an algorithm which analyzes the high-frequency phase response $\phi(\omega)$ and determines the high-frequency corner (f_g) and fraction of critical damping (h_g) from the frequency (ω) and corresponding slope ($d\phi/d\omega$) where the observed phase response has a 90° phase shift relative to the stimuli phase response.

The corresponding component sensitivity is determined using the Metrozet Scale Factor Calculator V1.20 Applet. The GUI Applet requires the sensor serial number and factory electronics box component values and sensitivity be input, and it returns the corresponding sensitivity when the E300 electronics is used in place of the factory electronics. The assumption is that the factory determined component values and sensitivity, which was measured two decades or more ago for the BDSN STS1 equipped stations, are still valid.

Calibration of the ES-T Accelerometer

The factory calibration data was adopted for the Kinometrics ES-T strong motion accelerometers. The sensitivity and full-scale range are jumper configurable by the user, and BSL sets the units to operate with a full scale range of $\pm 2g$ and with a differential output of $\pm 20V$ for a nominal sensitivity of 10Volts/g. Kinometrics has developed a good empirical pole/zero model of the system where the sensitivity, when corrected for the DC sensitivity of the sensor, is within ± 0.5 dB over the bandwidth of the sensor and the phase agreement is within $\pm 2.5^\circ$ in the 0-100 Hz band and within $\pm 5^\circ$ over the full bandwidth of the sensor. The pole/zero response is described in detail in the Episensor Model ES-T User Guide available via FTP from (<http://www.kinometrics.com>). The factory calibration sheet for the ES-T gives the DC sensor sensitivity in V/g for each of the sensor components. The sensitivity is verifiable via tilt tests at BSL.

The non-linearity of the sensor components are typically *approx* 500-600 $\mu\text{g}/g^2$ for all components. The sensor component alignments are typically within ± 0.25 degrees.

The Kinometrics ES-T strong motion accelerometers also provide an independent method for checking the sensitivity of the Streckeisen STS-1/E300 via comparison of the ground motions inferred from corresponding component of the two sensors.

Installation and Calibration of the Seismic Instrumentation at CMB

The BDSN station CMB (Columbia College) equipment was upgraded with ARRA funding December 16-17, 2010. The upgrade included, in part, a Quanterra Q330HR ultrahigh-resolution data logger, a Metrozet STS-1/E300 electronics package, and a Kinometrics Episensor ES-T triaxial strong motion accelerometer.

Factory calibration data were adopted for the Q330HR data logger and for the ES-T accelerometer. The STS-1/E300 was remotely checked out and calibrated from the BSL on January 12, 2011. The functionality of the E300 electronics package (s/n E300-ST51-120-202) was checked and verified, and low-frequency sweeps and high-frequency stepped-sine calibration stimuli were invoked to calibrate the STS1 seismometers. The sensitivity of each of the STS-1/E300 components was determined using the Metrozet Scale Factor Calculator applet V1.20. The veracity of the STS-1/E300 component sensitivities was verified by comparing the inferred ground motions from the STS-1/E300 very-broadband components with corresponding ES-T accelerometer components for a large ground motion signal. The results are discussed in the following subsections.

Calibration of the Q330HR Data Logger: The factory calibration data was adopted for the Quanterra Q330HR ultrahigh-resolution data logger. The sensitivity of all six ultrahigh-resolution channels is nominally 2^{26} counts/40Volts or 1677761.6 counts/Volt. The factory specifications indicate that a dynamic range of 147-148 dB wideband rms is typical and that in the the 0.02-20 Hz band it is typically 150-151 dB. Sampling rates of 200, 100, 50, 40, 20, 10, and 1 Hz are independently available on any channel. Quanterra does not explicitly specify the accuracy of the channel sensitivity. However, assuming that the wideband dynamic range is 147 dB, we can infer that the nominal accuracy is $\sim \pm 0.0002\%$.

Calibration of the ES-T Accelerometer: The factory calibration data was adopted for the Kinometrics ES-T strong motion accelerometer. The factory calibration sheet for the ES-T (s/n 3742) gives a DC sensor sensitivity of 9.982, 9.975 and 9.968 V/g for the Z, N and E components, respectively. The sensitivity was verified via tilt tests at BSL.

Calibration of the STS-1/E300 System: The frequency

response of each component of the STS-1/E300 seismometer system is determined via analysis of known calibration stimuli and the corresponding sensitivity is determined using the Metrozet Scale Factor Calculator Applet V1.20. The low-frequency response is determined using a low-frequency (~ 40 -1100 seconds period) sweep stimuli and the high-frequency response is determined using a stepped sine (0.5-40 Hz) stimuli. The seismometer natural period (T_s) and fraction of critical damping (h_s) are determined via a grid search algorithm that finds the solution that minimizes the variance between the observed and calculated responses to the low-frequency swept sine stimuli. An example result is shown in Figure 3.32. The high-frequency response is determined using an algorithm which analyzes the high-frequency phase response $\phi(\omega)$ and determines the high-frequency corner (f_g) and fraction of critical damping (h_g) from the frequency (ω) and corresponding slope ($d\phi/d\omega$) where the observed phase response has a 90° phase shift relative to the stimuli phase response. An example result is shown in Figure 3.33.

The corresponding component sensitivity is determined using the Metrozet Scale Factor Calculator V1.20 Applet. The GUI Applet requires the sensor serial number and factory electronics box component values and sensitivity be input, and it returns the corresponding sensitivity when the E300 electronics is used in place of the factory electronics. The assumption is that the factory determined component values and sensitivity, which was measured two decades or more ago for the BDSN STS1 equipped stations, are still valid. Examples of the Applet input and corresponding results are shown in Figures 3.34 and 3.35.

The results for the CMB STS-1/E300 system calibration are shown in Table 3.14.

	T_s (sec)	h_s	f_g (Hz)	h_g	Sens V/(m/s)
Z	365.70	0.7315	12.911	0.461	3097.2
N	365.44	0.7140	17.114	0.335	1974.0
E	365.00	0.7180	13.314	0.425	2592.6

Table 3.14: Synopsis of calibration results for the three STS-1/E300 sensors at CMB.

STS-1/E300 Calibration Check: As a check of the calibration accuracy of the STS-1/E300 very-broadband seismometers, we compare the 1-3 Hz bandpass filtered ground accelerations inferred from the STS-1/E300 seismometers with the corresponding ground accelerations inferred from the co-sited strong motion ES-T accelerometers for a Mw 4.5 which occurred 171 km southwest of CMB at 2011.012.0851 (the local/regional earthquake which had the largest theoretical ground motions a CMB since the STS-1/E300 was installed on December 17, 2010). The inferred peak ground accelerations from the two sensors (see Table 3.15) all agree within 1 percent

which shows that the two sensor types yield internally consistent results and also that the sensitivity of the STS-1/E300 components are accurately calculated by the Metrozet Scale Factor Calculator V1.20 Applet. The median coherence for all three components of ground motion is 0.999970 in the 1-3 Hz band which is also consistent with differences of less than 1 percent in the inferred ground motions.

Component	STS-1/E300 ($\mu\text{m}/\text{s}^2$)	ES-T ($\mu\text{m}/\text{s}^2$)	Percent Difference
Z	284	282	+0.71
N	480	477	+0.63
E	545	540	+0.93

Table 3.15: Comparison of inferred peak ground accelerations at CMB.

Installation and Calibration of the Seismic Instrumentation at BKS

The BDSN station BKS (Byerly Seismographic Vault) equipment was upgraded with ARRA funding February 25, 2011. The upgrade included, in part, a Quanterra Q330HR ultrahigh-resolution data logger, a Metrozet STS-1/E300 electronics package, and a Kinometrics Episensor ES-T triaxial strong motion accelerometer.

Factory calibration data were adopted for the Q330HR data logger and for the ES-T accelerometer. The STS-1/E300 was remotely checked out and calibrated from the BSL January 12, 2011. The functionality of the E300 electronics package (s/n E300-ST51-120-202) was checked and verified, and low-frequency sweeps and high-frequency stepped-sine calibration stimuli were invoked to calibrate the STS1 seismometers. The sensitivity of each of the STS-1/E300 components was determined using the Metrozet Scale Factor Calculator applet V1.20. The veracity of the STS-1/E300 component sensitivities was verified by comparing the inferred ground motions from the STS-1/E300 very-broadband components with corresponding ES-T accelerometer components for a large ground motion signal. The results are discussed in the following subsections.

Calibration of the Q330HR Data Logger: The factory calibration data was adopted for the Quanterra Q330HR ultrahigh-resolution data logger. The specifications are identical to those presented previously in the "Calibration of the Q330HR Data Logger" section for CMB.

Calibration of the ES-T Accelerometer: The factory calibration data was adopted for the Kinometrics ES-T strong motion accelerometer. The factory calibration sheet for the ES-T (s/n 3777) gives a DC sensor sensitivity of 10.076, 10.011 and 9.999 V/g for the Z, N and E components, respectively. The sensitivity was verified via tilt tests at BSL.

Calibration of the STS-1/E300 System: The calibration procedure to determine the frequency response and sensitivity is the same as that described previously for CMB. The results for the BKS STS-1/E300 system calibration are shown in Table 3.16.

	T_s (sec)	h_s	f_g (Hz)	h_g	Sens V/(m/s)
Z	359.80	0.7145	12.383	0.437	4384.8
N	360.67	0.7160	17.095	0.336	1966.3
E	360.51	0.7220	13.194	0.400	3590.7

Table 3.16: Synopsis of calibration results for the three STS-1/E300 sensors at BKS.

STS-1/E300 Calibration Check: The calibration was checked by comparing the broadband ground acceleration inferred from the BKS STS-1/E300s with the corresponding ground acceleration inferred from the co-sited BKS Episensor strong motion accelerometer for the local earthquake which had the largest theoretical ground motions at BKS since the ARRA upgrade was installed. The local earthquake is a Mw 3.6 which occurred 16.6 km SE of Berkeley along the Hayward fault at 2011.236.0636. The results, given in Table 3.17, show that the peak ground accelerations inferred from the broadband sensors and from the strong motion sensors all agree within 0.5 percent. This close agreement implies that the BKS STS-1/E300 sensor calibration is very accurate.

Component	STS-1/E300 Acceleration ($\mu\text{m}/\text{s}^2$)	Episensor Acceleration ($\mu\text{m}/\text{s}^2$)	Percent Difference
Z	18956	18864	0.488
N	21136	21128	0.038
E	18656	18653	0.016

Table 3.17: Comparison of ground accelerations at BKS inferred from the STS-1/E300 broadband sensors with the corresponding ground accelerations inferred from the co-sited Episensor strong motion sensors.

Installation and Calibration of the Seismic Instrumentation at YBH

The BDSN station YBH (Yreka Blue Horn Mine) equipment was upgraded with ARRA funding June 1-3, 2011. The upgrade included, in part, a Quanterra Q330HR ultrahigh-resolution data logger, and a Metrozet STS-1/E300 electronics package. A Kinometrics Episensor ES-T triaxial strong motion accelerometer had been installed previously on November 17, 2004.

Factory calibration data were adopted for the Q330HR data logger and for the ES-T accelerometer. The STS-1/E300 was remotely checked out and calibrated from the BSL June 6-9, 2011. The functionality of the

E300 electronics package (s/n STS1-E300-120-199) was checked and verified, and low-frequency sweeps and high-frequency stepped-sine calibration stimuli were invoked to calibrate the STS1 seismometers. The sensitivity of each of the STS-1/E300 components was determined using the Metrozet Scale Factor Calculator applet V1.20. The accuracy of the STS-1/E300 component sensitivities was checked by comparing the inferred ground motions from the STS-1/E300 very-broadband components with corresponding ES-T accelerometer components for two large ground motion signals, one regional and one teleseismic. The results are discussed in the following subsections.

Calibration of the Q330HR Data Logger: The factory calibration data was adopted for the Quanterra Q330HR ultrahigh-resolution data logger. The specifications are identical to those presented previously in the "Calibration of the Q330HR Data Logger" section for CMB.

Calibration of the ES-T Accelerometer: The factory calibration data was adopted for the Kinometrics ES-T strong motion accelerometer. The factory calibration sheet for the ES-T (s/n 1862) gives a DC sensor sensitivity of 9.998, 9.990 and 9.952 V/g for the Z, N and E components, respectively. The sensitivity was verified via tilt tests at BSL.

Calibration of the STS-1/E300 System: The calibration procedure to determine the frequency response and sensitivity is the same as that described previously for CMB. The results for the YBH STS-1/E300 system calibration are shown in Table 3.18.

	T_s (sec)	h_s	f_g (Hz)	h_g	Sens V/(m/s)
Z	371.47	0.7305	11.935	0.465	4194.1
N	388.97	1.0190	12.761	0.430	3419.6
E	370.23	0.7360	13.121	0.418	3314.8

Table 3.18: Synopsis of calibration results for the three STS-1/E300 sensors at YBH.

STS-1/E300 Calibration Check and Discussion: The calibration was checked by comparing the broadband ground acceleration inferred from the YBH STS-1/E300s with the corresponding ground acceleration inferred from the co-sited BKS Episensor strong motion accelerometer for the regional earthquake which had the largest theoretical ground motions at YBH since the ARRA upgrade was installed. The regional earthquake is a Mw 4.1 which occurred 219 km WSW of YBH at 2011.226.1927. The results, given in Table 3.19, show that the peak-to-peak ground accelerations inferred from the broadband sensors and from the strong motion sensors indicates that only the N component accelerations agree within 0.5 percent while the ground motions for the Z and E differ by approximately 20 percent with the STS-1/E300 sensor sensitivity too high.

To check this result we also compared the broadband ground acceleration inferred from the YBH STS-1/E300s with the corresponding ground acceleration inferred from the co-sited BKS Episensor strong motion accelerometer for the teleseism which had the largest theoretical ground motions at YBH. The teleseism is a Mw 7.3 which occurred 34.5 degrees W of YBH at 2011.175.0309. To the inferred ground accelerations were 0.05-0.1 Hz band pass filtered to enhance the signal-to-noise ratio. The results, given in Table 3.20, show that the peak-to-peak ground accelerations inferred from the broadband sensors and from the strong motion sensors are consistent with the results shown in Table 3.19 for the regional earthquake.

Thus only the YBH STS-1/E300 N component inferred ground motions agree closely while the Z and E components differ by approximately 20 percent. All three STS-1 components at YBH are from the oldest generation of BDSN STS-1s that were originally BRB sensors with 20 second pendulums which were later upgraded to VBB sensors with 360 second pendulums. The STS-1/E300 sensitivities were calculated using the Metrozet Scale Factor Calculator applet V1.20 and it is known that it does not necessarily provide accurate values when determining the sensitivity of the oldest generation of BRB STS-1 sensors. To accurately determine the sensitivity of the YBH STS-1/E300 sensors, we need to compare the ground motions from the STS-1/E300 sensors with the corresponding ground motions from a co-sited reference broadband seismometer, preferably a Streckeisen STS-2, which has a known calibration.

Component	STS-1/E300 Acceleration ($\mu\text{m}/\text{s}^2$)	Episensor Acceleration ($\mu\text{m}/\text{s}^2$)	Percent Difference
Z	57.569	69.948	17.769
N	98.970	98.571	0.405
E	133.799	109.377	22.328

Table 3.19: Comparison of largest peak-to-peak regional earthquake ground accelerations at YBH inferred from the STS-1/E300 broadband sensors with the corresponding ground accelerations inferred from the co-sited Episensor strong motion sensors.

7.7 Acknowledgements

Doug Neuhauser, Bob Uhrhammer, Taka Taira, Peggy Hellweg, Pete Lombard, Jennifer Taggart and Tom Weldon are involved in the data acquisition and quality control of BDSN/HRSN/NHFN/MBPO data. Development of the sensor test facility and analysis system was a collaborative effort of Bob Uhrhammer, Tom McEvelly, John Friday, and Bill Karavas. IRIS (Incorporated Research Institutions for Seismology) and DTRA (Defense Threat Reduction Agency) provided, in part, funding for and/or

Component	STS-1/E300 Acceleration ($\mu\text{m}/\text{s}^2$)	Episensor Acceleration ($\mu\text{m}/\text{s}^2$)	Percent Difference
Z	14.999	18.742	19.971
N	40.395	41.081	0.962
E	62.021	57.309	18.566

Table 3.20: Comparison of largest peak-to-peak teleseismic ground accelerations at YBH inferred from the STS-1/E300 broadband sensors with the corresponding ground accelerations inferred from the co-sited Episensor strong motion sensors.

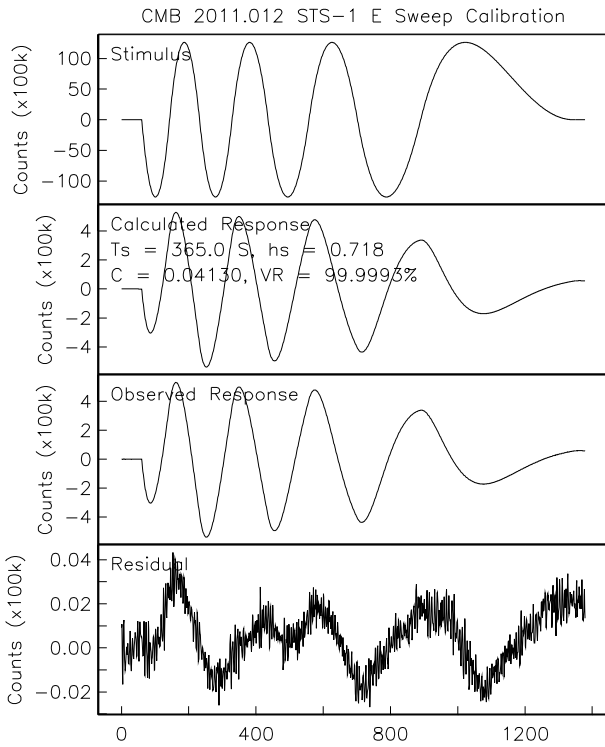


Figure 3.32: CMB STS-1/E300 East Component Low-Frequency Response. The plot shows, from top to bottom, the calibration stimuli, the observed response, the calculated response, and the residual between the observed and calculated response. The solution with the highest variance reduction (99.9993%) is $T_s=365.0\text{sec}$ and $h_s=0.718$. The residual is $>80\text{ dB}$ below the observed response signal level, so the signal-to-noise level is very good. The high-frequency component seen in the residual is the microseismic background noise and the low-frequency component is likely due to signal generated ground-loops that are unknown and thus not accounted for in calculating the response to the stimuli.

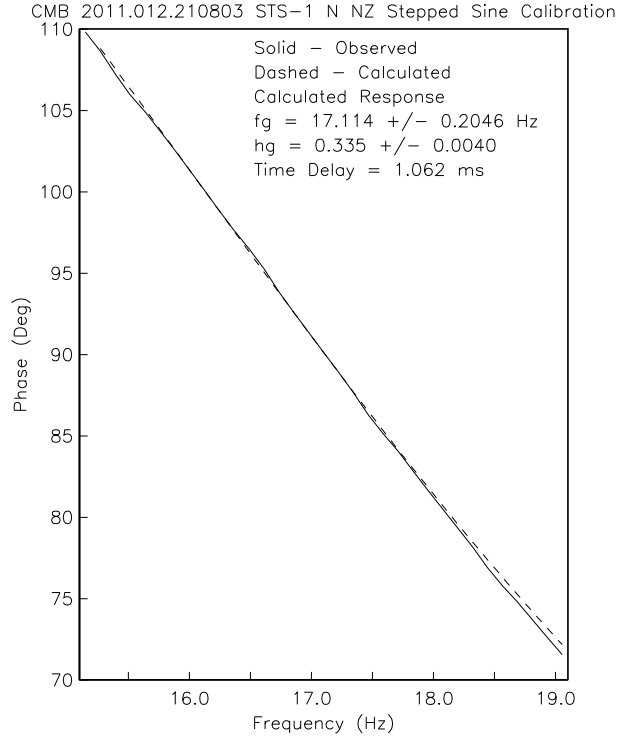


Figure 3.33: CMB STS-1/E300 North Component High-Frequency Response. The plot shows the observed (solid line) and calculated (dashed line) response to the stepped-sine stimuli. The least-squares solution is $f_g=17.114\pm 0.2046\text{Hz}$ and $h_g=0.335\pm 0.0040$. There is an internal time delay of 1.062 msec between the stimuli applied to the calibration coil and stimuli recorded by the data logger, which is accounted for in the algorithm.

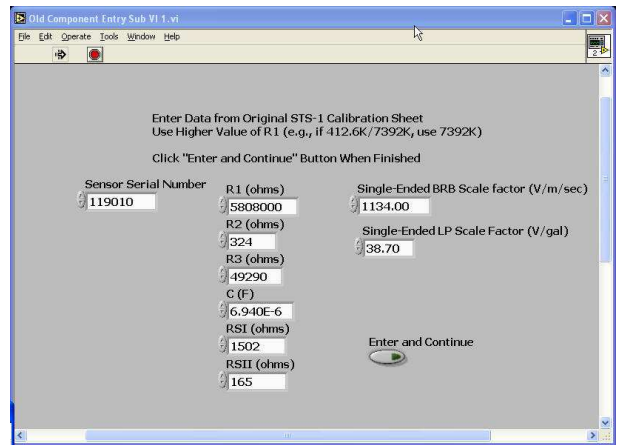


Figure 3.34: Example snapshot of the Metrozet Scale Factor Applet V1.20 input showing the serial number and component values.

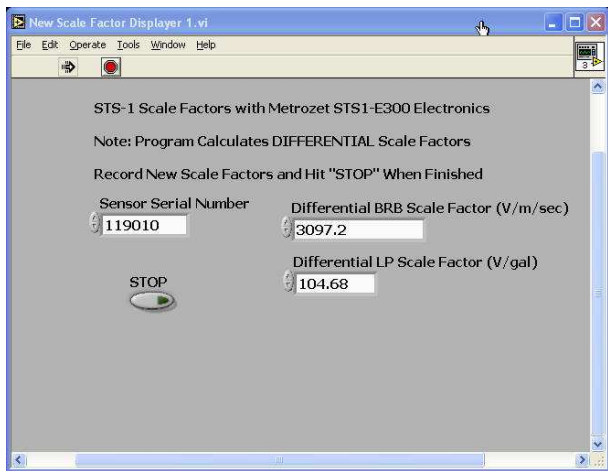


Figure 3.35: Example snapshot of the Metrozet Scale Factor Applet V1.20 results screen showing the serial number and corresponding differential BRB and LP scale factors for use with the E300 electronics.

incentive to set up and operate the facility, and we thank them for their support. Bob Uhrhammer, Taka Taira, Peggy Hellweg, Pete Lombard, Doug Neuhauser, John Friday, Bill Karavas, Barbara Romanowicz, and Tom Weldon contributed to the preparation of this section.

7.8 References

McNamara, D. and R. Buland, Ambient Noise Levels in the Continental United States *Bull. Seism. Soc. Am.*, 94, 4, 2004.

Rodgers, P.W., A.J. Martin, M.C. Robertson, M.M. Hsu and D.B. Harris, Signal-coil calibration of electromagnetic seismometers, *Bull. Seism. Soc. Am.*, 85, 845-850, 1995.

8 Northern California Earthquake Monitoring

8.1 Introduction

Earthquake information production and routine analysis in Northern California have been improving over the past two decades. The most recent step has been the implementation of mirrored software systems at the BSL and at the USGS in Menlo Park in June 2009 (see Operational Section 2). For this system, processing begins as the waveforms arrive at the computers operating the real-time, or AQMS, software, and ranges from automatic preparation of earthquake information for response to analyst review of earthquakes for catalogs and quality control.

This is the most recent step in a development at the BSL that began in the mid-1990s with the automated earthquake notification system called Rapid Earthquake Data Integration (REDI, *Gee et al.*, 1996; 2003a). This system determined earthquake parameters rapidly, producing near real-time locations and magnitudes of Northern and Central California earthquakes, estimates of the rupture characteristics and the distribution of ground shaking following significant earthquakes, and tools for the rapid assessment of damage and estimation of loss. A short time later, in 1996, the BSL and the USGS began a collaboration for reporting on Northern and Central California earthquakes. Software operating in Menlo Park and Berkeley were merged to form a single, improved earthquake notification system using data from both the NCSN and the BDSN (see past annual reports). The USGS and the BSL are now joined as the Northern California Earthquake Management Center (NCEMC) of the California Integrated Seismic Network (Operational Section 2).

With partial support from the USGS, the BSL is currently also participating in the development and assessment of a statewide prototype system for warning of imminent ground shaking in the seconds after an earthquake has initiated but before strong motion begins at sites that may be damaged (See Research Studies 2 and 1).

8.2 Northern California Earthquake Management Center

In this section, we describe how the Northern California Earthquake Management Center fits within the CISN system. Figure 3.11 in Operational Section 2 illustrates the NCEMC as part of the the CISN communications ring. The NCEMC is a distributed center, with elements in Berkeley and in Menlo Park. The 35 mile separation between these two centers is in sharp contrast to the Southern California Earthquake Management Center, where the USGS Pasadena is located across the street from the Caltech Seismological Laboratory. As de-

scribed in Operational Section 2, the CISN partners are connected by a dedicated T1 communications link, with the capability of falling back to the Internet. In addition to the CISN ring, the BSL and the USGS Menlo Park have a second dedicated communications link to provide bandwidth for shipping waveform data and other information between their processing systems.

Figure 3.36 provides more detail on the system operating at the NCEMC since mid-June, 2009. Now, complete earthquake information processing systems operate in parallel in Menlo Park and Berkeley. Incoming data from each network are processed locally at each of the two data centers in network services computers. The continuous reduced data, which include picks, codas, ground motion amplitudes, and ML100, are exchanged between the data centers and fed into both processing streams. Real time analysis is coordinated using up-to-date information from the local real-time database, which is replicated to the local data center database. Event review and automatic downstream processes such as computation of fault plane solutions access the internal data center databases. To maintain redundancy, robustness, and completeness, these two databases replicate with each other across the San Francisco Bay. They also replicate with the public database from which information is made available to the public. The system includes the production of location and origin time as well as estimates of M_d , M_L , and M_w . For events with $M > 3.5$, ShakeMaps are also calculated on two systems, one in Menlo Park and one in Berkeley. Finite fault calculation is not yet integrated into the new processing system. It is only calculated at the BSL at this time.

This new system combines the advantages of the NCSN with those of the BDSN. The dense network of the NCSN contributes to rapid and accurate earthquake locations, low magnitude detection thresholds, and first-motion mechanisms. The high dynamic range data loggers, digital telemetry, and broadband and strong-motion sensors of the BDSN provide reliable magnitude determination, moment tensor estimation, calculation of peak ground motions, and estimation of source rupture characteristics. Robust preliminary hypocenters, or “Quick Looks” are published within about 25 seconds of the origin time. Event information is updated when preliminary coda magnitudes are available, within 2-4 minutes of the origin time. Estimates of local magnitude are generally available less than 30 seconds later, and other parameters, such as the peak ground acceleration and moment magnitude, follow within 1-4 minutes (Figure 3.37).

Earthquake information is now distributed to the web through EIDS and is available through the USGS Earth-

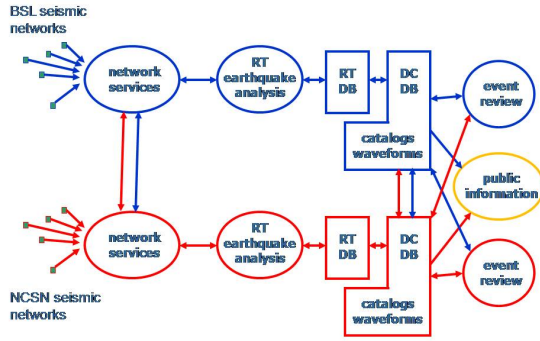


Figure 3.36: Details of the new Northern California processing system, which has been operational since mid-June, 2009. Network services processing, that is, production of picks, ground motion amplitudes, and other reduced information, occurs at both datacenters, and the information is exchanged. Complete earthquake information processing systems exist on both sides of the San Francisco Bay, and up-to-date information is exchanged by database replication.

quake Notification Service (<http://sslearnquake.usgs.gov/ens>). Organizations with the need for more rapid earthquake information should use CISN Display (<http://www.cisn.org/software/cisndisplay.htm>). The *recenteqs* site has enjoyed enormous popularity since its introduction and provides a valuable resource for information which is useful not only in the seconds immediately after an earthquake, but in the following hours and days as well.

8.3 2010-2011 Activities

In June 2009, we began operating the ANSS Quake Monitoring System (AQMS) software, formerly CISN Software, as the production system in the Northern California Seismic System (NCSS) for monitoring and reporting on Northern California earthquakes. This came as the result of a long effort to adapt and test software developed for the Trinet system operating in Southern California.

Data flow in the new Northern California system (Figure 3.38) has been modified to allow for local differences (such as very different forms of data acquisition and variability in network distribution). In addition, the BSL and the USGS want to minimize use of proprietary software in the system. One exception is the database program, Oracle. The NCEDC Oracle database hosts all earthquake information and parameters associated with the real time monitoring system. It is the centerpoint of the new system, providing up-to-date information to all pro-

cessing modules. Reliability and robustness are achieved by continuously replicating the databases. The public, read-only, database provides event and parametric information to catalog users and to the public.

During the last few years, BSL staff members, particularly Pete Lombard, have become extremely familiar with elements of the TriNet software. The software is now adapted for Northern California, with many adjustments and modifications completed along the way. For example, Pete Lombard adapted the TriNet magnitude module to Northern California. Pete made a number of suggestions on how to improve the performance of the magnitude module and has worked closely with Caltech and the USGS/Pasadena on modifications.

The BSL and the USGS Menlo Park are exchanging “reduced amplitude timeseries.” One of the important innovations of the TriNet software development is the concept of continuous processing (*Kanamori et al., 1999*). Waveform data are constantly processed to produce Wood Anderson synthetic amplitudes and peak ground motions. A program called *rad* produces a reduced timeseries, sampled every 5 seconds, and stores it in a memory area called an “Amplitude Data Area” or ADA. Other modules can access the ADA to retrieve amplitudes to calculate magnitude and ShakeMaps as needed. The BSL and the USGS Menlo Park have collaborated to establish tools for ADA-based exchange. The next step in improving reliability and robustness is to implement ADA exchange with Southern California as well.

Testing System Robustness

In fact, we tested robustness of operations in the NCEMC during the past year. In July 2010, the USGS was required to test their power systems. In preparation and on relatively short notice, we jointly developed and implemented a plan to ensure reliable data acquisition and earthquake reporting during the shutdown. Local telemetry support systems, and data acquisition and network services computers were operated with electricity from a rented generator. In this instance, all information for Northern California earthquakes was reported from UC Berkeley. In June 2011, the UC Berkeley data center was impacted by planned upgrades to power support services in Warren Hall. Again, a plan to maintain information services was developed and implemented. For the term of the shutdown, all earthquake information was provided from Menlo Park.

Moment Tensor Solutions with *tmts* and Finite Fault Analysis

The BSL continues to focus on the unique contributions that can be made from the broadband network, including moment tensor solutions and finite fault analysis.

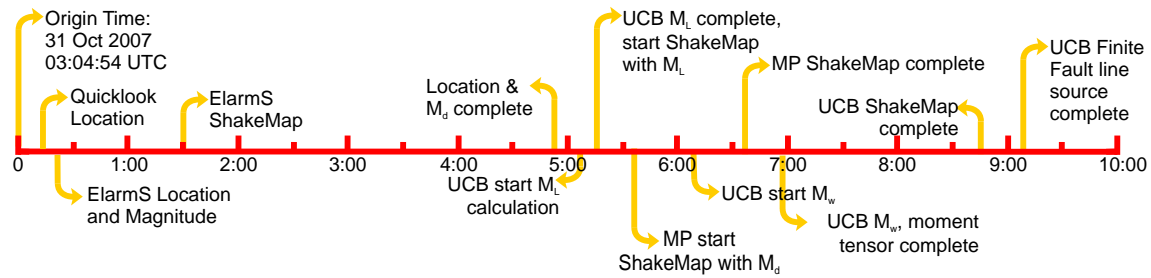


Figure 3.37: Illustration of the earthquake products timeline for the M_w 5.4 Alum Rock earthquake of October 30, 2007. Note that all processing was complete within 10 minutes of the origin time.

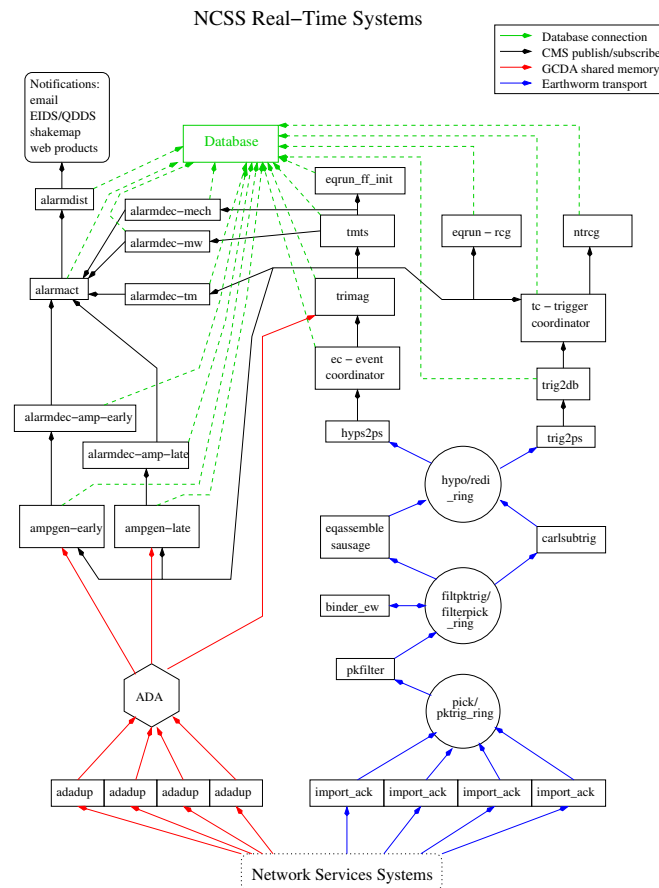


Figure 3.38: Schematic diagram of processing in the NCSS system. The design combines elements of the Earthworm, TriNet, and REDI systems

`tmts` is a Java and web-based moment tensor processing system and review interface based on the complete waveform modeling technique of *Dreger and Romanowicz* (1994). The improved, web-based review interface has been operating in Northern California since July 2007.

The automatically running version for real-time analysis was extensively tested and updated by Pete Lombard, and has been running since June 2009. Reporting rules now allow automatically produced solutions of high quality to be published to the web.

From July 2010 through June 2011, BSL analysts reviewed many earthquakes in Northern California and adjoining areas of magnitude 2.9 and higher. Reviewed moment tensor solutions were obtained for 69 of these events (through 6/30/2011). Figure 3.39 and Table 3.21 display the locations of earthquakes in the BSL moment tensor catalog and their mechanisms. During this year, no finite fault inversions were produced for Northern California earthquakes.

During the past year, we have implemented a new version of `tmts`, which allows full inversions that include an isotropic element of the source, i.e. explosions or collapses. With the advent of the new code, we have completed our review of “old” events by analyzing Geysers events from before 2007 with the new interface to produce and store deviatoric solutions for them in the database. In the next step, we will reanalyze events which exhibited anomalous radiation using the option for the full moment tensor (see 12). Some, but not all of these events will exhibit robust isotropic components.

We are currently developing a new version of the moment tensor system which will permit the use of records from strong motion sensors.

Station Metadata, Reversals and `fpfit`

In a review of the fault plane solution for a recent event near the Geysers, we discovered that the orientation information for many of the seismic stations there was inconsistent. The fault plane solution program, `fpfit`, uses a file listing the stations with “reversed” polarity from the standard orientation. In the past, this file has been generated by hand and updated only occasionally. We reviewed the orientations of the borehole sensors contributing data to NCEMC operations, at Parkfield, in the San Francisco Bay Area and at the Geysers, using regional or teleseismic earthquakes. This information has been fed into the instrument response data. In a final step, we developed a procedure to compile the reversals file for `fpfit` from the database.

8.4 Routine Earthquake Analysis

In fiscal year 2010-2011, more than 27,000 earthquakes were detected and located by the automatic systems in Northern California. This compares with over 25,000 in 2009-2010, 21,500 in 2008-2009, 26,000 in 2007-2008, 23,000 in 2006-2007, 30,000 in 2005-2006, and 38,800 in 2004-2005. Many of the large number of events in 2004-2005 are aftershocks of the 2003 San Simeon and 2004 Parkfield earthquakes. Of the more than 27,000 events, about 126 had preliminary magnitudes of three or greater. Nine events had M_L or M_w greater than 4. The three largest events (on March 6, 2011, January 12, 2011 and March 1, 2011) had magnitudes close to

4.5. They were located offshore of Petrolia, CA, near San Juan Bautista, CA and near the Geysers, CA, respectively (see Table 3.21 for more details).

Although BSL staff no longer read BDSN records for local and regional earthquakes (see Annual Report of 2003-2004), they now participating in timing and reviewing earthquakes with `Jiggle`, mainly working on events from past sequences that have not yet been timed. This work contributes to improving the earthquake catalog for Northern California, but also ensures robust response capabilities, should the Menlo Park campus be disabled for some reason.

8.5 Acknowledgements

Peggy Hellweg oversees our earthquake monitoring system and directs the routine analysis. Peter Lombard and Doug Neuhauser contribute to the development of software. Taka’aki Taira, Ingrid Johanson, Doug Dreger, Sierra Boyd, Holly Brown, Sanne Cottaar, Andrea Chiang, Shan Dou, Scott French, Aurelie Guilhem, Mong-Han Huang, Rob Porritt, Jennifer Taggart, Amanda Thomas, Tom Weldon, Kelly Wiseman, and Zhou (Allen) Zheng contribute to the routine analysis of moment tensors. Peggy Hellweg, Doug Neuhauser, and Taka’aki Taira contributed to the writing of this section. Partial support for the development, implementation and maintenance of the AQMS software, as well as for the production of earthquake information, is provided by the USGS under Cooperative Agreement G10AC00093.

8.6 References

- Dreger, D., and B. Romanowicz, Source characteristics of events in the San Francisco Bay region, *USGS Open File Report 94-176*, 301-309, 1994.
- Gee, L., J. Polet, R. Uhrhammer, and K. Hutton, Earthquake Magnitudes in California, *Seism. Res. Lett.*, 75(2), 272, 2004.
- Gee, L., D. Neuhauser, D. Dreger, M. Pasyanos, R. Uhrhammer, and B. Romanowicz, The Rapid Earthquake Data Integration Project, *Handbook of Earthquake and Engineering Seismology*, IASPEI, 1261-1273, 2003a.
- Gee, L., D. Dreger, G. Wurman, Y. Gung, B. Uhrhammer, and B. Romanowicz, A Decade of Regional Moment Tensor Analysis at UC Berkeley, *Eos Trans. AGU*, 84(46), Fall Meet. Suppl., Abstract S52C-0148, 2003b.
- Gee, L., D. Neuhauser, D. Dreger, M. Pasyanos, B. Romanowicz, and R. Uhrhammer, The Rapid Earthquake Data Integration System, *Bull. Seis. Soc. Am.*, 86, 936-945, 1996.
- Pasyanos, M., D. Dreger, and B. Romanowicz, Toward real-time estimation of regional moment tensors, *Bull. Seis. Soc. Am.*, 86, 1255-1269, 1996.
- Romanowicz, B., D. Dreger, M. Pasyanos, and R. Uhrhammer, Monitoring of strain release in central and northern California using broadband data, *Geophys. Res. Lett.*, 20, 1643-1646, 1993.

Location	Date	UTC Time	Lat.	Lon.	MT Depth	M_L	M_w	Mo	Str.	Dip	Rake
Hamilton City, CA	7/1/2010	00:29:47	39.77	-122.08	18	3.20	3.31	1.13E+21	336	67	-140
Gold Beach, OR	7/3/2010	22:25:20	42.44	-124.15	36	3.41	3.70	4.34E+21	238	59	-49
The Geysers, CA	7/4/2010	09:07:35	38.79	-122.81	5	2.93	3.27	1.02E+21	82	81	-30
Hayfork, CA	7/10/2010	16:04:30	40.42	-123.57	33	3.37	3.81	5.79E+21	16	65	-65
The Geysers, CA	7/15/2010	15:31:44	38.82	-122.81	5	3.66	3.95	1.06E+22	78	89	-11
The Geysers, CA	7/15/2010	23:54:20	38.82	-122.82	5	3.50	3.83	6.99E+21	51	63	-40
San Juan Bautista, CA	7/21/2010	06:54:35	36.83	-121.57	8	3.69	3.35	1.30E+21	49	89	-5
Toms Place, CA	7/22/2010	11:40:08	37.62	-118.81	5	3.95	3.76	5.44E+21	199	78	-36
Daly City, CA	7/23/2010	21:29:10	37.67	-122.51	8	3.32	3.15	6.61E+20	36	66	-35
Lake Pillsbury, CA	7/27/2010	21:21:40	39.5	-123.12	8	3.12	3.36	1.36E+21	346	74	-134
The Geysers, CA	7/28/2010	22:37:01	38.82	-122.79	5	2.97	3.31	1.13E+21	187	63	-117
Lake Pillsbury, CA	7/31/2010	01:31:58	39.31	-122.81	8	2.80	3.01	4.05E+20	75	73	-46
New Idria, CA	8/2/2010	04:00:09	36.25	-120.82	8	3.42	3.40	1.58E+21	149	88	170
Toms Place, CA	8/6/2010	01:20:03	37.62	-118.81	8	3.79	3.60	3.13E+21	27	85	34
Aromas, CA	8/10/2010	00:51:11	36.91	-121.64	8	3.99	3.85	6.08E+21	55	89	-11
Lake Davis, CA	8/10/2010	02:12:31	39.88	-120.48	8	3.51	3.45	1.89E+21	200	73	-36
The Geysers, CA	8/13/2010	15:51:58	38.8	-122.81	5	2.78	3.19	7.56E+20	27	77	-54
Cobb, CA	8/15/2010	18:51:56	38.82	-122.77	5	3.12	3.33	1.25E+21	46	59	-41
Ferndale, CA	8/16/2010	12:05:17	40.77	-125.15	14	4.34	4.37	4.53E+22	220	87	8
San Juan Bautista, CA	8/20/2010	00:50:03	36.83	-121.57	8	3.15	3.13	6.11E+20	51	88	-22
Petroliia, CA	8/25/2010	13:23:41	40.3	-124.57	18	2.93	3.28	1.03E+21	15	76	-20
San Simeon, CA	8/25/2010	17:20:00	35.82	-121.18	5	4.06	3.69	4.20E+21	251	84	17
Lake Pillsbury, CA	8/28/2010	11:49:56	39.31	-122.8	18	3.17	3.56	2.71E+21	70	63	-43
Aromas, CA	9/1/2010	05:58:36	36.86	-121.6	8	3.26	3.22	8.45E+20	238	67	28
San Pablo, CA	9/2/2010	16:35:34	37.96	-122.35	8	3.19	3.12	5.89E+20	62	87	9
Pinnacles, CA	9/7/2010	06:59:26	36.56	-121.07	8	3.20	3.11	5.83E+20	353	86	-164
Humboldt Hill, CA	10/5/2010	15:15:28	40.95	-124.8	24	4.26	4.39	4.78E+22	141	83	169
French Camp, CA	10/15/2010	11:04:10	37.88	-121.39	14	3.13	3.17	6.97E+20	297	81	101
Alum Rock, CA	10/15/2010	16:13:54	37.41	-121.75	8	2.94	3.00	4.00E+20	62	86	16
Tahoe Vista, CA	10/18/2010	03:44:43	39.35	-120.03	8	2.97	3.09	5.36E+20	220	76	-25
Myrtle town, CA	10/18/2010	15:21:38	40.73	-123.96	21	3.20	3.43	1.77E+21	38	66	-36
The Geysers, CA	10/19/2010	17:51:49	38.84	-122.79	5	3.41	3.54	2.53E+21	36	51	-87
Markleeville, CA	10/31/2010	01:02:06	38.64	-119.57	14	4.71	4.28	3.29E+22	233	89	-10
Viola, CA	11/21/2010	07:29:38	40.56	-121.72	8	3.44	3.48	2.09E+21	162	69	-113
Lake Davis, CA	11/21/2010	20:09:57	39.88	-120.49	8	3.86	3.64	3.59E+21	201	85	-39
Aromas, CA	11/24/2010	03:22:59	36.88	-121.62	8	3.22	3.30	1.11E+21	58	89	-6
Seven Trees, CA	11/25/2010	06:28:38	37.3	-121.67	11	3.15	3.25	9.40E+20	333	86	-165
Pinnacles, CA	11/30/2010	12:21:16	36.6	-121.21	8	3.00	3.14	6.45E+20	37	86	-10
The Geysers, CA	12/6/2010	13:57:38	38.8	-122.8	5	3.53	3.71	4.60E+21	42	74	-36
Petroliia, CA	12/8/2010	20:18:57	40.35	-125.28	18	3.55	3.95	1.03E+22	91	85	174
New Idria, CA	12/18/2010	02:03:19	36.46	-120.56	8	3.63	3.55	2.67E+21	295	49	66
Anderson Springs, CA	12/21/2010	10:10:30	38.79	-122.74	5	3.34	3.58	2.87E+21	156	88	176
Hydesville, CA	12/24/2010	12:59:20	40.54	-123.87	21	3.25	3.69	4.21E+21	331	70	-129
Seven Trees, CA	1/8/2011	00:10:17	37.29	-121.66	8	4.28	4.10	1.78E+22	235	86	-11
San Juan Bautista, CA	1/12/2011	08:51:04	36.77	-121.5	8	4.62	4.50	6.97E+22	227	87	21
San Juan Bautista, CA	1/13/2011	03:54:35	36.8	-121.54	8	3.56	3.68	4.06E+21	58	87	-20
San Juan Bautista, CA	1/13/2011	04:00:36	36.8	-121.54	8	4.23	3.92	9.30E+21	229	85	26
Lake Pillsbury, CA	2/23/2011	04:49:42	39.5	-122.95	14	4.06	4.29	3.41E+22	336	89	-163
Lake Pillsbury, CA	2/23/2011	04:50:14	39.49	-122.96	14	4.03	4.21	2.54E+22	247	86	6
The Geysers, CA	3/1/2011	02:19:47	38.82	-122.82	5	3.94	4.46	6.19E+22	342	61	-121
Bishop, CA	3/3/2011	02:58:17	37.4	-118.37	14	3.57	3.49	2.15E+21	240	83	31
Petroliia, CA	3/6/2011	13:46:38	40.4	-125.36	24	3.74	4.54	7.98E+22	95	83	162
Pinnacles, CA	3/17/2011	17:18:30	36.62	-121.23	8	3.26	3.27	1.01E+21	219	88	21
Ukiah, CA	3/21/2011	20:42:27	39.12	-123.42	5	3.36	3.47	2.02E+21	343	86	163
Chilcoot-Vinton, CA	3/24/2011	21:20:40	40.04	-120.06	5	3.74	3.49	2.15E+21	291	86	-174
Rio Dell, CA	3/31/2011	11:58:50	40.43	-124.22	27	3.24	3.60	3.12E+21	215	75	-22
Lopez Point, CA	4/5/2011	11:56:50	36.07	-121.62	5	4.11	3.89	8.45E+21	131	56	103
Petroliia, CA	4/10/2011	16:21:54	40.46	-125.9	21	3.66	3.90	8.90E+21	190	85	11
San Bruno, CA	4/18/2011	21:57:19	37.6	-122.45	11	3.67	3.37	1.41E+21	231	89	2
Blue Lake, CA	4/22/2011	01:32:14	40.81	-123.96	24	3.04	3.25	9.27E+20	303	86	-155
The Geysers, CA	4/23/2011	19:42:59	38.83	-122.79	5	2.91	3.38	1.49E+21	62	58	-51
East Shore, CA	4/26/2011	08:02:50	40.23	-121.05	5	3.02	3.28	1.03E+21	335	52	-128
The Geysers, CA	4/26/2011	17:43:08	38.81	-122.82	8	3.51	3.90	8.80E+21	84	85	-11
Lake Pillsbury, CA	5/2/2011	10:53:03	39.46	-122.94	14	3.05	3.40	1.55E+21	248	88	11
Ukiah, CA	5/17/2011	15:20:07	39.23	-123.18	11	3.21	3.74	5.08E+21	204	77	-23
Hercules, CA	5/22/2011	02:04:58	37.98	-122.25	8	3.44	3.36	1.36E+21	244	89	14
The Geysers, CA	5/28/2011	22:55:25	38.79	-122.76	5	3.63	3.71	4.62E+21	37	86	-12
Petroliia, CA	6/14/2011	12:20:48	40.29	-124.38	18	3.42	3.69	4.31E+21	100	89	175
Anderson Springs, CA	6/29/2011	11:13:31	38.74	-122.72	1.5	3.46	3.31	1.14E+21	271	47	-99

Table 3.21: Moment tensor solutions for significant events from July 1, 2010 through June 30, 2011 using a complete waveform fitting inversion. Epicentral information is from the UC Berkeley/USGS Northern California Earthquake Management Center. Moment is in dyne-cm and depth is in km.

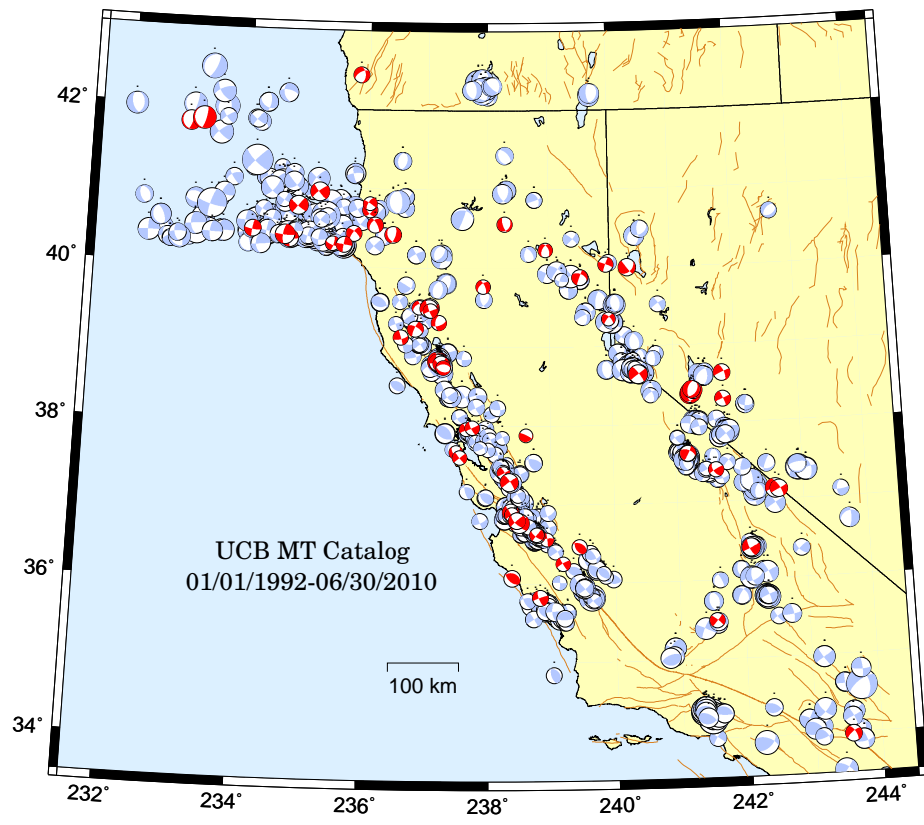


Figure 3.39: Map comparing reviewed moment tensor solutions determined by the BSL from past years (gray) with those from the fiscal year 2010-2011 (red/dark).

9 Outreach and Educational Activities

9.1 Introduction

BSL faculty, staff, and graduate students are involved in a wide variety of outreach activities, ranging from public lectures to science festivals to tours of Hayward Fault geomorphology on campus. Our public lectures and talks included this year's Lawson Lecture and participation in a special symposium on the Tohoku earthquake in Japan. Cal Day provided an opportunity to showcase our new large-screen SWARM display of seismic data as well as to guide the public in hands-on earthquake science activities. This year, our Web pages, which provide information on earthquakes and seismic hazards for northern and central California, underwent significant changes in their look and feel (<http://seismo.berkeley.edu/>).

9.2 Highlights of 2010-2011

Lawson Lecture

In this year's Lawson Lecture, Dr. Mary Comerio of UC Berkeley's Department of Architecture spoke on "Two Earthquakes in Christchurch, New Zealand: Lessons for California." Dr. Comerio introduced the tectonic setting of the Christchurch area and the perceived seismic hazard in the region. She then described the damage to the city from the 2011 Christchurch and 2010 Darfield earthquakes. These New Zealand earthquakes provided important points of comparison for California due to the similar ages of New Zealand and California cities and the similarly high-quality building codes. Showing slides highlighting the damage from these two quakes, she reflected on the large amount of damage even a moderate earthquake can cause, the high cost of nonstructural damage in both dollars and recovery time, and the tendency of hazard-mitigation and disaster-preparedness experts to focus almost exclusively on the highest-risk areas, often to the detriment of areas with only moderate risk. The Lawson Lectures are viewable as Flash video at http://seismo.berkeley.edu/news/lawson_lecture.

Tohoku Earthquake Symposium

On March 29, 2011, BSL members and other area scientists gathered to present a special symposium on the magnitude 9.0 Tohoku earthquake of March 11, 2011. The special focus of this event was whether a similar catastrophe can happen in California. The event was hosted by the Berkeley Institute of the Environment, the UC Berkeley College of Letters and Science, the Department of Earth and Planetary Science, the Berkeley Seismological Laboratory, and the Pacific Earthquake Engineering Research Center. The symposium, titled "Earth-

quakes, Tsunamis, and Nuclear Fallout: Is California at Risk Like Japan?" began with a brief presentation by each member of the panel, which was followed by questions from the audience. The BSL's Roland Bürgmann discussed the type and size of earthquake we could expect to see in the Bay Area and the Pacific Northwest, while BSL seismologist Doug Dreger (in lieu of Professor Richard Allen, on sabbatical) explained how earthquake early warning works and what would be needed for the state of California to have earthquake early warning like Japan. (In addition to participating in the symposium, the BSL responded to a large number of media enquiries about the Tohoku earthquake in the days following the event.)

SWARM Lobby Display

This year, the BSL used departmental Ramsden funds to purchase a large flatscreen monitor to be outfitted with the USGS SWARM program for viewing seismic data. Streaming real-time data from station BKS, the SWARM display allowed Cal Day visitors and visiting schoolchildren the opportunity to view up to 72 hours of seismic data and to zoom in on individual earthquakes of interest. The SWARM display will soon be outfitted with a special wall-mount touchscreen and mounted in the McCone Hall first floor lobby display case.

Resilience 2011

Each year, the Office of Emergency Preparedness organizes an emergency preparedness and response exercise. This year's scenario "Resilience 2011," again involved a moderate earthquake. The BSL provided consultation to staff at UCB's Office of Emergency Preparedness in developing this exercise.

9.3 Ongoing Activities

During 2010-2011, many groups, ranging from elementary-school students to international guests, visited the BSL for talks, tours, and hands-on science experiences. BSL faculty gave three presentations to international delegations; two to visitors in the U.S. State Department's International Visitor Leadership Program and one to the Israeli Home Front Command. Staff and graduate students conducted several talks and tours, with visiting groups ranging from local summer campers to high school students from Great Britain. BSL seismologist Peggy Hellweg collaborated with this year's Lawson Lecture speaker, Dr. Mary Comerio, giving talks to Dr. Comerio's freshman and graduate level architecture classes. Drs. Hellweg and Mayeda presented talks

on earthquakes and related phenomena to several local public groups, including Oakland Museum of California docents, and staff members at the Lawrence Hall of Science.

Recorded information on current earthquake activity is updated regularly on our information tape (510-642-2160).

Cal Day - BSL Open House

This year, *Cal Day* visitors to the BSL's open house could crank a friction display or jump up and down in front of a seismometer to make their own "earthquake," watch online videos of the Japan earthquake symposium, view current seismic data from our station BKS on a flatscreen monitor with the SWARM program, or learn about inertia and seismometers with a helium balloon tied to a radio-controlled car. Younger guests were offered their very own seismograms and stickers for their Cal Day Passports, and adults could pick up earthquake preparedness information provided by the BSL and the USGS. Guests were invited to write (or draw!) their earthquake questions for the BSL to try to answer later on our webpage. (Answers are available at <http://seismo.berkeley.edu/outreach/faq.html>.) Graduate student volunteers were on hand to explain our exhibits and talk with visitors about UC Berkeley's role in earthquake monitoring.

Displays

The BSL provides local waveform feeds for helicorders at visitor centers associated with BDSN stations (CMB and MHC). Organizations such as LHS, KRON, and KPIX receive feeds from BKS via dedicated phone lines for display, while the USGS Menlo Park uses data from CMB for display in the lobby of the seismology building.

BSL Web Pages

This year, the look and feel of the BSL Web pages was modernized (<http://seismo.berkeley.edu>). A template web page with flyout menu links provided by the UCB Public Affairs served as a starting point. Jennifer Taggart added a second level of nested flyout menu links and a homepage seismogram that changes on page refresh. Ms. Taggart created several color schemes from which BSL faculty selected the finalist. She also put the web pages under the control of wsmake, our current website maintenance software. The new look reflects the progress made in the past decade with Web design using Cascading Style Sheets (CSS).

The BSL's main Web pages describe our mission, introduce our research groups, provide information on our seminars and other special events (such as the Lawson Lecture), and point the public to sources of frequently sought-after earthquake-related information such

as Alquist Priolo Zoning Act maps. The "seismic networks" Web pages provide detailed information on each of our seismic stations, of interest to the research community. Our recently expanded education and outreach Web site (<http://seismo.berkeley.edu/outreach>) teaches the public about earthquakes and about Bay Area seismicity and hazards through Flash videos and FAQs while acting as a resource clearinghouse for teachers and those who wish to dig deeper. In addition, since September, 2008, the BSL has hosted its own blog, written by Horst Rademacher (<http://seismo.berkeley.edu/seismo.blog>).

Earthquake Research Affiliates Program

The UC Berkeley Earthquake Research Affiliates (ERA) Program is an outreach project of the BSL. The purpose is to promote the support of earthquake research while involving corporations and governmental agencies in academic investigation and education activities such as conferences and field trips. The ERA program provides an interface between the academic investigation and practical application of earthquake studies.

9.4 Acknowledgements

Peggy Hellweg oversees the outreach activities at the BSL. Barbara Romanowicz, Bob Uhrhammer, Jennifer Taggart, Tom Weldon, and many other faculty, staff, and students at the BSL contribute to the outreach activities. Jennifer Taggart and Peggy Hellweg contributed to the preparation of this section.

Glossary of Common Acronyms

Table 3.22: Standard abbreviations used in this report.

Acronym	Definition
ADA	Amplitude Data Area
ANSS	Advanced National Seismic System
ANSS NIC	ANSS National Implementation Committee
AQMS	ANSS Quake Monitoring System
ARRA	American Recovery and Reinvestment Act
BARD	Bay Area Regional Deformation
BAVU	Bay Area Velocity Unification
BDSN	Berkeley Digital Seismic Network
BSL	Berkeley Seismological Laboratory
CalEMA	California Emergency Management Agency
Caltrans	California Department of Transportation
CDF	California Department of Forestry
CGS	California Geological Survey
CISN	California Integrated Seismic Network
DART	Data Available in Real Time
EEW	Earthquake Early Warning
ElarmS	Earthquake Alarm Systems
EM	Electromagnetic
FACES	FlexArray along Cascadia Experiment for Segmentation
FEMA	Federal Emergency Management Agency
HFN	Hayward Fault Network
HRSN	High Resolution Seismic Network
InSAR	Interferometric Synthetic Aperture Radar
IRIS	Incorporated Research Institutions in Seismology
IRIS DMC	IRIS Data Management Center
LBNL	Lawrence Berkeley National Laboratory
LFE	Low Frequency Event
LLNL	Lawrence Livermore National Laboratory
MARS	Monterey Accelerated Research System
MBARI	Monterey Bay Aquarium Research Institute
MOBB	Monterey Ocean Bottom Broadband Observatory
mPBO	Mini-Plate Boundary Observatory
MT	Magnetotelluric
MT	Moment Tensor
MTJ	Mendocino Triple Junction
NCEDC	Northern California Earthquake Data Center
NCEMC	Northern California Earthquake Management Center
NCSN	Northern California Seismic Network
NCSS	Northern California Seismic System
NHFN	Northern Hayward Fault Network

continued on next page

Table 3.22: *continued*

Acronym	Definition
NVT	Non-volcanic Tremor
PBO	Plate Boundary Observatory
PDF	Probability Density Function
PGV	Peak Ground Velocity
PSD	Power Spectral Density
QDDS/EIDS	Quake Data Distribution System/Earthquake Information Distribution System
REDI	Rapid Earthquake Data Integration
RES	Repeating Earthquake Sequence
SAF	San Andreas Fault
SAFOD	San Andreas Fault Observatory at Depth
SEED	Standard for Exchange of Earthquake Data
SEM	Spectral Element Method
SHFN	Southern Hayward Fault Network
SOH	State of Health
SCSN	Southern California Seismic Network
UNAVCO	University NAVSTAR Consortium
USGS/MP	United States Geological Survey/ Menlo Park
USNSN	United States National Seismic Network

Appendix I: Publications, Presentations, Awards, and Panels 2010-2011

Publications

- Aagaard, B. T., R. W. Graves, A. Rodgers, T. M. Brocher, R. W. Simpson, D. Dreger, N. Anders Petersson, S. C. Larsen, S. Ma, and R. C. Jachens, Ground-motion modeling of Hayward fault scenario earthquakes, Part II: Simulation of long-period and broadband ground motions *Bull. Seism. Soc. Am.*, *100*, 2945-2977, 2010.
- Allen, R.M., Earthquakes, Early and Strong Motion Warning, in *Encyclopedia of Solid Earth Geophysics*, Harsh Gupta (ed.), p226-233, Springer, 2011.
- Allen, R.M., Seconds before the big one, *Scientific American*, 74-79, April 2011.
- Allen, R.M. and A. Ziv, Application of real-time GPS to earthquake early warning, *Geophys. Res. Lett.*, *38*, L16310, doi:10.1029/2011GL047947, 2011.
- Amos, C.B., J.J. Lapwood, D.C. Nobes, D.W. Burbank, U. Rieser, and A. Wade, Paleoseismic Constraints on Holocene Surface Ruptures along the Ostler Fault, Southern New Zealand, *New Zealand Journal of Geology and Geophysics*, in press.
- Audet, P., Directional wavelet analysis on the sphere: Application to gravity and topography of the terrestrial planets, *Journal of Geophysical Research - Planets*, *116*, E01003, doi:10.1029/2010JE003710, 2011.
- Audet, P., and R. Bürgmann, Dominant role of tectonic inheritance in supercontinent cycles, *Nature Geoscience*, *4*, 184-187, doi:10.1038/ngeo1080, 2011.
- Audet, P., and Bürgmann, R., Global effective elastic thickness, mechanical anisotropy and the supercontinent cycle: *Nature Geoscience*, *4*, 184-187, doi:10.1038/NGEO1080, 2011.
- Brown, H., R.M. Allen, M. Hellweg, O. Khainovski, D. Neuhauser, A. Souf, Development of the ElarmS methodology for earthquake early warning: Realtime application in California and offline testing in Japan, *Soil Dyn. Earthquake Eng.* *31*, 188-200, doi:10.1016/j.soildyn.2010.03.008, 2011.
- Bürgmann, R., and P. Audet, Continental jelly, *Nature*, *471*, 312-313 (News & Views), 2011.
- Chen, K-H., R. Bürgmann, R.M. Nadeau, T. Chen, and N. Lapusta, Postseismic variations in seismic moment and recurrence interval of repeating earthquakes, *Earth Planet. Sci. Lett.*, *299*, 118-125, doi:10.1016/J.epsl.2010.08.027, 2010.
- Cheng, X., F. Niu, P.G. Silver, and R. M. Nadeau, Seismic imaging of scatterer migration associated with the 2004 Parkfield earthquake using waveform data of repeating earthquakes and active sources, *Bull. Seismol. Soc. Am.*, *101*, 1291-1301, doi:10.1785/0120100261, 2011.
- Chong, J.J., S.D. Ni and X.F. Zeng, sPL, an effective seismic phase for determining focal depth at near distance, *Chinese J Geophys* *53(11)* 2620-2630, 2011 (in Chinese with English abstract).
- Cupillard, P., L. Stehly and B. Romanowicz, The one-bit noise correlation: a theory based on the concepts of coherent and incoherent noise, *Geophys. J. Int.* *184*, 1397-1414, 2010.

- Dreger, D., G. Hurtado, A. Chopra, and S. Larsen, Near-Field Across-Fault Seismic Ground Motions, *Bull. Seism. Soc. Am.* *101*(1), 202-221; DOI: 10.1785/0120090271, 2010.
- Durand, S., J.P. Montagner, P. Roux, F. Brenguier, and R.M. Nadeau, Passive monitoring of anisotropy change for the Parkfield 2004 earthquake, *Geophys. Res. Lett.*, accepted.
- Dziewonski, A. M., V. Lekic and B. Romanowicz, Mantle Anchor Structure: an Argument for Bottom up Tectonics, *Earth and Planetary Science Lett.*, *299*, 69-79, 2010 (Highlighted in *Nature Geosciences*).
- Farrell, J., R. B. Smith, T. Taira, W.-L. Chang, and C. M. Puskas, Dynamics and rapid migration of the energetic 2008-2009 Yellowstone Lake earthquake swarm, *Geophys. Res. Lett.*, *37*, L19305, doi:10.1029/2010GL044605, 2010.
- Ford, S.R., R.A. Uhrhammer and M. Hellweg, Local Magnitude Tomography in California. *Bull. Seismol. Soc. Am.*, *101*, 427 - 432, 2011.
- Freed, A.M., Herring, T.A., and Bürgmann, R., Steady-state laboratory flow laws alone fail to explain postseismic observations, *Earth and Planetary Science Letters*, *300*, doi:10.1016/j.epsl.2010.1010.1005, 2010.
- Guilhem, A. and D. S. Dreger, Rapid detection and characterization of large earthquakes using quasi-finite source Green's functions in continuous moment tensor inversion, *Geophysical Research Letter*, *38*, L13318, doi:10.1029/2011GL047550, 2011.
- Guilhem, A., Z. Peng, and R.M. Nadeau, High-frequency identification of non-volcanic tremor triggered by regional earthquakes, *Geophys. Res. Lett.*, *37*, L16309, doi:10.1029/2010GL044660, 2010.
- Hammond, W. C., Brooks, B. A., Bürgmann, R., Heaton, T., Jackson, M., Lowry, A. R., and Anandakrishnan, S., Scientific value of real-time Global Positioning System data *Eos*, *92*(15), 125-132, 2011.
- Houlié, N. and B. Romanowicz, Asymmetric deformation across the San Francisco Bay Area faults from GPS observations in northern California, *Phys. Earth. Planet. Inter.*, *184*, 143-153, 2011.
- Hsieh, C.-S., T.-Y. Shih, J.-C. Hu, H. Tung, M.-H. Huang, and J. Angelier, Using differential SAR interferometry to map land subsidence: a case study in the Pingtung Plain of SW Taiwan, *Nat. Hazards*, doi:10.1007/s11069-011-9734-7, 2011.
- Johanson, I. A. and R. Bürgmann, Coseismic and postseismic slip from the 2003 San Simeon earthquake and their effects on backthrust slip and the 2004 Parkfield earthquake, *J. Geophys. Res.*, *115*, B07411, doi:10.1029/2009JB006599, 2010.
- Kelson, K., D. Simpson, A. Lutz, B. Kozlowicz, C. Brossy, O. Kozaci, C. Amos, J. Baldwin, R. Turner Jr., A. Streig, J. Sowers, P. Maat, D. Rood, J. Unruh, and D. Serafini, Segmentation and Seismic Source Characterization of the Kern Canyon Fault for Isabella Dam, Sierra Nevada, California, *Earthquake Spectra*, in revision.
- Lekic, V. and B. Romanowicz, Global tomography using the Spectral Element Method: a clustering analysis of upper mantle structure, *Earth Planet. Sci. Lett.*, *308*, 151-160, 2010.
- Lekic, V. and B. Romanowicz, Inferring mantle structure by full waveform tomography using the Spectral Element Method, *Geophys. J. Int.*, *185*, 799-831, doi: 10.1111/j.1365-246X.2011.04969.x, 2011.
- Lin, K.-C., J.-C. Hu, K.-E. Ching, J. Angelier, R.-J. Rau, S.-B. Yu, C.-H. Hsai, T.-C. Shin, and M.-H. Huang, GPS crustal deformation, strain rate, and seismic activity after the 1999 Chi-Chi earthquake in Taiwan, *J. Geophys. Res.*, *115*, B07404, doi:10.1029/2009JB006417, 2010.
- Liu Y., Chong J.J., Ni S., Near surface wave velocity structure in Chinese Capital region based on borehole seismic records, *Acta Seismologica Sinica*, *33*, 342-350, 2011, (in Chinese).
- Milluzzo, V., A. Cannata, S. Alparone, S. Gambino, M. Hellweg, P. Montalto, L. Cammarata, I.S. Diliberto, S. Gresta, M. Liotta, A. Paonita, Tornillos at Vulcano: Clues to the dynamics of the hydrothermal system, *J. Volcanol. Geotherm. Res.*, *198*, 377-393, 2010.
- Obrebski, M., R.M. Allen, F. Pollitz, S.-H. Hung, Lithosphere-asthenosphere interaction beneath the western United States from the joint inversion of body-wave traveltimes and surface-wave phase velocities, *Geophys. J. Int.*, *185*, 1003-1021, doi:10.1111/j.1365-246X.2011.04990.x, 2011.

- Obrebski, M., R.M. Allen, M. Xue, S.-H. Hung, Slab-plume interaction beneath the Pacific Northwest, *Geophys. Res. Lett.*, *37*, L14305, doi:10.1029/2010GL043489, 2010.
- Panning, M., V. Lekic and B. Romanowicz, The importance of crustal corrections in the development of a new global model of radial anisotropy, *J. Geophys. Res.* doi:10.1029/2010JB007520, 2010.
- Peacock, S. M., N. I. Christensen, M. G. Bostock, and P. Audet, High pore pressures and porosity at 35 km depth in the Cascadia subduction zone, *Geology*, *39*, 471-474, doi:10.1130/G31649.1, 2011.
- Pollitz, F. F., Brooks, B., Tong, X., Bevis, M. G., Foster, J. H., Bürgmann, R., Smalley, R., Vigny, C., Socquet, A., Ruegg, J.-C., Campos, J., Barrientos, S., and Parra, H., Coseismic slip distribution of the February 27, 2010 Mw 8.8 Maule, Chile earthquake, *Geophys. Res. Lett.*, *38*, L09309, doi:10.1029/2011GL047065, 2011.
- Porritt, R.W. Allen, R. M., Boyarko D.C., Brudzinski, M.R., Investigation of Cascadia segmentation with ambient noise tomography, *Earth and Planetary Science Letters*, *309(1-2)*, 67-76, ISSN 0012-821X, DOI: 10.1016/j.epsl.2011.06.026, 2011.
- Quigley, K. C., R. Bürgmann, C. Giannico, and F. Novali, Seasonal Acceleration and Structure of Slow Moving Landslides in the Berkeley Hills, California Geological Survey Special Report 219, Proceedings of the Third Conference on Earthquake Hazards in the Eastern San Francisco Bay Area, Keith Knudsen (ed.), 169-178, 2010.
- Scognamiglio, L., E. Tinti, A. Michelini, D. Dreger, A. Cirella, M. Cocco, S. Mazza, and A. Piatanesi, Fast Determination of Moment Tensors and Rupture History: What has been learned from the April 6, 2009, L'Aquila Earthquake, *Seism. Res. Lett.*, *81*, 892, 2010.
- Serpelloni, E., Bürgmann, R., Anzidei, M., Baldi, P., Mastrolembo, B., and Boschi, E., Strain accumulation across the Messina Straits and kinematics of Sicily and Calabria from GPS data and dislocation modeling, *Earth Planet. Sci. Lett.*, *298*, doi:10.1016/j.epsl.2010.1008.1005, 2010.
- Stehly, L., P. Cupillard and B. Romanowicz, Towards improving ambient noise tomography using simultaneously curvelet denoising filters and SEM simulations of seismic ambient noise, *C.R. Geoscience*, doi:10.1016/j.crte.2011.03.005, 2011.
- Sun, J., Johnson, K. M., Cao, Z., Shen, Z. K., Bürgmann, R., and Xu, X., Mechanical constraints on inversion of co-seismic geodetic data for fault slip and geometry: example from InSAR observation of the 6 October 2008 Mw 6.3 Dangxiong-Yangyi (Tibet) earthquake, *J. Geophys. Res.*, *116*, B01406, doi:10.1029/2010JB007849, 2010.
- Titus, S. J., Dyson, M., DeMets, C., Tikoff, B., Rolandone, F., and Bürgmann, R., Geologic versus geodetic deformation adjacent to the San Andreas fault, central California, *Geol. Soc. Amer. Bull.*, doi:10.1130/B30150.1, 2011.
- Uhrhammer, R.A., M. Hellweg, K. Hutton, P. Lombard, A.W. Walters, E. Hauksson and D. Oppenheimer, California Integrated Seismic Network (CISN) Local Magnitude Determination in California and Vicinity, *Bull. Seismol. Soc. Am.*, *101*, in press.
- Wang, Z.J., J.J. Chong, S.D. Ni, and B. Romanowicz, Determination of focal depth by two waveform-based methods: A case study for the 2008 Panzhihua earthquake, *Earthq. Sci.*, in press.
- Wenk, H.-R., Cottaar, S., Tome, C.N., Allen McNamara, A., Romanowicz, B., Deformation in the lowermost mantle: From polycrystal plasticity to seismic anisotropy, *Earth and Planetary Science Letters*, *306(1-2)*, 33-45, DOI: 10.1016/j.epsl.2011.03.021, 2011.
- Wiseman, K., P. Banerjee, K. Sieh, R. Bürgmann, and D. H. Natawidjaja, Another potential source of destructive earthquakes and tsunami offshore of Sumatra, *Geophys. Res. Lett.*, *38*, doi:10.1029/2011GL047226, 2011.
- Wiseman, K. and R. Bürgmann, Stress and seismicity changes on the Sunda megathrust preceding the 2007 Mw 8.4 Earthquake, *Bull. Seis. Soc. Am.*, *101*, doi:10.1785/0120100063, 2011.
- Yoo, S.-H., J. Rhie, H. Choi, and K. Mayeda, Evidence for non-self-similarity and transitional increment of scaled energy in the 2005 west off Fukuoka seismic sequence, *J. Geophys. Res.*, *115*, B08308, 2010.

- Yoo, S.-H., J. Rhie, H. Choi, and K. Mayeda, Coda-Derived Source Parameters of Earthquakes and Their Scaling Relationships in the Korean Peninsula, *Bull. Seismol. Soc. Am.*, in press, doi:10.1785/0120100318, 2011.
- Yuan, H., and B. Romanowicz, Depth dependent azimuthal anisotropy in the western US upper mantle, *Earth Planet. Sci. Lett.*, 300(3-4), 385-394, 2010.
- Yuan, H., B. Romanowicz, K. Fischer and D. Abt, 3-D shear wave radially and azimuthally anisotropic velocity model of the north American upper mantle, *Geophys. J. Int.*, 184, 1237-1260, doi:10.1111/j.1365-246X.2010.04901.x, 2011.
- Zhang, H., R. M. Nadeau, and M. N. Toksoz, Locating nonvolcanic tremors beneath the San Andreas Fault using a station-pair double-difference location method, *Geophys. Res. Lett.*, 37, L13304, doi:10.1029/2010GL043577, 2010.

Presentations

12th Symposium of SEDI, Santa Barbara, CA, July 18-23, 2010

- Cottaar, S., McNamara, A.K., Romanowicz, B.A., Wenk, H.-R., Forward modeling the origin of seismic anisotropy at the base of the mantle.
- Dou, S., Barbara, R., Towards a three-dimensional attenuation model of the lower mantle from the normal modes of the Earth's free oscillations.
- French, S. W., V. Lekic, and B. A. Romanowicz, Towards global waveform tomography of the lower mantle using SEM: preliminary investigations.
- Zheng, Z. and B. Romanowicz, Efficient Computation of NACT Seismograms.

2010 IEEE International Geoscience and Remote Sensing Symposium, Honolulu, HI, July 25-30, 2010

- Lei, L., Bürgmann, R., Monitoring Slow Moving Landslides in the Berkeley Hills with TerraSAR-X Data.

Geological Society of America Penrose Conference: Origin and Uplift of the Sierra Nevada, California, Bridgeport, CA, August 16-20, 2010

- Amos, C.B., K. Kelson, D. Simpson, D. Rood, A. Lutz, O. Kozaci, B. Kozlowicz, A. Streig, R. Turner Jr., J. Sowers, M. Ticci, R. Rose, Late-Quaternary slip-rate on the northern Kern Canyon fault from lidar topography and cosmogenic radionuclide dating.

ESC 2010 European Seismological Commission 32nd General Assembly, Montpellier, France, September 6-10, 2010

- Zechar, J.D. and R.M. Nadeau, Predictability experiments with repeating microearthquakes near Parkfield, California.

The International Geological Correlation Programme (IGCP) 565 Workshop 3, Reno, NV, October 11-13, 2010

- Johanson, I., R. Bürgmann, Combining InSAR and GPS data to distinguish coseismic and postseismic slip in the 2003 San Simeon and 2004 Parkfield earthquakes, invited.

The First EarthScope Institute on the Spectrum of Fault Slip Behaviors, Portland, OR, October 11-14, 2010

- Johanson, I., R. Bürgmann, Correspondence between coseismic stress change and backthrust slip in the 2003 San Simeon earthquake.
- Nadeau R.M., Seismic Indicators of Aseismic Slip and Stress Transients in Central California: Repeating Earthquakes and Non-volcanic Tremor.
- Thomas, A.M., Bürgmann R., and Shelly D., Tidal triggering of LFEs near Parkfield, CA.

8th Joint Meeting of the UJNR Panel on Earthquake Research, Nagaoka, Japan, October 20-22, 2010.

Thomas, A.M., Bürgmann R., and Shelly D., Tidal triggering of LFEs near Parkfield, CA.

Geological Society of America Annual Meeting, Denver, CO, October 31 - November 3, 2010

Amos, C.B., G.B. Fisher III, D.H. Rood, A.S. Jayko, and R. Bürgmann, New terrestrial lidar and cosmogenic radionuclide constraints on the Little Lake fault, eastern California shear zone, *Geological Society of America Annual Meeting, Abstracts with Programs*, 42(5), 134.

4th Joint PI Symposium of ALOS Data Nodes for ALOS Science Program 2010, Tokyo, Japan, November 15-17, 2010

Huang, M.-H., I. Ryder, E. Fielding, and R. Bürgmann, Investigation of Earthquake-Cycle Deformation in Tibet from ALOS PALSAR Data.

Johanson I., I. Ryder, M.-H. Huang, L. Lei, E. Fielding, and R. Bürgmann, ALOS PALSAR Measurements of Deformation in the San Francisco Bay Area, California.

American Geophysical Union Fall Meeting, San Francisco, CA, December 13-17, 2010

Amos, C.B., R. Bürgmann, A.S. Jayko, G.B. Fisher III, and D.H. Rood, Temporal patterns of slip rate on the Little Lake fault, eastern California shear zone, from terrestrial lidar, cosmogenic radionuclides, and InSAR analysis, Abstract T44A-03 (invited).

Audet, P., Spherical wavelet analysis of gravity and topography of the terrestrial planets, Abstract P21A-1595, 2010.

Böse, M., K. Solanki, R. M. Allen, H. Brown, G. B. Cua, D. Given, E. Hauksson, T. H. Heaton, CISN ShakeAlert: Development of a Prototype User Display for Providing Earthquake Alerts to End Users, Abstract NH33A-1369.

Brossy, C.C., J.N. Baldwin, K.I. Kelson, D.H. Rood, B. Kozlowicz, D. Simpson, M. Ticci, C.B. Amos, O. Kozaci, and A. Lutz, Late Pleistocene displacement and slip rate for the Breckenridge fault, Walker Basin, southern Sierra Nevada, California, Abstract EP53B-0612.

Brown, H., I. Lim, R. M. Allen, M. Böse, G. B. Cua, T. H. Heaton, CISN Earthquake Early Warning: ShakeAlert Hybrid Branch, Abstract NH33A-1372.

Brown, H., Lim, I., Allen, R.M., Neuhauser, D., Khainovski, O., and Hellweg, M., CISN Earthquake Early Warning: ElarmS, Abstract NH33A-1372.

Chong, J.J., Sidao Ni. sPL, an effective seismic phase for determining focal depth at near distances, Abstract S21C-2049.

Cottaar, S., Buffett, B. A., Convection in the inner core, Abstract DI21C-05.

Cottaar, S., McNamara, A.K., Romanowicz, B. A., Wenk, H.-R., On the origin of seismic anisotropy at the base of the mantle, Abstract DI33C-08 (invited).

Cupillard, P., H. Yuan, B.A. Romanowicz, Y. Capdeville, J. Montagner, G. Festa, RegSEM, a flexible regional Spectral Element code: application to continental scale problems, Abstract S31A-2003.

Dou, S., Romanowicz, B., Constraining Three-dimensional Anelastic Structure of the Lower Mantle from Earth's Free Oscillation, Abstract DI33A-1960.

Dreger, D. S. and S. R. Ford, Joint inversion of InSAR and seismic waveform data for the finite-fault solution of the Wells, Nevada earthquake, Abstract S41D-07.

Durand, S., S.R. Ford, J. Matas, V. Lekic, B.A. Romanowicz, Heterogeneous lower mantle shear attenuation from ScS-S differential t^* measurements via instantaneous frequency, Abstract DI21A-1940.

Dziewonski, A.M., V. Lekic, C. Houser, J. Matas and B. Romanowicz, Developing three dimensional reference earth models for Mineral Physics Interpretations, Abstract DI52A-07.

- Fischer, K.M., H A Ford, D Abt, H Yuan, B Romanowicz, The lithosphere-asthenosphere boundary and cratonic lithospheric layering beneath stable North America, Abstract T31F-02 (invited).
- French, S.W., V. Lekic, and B.A. Romanowicz, Toward global waveform tomography of the whole mantle using SEM: Efficient simulation of the global wavefield using an homogenized crust, Abstract S31A-2002.
- Guilhem, A., and Dreger, D. S., Development and implementation of continuous moment tensor scanning for offshore seismicity and tsunami early warning, Abstract S34B-03.
- Hellweg, M., R.M. Allen, H. Brown, D. S. Neuhauser, O. Khainovsky, CISN ShakeAlert: Progress Toward Using Early Warnings for Earthquakes in California, Abstract NH33A-1368.
- Huang, M.-H., D. S. Dreger, R. Bürgmann, J. Suppe, and M. Hashimoto, Joint Inversion of Seismic and Geodetic Data for the Source of the 4th March 2010 Mw 6.3 Jia-Shian, SW Taiwan, Earthquake, Abstract T11B-2079.
- Johanson, I., Rapid estimates of postseismic slip from GPS data in Northern California, Abstract G13A-0648.
- Kelson, K.I., C.B. Amos, D.T. Simpson, J.N. Baldwin, R. Rose, M. Ticci, J. Kelson, E. Salesky, and J.W. Chipman, Structural and Geomorphic Control on Landscape Evolution by the Kern Canyon Fault, Southern Sierra Nevada, California, Abstract EP53B-0611.
- Lei, L., Bürgmann, R., Application of PSI to Investigate the Berkeley Hills Landslides, Abstract G13A-0666.
- Lim, I., R. M. Allen, H. Brown, M. Hellweg, D. S. Neuhauser, O. Khainovsky, Earthquake Early Warning: Tools for System Assessment, Abstract NH33A-1373.
- Liu, K., Zhai, Y., Levander, A., Porritt, R., Allen, R., Schmandt, B., Humphreys, E., O'Driscoll, L., Lithosphere/Asthenosphere Structure beneath the Mendocino Triple Junction from the Analysis of Surface Wave, Ambient Noise, and Receiver Functions, Abstract DI11A-1832.
- Lutz, A., O. Kozaci, K.I. Kelson, D. Simpson, J.N. Baldwin, C.B. Amos, R. Turner, and R. Rose, A Record of Late Pleistocene and Holocene Surface-rupturing Earthquakes Along the Lake Isabella Section of the Kern Canyon Fault, California, Abstract EP53B-0613.
- Maceira, M., C. A. Rowe, R. M. Allen, M. J. Obrebski, Validating 3D Seismic Velocity Models Using the Spectral Element Method, Abstract S43B-2079.
- McDonough, W.F., Buffett, B.A., Cormier, V.F., Cottaar S., Day, E., Dou, S., French S., Irving, J., Kavner A., Panning, M., Parai, R., Rose, I., A stratified layer of light elements at the top of the outer core, Abstract DI41A-1935.
- Meltzner, A. J., K. Wiseman, A. Sladen, K. E. Sieh, R. Bürgmann, P. Banerjee, J. F. Genrich, D. H. Natawidjaja, B. W. Suwargadi, J. E. Galetzka, Moderate ruptures at a megathrust segment boundary: the Mw 7.2-7.3 Simeulue earthquakes of 2002, 2008, and 2010, Abstract T11D-2124.
- Neuhauser, D.S., O. Khainovsky, M. Böse, K. Solanki, G. B. Cua, T. H. Heaton, R. M. Allen, CISN ShakeAlert: The Decision Module for Earthquake Alerts, Abstract NH33A-1370.
- Obrebski, M., Allen, R., Pollitz, F., Porritt, R., Hung, S., New Tomographic Images of the Yellowstone Plume and its Interaction with the Farallon Plate From the Integrated Analysis of Body and Surface Waves., Abstract U44A-05.
- Pan, J., M. J. Obrebski, Q. Wu, Y. Li, R.M. Allen, The ambient noise and earthquake surface wave tomography of the North China Craton, Abstract S33A-2059
- Porritt, R., Allen, R., Brudzinski, M., Boyarko, D., O'Driscoll, L., Zhai, Y., Levander, A., Humphreys, E., Pollitz, F., Imaging Lithospheric Cascadia Structure with Ambient Noise Tomography, Abstract T41E-05.
- Romanowicz, B.A., Cooperative Institute for Dynamic Earth Research (CIDER): Contributions to Education, Abstract ED44A-08 (invited).

- Romanowicz, B. J. Rhie and D. Dolenc, On the generation of the Earth's low frequency "Hum" through non-linear interactions between Atmosphere, Ocean and Solid Earth, Abstract NG44A-01 (invited).
- Romanowicz, B.A., H. Yuan, H.A. Ford, K.M. Fischer, D. Abt, Stratification of Azimuthal Anisotropy in the North American Craton, Abstract T31F-03 (invited).
- Stehly, L., P Cupillard, B Romanowicz, Using simultaneously curvelet filters and SEM simulation of seismic ambient noise: a possible way to improve ambient noise tomography, Abstract S33A-2067.
- Taira, T., R.M. Nadeau, and D.S. Dreger, Seismic Constraints on Fault-Zone Rheology from Repeating Earthquakes at Parkfield, California, Abstract T33B-2252.
- Thomas, A.M., Bürgmann R., Shelly D., and Beeler N., The Frequency Dependence of Friction and Tidal triggering of LFEs near Parkfield, CA, Abstract S12A-04.
- Tu, F., Y. Gung, S.-H. Yoo, and J. Rhie, Earthquake magnitudes based on Coda-Derived Moment-Rate Spectra in Taiwan, Abstract S53A-1957.
- Wiseman, K., P. Banerjee, K. E. Sieh, R. Bürgmann, and D. H. Natawidjaja, Backthrust earthquake clusters over intermittently coupled portion of the Sunda megathrust, Abstract T44B-06.
- Yoo., S.-H., J. Rhie, and W.-Y. Kim, 3-D Waveform Modeling of the 11 September 2001 World Trade Center Collapse Events in New York City, Abstract S43B-2083.
- Yuan, H., P. Cupillard, S.W. French, and Barbara Romanowicz, Refining the cratonic upper mantle: modeling North American upper mantle and crustal structure using the Spectral Element method, Abstract T51C-2060.
- Zhai, Y., Mackenzie, J., Levander, A., Cao, A., Porritt, R., Allen, M., Crust and Upper mantle heterogeneity in the Mendocino Triple Junction from teleseismic P-to-S scattered waves, Abstract T51C-2058.
- Zhang, F., M. J. Obrebski, J. Pan, Q. Wu, R. M. Allen, New Insights Into Decratonization Beneath Northeastern China From the Joint Inversion of Body and Surface Waves, Abstract S32C-02.
- Zheng, Z. and B. Romanowicz, Toward a Joint Inversion for Global Mantle Shear Velocity and Discontinuity Topography by Incorporating SS Precursor Waveforms into NACT, Abstract S31A-2001.

8th Annual Northern California Earthquake Hazards Workshop, USGS Menlo Park, CA, January 2011

- Guilhem, A., and D.S. Dreger, Development and implementation of continuous moment tensor scanning for offshore seismicity and tsunami early warning.

42nd Lunar and Planetary Science Conference, The Woodlands, TX, March 7-11, 2011

- Audet, P., and C. L. Johnson, Lithospheric structure of the Moon and correlation with deep moonquake source regions, Abstract 1742.

European Geosciences Union, 2011 Annual Meeting, Vienna, Austria, April 3-8, 2011

- Guilhem, A., and D.S. Dreger, Rapid detection of large subduction zone earthquakes using quasi-finite-source Green's functions in moment tensor inversion, vol. 13, Abstract EGU2011-4688.
- Levander, A., Y. Zhai, K. Liu, J. Mackenzie, R. Poritt, R.M. Allen, The lithosphere and the asthenosphere in the Mendocino Triple Junction Region.

105th Seismological Society of America, Annual Meeting, Memphis, TN, April 13-15, 2011

- Boyd, O.S., D.S. Dreger, M. Hellweg, J. Taggart, P. Lombard, S.R. Ford, and A. Nayak, Deviatoric Moment Tensor Analysis at The Geysers Geothermal Field, *Seism. Res. Lett.*, 82(2), 290, 2011.
- Dreger, D. S., S. Larsen, S.-H. Yoo, and A. Chopra, Very Near-Fault Ground Motion Simulation, *Seism. Res. Lett.*, 82(2), 296, 2011.

- Dreger, D.S., R.M. Nadeau, T. Taira, A. Kim, Finite-Source Parameters and Scaling of Repeating and Non-Repeating Earthquakes at Parkfield, *Seism. Res. Lett.*, 82(2), 323, 2011.
- Hellweg, M., H. Rademacher and D. SEIDL, The Multiparameter Station at Galeras Volcano (Colombia): an International Collaboration, *Seismol. Res. Lett.*, 81, 356, 2011.
- Hellweg, M., and D. Oppenheimer, Earthquake Magnitudes in Northern California, *Seismol. Res. Lett.*, 81, 277, 2011.
- Malagnini, L., S. Nielsen, K. Mayeda, I. Munafo, S.-H. Yoo, and E. Boschi, Breakdown of Earthquake Self-Similarity Observed Globally at Mw 5.5, *Seism. Res. Lett.*, 82(2), 317, 2011.
- Mayeda, K., C. Rawles, L. Malagnini, and S.-H. Yoo, Variable Apparent Stress Scaling from Coda Envelopes for Southern California Sequences, *Seism. Res. Lett.*, 82(2), 323, 2011.
- Melgar, D., Y. Bock, B. Crowell, M. Jackson, R.M. Allen, Strong Motion Displacement and Velocity Seismograms.
- Porritt, R., Allen, R., Boyarko, D., Brudzinski, M., O'Driscoll, L., Zhai, Y., Levander, R., and Pollitz, F., Segmentation of lithospheric structure in the Cascadia Subduction Zone.
- Walter, W. R., R. Gok, K. Mayeda, and L. Malagnini, Investigating Earthquake Scaling Using Spectral Ratios and Simple Earthquake Models, *Seism. Res. Lett.*, 82(2), 316, 2011.
- Whidden, K. M., K. L. Pankow, and T. Taira, A Catalog of Regional Moment Tensors in Utah, 2010.
- Zhang, H., R.M. Nadeau, M.N. Toksoz, C.H. Thurber, and M. Fehler, Nonvolcanic Tremors in Localized Low Shear Wave Velocity Zones Beneath the San Andreas Fault, *Seism. Res. Lett.*, 82(2), 307, 2011.

2011 Earthscope National Meeting, Austin, TX, May 17-20, 2011

- Porritt, R., Allen, R., Boyarko, D., and Brudzinski, M., Investigation of Cascadia segmentation with ambient noise tomography.
- Neuhauser, D., Aranha, M., Zuzlewski, S., and Romanowicz, B., Accessing EarthScope and Complementary Data Sets at the Northern California Earthquake Data Center.
- Taira, T., R. Bürgmann, and R.M. Nadeau, Identifying undetected early aftershocks and non-volcanic tremors associated with the 12 August 1998 Mw 5.1 San Juan Bautista earthquake and slow slip event.
- Yuan, H., and B. Romanowicz, Depth Dependent Azimuthal Anisotropy in the Western US Upper Mantle.

Advances in Seismology and Implications for Interdisciplinary Research, Adam M. Dziewonski Symposium - Harvard University, Cambridge, MA, June 4-5, 2011

- French, S.W., V. Lekic, and B.A. Romanowicz, Toward Full-Waveform Global Tomography with the SEM: Constraining Observations at Upper Mantle Depths.

2011 Gordon Research Conference, Mount Holyoke, Massachusetts, June 5-10, 2011

- French, S.W., V. Lekic, and B.A. Romanowicz, Toward Full-Waveform Global Tomography with the SEM: Constraining Observations at Upper Mantle Depths.
- Porritt, R., Allen, R., Boyarko, D., Brudzinski, M., Obrebski, M., Pollitz, F., and Hung, S., Investigation of Cascadia Segmentation with Ambient Noise Tomography and DNA11-S: Multi-phase finite frequency velocity model of the western US.
- Yuan, H., B. Romanowicz, D. Abt, K. Fischer, Anisotropic stratification in the continental upper mantle.

Speaking Engagements

- Allen, R.M., M.J. Obrebski, M. Xue, F. Pollitz, S. Hung, The destruction of North America by dueling tectonic processes, Global Seismology and Geophysics, Tongji University, Shanghai, China, July 2010.
- Allen, R.M., First Jolt: ShakeAlert for the next big earthquake in California, Global Seismology and Geophysics, Tongji University, Shanghai, China, July 2010.

- Allen, R.M., First Jolt: ShakeAlert for the next big earthquake in California, National Data Center, China Earthquake Administration, Beijing, China, July 2010.
- Allen, R.M., M.J. Obrebski, M. Xue, F. Pollitz, S. Hung, The destruction of North America by dueling tectonic processes, Institute of Geology and Geophysics, Chinese Academy of Sciences, Beijing, China, July 2010.
- Allen, R.M., First Jolt: ShakeAlert for the next big earthquake in California, Institute of Geology and Geophysics, Chinese Academy of Sciences, Beijing, China, July 2010.
- Allen, R.M., First Jolt: ShakeAlert for the next big earthquake in California, Institute of Geophysics, China Earthquake Administration, Beijing, China, July 2010.
- Allen, R.M., M.J. Obrebski, M. Xue, F. Pollitz, S. Hung, The destruction of North America by dueling tectonic processes, Institute of Geophysics, China Earthquake Administration, Beijing, China, July 2010.
- Allen, R., Scientific Briefing for Bay Area Rapid Transit (BART), July 2010.
- Allen, R.M., M.J. Obrebski, R. Porritt, F. Pollitz, S. Hung, Segmentation along Cascadia: Integrated study of multi-scale processes, Cascadia Initiative Science Planning Workshop, Portland, Oregon, October 2010.
- Allen, R.M., M.J. Obrebski, F. Pollitz, S. Hung, Creation, destruction and modification of the western United States, École Normale Supérieure, Paris, France, November 2010.
- Allen, R.M., M.J. Obrebski, F. Pollitz, S. Hung, Creation, destruction and modification of the western United States, Institut de Physique du Globe de Paris, France, November 2010.
- Allen, R.M., M.J. Obrebski, F. Pollitz, S. Hung, Mantle upwelling and lithospheric destruction beneath western North America, The Bullard Laboratories, University of Cambridge, UK, February 2011.
- Allen, R.M., Warning California: ShakeAlert for the next big earthquake, Earth and Environmental Science, Leeds University, UK, February 2011.
- Allen, R.M., M.J. Obrebski, C. Eakin, R. Porritt, F. Pollitz, S. Hung, Mantle upwelling and lithospheric destruction beneath western North America, Geophysics Institute, ETH Zurich, Switzerland, March 2011.
- Allen, R.M., Delivering earthquake early warning to California, Department of Earth Sciences, ETH Zurich, Switzerland, March 2011.
- Allen, R.M., M.J. Obrebski, C. Eakin, R. Porritt, F. Pollitz, S. Hung, Mantle upwelling and lithospheric destruction beneath western North America, Geosciences Azur, Nice, France, April 2011.
- Allen, R., Scientific Briefing for BART, CalEMA, CalTrans, California Seismic Safety Commission, City of San Francisco, April 2011.
- Allen, R., Scientific Briefing for Boeing, Google, Hewlett Packard, Lam Research, Life Technologies, Intel, Microsoft, PG&E, Red Cross, So. Cal Edison, April 2011.
- Allen, R.M., M.J. Obrebski, R. Porritt, F. Pollitz, S. Hung, Mantle upwelling and lithospheric destruction beneath North America, Gordon Research Conference, Mt. Holyoke, Massachusetts, USA, June 2011.
- Amos, C.B., Geomorphic constraints on active thrust fault, Southern New Zealand, University of California, Davis, departmental seminar, December 8, 2010.
- Amos, C.B. Active faulting and deformation of the Southeastern Sierra Nevada, California, University of California White Mountain Research Station, Bishop, CA, Public lecture series, April 21, 2011.
- Amos, C.B., Active Deformation of the Southeastern Sierra Nevada, California, U.S. Geological Survey, Alaska Science Center, Anchorage, AK, May 3, 2011.
- Audet P., Slab morphology and tremor along Cascadia, Cascadia Initiative workshop, Portland, October 15, 2010.
- Audet P., Fluids in the fore arc of Cascadia: Evidence from seismic imaging, University of Texas Institute of Geophysics, Austin, October 22, 2010.

- Audet P., New views of subduction zone structure and fault mechanics, University of Ottawa, November 3, 2010.
- Audet P., The seismic signature of water in the fore arc of Cascadia, University of Oregon, Eugene, November 17, 2010
- Audet P., Seismic imaging of plate boundary fault zones: Cascadia and San Andreas, University of California, Davis, February 23, 2011.
- Audet P., Lithospheric and thermal structure of the Moon from gravity and topography, University of California, Santa Cruz, April 15, 2011.
- Audet P., Seismic imaging of plate boundary fault zones: Cascadia and San Andreas, Swiss Federal Institute of Technology, Zurich, June 24, 2011.
- Audet P., Seismic imaging of the subducting oceanic crust in Cascadia, ILP workshop on nature of the plate interface, Italy, July 4, 2011.
- Bürgmann, R., Triggering and Modulation of Slow Slip: Implications for Mechanics and Hazard?, Institute on the Spectrum of Fault Slip Behavior, Portland, October, 14, 2010.
- Bürgmann, R., What does the future hold for earthquakes in CA?, UC Berkeley Panel Discussion on “Earthquakes, tsunamis and nuclear fallout: Is California at risk like Japan?”, March 29, 2011.
- Dreger, D. S., Realtime earthquake reporting, Invited lecture at Nuclear Regulatory Commission public symposium for Diablo Canyon science, San Luis Obispo, CA, September 8, 2010.
- Dreger, D. S., What advance warning can we receive?, Invited talk at UC Berkeley’s “Earthquakes, Tsunamis, and Nuclear Fallout: Is California at risk like Japan?” Panel Discussion, Berkeley, CA, March 29, 2011.
- Dreger, D. S., Earthquake scaling at parkfield, Invited lecture UC Santa Barbara, Santa Barbara, CA, April 21, 2011.
- Guilhem, A., Detecting and characterizing large earthquakes: realtime moment tensor inversions, ETH, Zurich, April 14, 2011.
- Guilhem, A., Nonvolcanic tremors: what they tell us about the San Andreas Fault, Caltech Dix Seismological Laboratory Seminar, May 20, 2011.
- Guilhem, A., Rapid detection of large subduction zone earthquakes using quasi-finite-source Green’s functions in moment tensor inversion, Geophysics seminar, Lawrence Berkeley National Laboratory, June 3, 2011.
- Hellweg, M., A tectonic timebomb: The Hayward Fault, Oakland Museum, Oakland, California, October 4, 2010.
- Hellweg, M., Bubble, Bubble: An Overview of Volcanic Tremor, Department of Geophysics, Humboldt State University, October 25, 2010.
- Hellweg, M., Moment Tensors in California (and Why They Matter), Department of Geophysics, Humboldt State University, October 25, 2010.
- Hellweg, M., Earthquakes in our Backyard, UC Berkeley Building Coordinators and Emergency Management Coordinators Annual Meeting, UC Berkeley, February 10, 2011.
- Taira, T., Seismic Constraints on Fault-Zone Strength and Rheology at Seismogenic Depth on the San Andreas Fault, Parkfield, Berkeley Seismological Laboratory Seminar, UC Berkeley, Berkeley, CA, September 14, 2010.
- Romanowicz, B., Continental lithosphere structure and formation: New insights from seismic anisotropic waveform tomography, University of Washington, Seattle, October 27, 2010.
- Romanowicz, B., Recent advances in full waveform global seismic tomography of the Earth’s mantle, Mathematical Sciences Research Institute, Berkeley, CA, November 12, 2010.
- Romanowicz, B., Modélisation de la structure profonde de la Terre à l’échelle globale et continentale par inversion de forme d’onde complete, IPG, Paris, January 2011.

Romanowicz, B., Recent advances in full waveform global seismic tomography of the Earth's mantle, SIAM keynote speaker, Los Angeles, CA, March 23, 2011.

Romanowicz, B., Stratification of the lithosphere in archaic cratons: inferences from seismic waveform tomography, Zatman Lecture, St. Louis, MO, March 31, 2011.

Romanowicz, B., Thirty years of mantle tomography: old challenges and new opportunities, Adam Dziewonski Symposium, Harvard, Cambridge MA, June 4-5, 2011.

Romanowicz, B., Global and continental scale waveform tomography: elastic and anisotropic, Imaging Workshop, UC Berkeley, Berkeley, CA, June 21, 2011.

Yuan, H., B. Romanowicz, Lithospheric layering of the North American Craton, Gordon-Kenan Research Seminar, 2011 Gordon Research conferences (Interior of the Earth), Mount Holyoke College, South Hadley, MA (invited), June 4, 2011.

Yuan, H., B. Romanowicz, Seismic anisotropy in the North American upper mantle and its tectonic implications, Berkeley Seismological Lab Spring 2011 Seminar series, Berkeley, CA, February 22, 2011.

Yuan, H., B. Romanowicz, Depth Dependent Azimuthal anisotropy in the western US upper mantle, USGS Earthquake Science Seminar in Menlo Park, CA (invited), January 26, 2011.

Awards

Barbara Romanowicz

Selected to receive the Seismological Society of America's Harry F. Reid Medal in 2012

Taka'aki Taira

2011 Research Award for Young Scientist, The Seismological Society of Japan

Panels and Professional Service

Richard M. Allen

Principal Organizer, Earthquake Early Warning Summit, April 2011.

Member, Cascadia Initiative Expedition Team

Chair, Amphibious Array Steering Committee (for the NSF Cascadia Initiative)

Chair, IRIS PASSCAL Standing Committee

Member, Scientific Advisory Board, European Union Framework 6 Project: Strategies and tools for Real Time Earthquake Risk Reduction (REAKT)

Roland Bürgmann

Associate Editor, Bulletin of the Seismological Society of America

Editorial Advisory Board, Eos

Editorial Board, Earth and Planetary Science Letters

Member, EarthScope PBO Advisory Committee

Vice-chair, WInSAR Standing Committee

Co-chair, EarthScope Thematic Working Group on Crustal Strain and Deformation

Member, USGS-NEHRP proposal review panel, Earthquake Physics

Douglas S. Dreger

Reviewer for Journal of Geophysical Research

Reviewer for Bulletin of the Seismological Society of America

Reviewer for Physical Review Letters

Cosmos Board of Directors

Margaret Hellweg

Member, CISN Program Management Committee
Member, CISN Standards Committee
Member, CISN Steering Committee
Member, CISN Outreach Committee
Member, ANSS Performance Standards Committee
Member, ANSS Comprehensive Catalog Advisory Committee
Chair, ANSS Class C Instrumentation Evaluation Committee
Member, Bay Area Earthquake Alliance Committee
Member, Bay Area Earthquake Alliance Executive Committee
Member, Editorial Board of Journal of Volcanology and Geothermal Research

Douglas S. Neuhauser

Chair, Standards Group, California Integrated Seismic Network (CISN)
Acting Member, CISN Program Management Committee

Barbara Romanowicz

Chair CISN Steering Committee
Member, National Earthquake Prediction Evaluation Council
Member, Planning Committee, IRIS
Member, Inge Lehmann Medal Committee, AGU
Member, Geophysics Panel, NSF
Review Committee, Centers of Excellence in Science, Oslo Norway -March 2011
Scientific Advisory Committee, Geoscope Program (France)
Member, Holmes Medal Committee, EGU
Vice Chair, Gordon Conference on the Interior of The Earth, Mount Holyoke College, Mass, June 5-10, 2011

Taka'aki Taira

Member, California Integrated Seismic Network, Standards Committee
Member, California Integrated Seismic Network, ShakeMap Working Group
Member, Plate Boundary Observatory, Data Working Group

Appendix II
Seminar Speakers 2010-2011

SEOK GOO SONG
URS Corporation, Pasadena
"Earthquake source statistics inferred from modeling and data -- A noble framework for finite-fault source modeling for strong motion simulation."
Tuesday, August 24, 2010

No seminar
Tuesday, August 31, 2010

MIKE OSKIN
UC Davis
"Fault system behavior of the eastern California shear zone: Unsteady loading rates and clustered earthquake activity"
Tuesday, September 7, 2010

TAKA'AKI TAIRA
Berkeley Seismological Laboratory
"Seismic constraints on fault-zone strength and rheology at seismogenic depth on the San Andreas fault, Parkfield"
Tuesday, September 14, 2010

THORNE LAY
UC Santa Cruz
"The 2009 Samoa-Tonga Great Earthquake Triggered Doublet; a Magnitude 8 Stealth Earthquake"
Tuesday, September 21, 2010

JEREMY ZECHAR
"Swiss Seismological Service of ETH Zurich A sampling of statistical seismology"
Tuesday, September 28, 2010

JUSTIN BROWN
Stanford
"Seismology by Analogy: Using autocorrelation to detect repeating events within continuous data"
Tuesday, October 5, 2010

IAN BOURG
LBNL
"Minerals, Brines, and CO₂: Molecular Modeling and Carbon Storage"
Tuesday, October 12, 2010

ERIC KING
Visiting Miller fellow from UCLA
"Regimes of rotating convection: the importance of boundary layers"
Tuesday, October 19, 2010

GABI LASKE
UC San Diego
"The Hawaiian PLUME project: searching for Hawaii's magma source"
Tuesday, October 26, 2010

GREG MCLASKEY
UC Berkeley
"The Sound of Friction: Nanoseismic analysis and implications for earthquake studies"
Tuesday, November 2, 2010

ERIC DUNHAM
Stanford
"Complexity of the Earthquake Source and its Influence on Strong Ground Motion"
Tuesday, November 9, 2010

PAUL BODIN
University of Washington
"Seismicity, Aseismicity, and Episeismicity of Cascadia"
Tuesday, November 16, 2010

HIROO KANAMORI
Caltech
"The 1960 Chilean Earthquake"
Tuesday, November 23, 2010

MAARTEN DE HOOP
Purdue University
"Wave-equation imaging and inverse scattering: Multi-scale techniques and applications to the mantle beneath Hawaii"
Tuesday, November 30, 2010

RUDY WENK
UC Berkeley
"Anisotropy in the Deep Earth: From microscopic mechanisms (nm) to macroscopic evidence (1000km)"
Tuesday, December 7, 2010

MARK QUIGLEY
University of Canterbury, New Zealand
"The 2010 Mw 7.1 Darfield (Canterbury) earthquake in New Zealand: a personal account"
Tuesday, January 25, 2011

SJOERD DE RIDDER
Stanford University
"Ambient seismic noise correlations for seismic exploration and reservoir monitoring"
Tuesday, February 1, 2011

JAMES BADRO
IPGP
"Experimental constraints on core composition and the paradigm of core formation"
Tuesday, February 8, 2011

MIKE PASYANOS
LLNL
"Attenuation of the Crust and Upper Mantle: Method, Results, and Applications"
Tuesday, February 15, 2011

HUAIYU YUAN
UC Berkeley
"Seismic anisotropy in the North American upper mantle and its tectonic implications"
Tuesday, February 22, 2011

WILLIAM ELLSWORTH
USGS, Menlo Park
"Gutenberg-Richter breakdown and the smallest earthquakes at the San Andreas Observatory at Depth"
Tuesday, March 1, 2011

ROBERT MELLORS
LLNL
"Earthquakes, mud volcanoes, and InSAR"
Tuesday, March 8, 2011

ANDY MICHAELS
USGS, Menlo Park
"Was that a foreshock? A tale of earthquake fundamentals and public warnings"
Tuesday, March 15, 2011

Tuesday, March 22, 2011
Spring Break - no seminar

BRUCE BUFFETT
UC Berkeley
"Chemical interactions between the core and the mantle"
Tuesday, March 29, 2011

NICK BEELER
USGS, Vancouver
"Seismicity triggered by deep fault slip and tidal forcing, as expected from laboratory friction experiments"
Tuesday, April 5, 2011

BENJAMIN BROOKS
University of Hawaii
"Great Earthquakes and Andean Mountain Building"
Tuesday, April 10, 2011

ANNEMARIE BALTAY
Stanford University
"Radiated Seismic Energy and Stress Drop of Magnitude 2-9 Earthquakes in Tohoku, Japan"
Tuesday, April 19, 2011

PETER GEISER
Global Geophysical Services
"Tomographic fracture imaging and mapping: geology, geophysics, case studies and its application to earthquake seismology"
Tuesday, April 26, 2011

HUGH WILSON
UC Berkeley
"Understanding planets one atom at a time: ab initio calculations of planetary interiors"
Tuesday, May 3, 2011

SHEMIN GE
University of Colorado – Boulder
"Groundwater earthquake interactions: stress change beneath a reservoir"
Tuesday, May 10, 2011

